The layered structure of the ocular coats can be visualized with high contrast using the RCM attachment with the HRT II and, because of the good quality of depth resolution, can be imaged in optical sections a few micrometers thick. The description of the normal in vivo microanatomy will proceed inward, beginning with the outer structures.

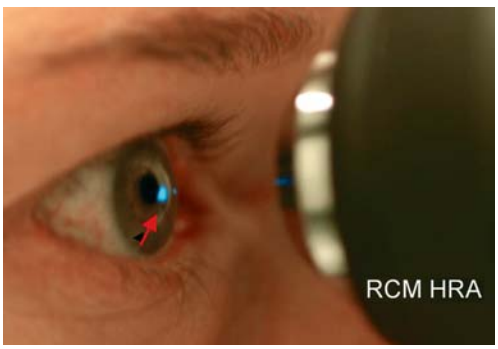

Fig. 5.1 Noncontact microscopy. Scanning laser reflex (*arrow*) on the cornea (argon laser/Heidelberg Retina Angiograph Classic)

5.1 Tear Film

5.1.1 Normal Anatomy

The preocular tear film with its complex fluid structure bathes the cornea and conjunctiva. Tear film structure and function are maintained by a highly differentiated system of secretory, distributive, and excretory interactions [24, 62, 73]. In particular, these function to smooth the corneal surface and maintain its optical clarity. The water content of the cornea is regulated by evaporation and the resultant osmotic gradient. The oxygen in the air is dissolved in the tear fluid and thus supports the aerobic metabolism of the epithelium.

The tear film is 7–10 µm thick and is characterized by a three-layered structure. The external lipid layer, which is produced chiefly by the meibomian glands close to the margin of the eyelids, prevents rapid evaporation of the aqueous layer and renders the surface hydrophobic. The inner mucin layer consists of glycoproteins. Its task is to make the epithelial surface hydrophobic and thus guarantee wettability.

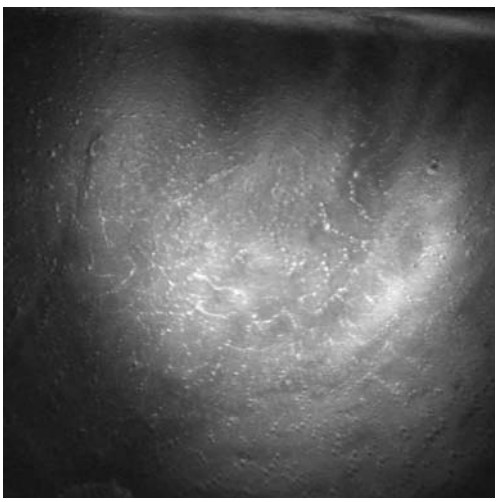

Fig. 5.2 Normal tear film

Replacing the contact system in the confocal laser scanning microscope with a dry objective lens, combined with an 80–90% absorption gray filter to decrease laser intensity (Fig. 5.1), enables the fine structure of the tear film to be imaged (Fig. 5.2). The rapid imaging sequence in the device also permits dynamic processes to be recorded [51, 77, 88].

5.1.2 Pathological Findings

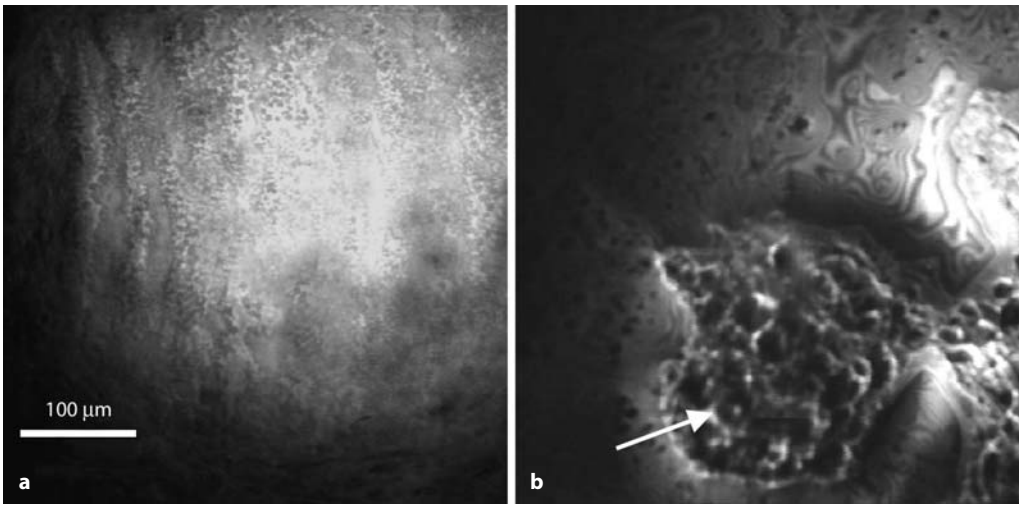

Fig. 5.3 Normal and pathological tear film. **a** Normal tear film, noncontact examination. **b** Tear film with dry spot (*arrow*) in a patient with pathological break-up time; the surface of the superficial cells is visible in the area of the dry spot

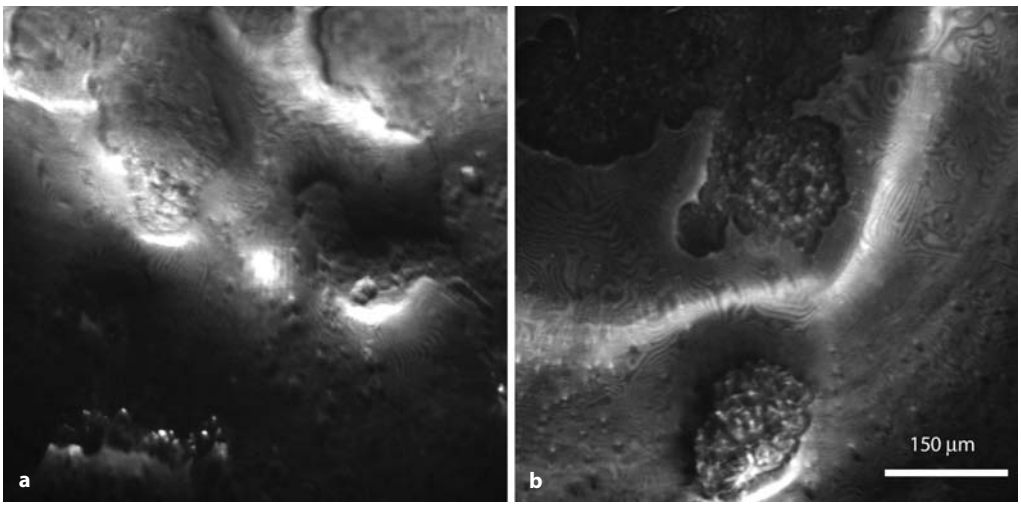

Fig. 5.4 Further dry spots in the tear film (**a, b;** Heidelberg Retina Angiograph, red-free mode)

5.2 Epithelium

5.2.1 Normal Anatomy

5.2.1.1 Superficial Cells (Up to Approximately 50 μm in Diameter)

In the case of the most superficial epithelial cells, bright cell borders and a dark cell nucleus and cytoplasm are readily visualized on confocal laser scanning microscopy. The cells characteristically display a polygonal – often hexagonal – shape. Cells undergoing desquamation are characterized by a highly reflective cytoplasm, in the center of which the brightly appearing (pyknic) cell nucleus with its dark perinuclear space is clearly visible (Fig. 5.5). The average density of superficial cells in the central and peripheral cornea is approximately 850 cells/mm²

5.2.1.2 Intermediate Cells/Wing Cells (Up to Approximately 20 μm in Diameter)

The cells of the intermediate layers are characterized by bright cell borders and a dark cytoplasm. The cell nucleus can be distinguished only with difficulty. In terms of size and appearance, wing cells in healthy subjects exhibit only minimal variation (Fig. 5.6). The average density is approximately 5,000 cells/mm² in the central cornea and approximately 5,500 cells/mm² in the periphery.

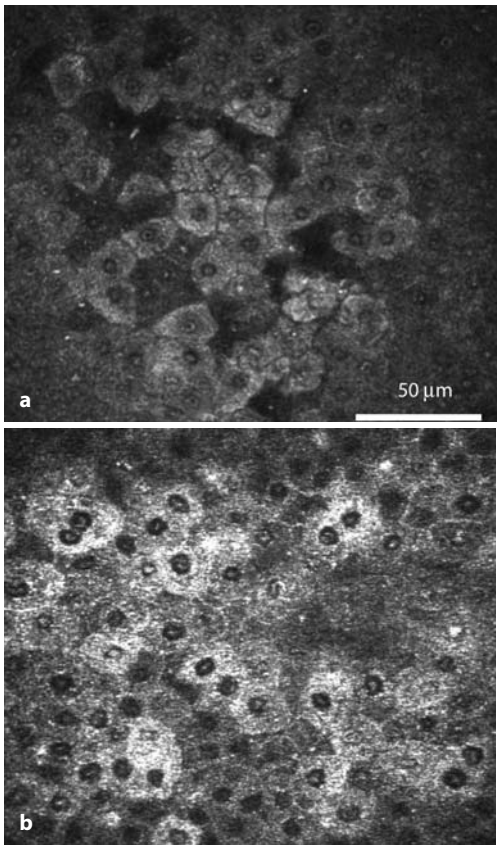

Fig. 5.5 Superficial cells: the cytoplasm and cell nuclei are visualized; cells in the process of desquamation possess a highly reflective cytoplasm, in the center of which the bright (pyknic) cell nucleus with its dark perinuclear space is clearly visible. **a** Uncompressed superficial cells, using a special TomoCap with a central hole. **b** Compressed superficial cells, using the standard TomoCap

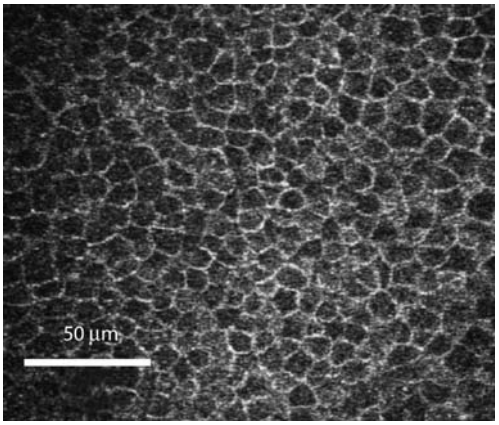

Fig. 5.6 Intermediate cells: the cells of the intermediate layers are characterized by bright cell borders and a dark cytoplasm. The cell nucleus can be identified only with difficulty. The wing cells display only minimal variation in terms of size and appearance

5.2.1.3 Basal Cells (Up to Approximately 10 µm in Diameter)

The basal cells are located immediately above Bowman's membrane. They present as brightly bordered cells in which the cell nucleus is not visible. Between-cell comparison reveals inhomogeneous reflectivity of the cytoplasm. Like the wing cells above them, the basal cells display only minimal variation in shape and size (Fig. 5.7). The average density is approximately 9,000 cells/mm² in the center of the cornea and 10,000 cells/mm² in the periphery. Therefore, in terms of cell densities in normal subjects, the ratio between superficial cells, intermediate cells, and basal cells is 1:5:10.

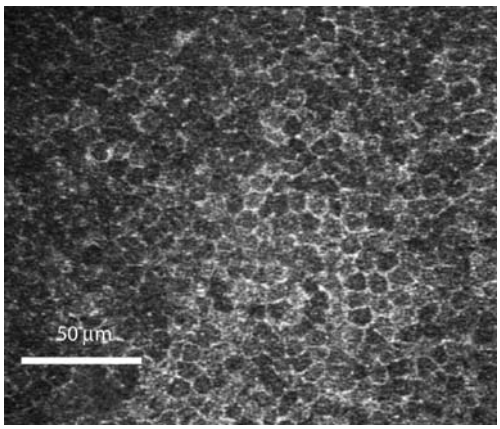

Fig. 5.7 Basal cells. These are regularly arranged cells with bright borders, but the cell nucleus is not visualized. Intercellular comparison reveals inhomogeneous cytoplasmic reflectivity

5.2.1.4 Langerhans Cells

Confocal microscopy permits in vivo evaluation of Langerhans cells (LCs) within the human cornea, with a particular emphasis on cell morphology and cell distribution.

LCs present as bright corpuscular particles with dendritic cell morphology and a diameter of up to 15 µm. LC distribution follows a gradient from low numbers in the center to higher cell densities in the periphery of the cornea. Moreover, confocal in vivo microscopy permits differentiation of LC bodies lacking dendrites, LCs with small dendritic processes forming a local network, and LCs forming a meshwork via long interdigitating dendrites (Fig. 5.8a–c). Whereas almost all the cells located in the periphery of the cornea demonstrate long processes interdigitating with the corneal epithelium, those in the center of the cornea often lack dendrites, most probably underlining their immature phenotype [26]. Immature LCs are equipped to capture antigens, while mature forms are able to sensitize naive T-cells through MHC molecules and secretion of interleukin-12 as well as costimulatory molecules, and thus represent an integral part of the immune system [3].

The average density of LCs in normal subjects is 34±3 cells/mm² (range 0–64 cells/mm²) in the central cornea and 98±8 cells/mm² (range 0–208 cells/mm²) in the periphery [96]. In contact lens wearers, LC density varies from 78±25 cells/mm² (range 0–600 cells/mm²) in the central cornea to 210±24 cells/mm² (range 0–700 cells/mm²) in the periphery. LC densities differ significantly between healthy volunteers and contact lens wearers both in the central (p=0.03) and in the peripheral cornea (p=0.001), while the gradient of LC density from periphery to center has been found to be almost identical in the two groups (unpublished data).

It has been suggested that LCs participate in immune and inflammatory responses, thereby determining cell-mediated immunity. In light of this theory, the present data on LCs in the human cornea provide a helpful basis for further investigations in ocular pathology.

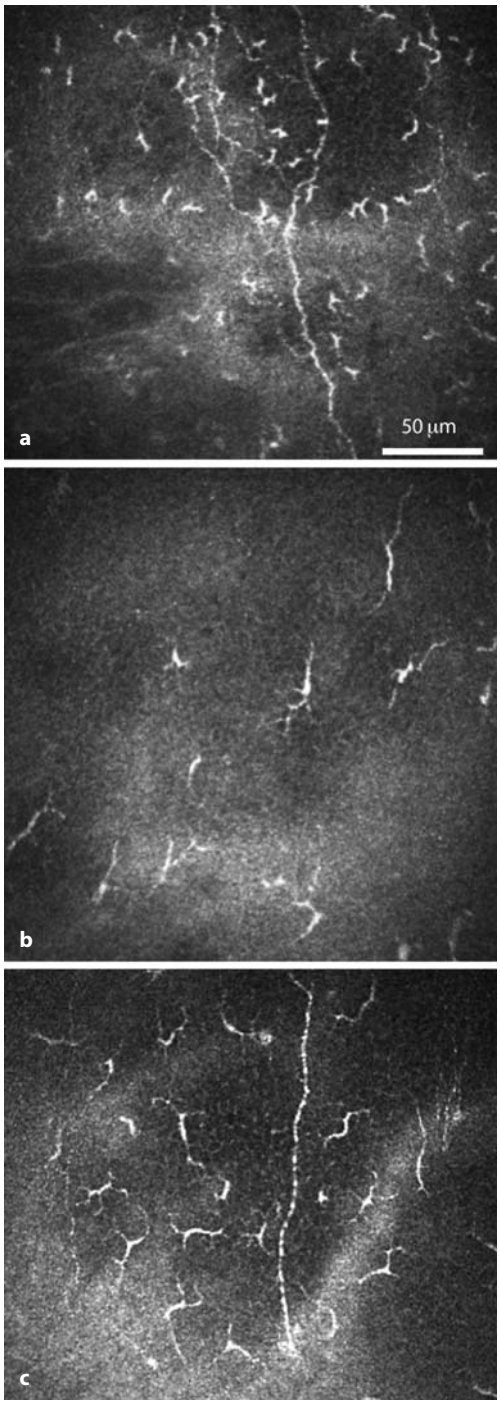

Fig. 5.8 In vivo confocal microscopic images, representing different forms of Langerhans cells. **a** Individual cell bodies without processes. **b** Cells bearing dendrites. **c** Cells arranged in a meshwork via long interdigitating dendrites

5.2.2 Pathological Findings

5.2.2.1 Dry Eye

Disturbances of tear film secretion or tear film structure give rise to a condition known as dry eye. On microscopy such disturbances are evident as altered reflection or dry spots on the epithelium.

As the most important component of the corneal diffusion barrier, the corneal epithelium displays differing permeability for aqueous ionic substances such as NaF. Patients with diabetes, for example, have significantly increased permeability for NaF. NaF also penetrates areas of microerosions and pathologically altered cells. The literature reveals discrepant views concerning the nature of the penetration process. Most authors subscribe to the view that the fluorescein fills the "footprint" spaces vacated by cells that have been lost. Others, however, assume that fluorescein fills the intercellular space. At present, only confocal slit-scanning microscopes and fluorophotometers are used to analyze this phenomenon.

The HRA in combination with the RCM can be used for confocal laser scanning fluorescence microscopy of the microstructure of the corneal epithelium and tear film using contact and non-contact techniques (see Fig. 2.18) with a lateral resolution of 1 µm and up to ×1,000 magnification. The red-free reflection and fluorescence images display the intercellular microstructure with stained cell nuclei and altered cell surfaces and borders. The same area examined on the cornea can be visualized simultaneously in reflection and fluorescence mode. The penetration profile of NaF can be measured with precise depth resolution over a prolonged time using the contact technique. Autofluorescence measurements are also possible. Figure 5.11 shows the tear film and epithelium in fluorescence mode.

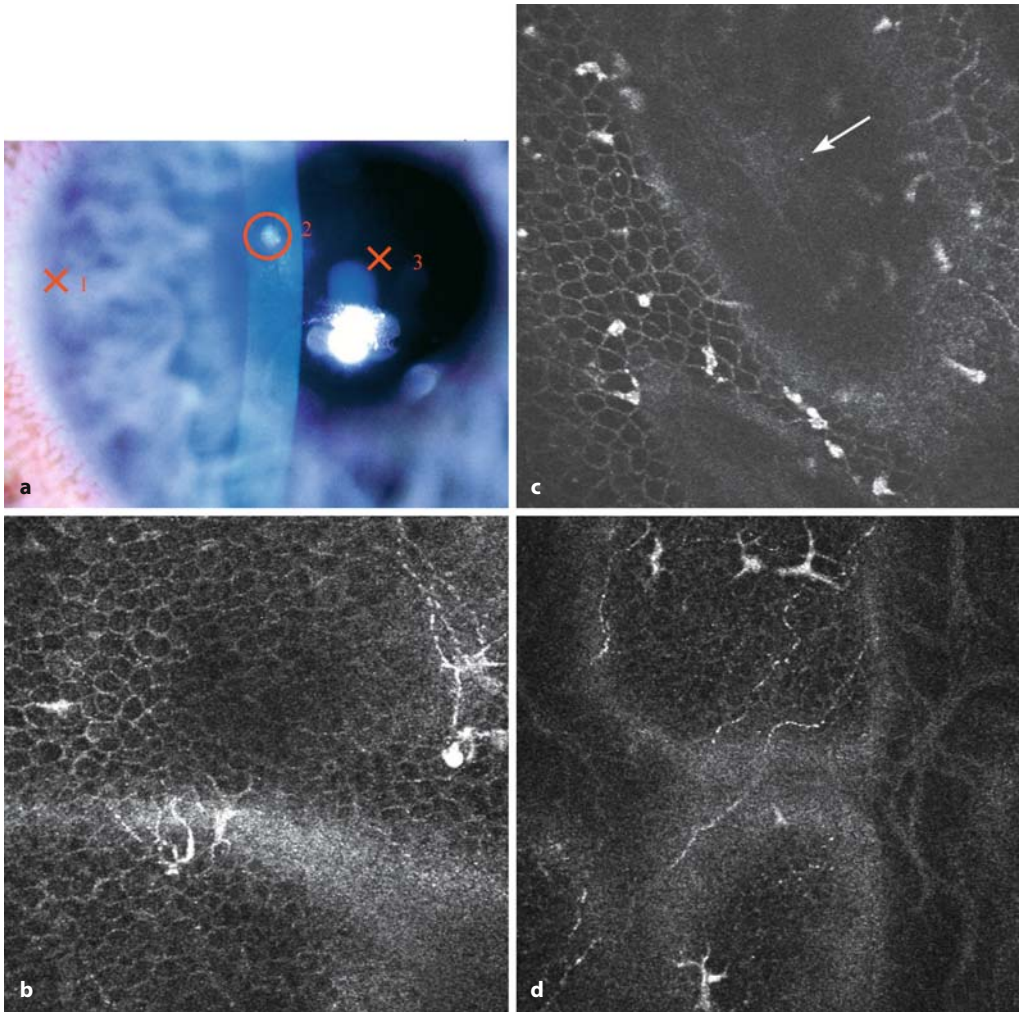

Fig. 5.9 Corneal erosion. **a** Slit-lamp photograph of 25-year-old man on day 2 after foreign body removal. Fluorescein discoloration is minimal, other corneal areas are clear, and there are no signs of intraocular inflammation. **b–d** Confocal images of the corneal periphery. **b** Level of lower intermediate and basal cells and subepithelial nerve plexus with dendritic cells. **c** Intraepithelial defect at the level of Bowman's membrane with leukocyte infiltration. Note the visible anterior stroma (*arrow*), **d** the mature form of Langerhans cells at the levels of the basal cells, and Bowman's membrane in the central cornea

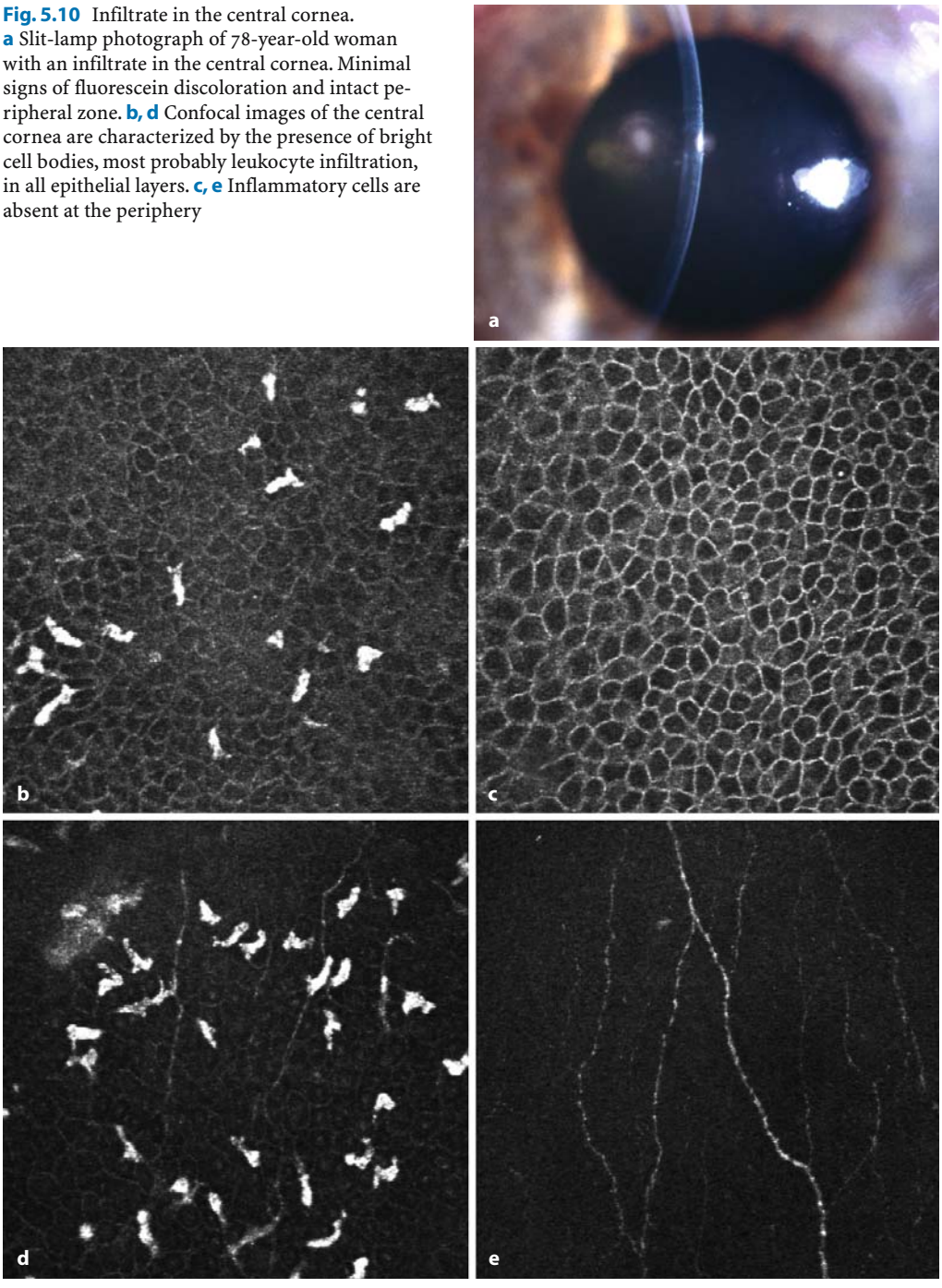

Fig. 5.10 Infiltrate in the central cornea. **a** Slit-lamp photograph of 78-year-old woman with an infiltrate in the central cornea. Minimal signs of fluorescein discoloration and intact peripheral zone. **b, d** Confocal images of the central cornea are characterized by the presence of bright cell bodies, most probably leukocyte infiltration, in all epithelial layers. **c, e** Inflammatory cells are absent at the periphery

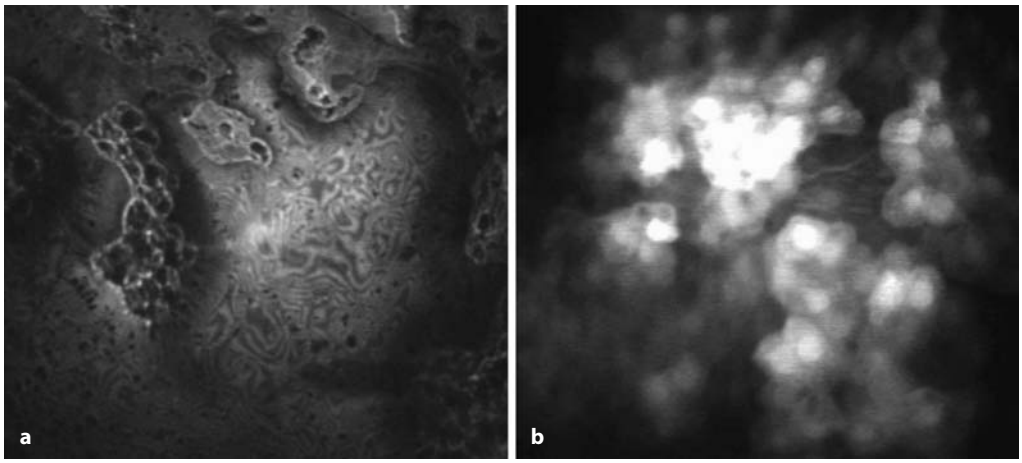

Fig. 5.11 Tear film (Heidelberg Retina Angiograph Classic). **a** Reflection mode: tear film defect causing the surface of the superficial epithelial cells to be visible. **b** Fluorescence mode: individual epithelial cells visible on sodium fluorescein staining

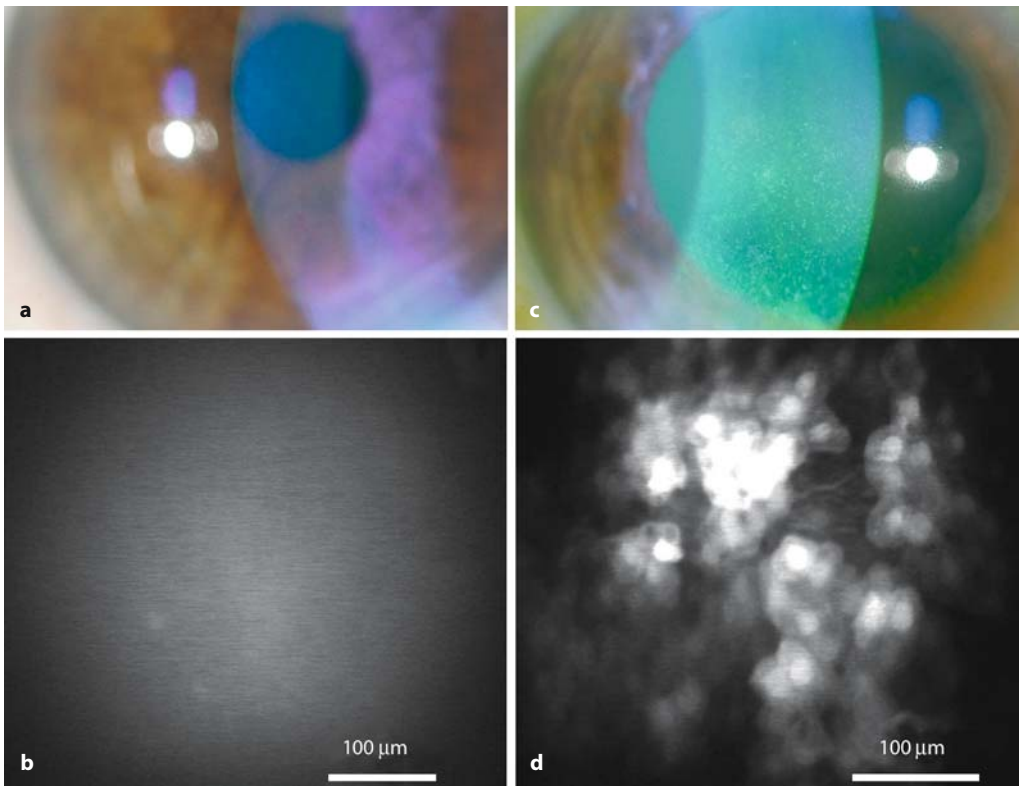

Fig. 5.12 Confocal fluorescence microscopy before and after applanation tonometry. **a** Slit-lamp photograph before applanation tonometry. **b** Fluorescence microscopy: no relevant fluorescein staining. **c** Slit-lamp photograph after applanation tonometry: stippled epithelial lesions. **d** Fluorescence microscopy: fluorescein-stained superficial cells

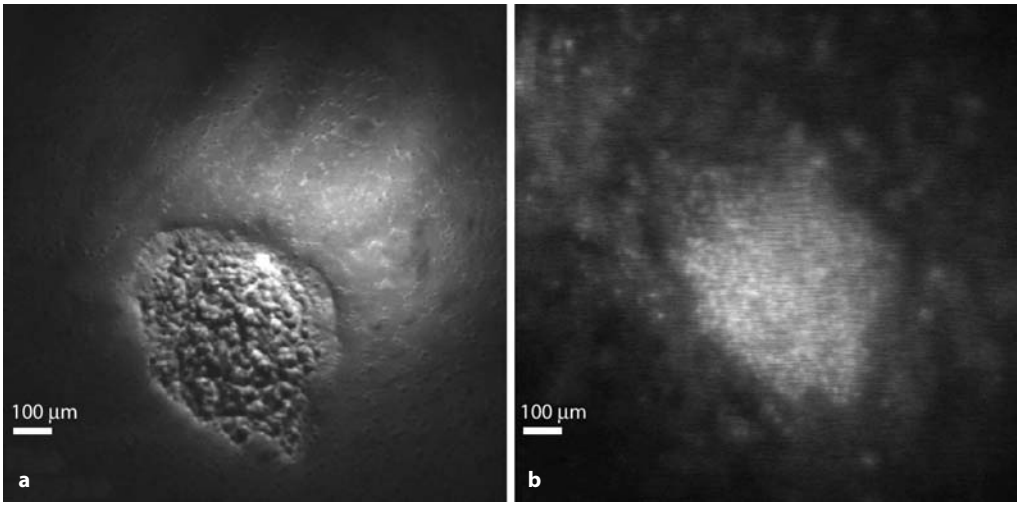

Fig. 5.13 Dry eye. **a** Dry spot in the tear film; non-contact examination using the Heidelberg Retina Angiograph Classic and the Rostock Cornea Module. **b** Same area after switching to fluorescence mode. The superficial cells in the region of the dry spot are stained with fluorescein

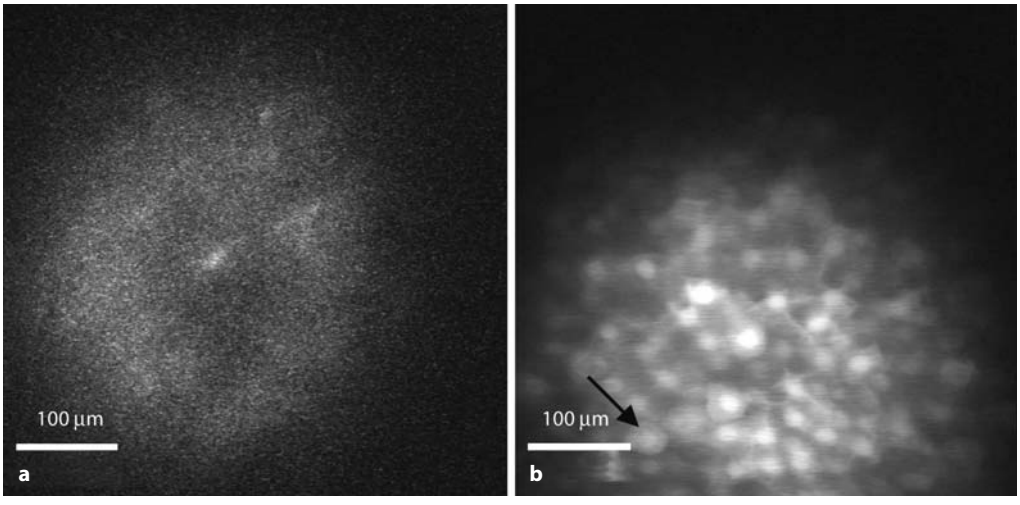

Fig. 5.14 Dry eye (fluorescence mode, contact examination). **a** Superficial cells of the normal cornea: only a few cells with minimal fluorescence. **b** Superficial cells of a stippled cornea: many cells are fluorescein-stained, and there is intracellular staining of the cell nuclei (*arrow*)

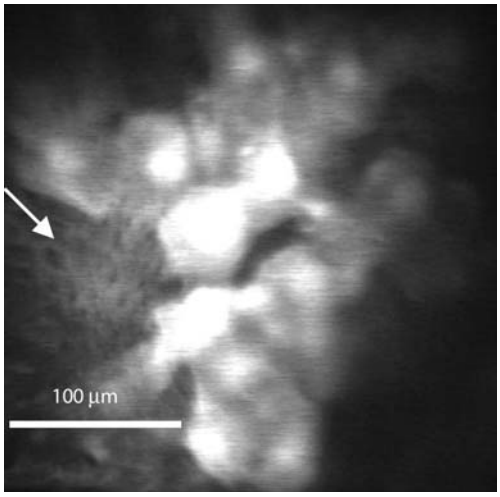

Fig. 5.15 Corneal erosion (fluorescence mode, contact examination). Fluorescein-stained superficial cells (up to 50 µm in size). In the left part of the picture (*arrow*), the borders of the smaller intermediate cells are visible

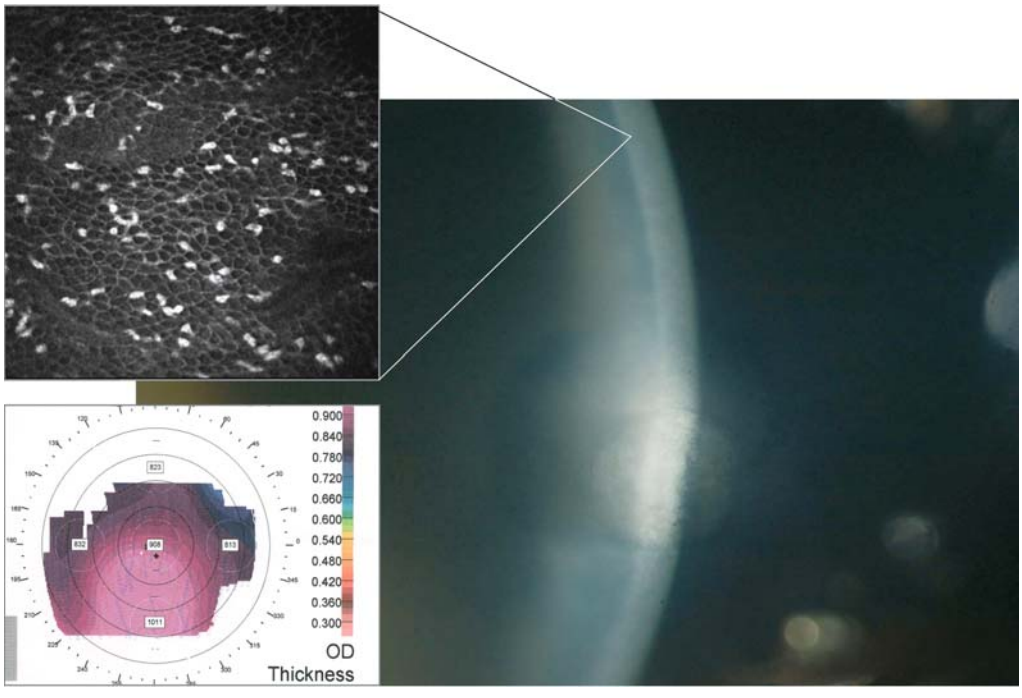

Fig. 5.16 Corneal edema. Confocal images of central cornea. Infiltration of epithelium with antigen-presenting cells and leukocytes; corneal thickness (Orbscan) 908 µm in center

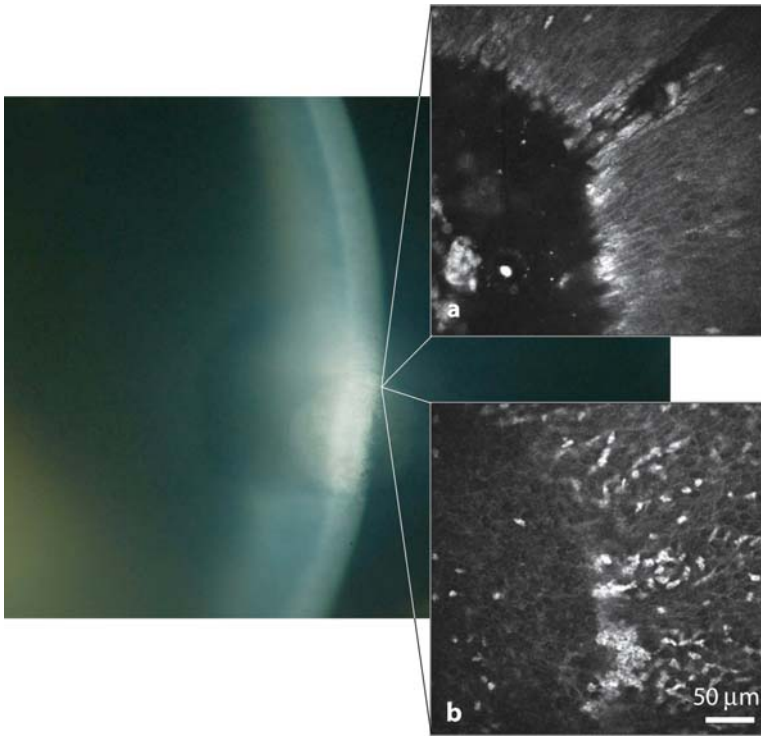

Fig. 5.17 Corneal infiltrate due to contact lens wear. Confocal images of transition area (from normal cornea to ulcer). **a** Edematous changes in epithelium and absence of cells in ulcer zone. **b** Massive leukocyte infiltration in transition area at the level of wing cells

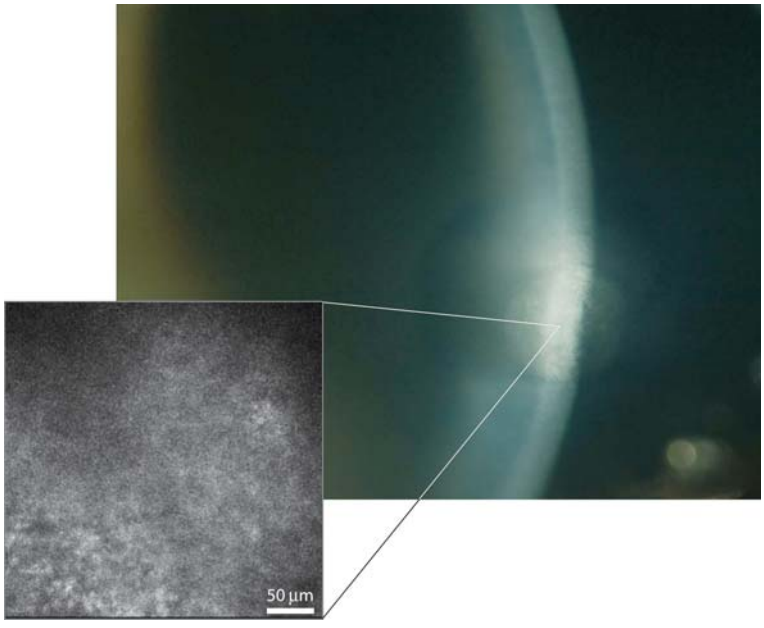

Fig. 5.18 Corneal infiltrate due to contact lens wear. Confocal image of infiltrate zone. Absence of cellular or structural elements in the defect area

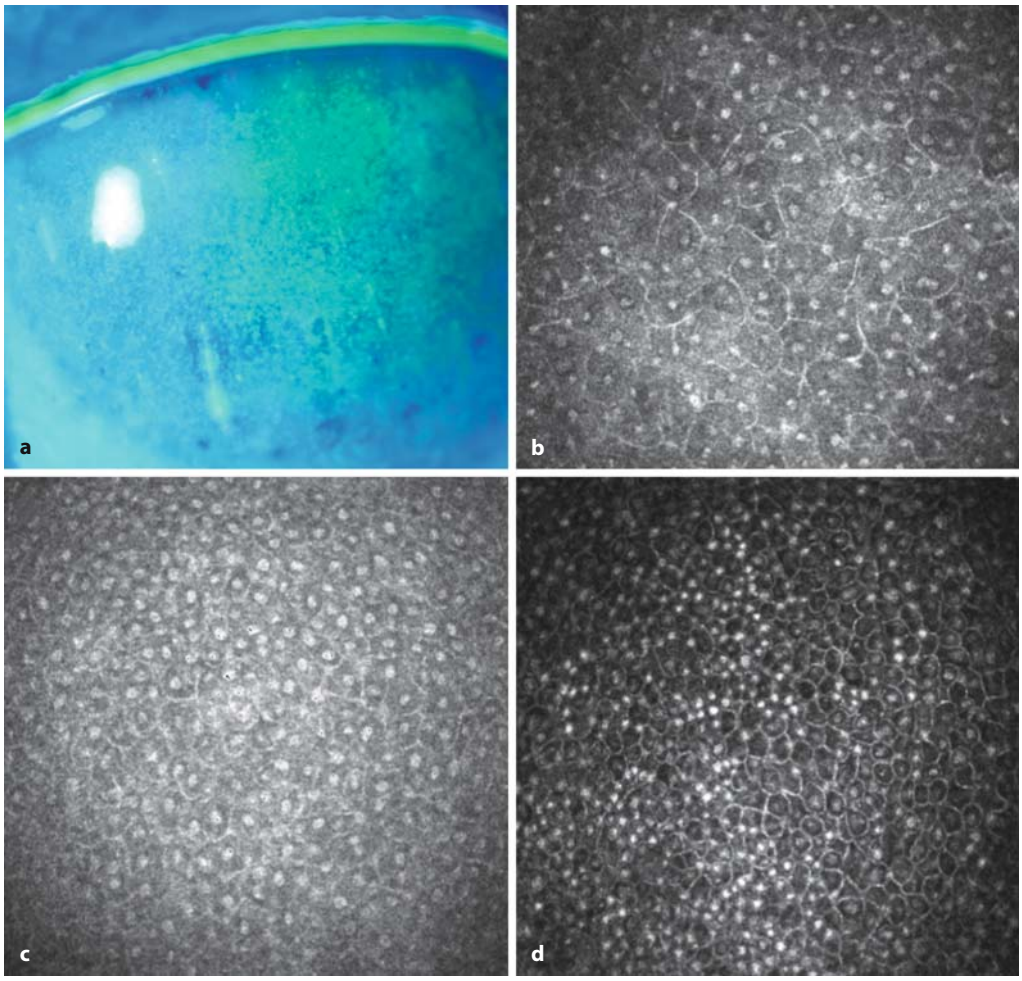

Fig. 5.19 Keratoconjunctivitis sicca. **a** Slit-lamp photograph of a 45-year-old woman with keratoconjunctivitis sicca. Severe punctate keratitis on fluorescein staining. **b–d** Confocal in vivo microscopy images showing corneal epithelial metaplasia with enlarged cells, activated nuclei, and decreased nucleus/cytoplasm ratio

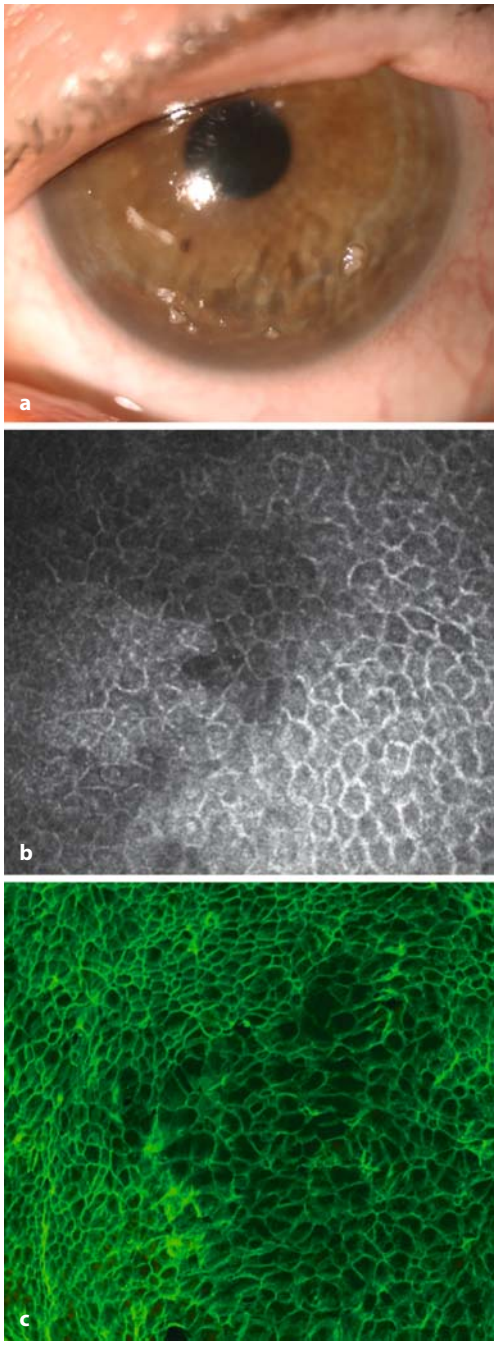

Fig. 5.20 Keratoconjunctivitis sicca in a case of Sjögren's syndrome. **a** Slit-lamp photograph of a 50-year-old woman with severe keratoconjunctivitis sicca. **b** Confocal in-vivo microscopy image of abnormal corneal-conjunctival junction at the limbus. **c** Impression cytology of the limbus showing the same abnormal corneal–conjunctival junction

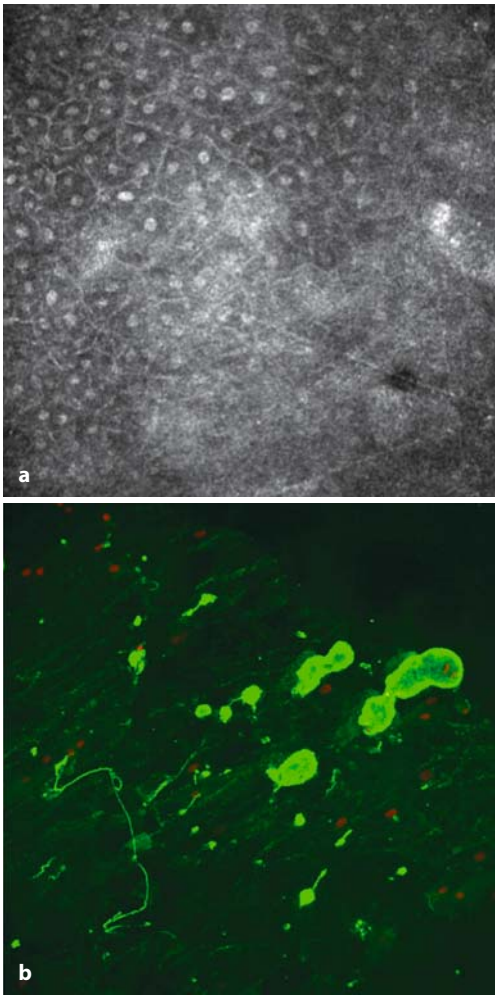

Fig. 5.21 Keratoconjunctivitis sicca in a case of Sjögren's syndrome. **a** Confocal in-vivo microscopy image showing corneal metaplasia. Enlarged corneal cells displaying reflective nuclei and polymorphism. **b** Impression cytology immunostaining: goblet cells (*green*) in the corneal epithelium

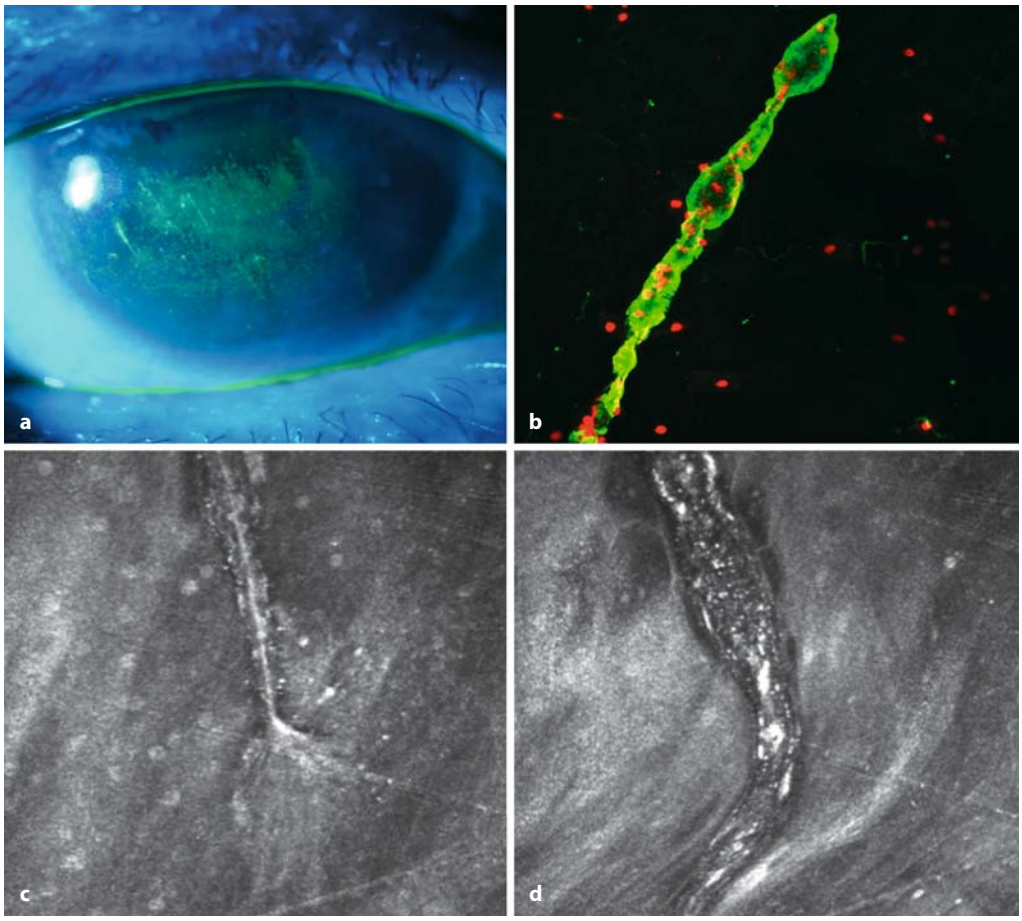

Fig. 5.22 Filamentous keratitis in a case of Sjögren's syndrome. **a** Slit-lamp photograph of a 51-year-old woman showing severe filamentous keratitis. **b** Impression cytology and immunostaining of a filament. **c, d** Confocal in vivo microscopy image of the same filament

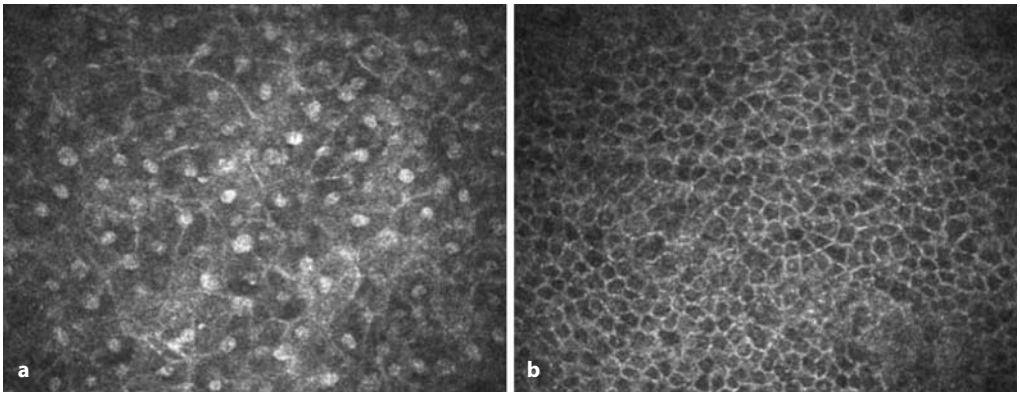

Fig. 5.23 Keratoconjunctivitis sicca. **a** Corneal metaplasia before treatment: polymorphism, enlarged cells, and reflective nuclei. **b** After treatment with topical cyclosporin A and clinical improvement: recovery of normal basal corneal cell appearance

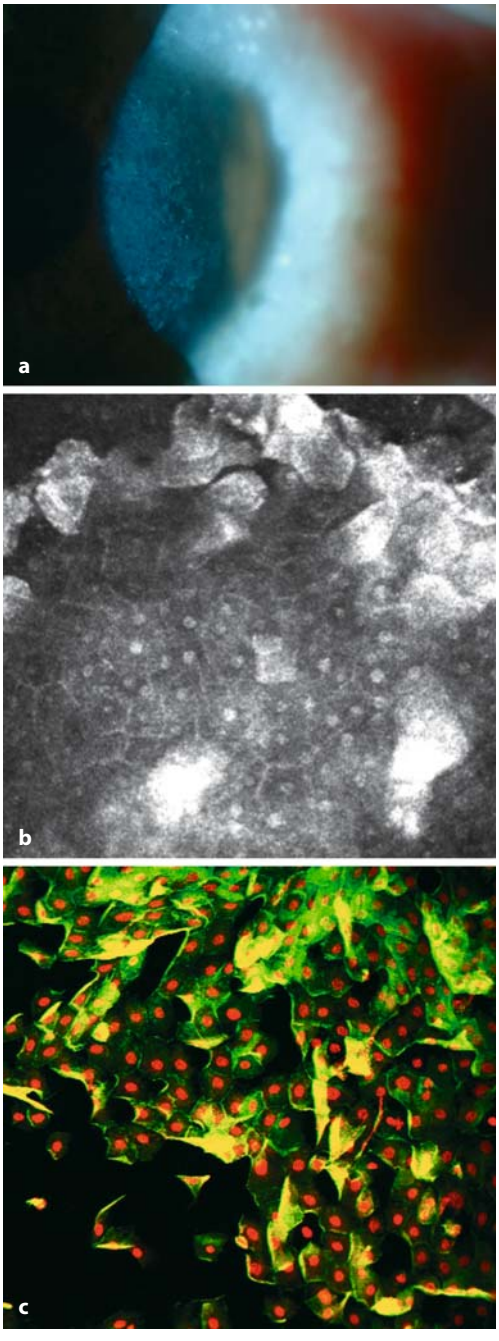

Fig. 5.24 Allergic keratoconjunctivitis: vernal keratoconjunctivitis. **a** Slit-lamp photograph of a 16-year-old boy with severe vernal keratoconjunctivitis causing corneal desiccation and corneal cell desquamation. **b** Confocal in vivo microscopy showing corneal epithelial metaplasia and hyperreflective desquamating superficial corneal cells. **c** Impression cytology image confirming corneal metaplasia

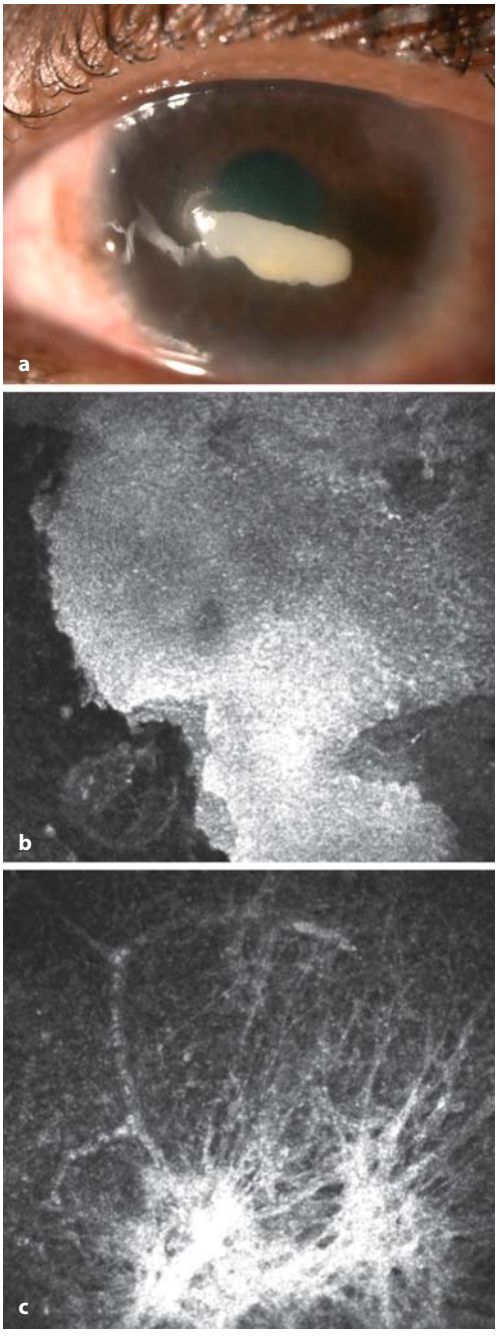

Fig. 5.25 Vernal keratoconjunctivitis. **a** Slit-lamp photograph of the same patient as in Fig. 5.24 1 year later, showing corneal vernal plaque. **b** Confocal in vivo microscopy image of the plaque with hyperreflective area within the corneal epithelium. **c** Confocal in vivo microscopy image of the scar after surgical scraping of the plaque

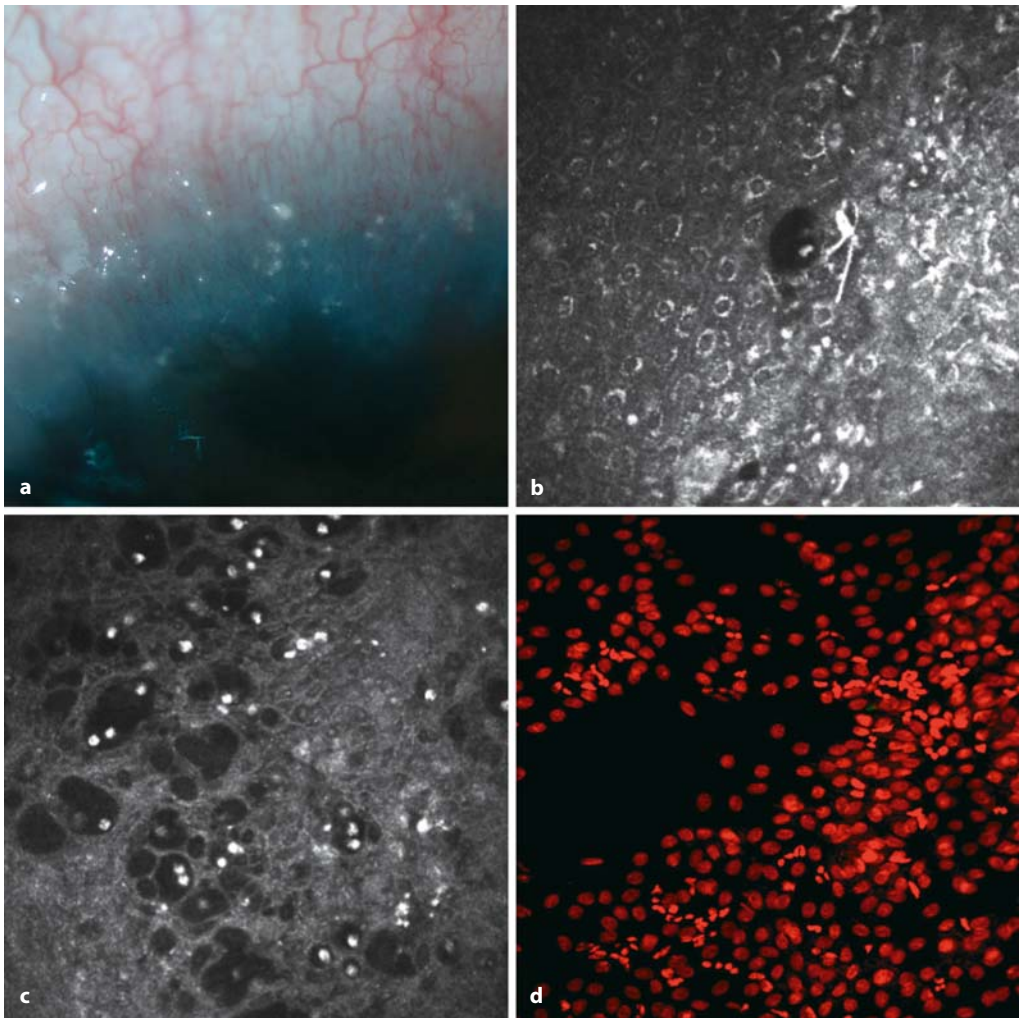

Fig. 5.26 Vernal keratoconjunctivitis. **a** Slit-lamp photograph of a 13-year-old boy with vernal keratoconjunctivitis: Trantas dots. **b** Confocal in vivo microscopy image of the limbus. Epithelial infiltration by dendritic cells. **c** Confocal in vivo microscopy image of Trantas dots: microcysts and inflammatory cells (*hyperreflective cells*). **d** Limbal impression cytology showing numerous inflammatory cells (*small red nuclei*) within the epithelium

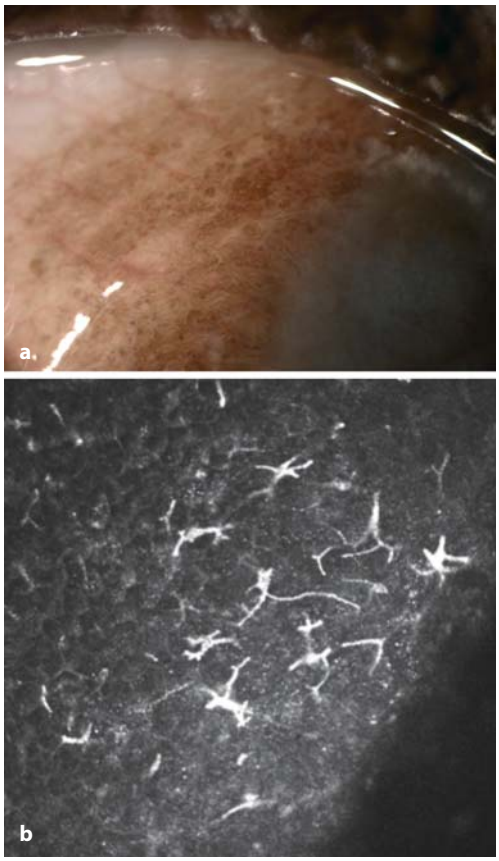

Fig. 5.27 Vernal keratoconjunctivitis. **a** Slit-lamp photograph of an 18-year-old man with vernal keratoconjunctivitis. Trantas dots. **b** Confocal in vivo microscopy image of the limbus. Numerous (*hyperreflective*) dendritic cells within the epithelium

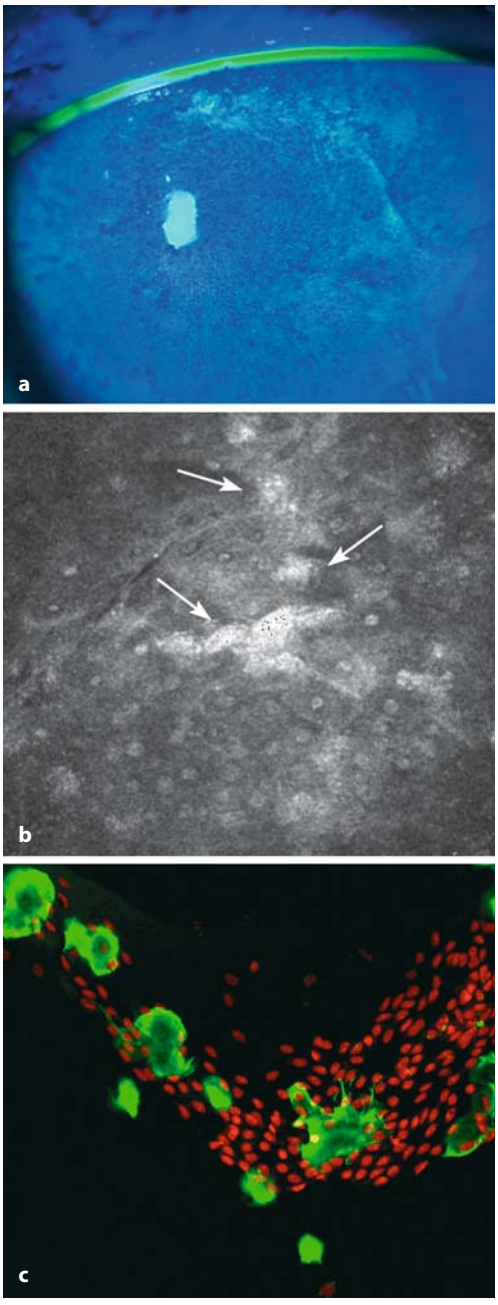

Fig. 5.28 Limbal stem cell deficiency and corneal conjunctivalization. **a** Slit-lamp photograph and fluorescein staining in a patient with corneal conjunctivalization. **b** Confocal in vivo microscopy image of corneal metaplasia with goblet cells within the corneal epithelium. **c** Impression cytology showing goblet cells (*green*) within the corneal epithelium (*red nuclei*)

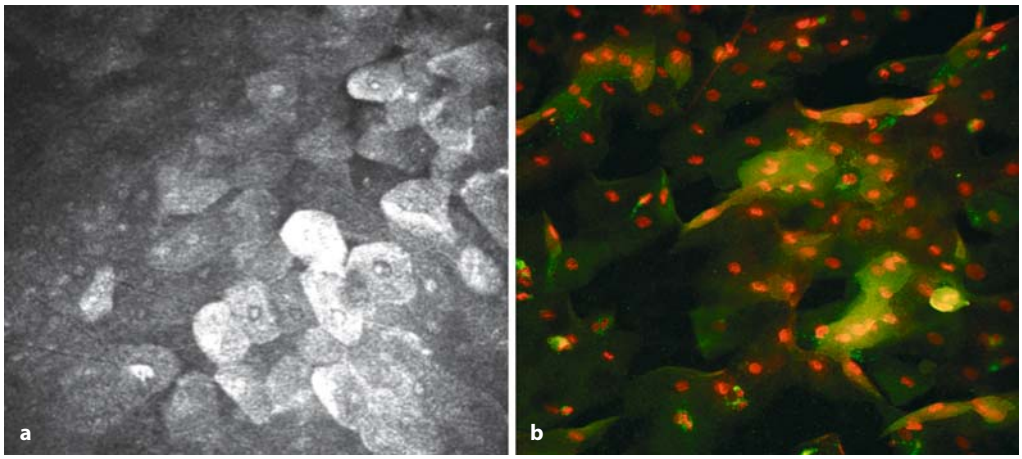

Fig. 5.29 Limbal stem cell deficiency. **a** Corneal metaplasia with hyperreflective enlarged cells similar to conjunctival cells. **b** Impression cytology of the cornea from the same patient

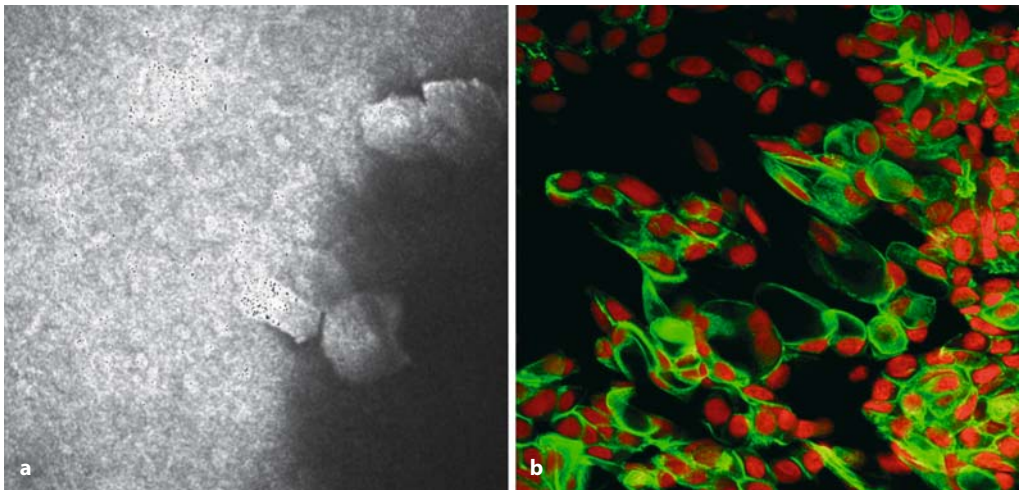

Fig. 5.30 Limbal stem cell deficiency. **a** Conjunctival epithelial and goblet cell migration within the corneal epithelium. **b** Impression cytology from the same patient showing goblet cells (*green*) within the corneal epithelium

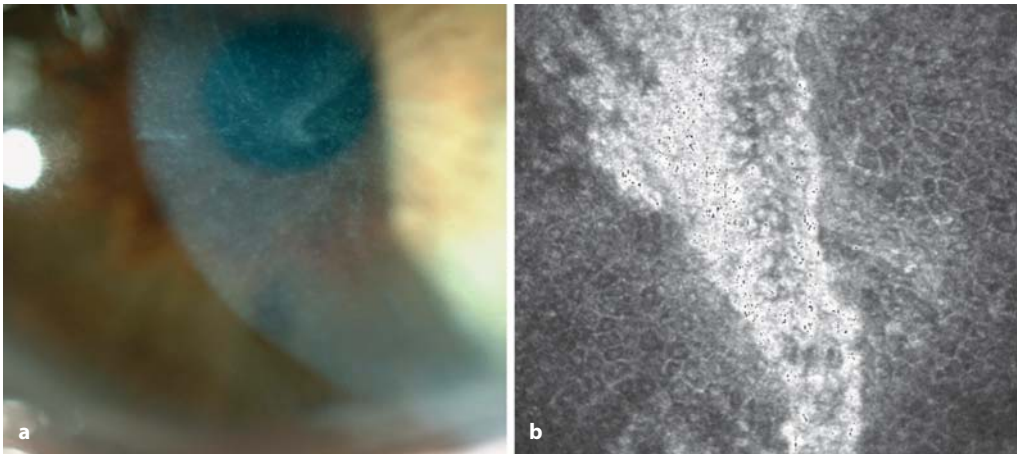

Fig. 5.31 Corneal epitheliopathy. **a** Slit-lamp photograph of a patient with severe ocular rosacea and conjunctival cell migration within the corneal epithelium. **b** Confocal in vivo microscopy image from the same patient. Conjunctival cells (*hyperreflective cells*) migrating into an abnormal corneal epithelium (*hyporeflective cells*)

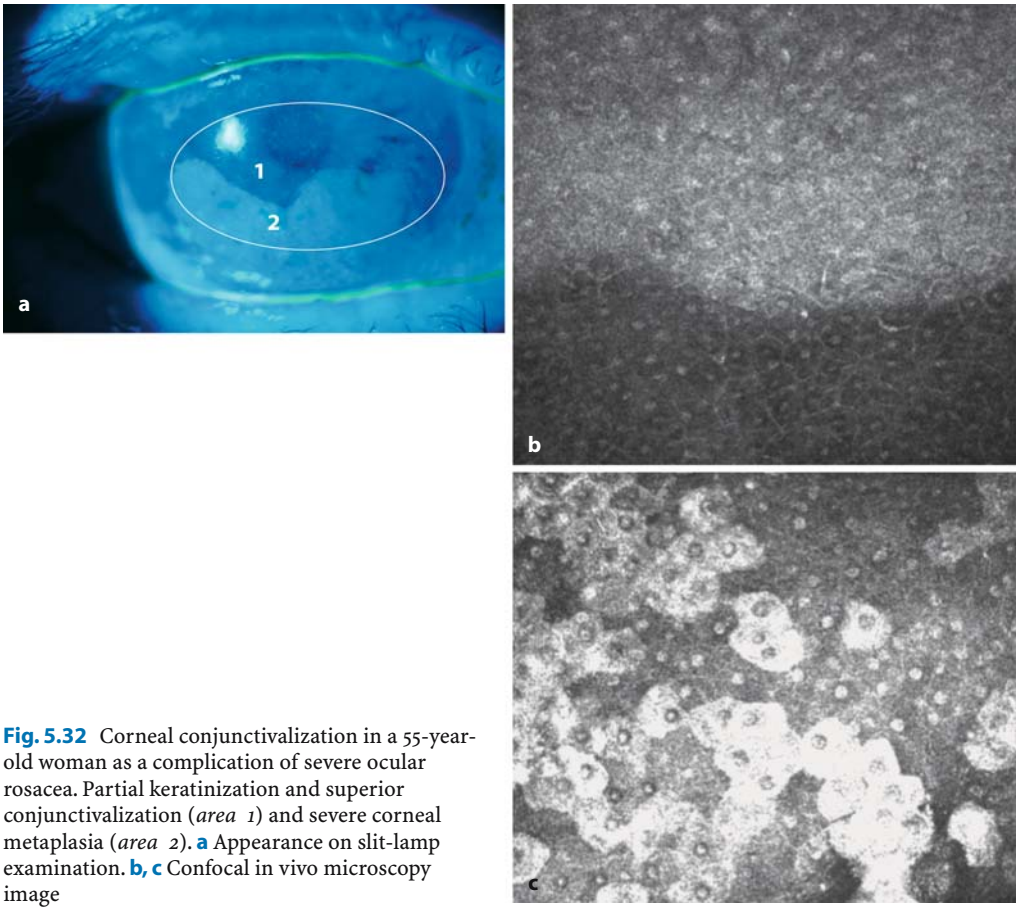

Fig. 5.32 Corneal conjunctivalization in a 55-year-old woman as a complication of severe ocular rosacea. Partial keratinization and superior conjunctivalization (*area 1*) and severe corneal metaplasia (*area 2*). **a** Appearance on slit-lamp examination. **b, c** Confocal in vivo microscopy image

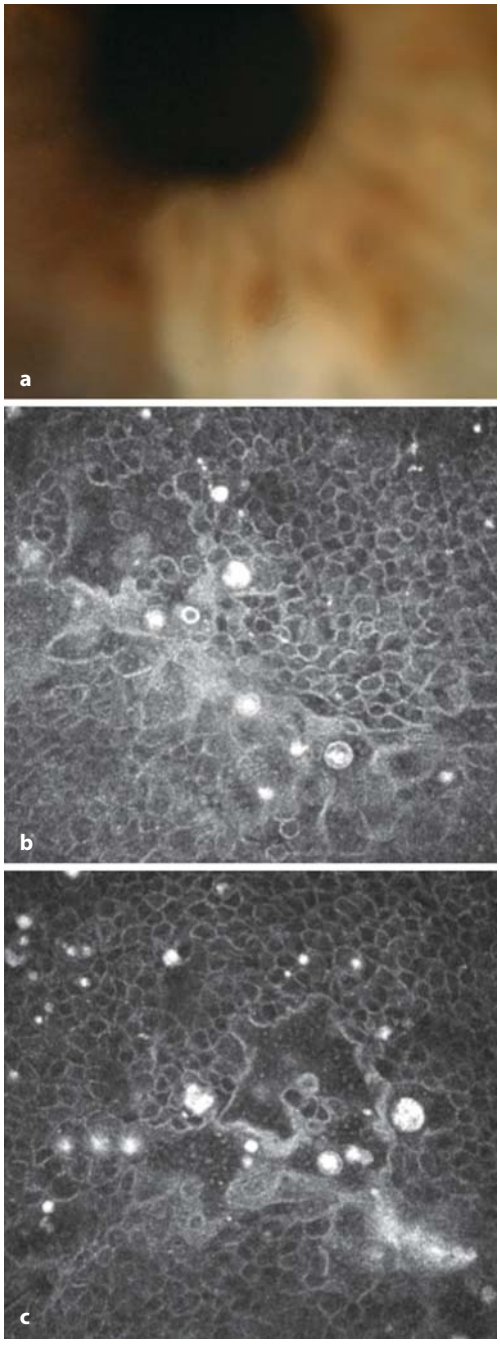

Fig. 5.33 Meesmann's corneal dystrophy. **a** Slit-lamp photograph of a patient with Meesmann's corneal dystrophy. Multiple epithelial cystic lesions. **b, c** Confocal in vivo microscopy images. Microcysts are seen as hyporeflective areas in the basal epithelial layer. Hyperreflective dots are observed inside most of the microcysts

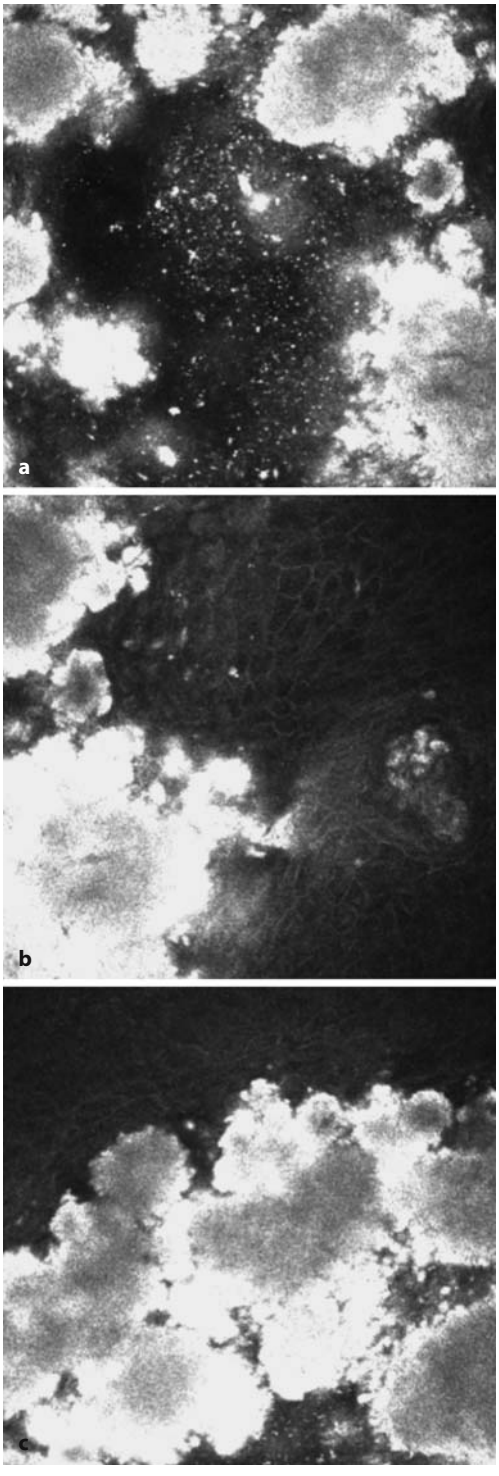

Fig. 5.34 Calcific band keratopathy. Hyperreflective areas in the corneal epithelium

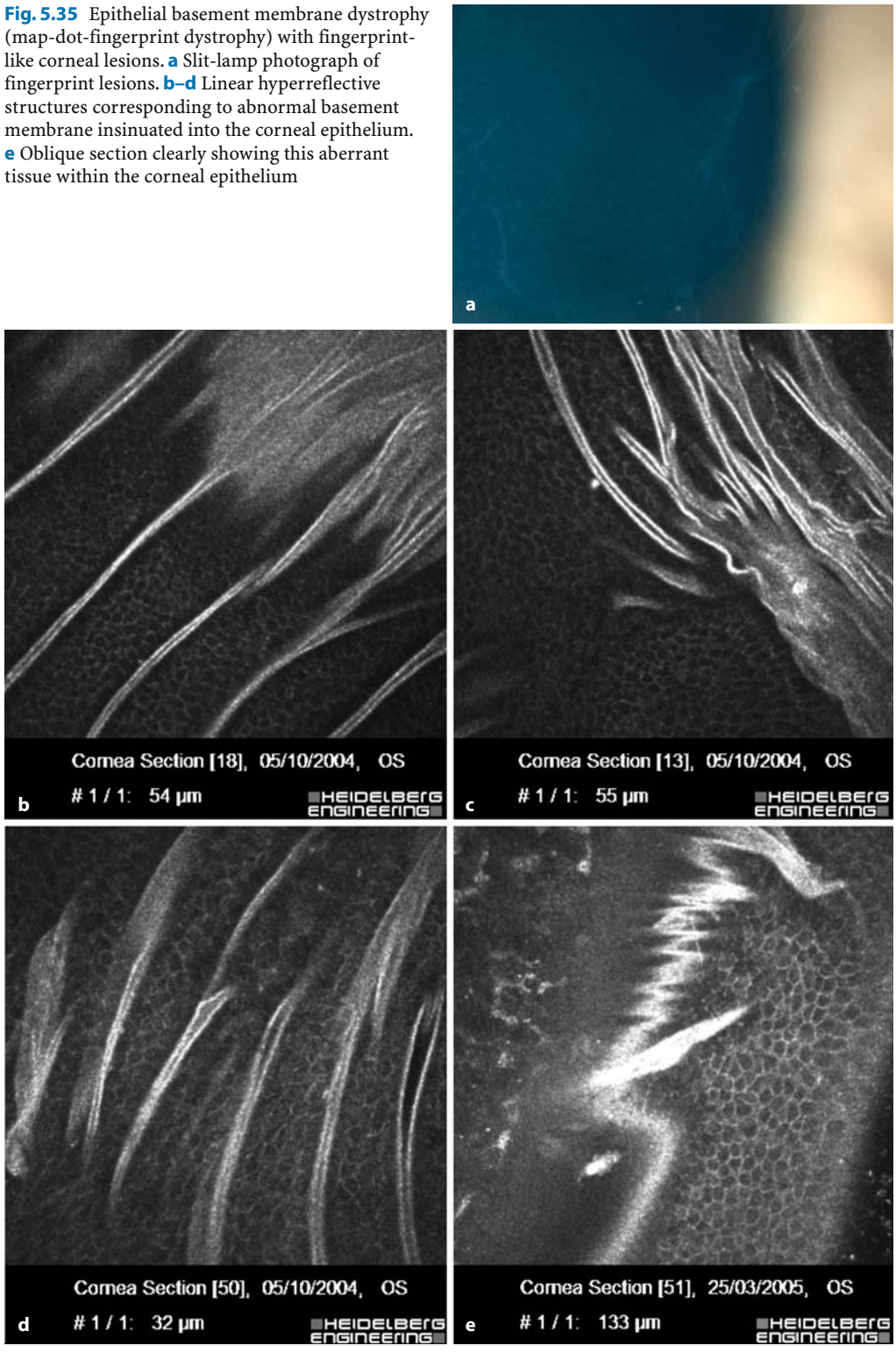

Fig. 5.35 Epithelial basement membrane dystrophy (map-dot-fingerprint dystrophy) with fingerprint-like corneal lesions. **a** Slit-lamp photograph of fingerprint lesions. **b–d** Linear hyperreflective structures corresponding to abnormal basement membrane insinuated into the corneal epithelium. **e** Oblique section clearly showing this aberrant tissue within the corneal epithelium

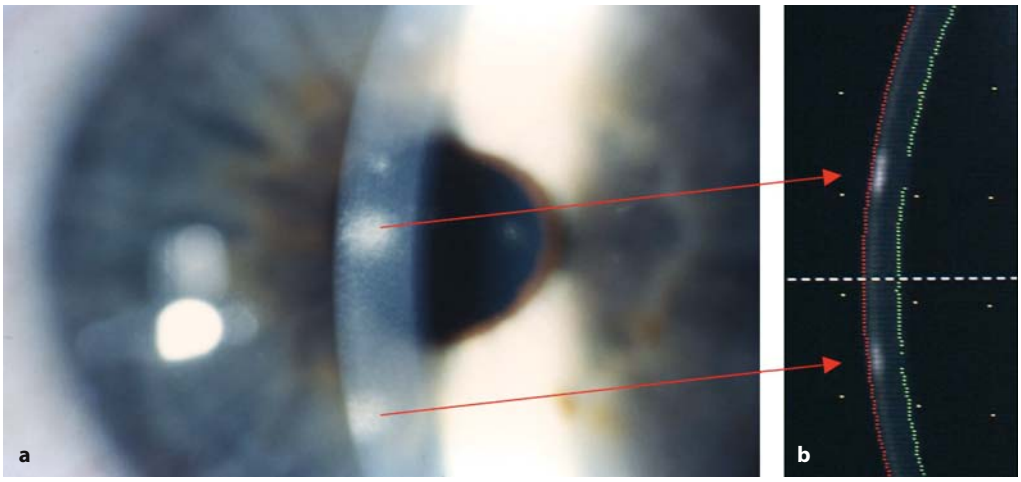

Fig. 5.36 Epidemic keratoconjunctivitis. Slit-lamp microscopy photograph: right eye of a 28-year-old woman on day 14 after the onset of symptoms of epidemic keratoconjunctivitis, showing the subepithelial nummular lesions as fleecy-fused areas of opacity with unclear margins. **a** Slit-lamp microscopy. **b** Pentacam Scheimpflug camera (Oculus Optikgeräte, Wetzlar, Germany)

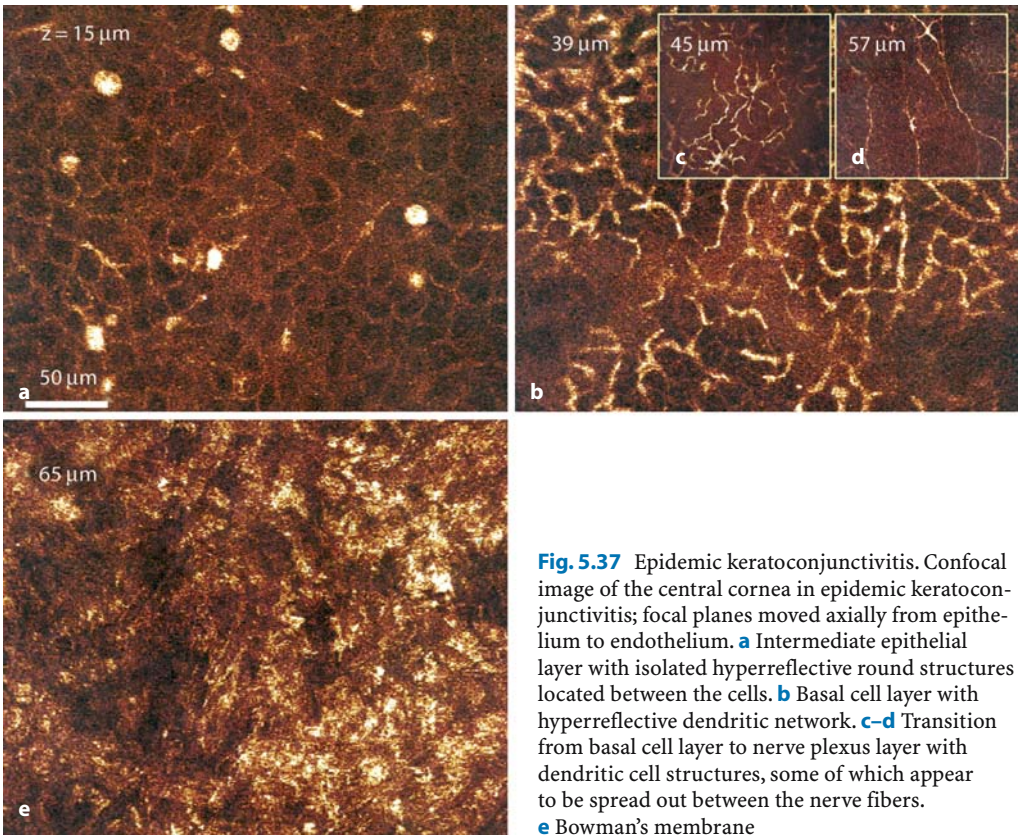

Fig. 5.37 Epidemic keratoconjunctivitis. Confocal image of the central cornea in epidemic keratoconjunctivitis; focal planes moved axially from epithelium to endothelium. **a** Intermediate epithelial layer with isolated hyperreflective round structures located between the cells. **b** Basal cell layer with hyperreflective dendritic network. **c–d** Transition from basal cell layer to nerve plexus layer with dendritic cell structures, some of which appear to be spread out between the nerve fibers. **e** Bowman's membrane

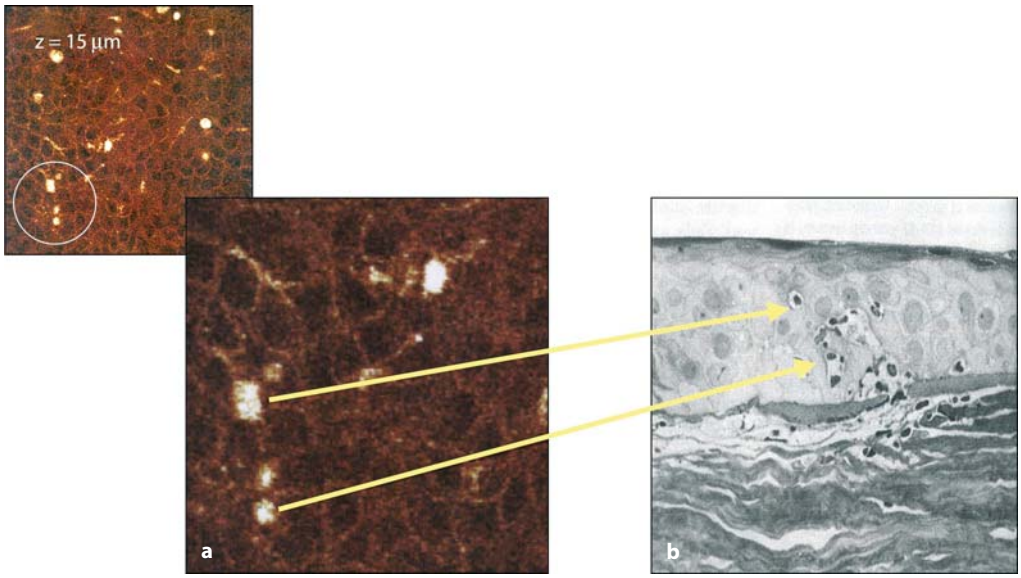

Fig. 5.38 Comparison between (**a**) confocal microscopy images and (**b**) histological sections, (reproduced from Lund O-E, Stefani FH. Corneal histology after epidemic keratoconjunctivitis. *Arch Ophthalmol* 1978;**96**:2085–2088 [45]). The infiltrates within the epithelium could be lymphocytes, histiocytes, or fibroblasts

5.3 Corneal Nerves

5.3.1 Normal Anatomy

The cornea is one of the most sensitive structures in the human body, and even the most minimal contact provokes the lid reflex to protect the eye. This sensitivity is attributable to the large numbers of nerve fibers that pass through the cornea. Furthermore, the corneal nerves exert an influence on the regulation of epithelial integrity and on wound healing [23]. In vivo visualization of these nerve structures is possible by confocal corneal microscopy.

The cornea is innervated primarily by sensory fibers arising from the ophthalmic nerve, a terminal division of the trigeminal nerve. Human corneal nerves are nonmyelinated and vary in thickness between 0.2 µm and 10 µm.

The nerve fiber bundles, which enter the anterior and central stroma in the corneal periphery, run parallel to the corneal surface in a radial pattern before making an abrupt 90° turn in the direction of Bowman's membrane [60]. On confocal corneal microscopy, these nerve fibers mostly present as thick, almost always stretched, highly reflective structures. Frequently, the stromal nerves are found in close proximity to keratocytes. The deep stroma is devoid of nerves that can be visualized on confocal microscopy.

In the anterior stroma, immediately before Bowman's membrane, the nerve fiber bundles display three different patterns. Some of the nerve fibers ramify before reaching Bowman's membrane without penetrating it and form the subepithelial plexus [63] (Fig. 5.39). Other nerves penetrate Bowman's membrane either directly, following a perpendicular or slightly oblique course, or by ramifying into several fine branchlets just before penetration. After they have penetrated Bowman's membrane, they again make a 90° directional change and pass between the basal cell layer of the epithelium and Bowman's membrane toward the corneal

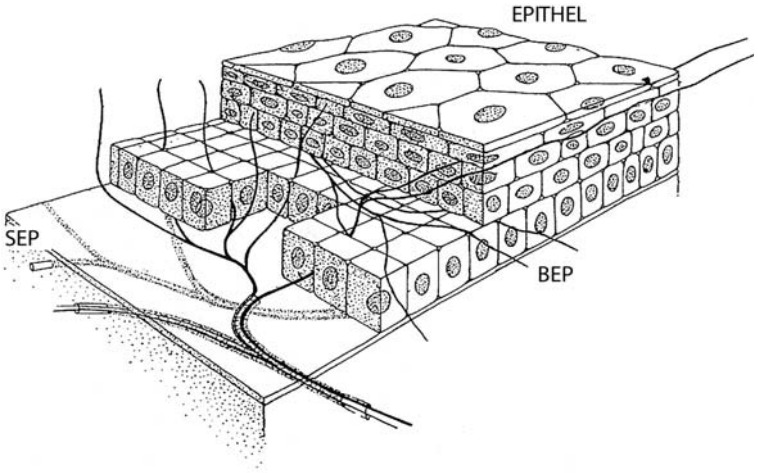

Fig. 5.39 Schematic illustration of the subepithelial plexus (*SEP*) and its branches in the corneal epithelial layers (*BEP* basal epithelial plexus)

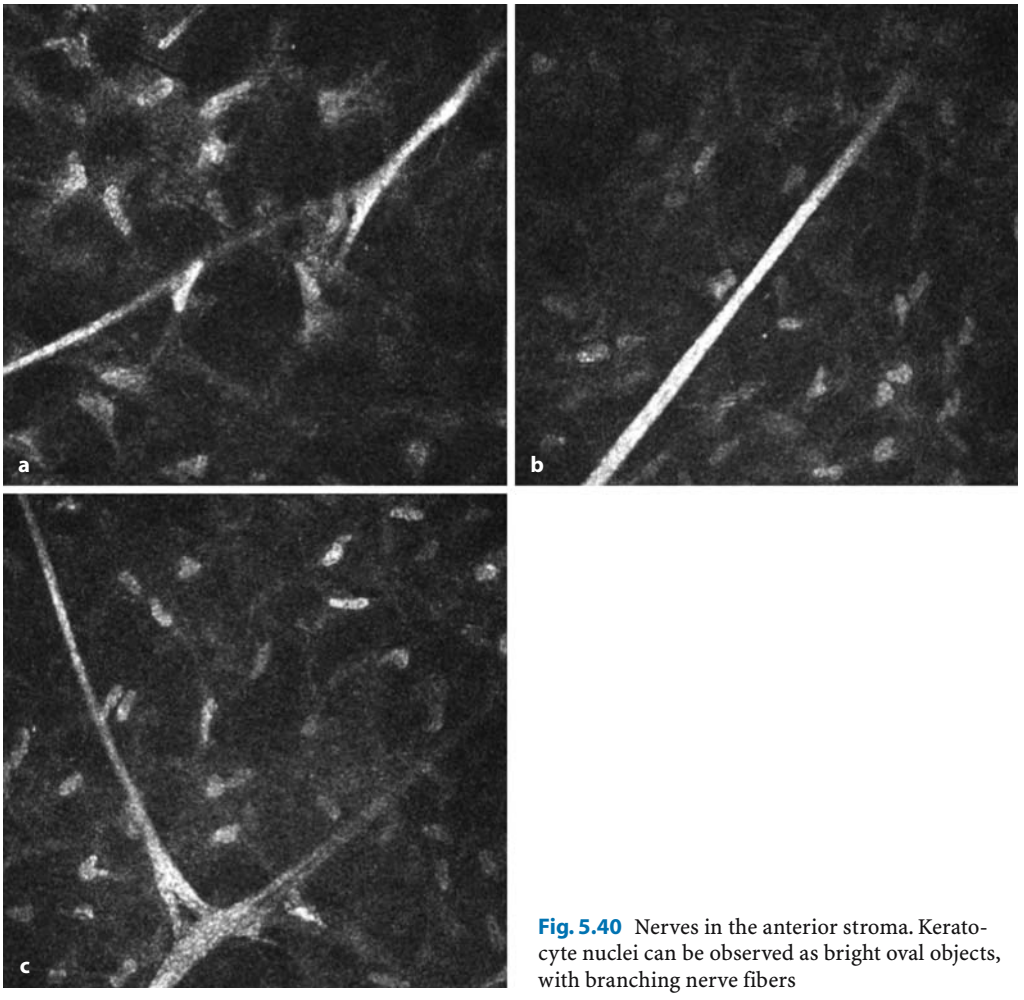

Fig. 5.40 Nerves in the anterior stroma. Keratocyte nuclei can be observed as bright oval objects, with branching nerve fibers

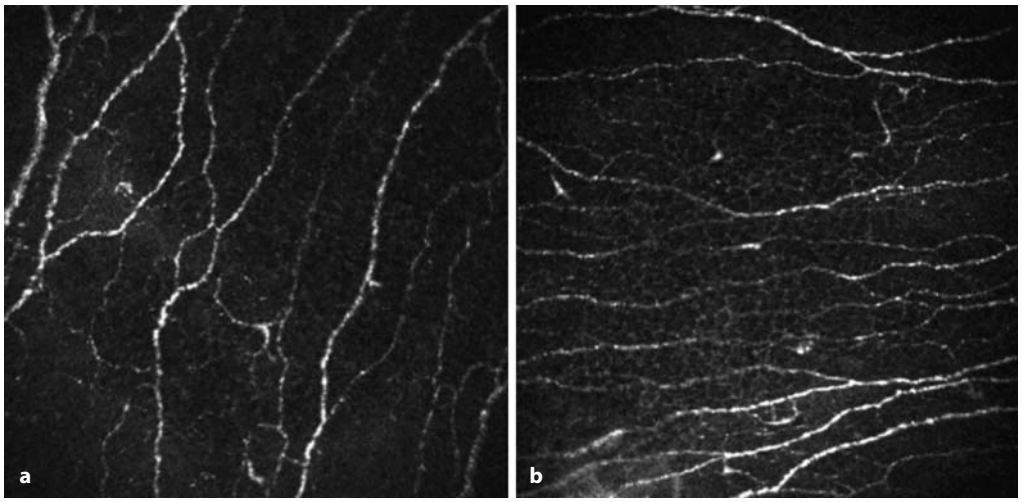

Fig. 5.41 Confocal laser scanning in vivo microscopy image of parallel nerve fiber bundles with bunches in the subepithelial plexus in a normal human cornea. **a** Vertical view. **b** Horizontal view

center and form the basal epithelial plexus (see Fig. 5.39). In so doing, they give off many small side branchlets directed both toward the corneal surface, where they end freely, and toward the center [60, 61]. The nerve fibers of the basal epithelial plexus mostly run parallel to each other and often form Y-shaped or T-shaped branches. Their predominantly granular, "string of pearl" structure is characteristic; more rarely they display a smooth surface. Unlike the stromal nerves, they are characterized by lesser reflectivity and frequently follow a meandering path. Occasionally, a thicker nerve fiber bundle will divide into two finer nerve fibers, which then reunite after a short distance into a single nerve fiber with the same thickness as before. The finer branchlets also form connections between larger nerve fibers (Figs. 5.40–5.44)

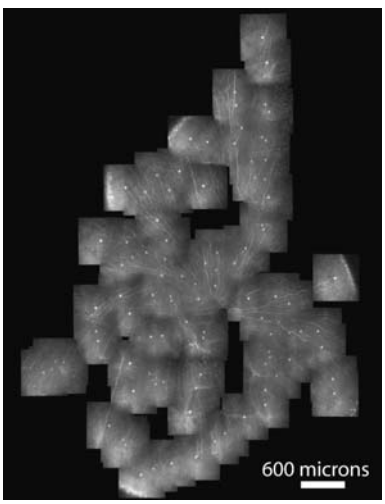

Fig. 5.42 Two-dimensional mapping of parallel nerve fiber bundles in the subepithelial plexus in a normal human cornea

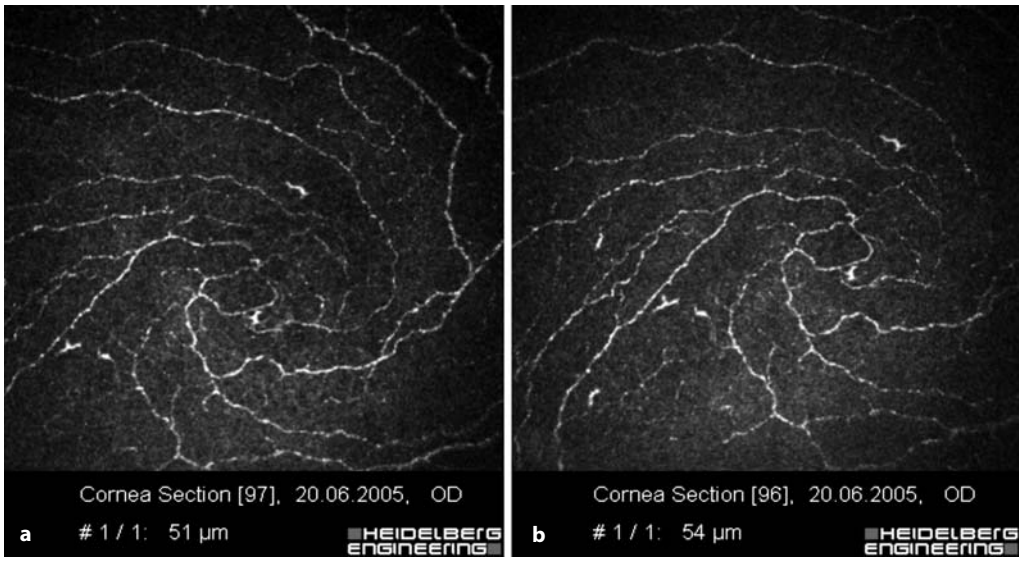

Fig. 5.43 Nerve structure of the cornea; individual image from a z-scan series. **a** Subepithelial nerve plexus in the cornea (z=51 µm). **b** Nerve plexus (z=53 µm)

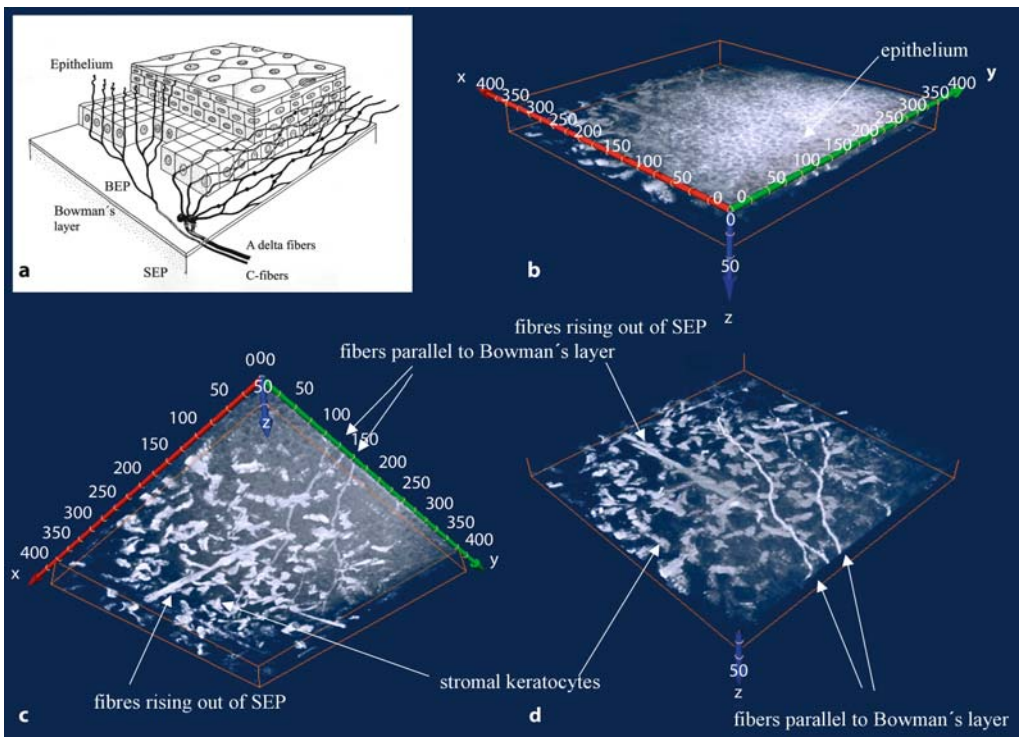

Fig. 5.44 Schematic illustration (**a**) and three-dimensional reconstruction (**b–d**) of the corneal epithelium with anterior stroma and nerves in a healthy human subject. **b** Anterior view. **c** Posterior view. **d** Anterior view with virtual removal of the epithelium Thin nerves run parallel with Bowman's membrane in the basal epithelial plexus, with thicker fibers originating from the subepithelial plexus

5.3.2 Pathological Findings

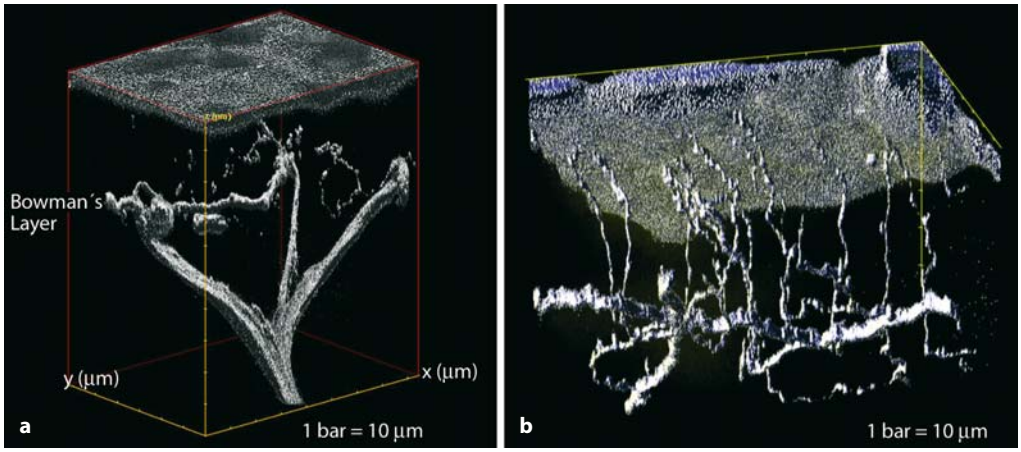

Fig. 5.45 Trephinates freshly obtained in cases of Fuchs corneal dystrophy, stained with calcein-AM/ethidium homodimer and evaluated by confocal microscopy. **a** Aδ-fiber rising out of the SEP, dividing trichotomously and kinking into the BEP; stepsize 0.5 µm, steps *n*=200, depth 10 µm, zoom 1.0, objective (water-immersion) ×60, average 32. **b** C-fibers sending off multiple branches that penetrate epithelial cell layers orthogonally, ending blindly underneath the superficial cells; stepsize 0.5 µm, steps *n*=132, depth 66 µm, zoom 0.82, objective (water-immersion) ×60, average 16

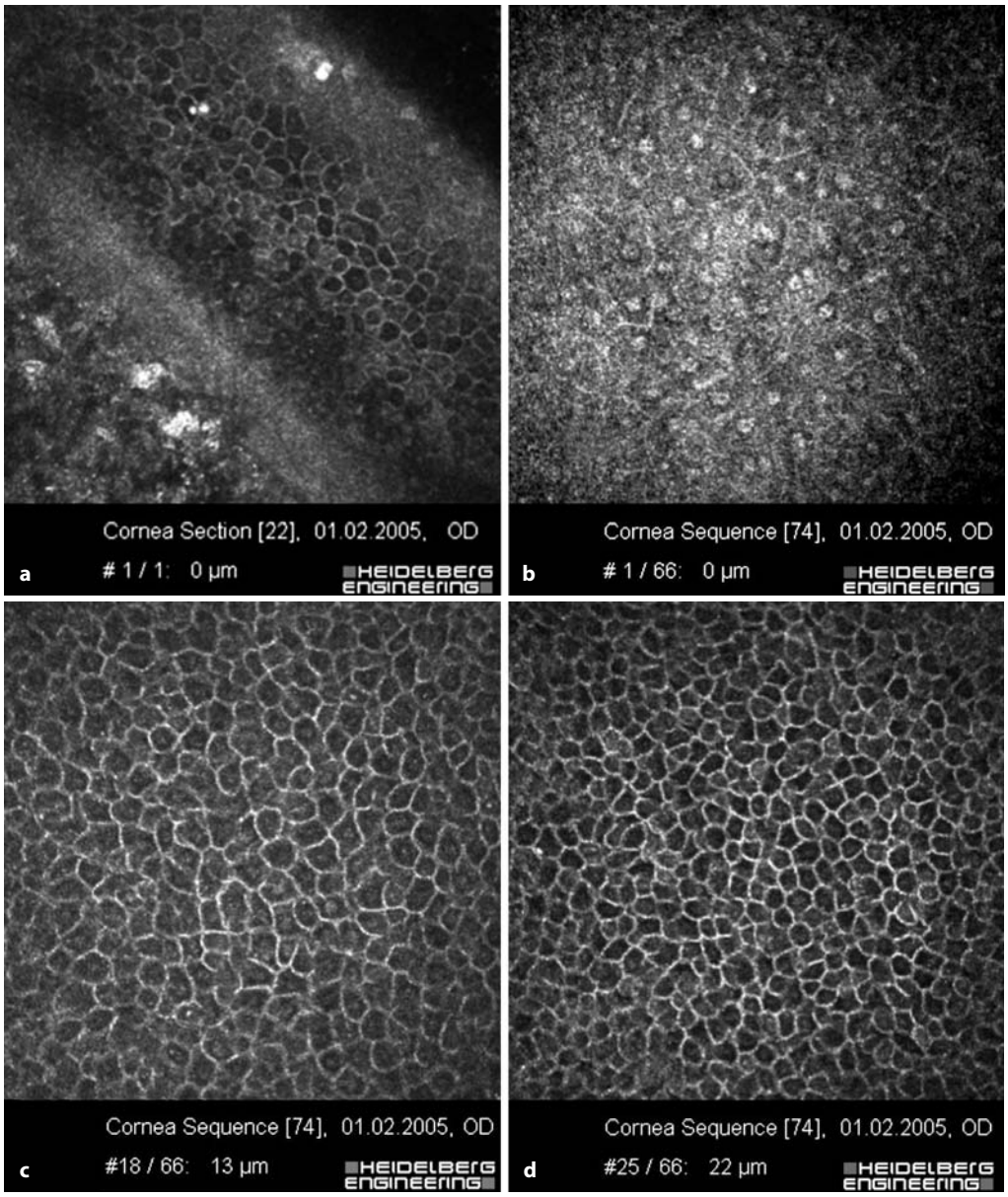

Fig. 5.46 a–h Status 4 weeks after corneal erosion. External *z*-scan through the corneal epithelium, no nerves can be visualized. **a** Oblique section through the epithelium/anterior stroma. **b–h** Surface-parallel sections through the epithelium/anterior stroma

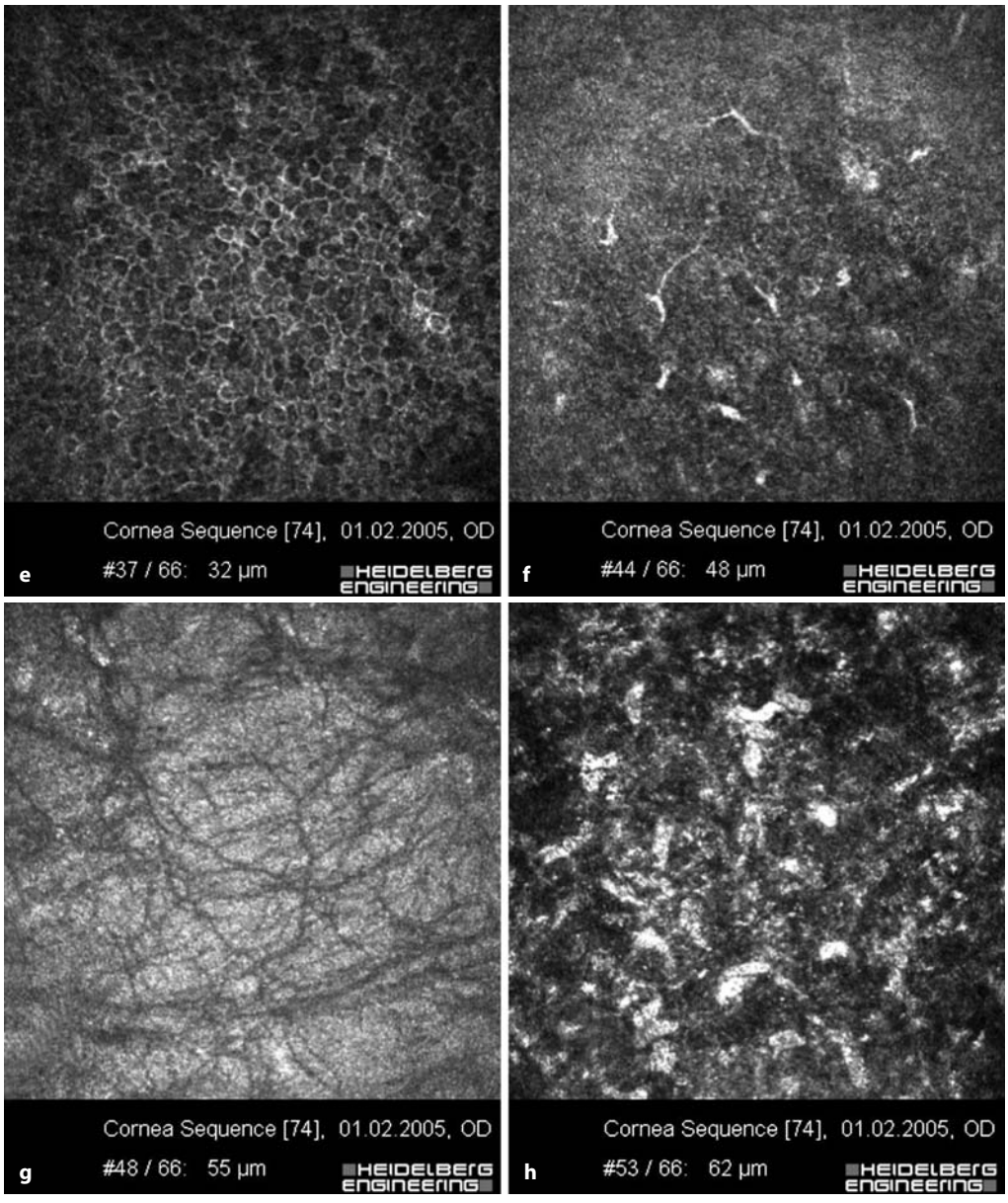

Fig. 5.46 (*continued*) **b–h** Surface-parallel sections through the epithelium/anterior stroma

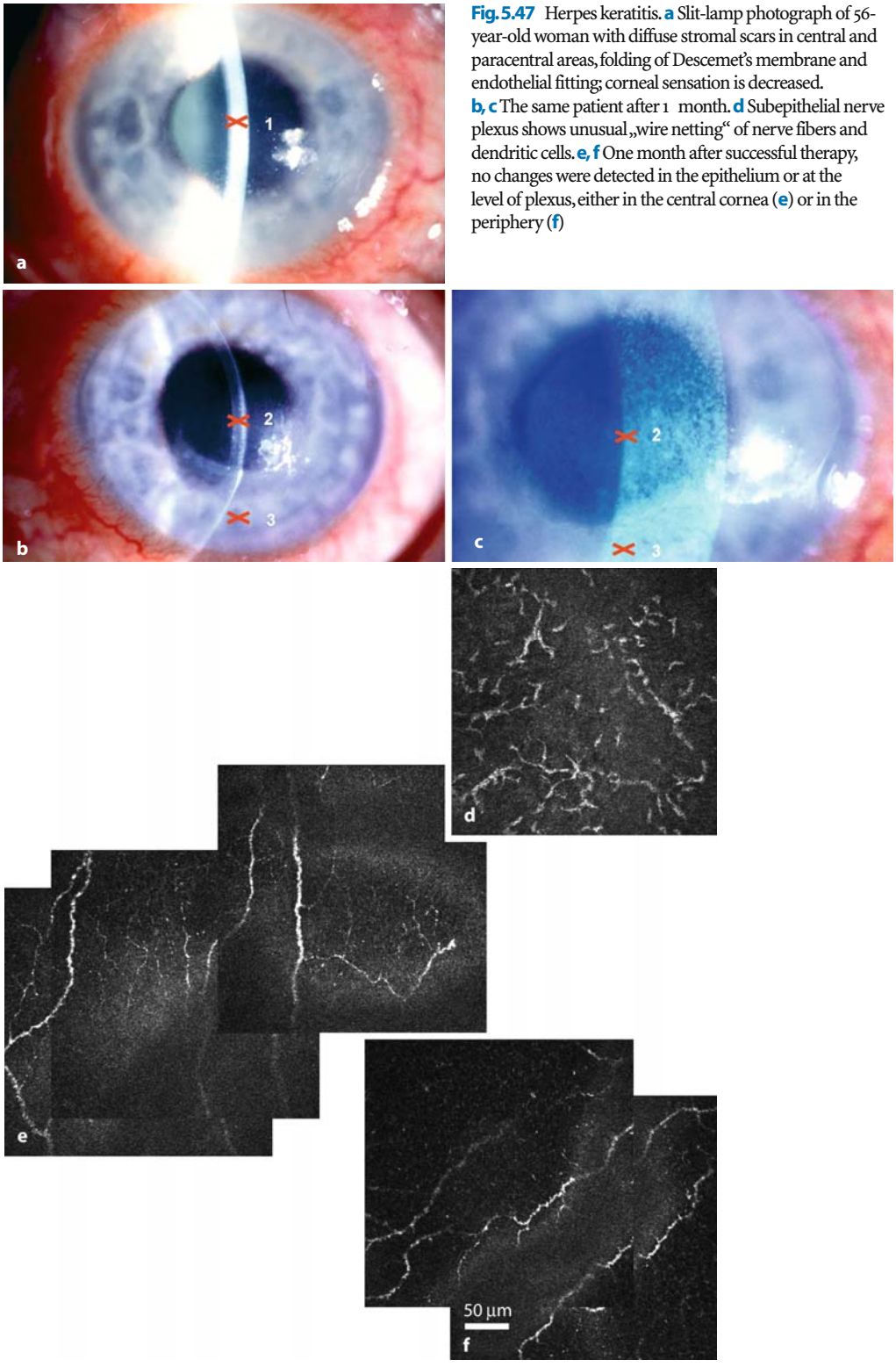

Fig. 5.47 Herpes keratitis. **a** Slit-lamp photograph of 56-year-old woman with diffuse stromal scars in central and paracentral areas, folding of Descemet's membrane and endothelial fitting; corneal sensation is decreased. **b, c** The same patient after 1 month. **d** Subepithelial nerve plexus shows unusual „wire netting" of nerve fibers and dendritic cells. **e, f** One month after successful therapy, no changes were detected in the epithelium or at the level of plexus, either in the central cornea (**e**) or in the periphery (**f**)

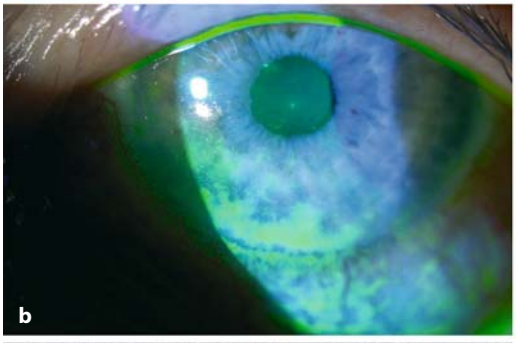

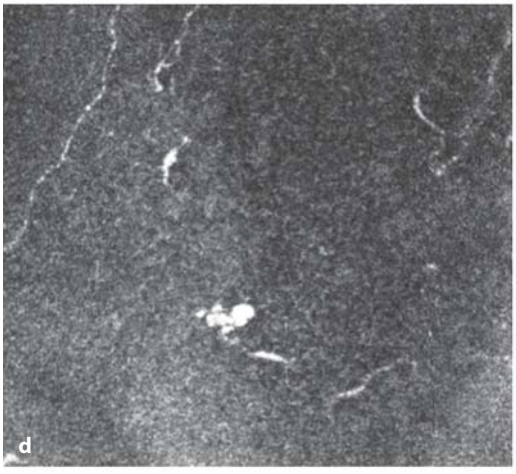

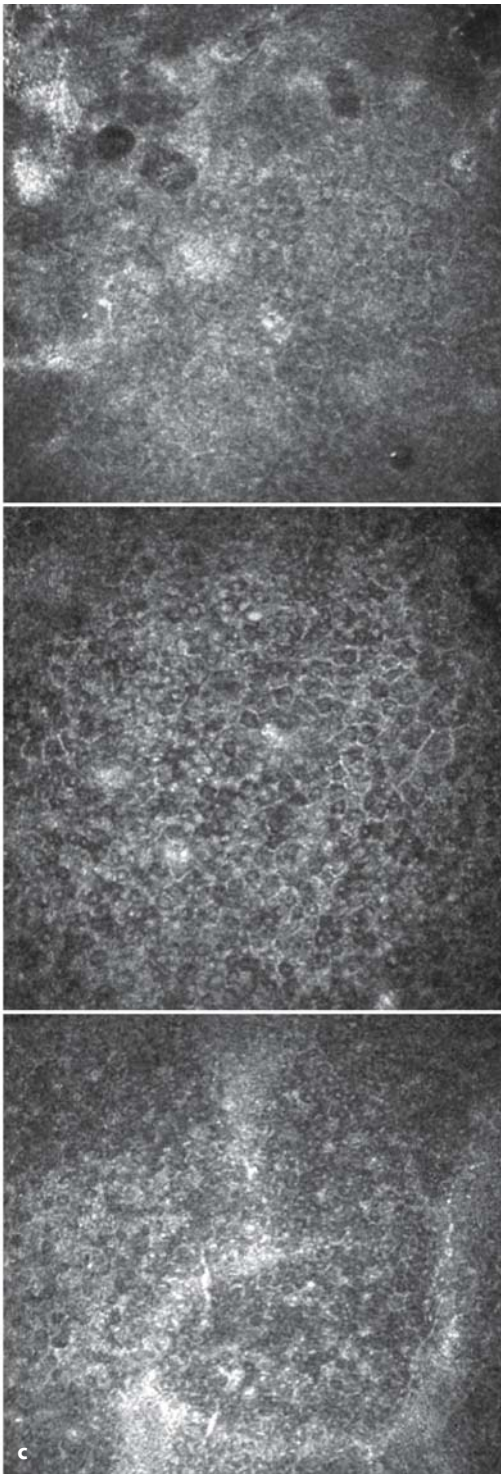

Fig. 5.48 Lagophthalmos. **a** A 70-year-old man with lagophthalmos due to facial nerve paresis. **b** Slit-lamp photograph of the affected left eye. **c** Confocal images: superficial, intermediate, and basal cell layers. **d** Confocal image: rarefaction of the subbasal nerves

5.3.2.1 Corneal Innervation After Refractive Surgery

The physiological structure of the corneal nerves is appreciably disturbed in the course of refractive surgery. This is considered to be the reason why keratoconjunctivitis sicca is the most common complication following LASIK, being encountered for a certain time in virtually all patients in varying degrees of severity.

In the undamaged cornea, the corneal nerves arising from the long ciliary nerves enter the middle stroma at 3 o'clock and 9 o'clock and ramify horizontally and vertically in their further course toward the middle of the cornea, ultimately forming a dense and branched subepithelial nerve plexus underneath Bowman's

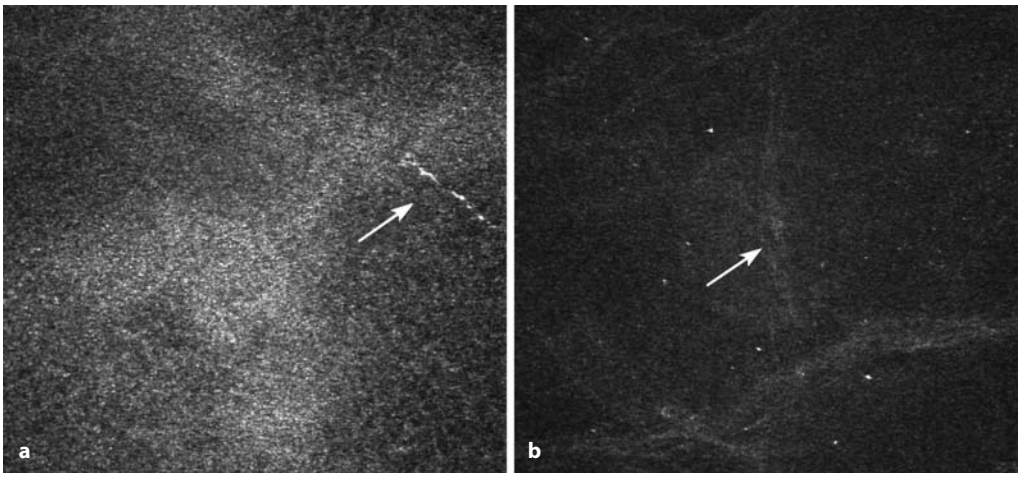

Fig. 5.49 Innervation after refractive surgery. Rarefaction of the nerve structures a few hours after laser-assisted in situ keratomileusis; rare and only thin subbasal nerve fibers. **a** Nerve fibers near subbasal layer. **b** Nerve fibers near Bowman's membrane

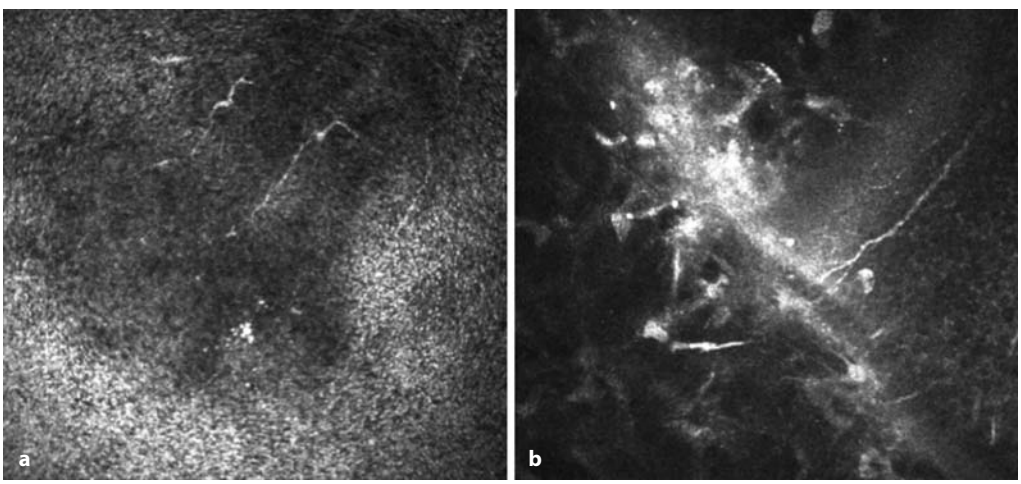

Fig. 5.50 Innervation after refractive surgery. **a** Two months after laser-assisted in situ keratomileusis (LASIK): small regenerating nerve fibers in central cornea. **b** Nine months after LASIK: new nerve fiber growing from the edge of flap region to center

membrane. From there, the nerve fibers travel vertically as far as the subbasal nerve plexus, before finally ascending into the upper epithelial layers [61].

Photorefractive keratectomy (PRK) involves ablation of the densely innervated epithelium, the branched subepithelial nerve plexus, and the anterior stroma. In the LASIK procedure, the microkeratome separates the subbasal nerve fiber bundles and the nerves of the anterior stroma along the flap region.

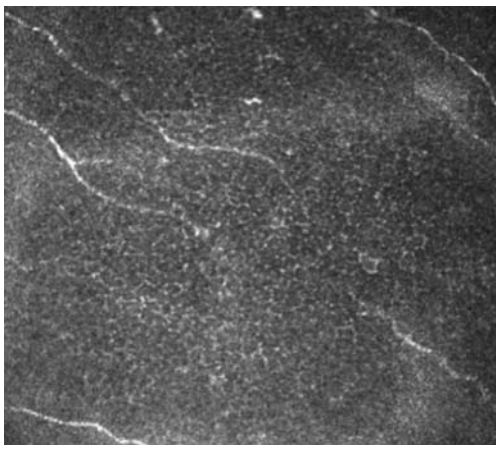

Fig. 5.51 Innervation after refractive surgery. Two years after laser-assisted in situ keratomileusis, there is still rarefaction of the subepithelial nerves, with short and unbranched nerve fibers

Degeneration of nerve structures in the flap vicinity can be detected on confocal microscopy just a few hours after LASIK, as reflected in rarefaction of the subbasal and stromal nerves (Fig. 5.49).

According to Donnenfeld et al., transection of both arms of the corneal nerve plexus following creation of a superior-hinge flap leads to more pronounced loss of corneal sensation and more pronounced dry eye signs and symptoms than with a nasal-hinge flap [13]. The same phenomenon has been reported with a narrow nasal hinge flap compared with a wider hinge flap in which more nerve fibers are left undamaged [14].

The onset of corneal nerve regeneration appears to occur early. Thus, Linna et al. were able to demonstrate gentle nerve regeneration 1 week after LASIK. Central corneal sensation was restored after 6 months. However, even after 6 months, short unconnected subbasal nerve fibers were still found, in contrast with long interconnected nerve fibers in a control population [44] (Fig. 5.50). Rarefied subbasal nerve fibers of this kind can still be detected 2 years after LASIK (Fig. 5.51). In addition, morphological changes have also been found in the area of the anterior stromal nerves or in the flap region [42] (Fig. 5.52). Using refractive corneal surgery as an example, confocal microscopy is thus able to provide a direct comparison between innervation detectable on microscopy and the sensitivity or symptom severity of the dry eye.

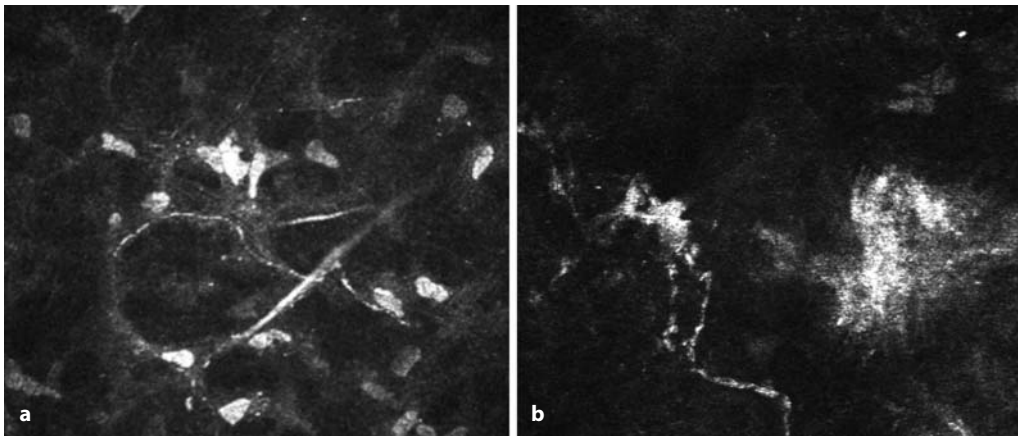

Fig. 5.52 Innervation after refractive surgery. Abnormal stromal nerves after laser-assisted in situ keratomileusis: curved pattern and very thin nerve fibers

5.3.2.2 Reinnervation After Penetrating Keratoplasty

Corneal innervation is the cornerstone of the normally functioning cornea. Although reinnervation processes have formerly been discussed in the literature, no suitable model was previously available. Different investigators [50, 71, 72, 76, 90] have used a Cochet–Bonnet esthesiometer to estimate graft innervation. Most studies have failed to differentiate between the peripheral and central sensitivity of the corneal graft. The results of these studies are summarized in Table 5.1.

Tervo et al. have demonstrated histochemically that complete regeneration does not occur either in the subepithelial nerve plexus or in the stromal nerves during the 3 years following penetrating keratoplasty. Moreover, a grafted cornea obtained 29 years after surgery did not show normal corneal sensitivity: The subepithelial nerve plexus presented with branched nerve fibers, but only a few stromal nerve trunks had regenerated [85].

Richter et al. [70] investigated corneal grafts using a Microphthal confocal microscope and compared the results with those obtained by esthesiometry. In the peripheral graft, the first atypically curved nerve fibers were detected in the middle stroma at 2 months and under Bowman's membrane at 3 months after surgery. In the central cornea, the first stromal nerve trunks were detected at 7 months after kera-

Table 5.1 Studies of corneal graft innervation

Study	Follow-up	Number of grafts investigated	Sensitivity (Cochet–Bonnet esthesiometry)
Ruben and Colebrook, 1979 [72]	7 months to 10 years	48	Incomplete sensitivity after 3 years
Skriver, 1978 [76]	12 months	45	Close to normal after 12 months
Mathers et al., 1988 [50]	1 month to 10 years	91	– With the exception of herpes simplex keratitis, the level of sensitivity did not depend on the diagnosis – Corneal sensitivity returned progressively from the periphery toward the center of the graft – The rate of return of sensitivity averaged 0.029 mm/month
Tugal Tutkun et al., 1993 [90] sensitivity	2 weeks to 15 years	71	– 36 grafts were completely anesthetic – 35 grafts had some level of sensitivity – Of these 35, only one graft had normal central
Richter et al., 1996 [70]	3 years	46	Graft center: – At 1 month, completely anesthetic – At 6 months, incomplete sensitivity – At 24 months, one-third of grafts had normal sensitivity, and one-seventh were completely anesthetic Graft periphery: – At 12 months, 50% of the grafts were completely anesthetic – At 24 months, 25% of the grafts were completely anesthetic – Best innervation in keratoconus or scars

toplasty, while the first bunches of subepithelial nerve plexus were noted only after 24 months. To date, the results of confocal microscopy appear to correspond to esthesiometry findings.

Confocal microscopy provides insights into the morphological and functional aspects of corneal reinnervation after surgery. The sample images of corneal innervation after grafting illustrate the structures of the subepithelial nerve plexus and stromal nerves at about 24 months after surgery (Fig. 5.53).

Figure 5.54a–c shows hypertrophy of corneal nerves in a patient with neurofibromatosis.

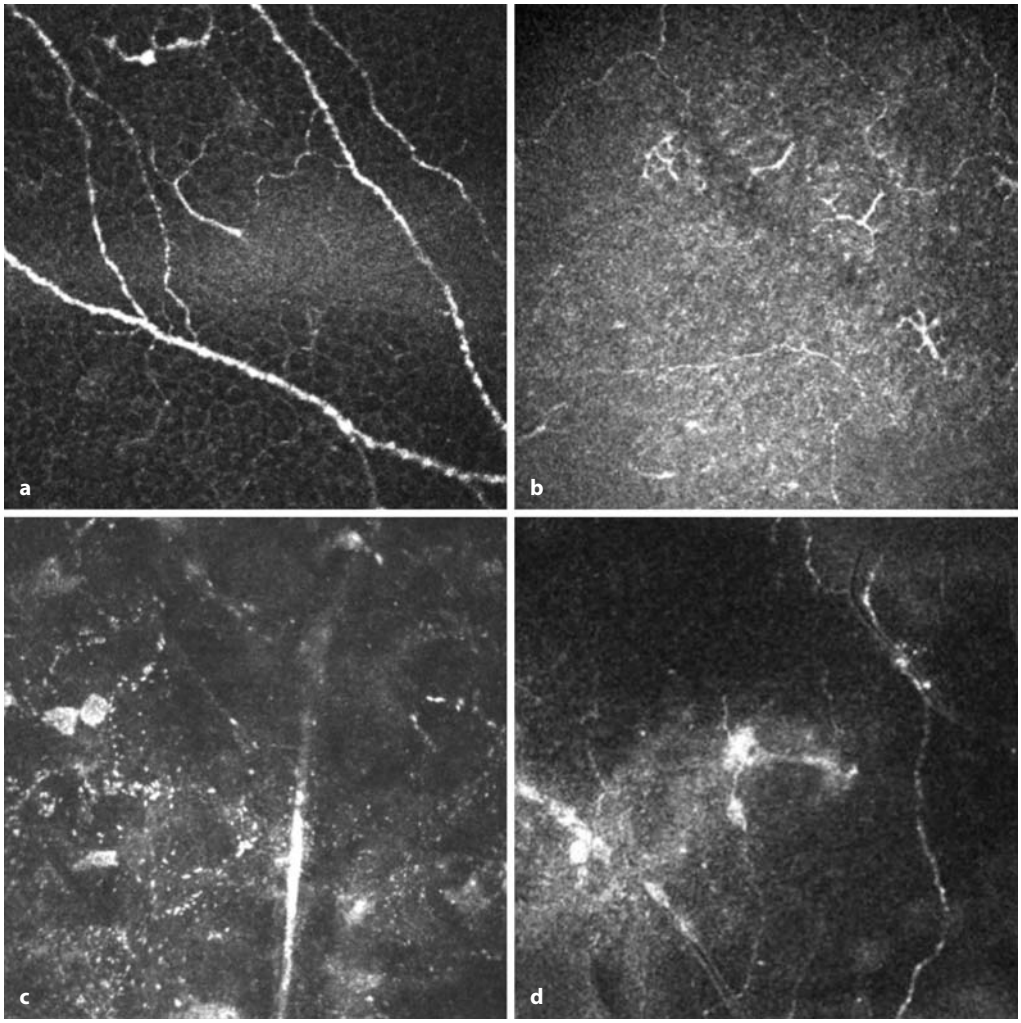

Fig. 5.53 Reinnervation after penetrating keratoplasty. **a** Graft center: complete reinnervation of subepithelial nerve plexus 24 months after surgery. **b** Graft center: incomplete reinnervation of subepithelial nerve plexus; curved nerve bunches 25 months after surgery; dendritic cells. **c** Graft center: nerve trunk in middle stroma 24 months after surgery. **d** Graft periphery: incomplete reinnervation of subepithelial nerve plexus, hyperreflective scattering at the level of Bowman's membrane 24 months after surgery

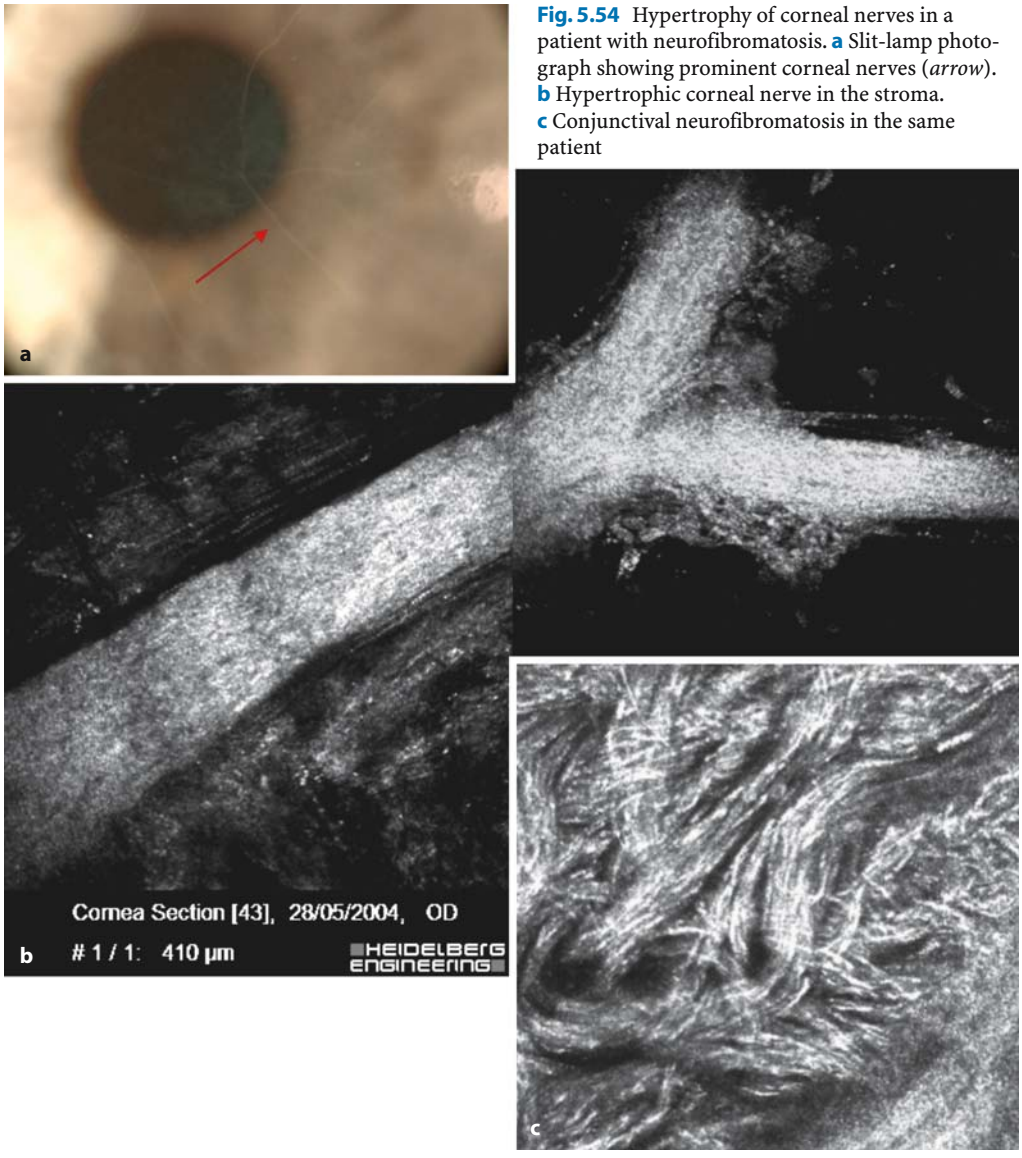

Fig. 5.54 Hypertrophy of corneal nerves in a patient with neurofibromatosis. **a** Slit-lamp photograph showing prominent corneal nerves (*arrow*). **b** Hypertrophic corneal nerve in the stroma. **c** Conjunctival neurofibromatosis in the same patient

5.4 Bowman's Membrane

5.4.1 Normal Anatomy

The anterior limiting membrane has an amorphous appearance. Its location can be established from the nerves of the basal epithelial plexus, which ramify there (Fig. 5.55a–c).

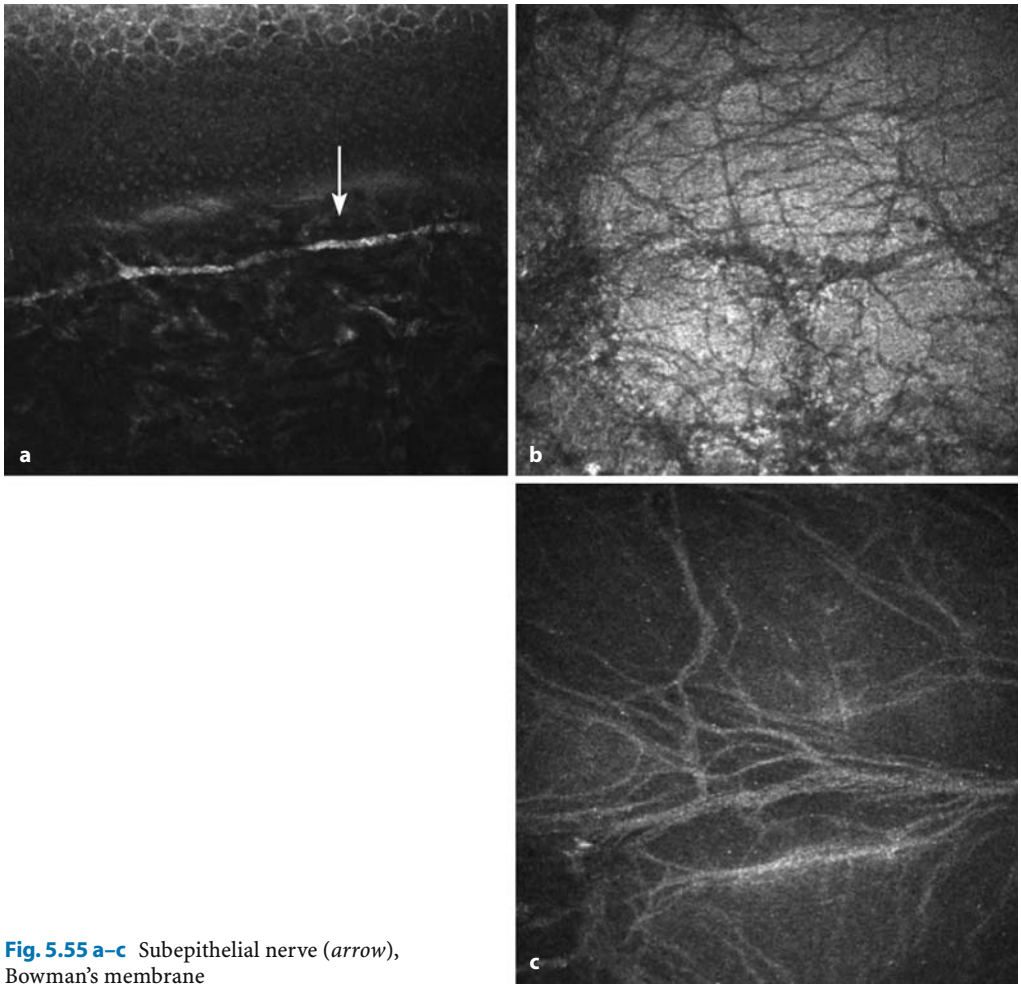

Fig. 5.55 a–c Subepithelial nerve (*arrow*), Bowman's membrane

5.4.2 Pathological Findings

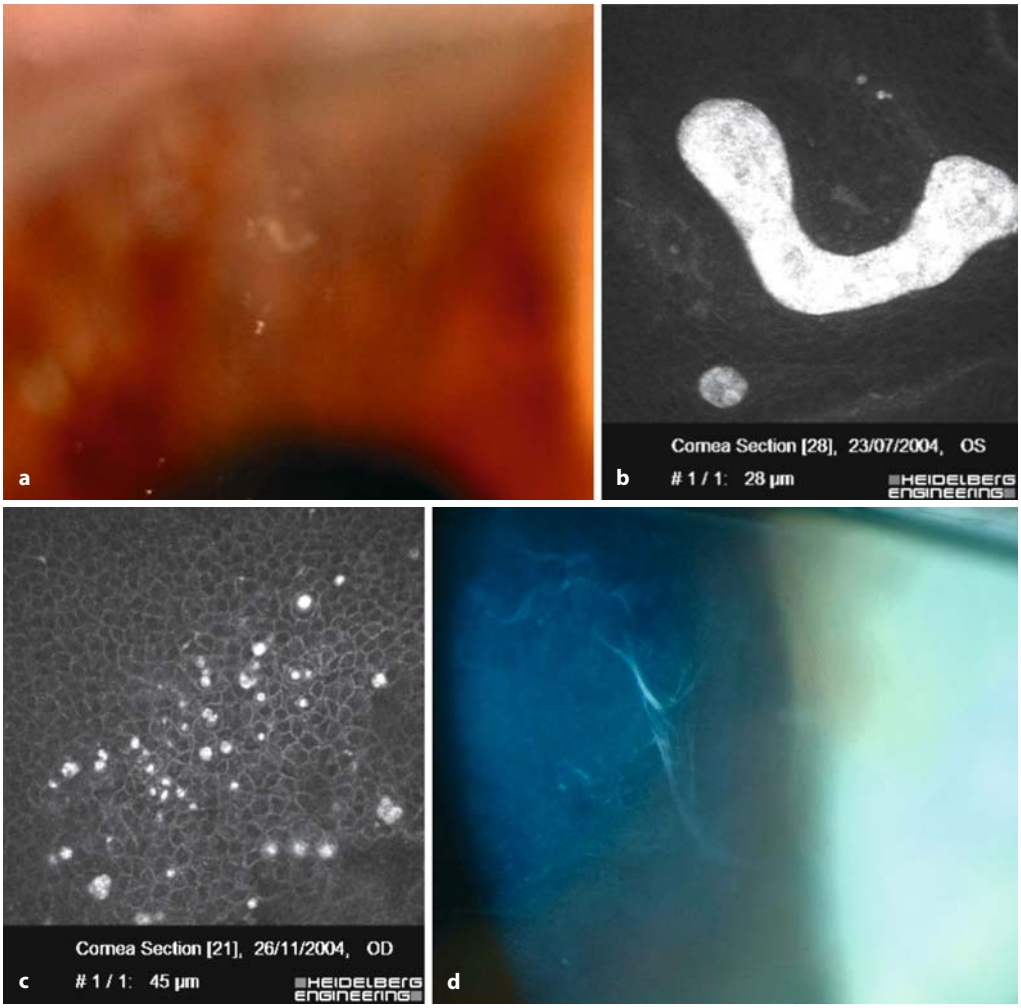

Fig. 5.56 a–f Dots and maplike lesions. **a** Slit-lamp photograph of dots. **b, c** Round structures corresponding to microcysts containing hyperreflective material. **d** Slit-lamp photograph of maplike lesions

Fig. 5.56 a–f (*continued*) **e, f** Abnormal basement membrane within the corneal epithelium. This abnormal tissue terminates in bizarre shapes.

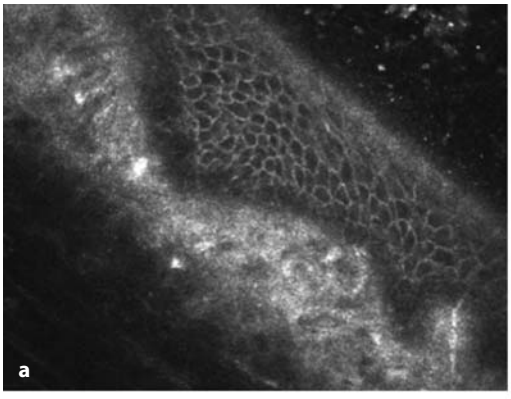

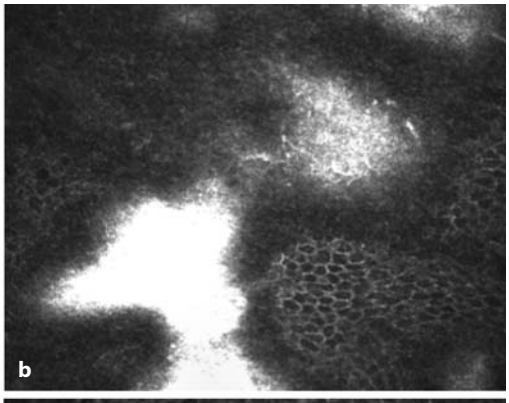

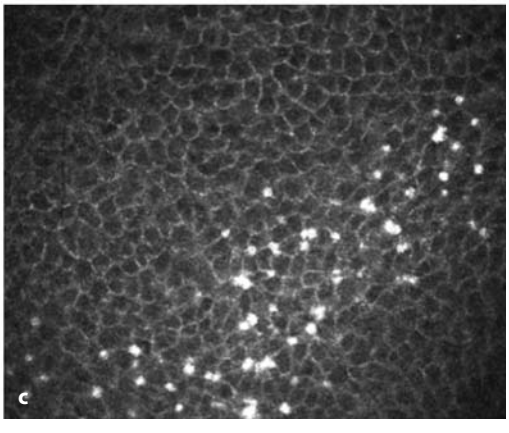

Fig. 5.57 Reis–Bückler corneal dystrophy. **a** Oblique section showing reflective and irregular material at the level of Bowman's layer and the anterior stroma. **b** Highly reflective tissue at the level of Bowman's layer. **c** Deposition of fine reflective material in the basal cell layer

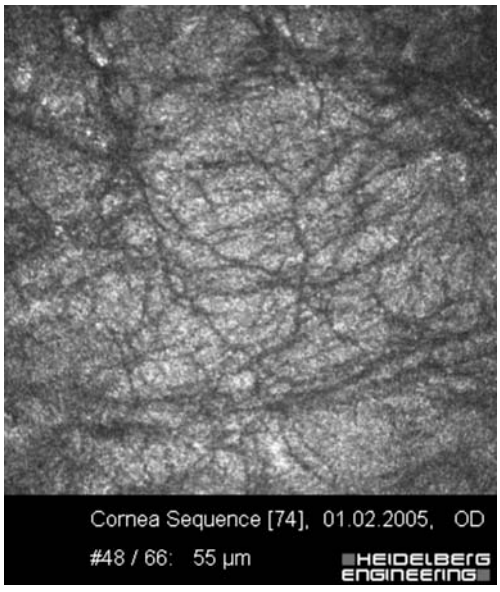

Fig. 5.58 Bowman's membrane 4 weeks after ammonia burn injury and complete epithelial wound healing with extreme development of a fiber matrix structure

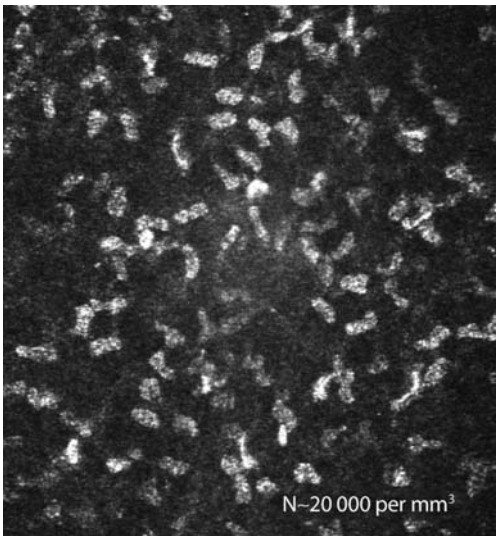

Fig. 5.59 Anterior stroma. In the corneal stroma only the keratocyte nuclei are visualized. Cell nucleus density is highest in the anterior stroma; the cell nuclei shown are approximately 15 µm in diameter

5.5 Stroma

5.5.1 Normal Anatomy

Apart from neural structures, only the highly reflective, sharply demarcated cell nuclei of the keratocytes are visualized on examination of the stroma. The cytoplasm of this fibroblast subpopulation and the collagen fibers produced by them are not visible. Keratocyte nucleus density is higher in the anterior stroma close to Bowman's membrane than in the central and deep stroma (Figs. 5.59 and 5.60). Keratocyte density is highest in the anterior stroma, clearly declines toward the central stroma, and increases again slightly in the region immediately before Descemet's membrane.

Fig. 5.61 depicts posterior stroma, and Fig. 5.62 compares normal and activated stroma.

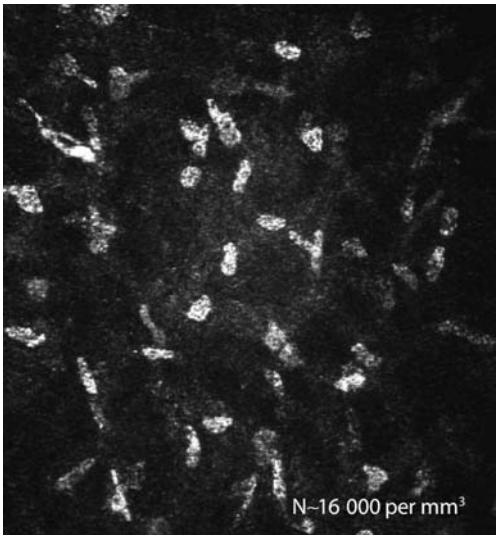

Fig. 5.60 Central stroma. Clearly demarcated, highly reflective, oval keratocyte nuclei in the central stroma; cell nucleus density is lowest in the central stroma

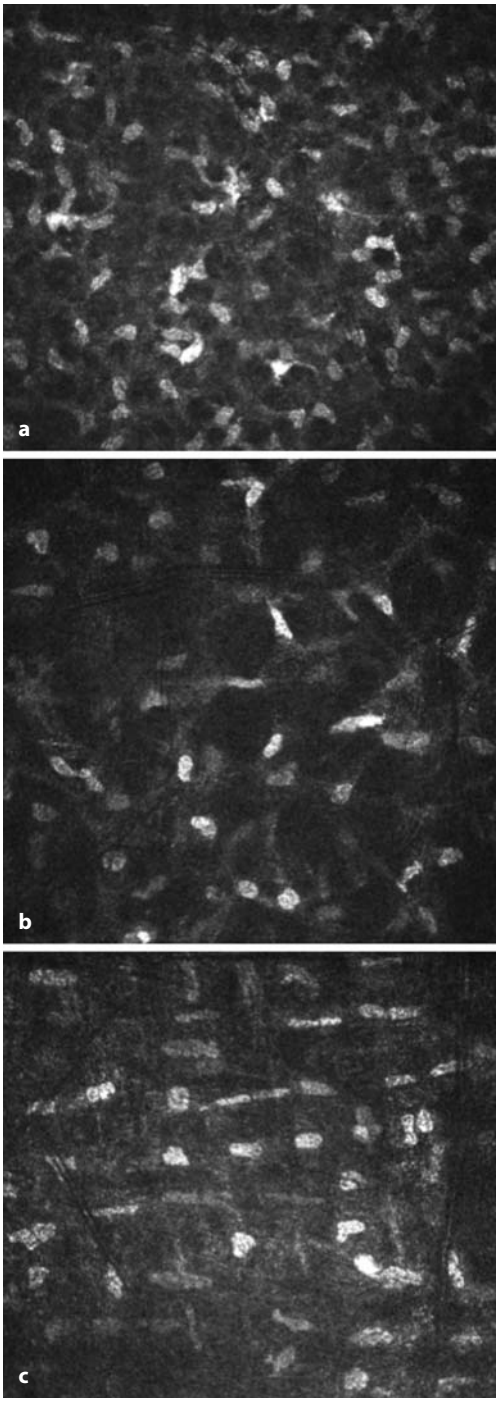

Fig. 5.61 Posterior stroma. Clearly demarcated, highly reflective, oval nuclei, which appear larger and are more numerous than in the central stroma but less numerous than in the anterior stroma. Anterior (**a**), central (**b**), and posterior stroma (**c**)

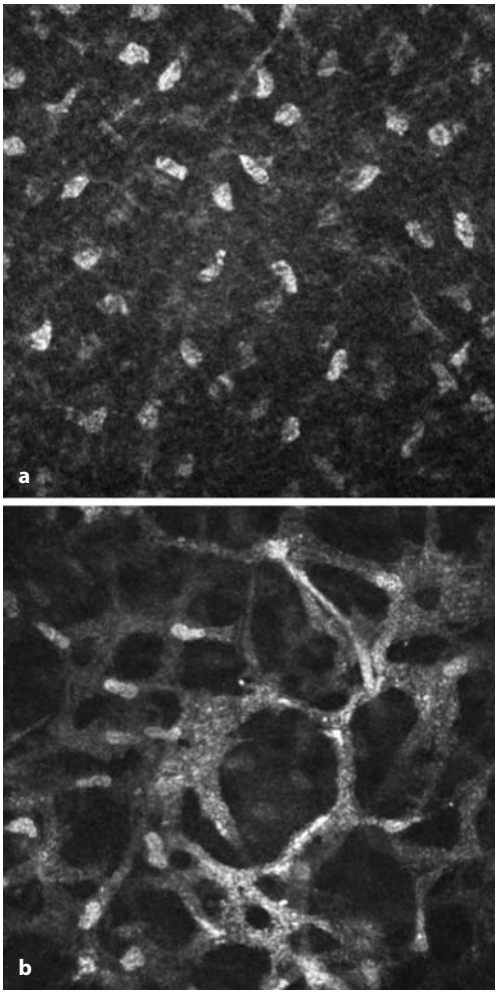

Fig. 5.62 Central stroma. **a** Normal keratocytes. **b** Activated keratocytes

5.5.2 Pathological Findings

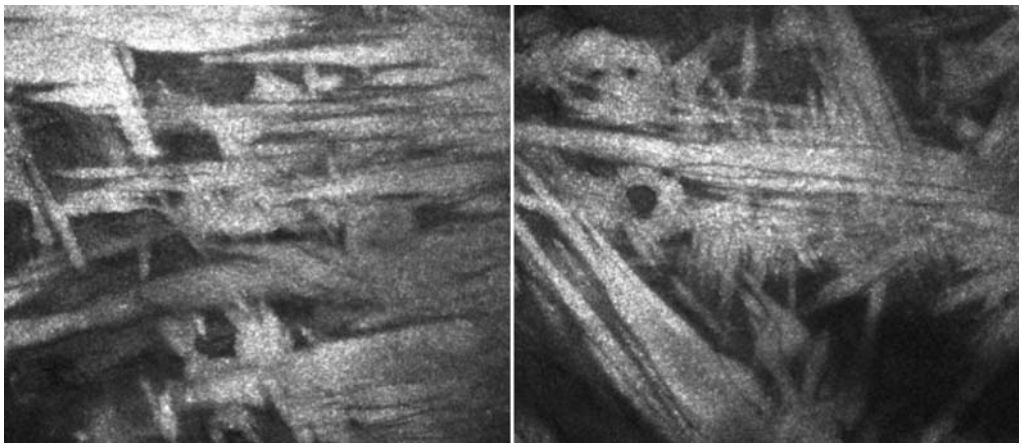

Fig. 5.63 Schnyder's crystalline dystrophy. Accumulation of reflective material consistent with subepithelial crystalline deposits

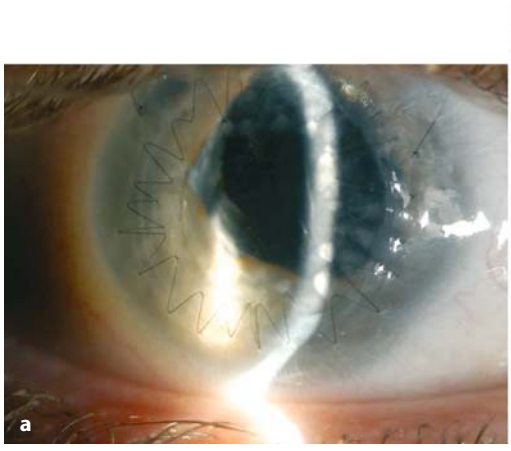

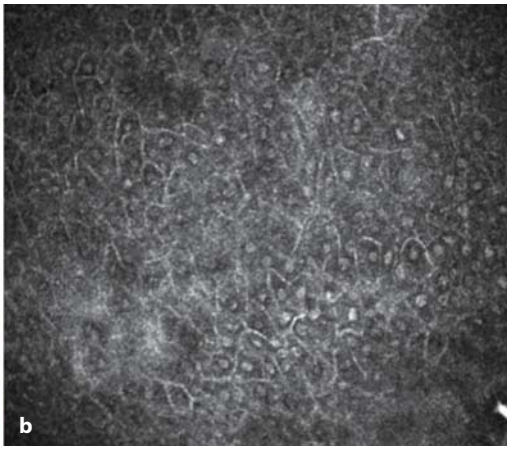

Fig. 5.64 **a–f** Penetrating keratoplasty. **a** Slit-lamp photograph of 72-year-old woman after penetrating keratoplasty. The graft is well located, clear, and fully epithelialized, with small areas of fibrination near the endocorneal suture. **b–f** Normal epithelial structure with a number of Langerhans cells (arrow) at the level of the basal cells and subepithelial nerve plexus. Scar areas (**d**) of basal epithelium in fibrination zones. Nerve fibers are absent both in the epithelium and in the stroma of the graft

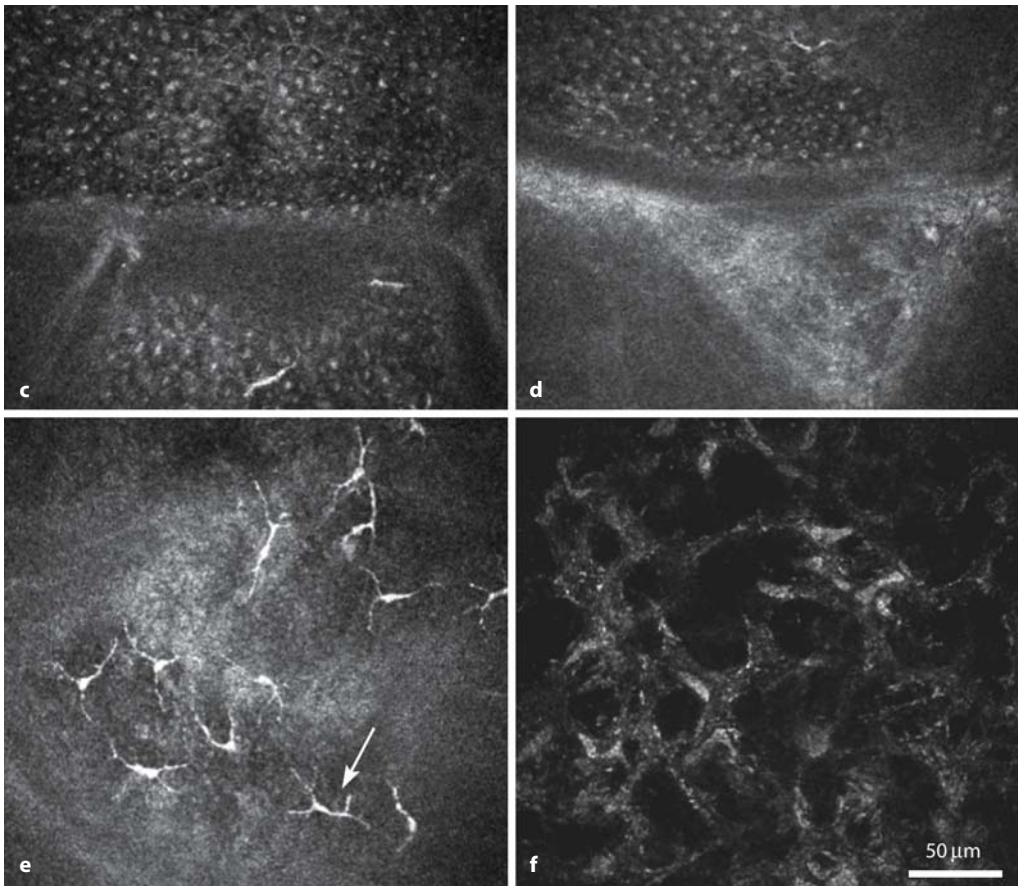

Fig. 5.64 (*continued*) **b–f** Normal epithelial structure with a number of Langerhans cells (arrow) at the level of the basal cells and subepithelial nerve plexus (**e**). Scar areas (**d**) of basal epithelium in fibrination zones. Nerve fibers are absent both in the epithelium and in the stroma of the graft

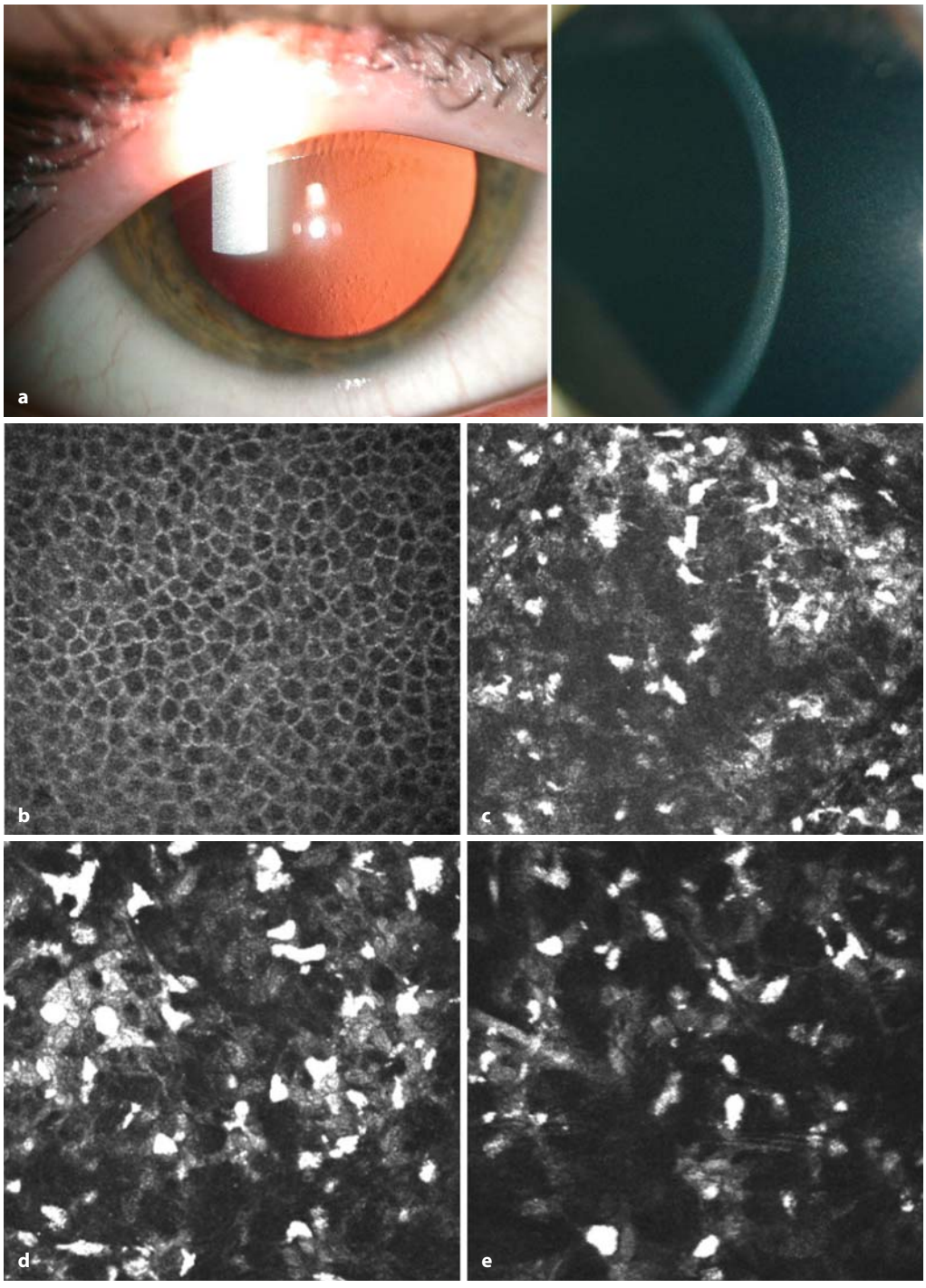

Fig. 5.65 a–f Cystinosis. **a** Slit-lamp photographs of an 18-year-old woman with dazzling; visual acuity 20/20. **b–f** Confocal images from the same patient: normal epithelium, 14 µm (**b**); highly reflective structures in the stroma at depths of 60 µm, 160 µm, and 540 µm, precise differentiation from keratocytes not possible (**c–e**)

Fig. 5.65 (*continued*) normal endothelium (**f**)

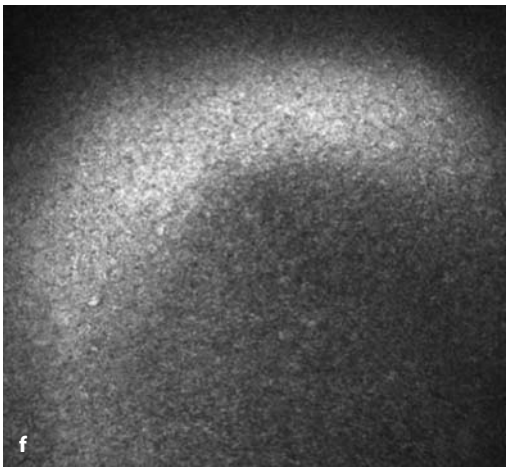

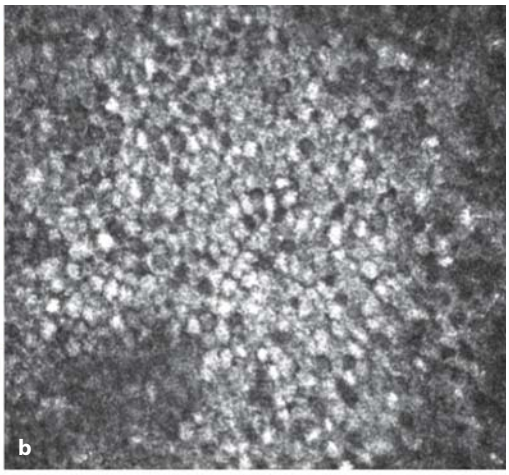

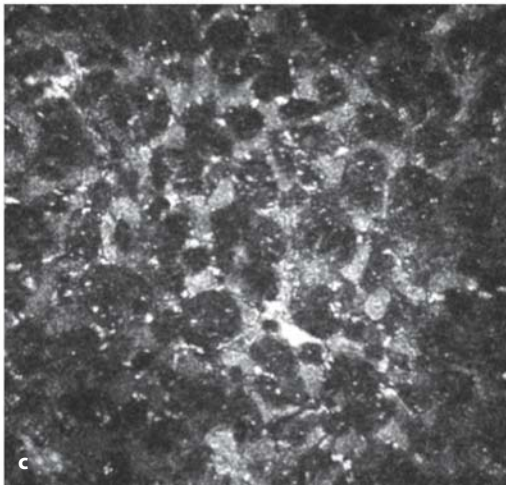

Fig. 5.66 Fabry's disease. **a** Slit-lamp photograph of a 40-year-old man. **b, c** Confocal images from the same patient: highly reflective round structures in the basal epithelium (z=28 µm; **b**) and the very anterior stroma (z=77 µm; c)

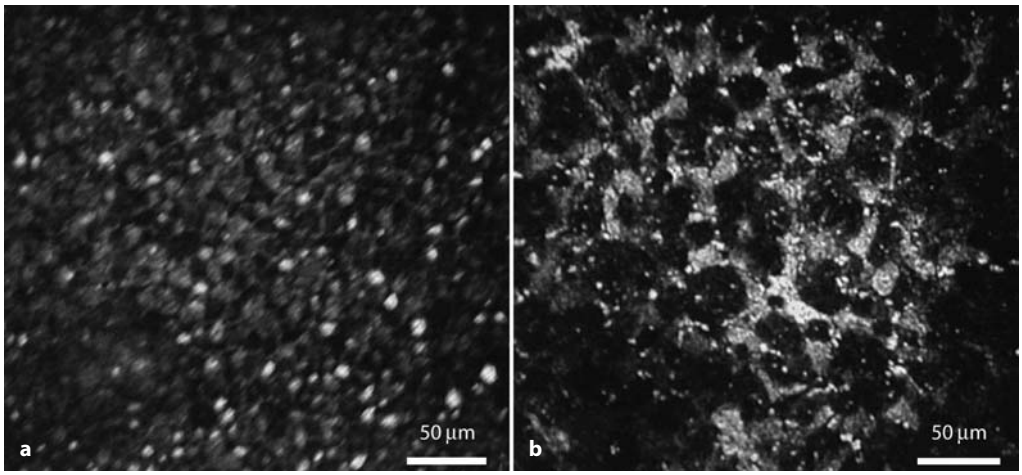

Fig. 5.67 Confocal images from a patient after amiodarone therapy: consistent finding of highly reflective round structures in the basal epithelium (z=20 µm)

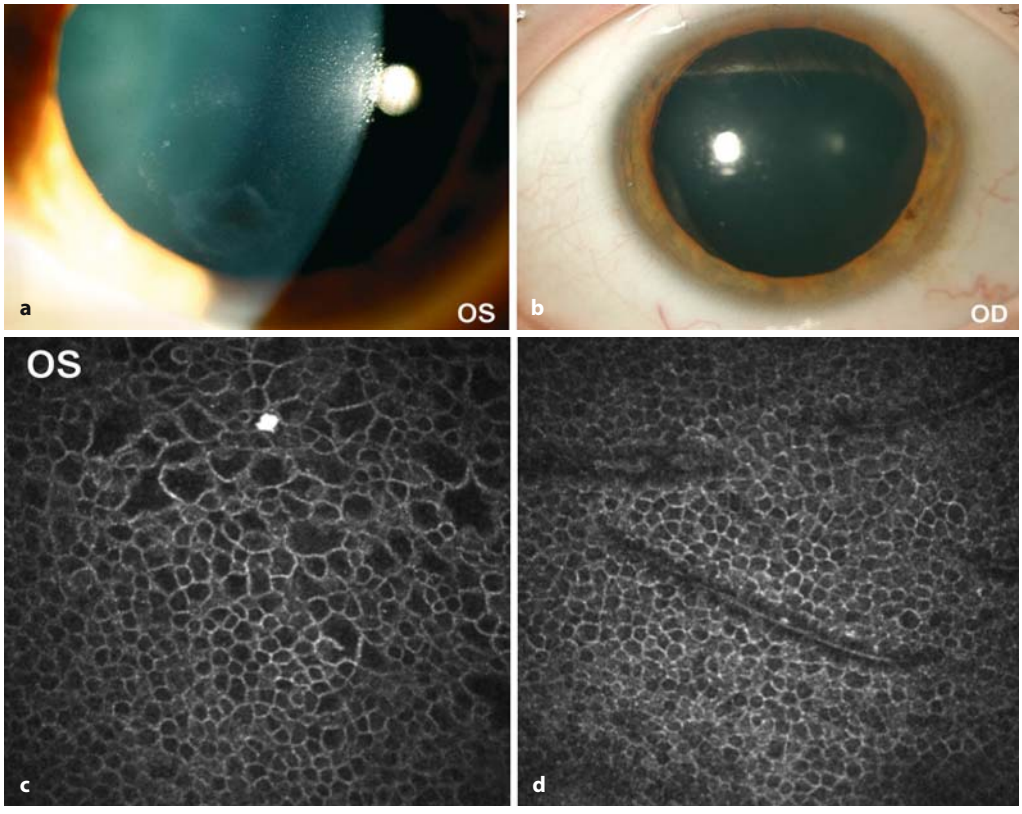

Fig. 5.68 a–h Interstitial keratitis. **a, b** Slit-lamp photographs of a 34-year-old man after bilateral interstitial keratitis. No signs of inflammation. On the left side, scar tissue is visible at the periphery and minimally in the central area (**a**); the cornea of the right eye is clear (**b**). **c–h** Confocal images of the left eye show structural changes at the level of lower intermediate-basal cells with formation of microscars and opacities (**c–e**) with an inconspicuous stroma (**f**).

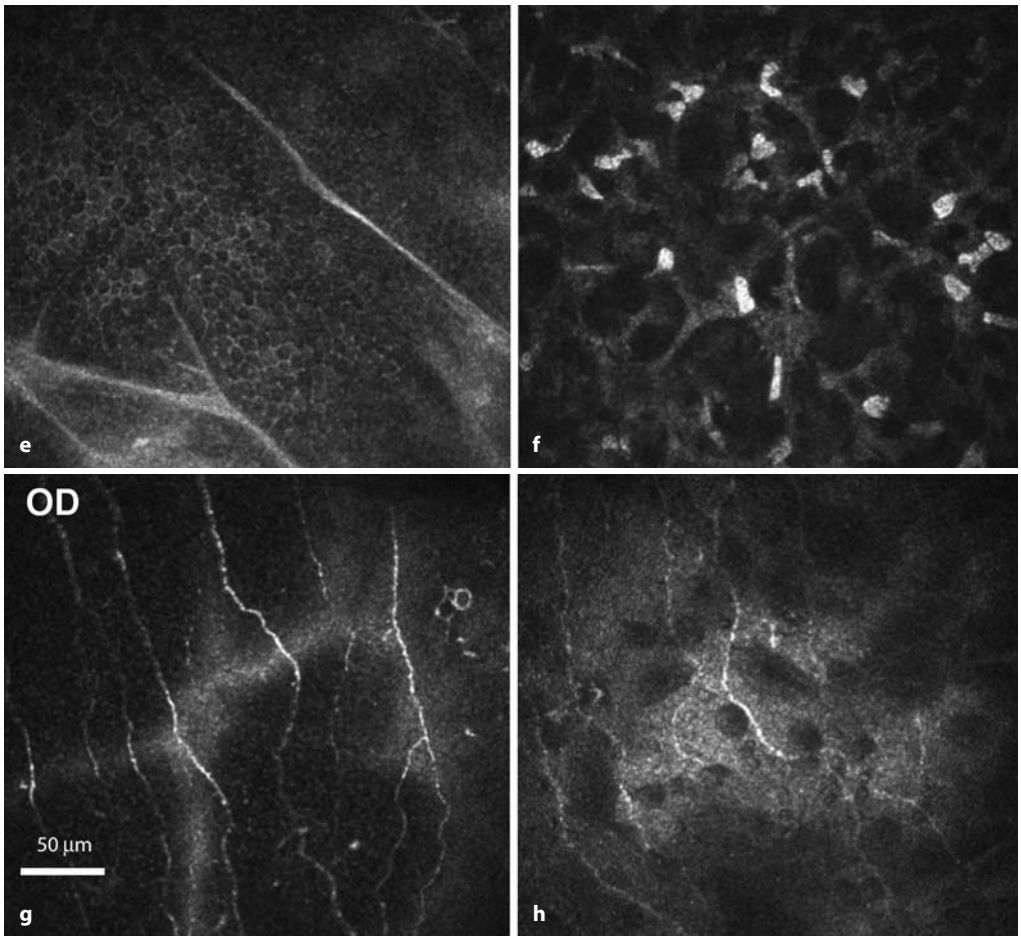

Fig. 5.68 (*continued*) The right side shows normal structure in the center (**g**) with peripheral dystrophic areas at the level of the subepithelial nerve plexus and Bowman's membrane (**h**)

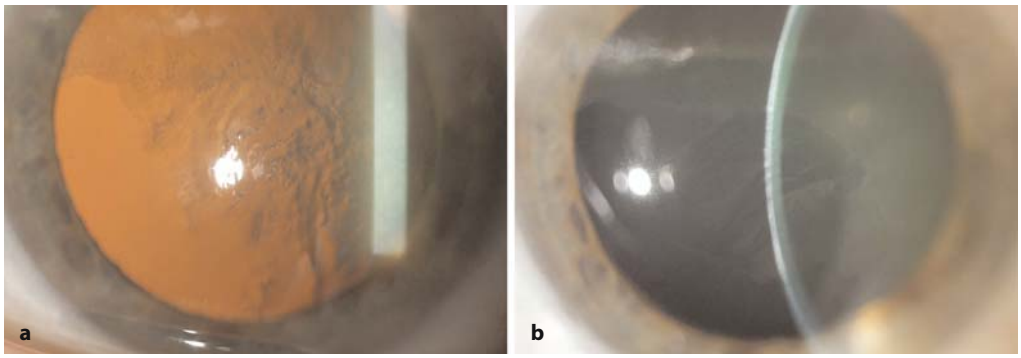

Fig. 5.69 a–h Interstitial keratitis. (**a, b**) Slit-lamp photographs of 61-year-old woman after interstitial keratitis. Scar tissues are visible in the anterior stroma on retro-illumination

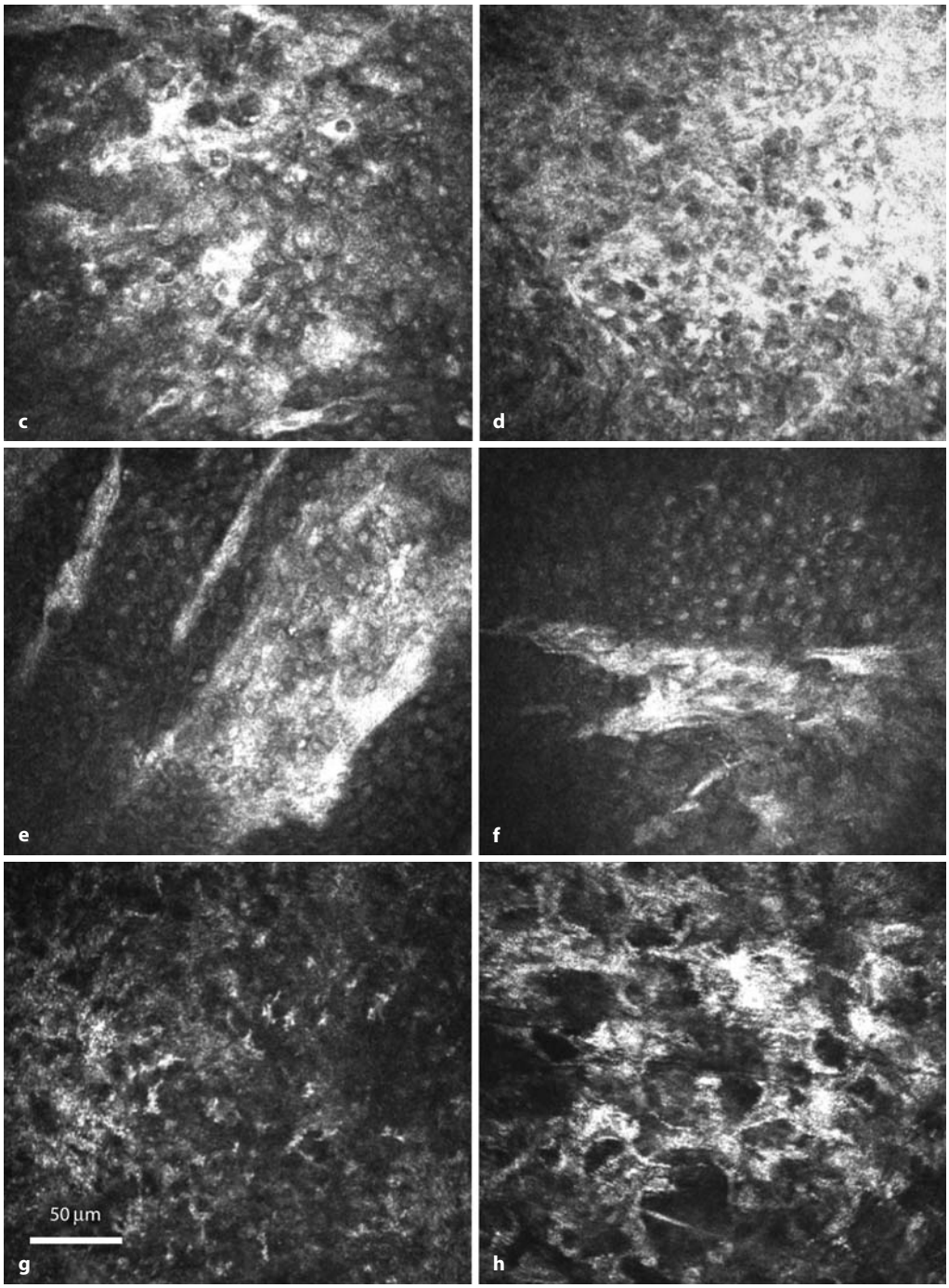

Fig. 5.69 (*continued*) **c–h** Pathological changes corresponding to opacities in the epithelium; minimal degree of corneal edema in the superficial and upper intermediate cells (**c, d**); highly reflective acellular structures at the level of the deeper intermediate and basal cells and absence of subepithelial nerve plexus in the area concerned (**e, f, g**). The anterior stroma displays an irregular collagen fiber structure with an atypical keratocyte pattern (**h**)

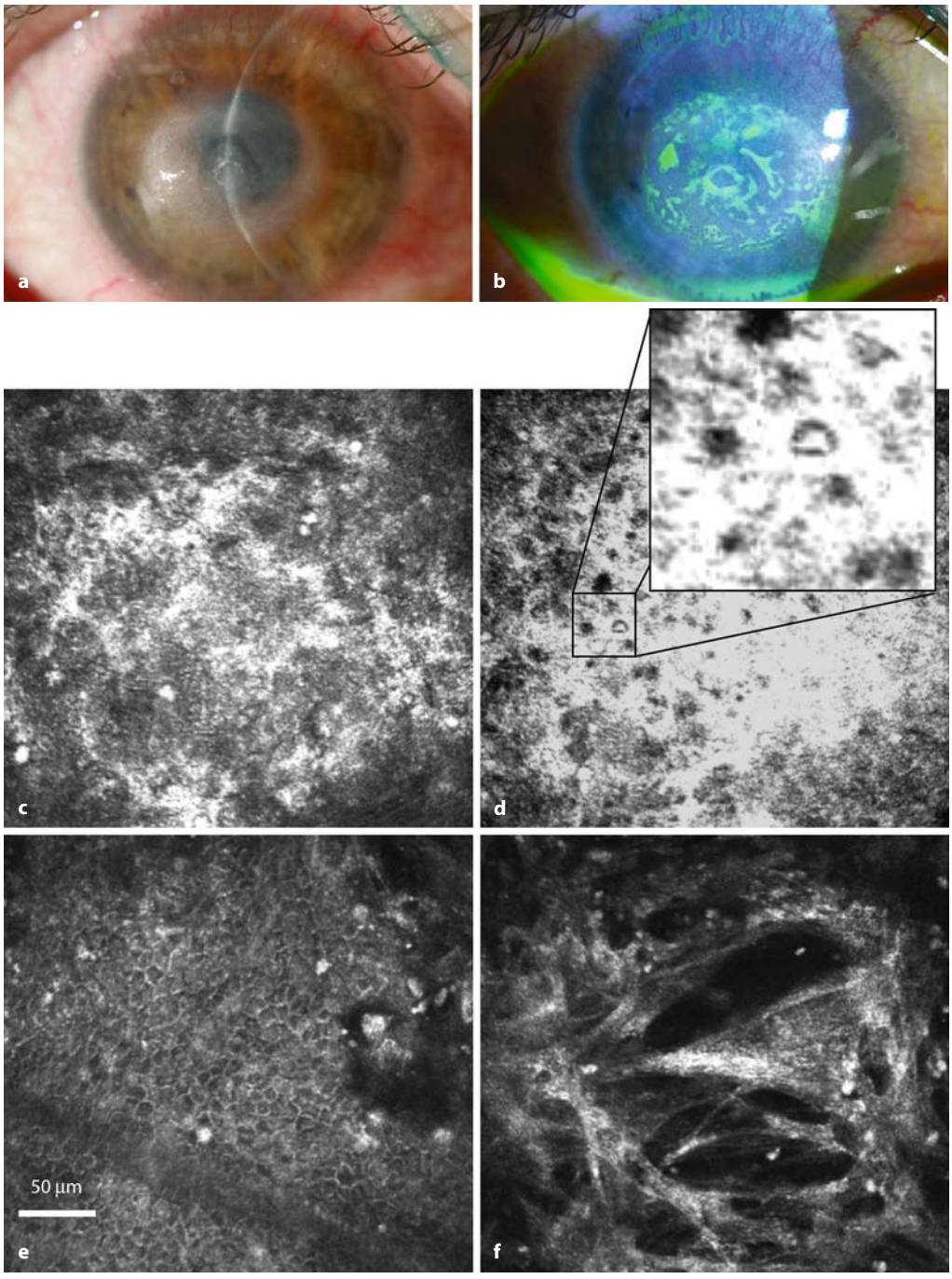

Fig. 5.70 *Acanthamoeba* keratitis. **a, b** Slit-lamp photographs from a 42-year-old woman with *Acanthamoeba* keratitis with epithelial and stromal ring infiltrate formation after dendritic epitheliopathy; corneal sensitivity is decreased. PCR (herpes zoster) and corneal culturing (for pathogens including *Acanthamoeba*) was negative. **c–f** Corneal microcysts (cystic stage of life cycle, round and up to 10 µm with double wall) are visible at the level of the deeper intermediate-basal cells (**c**) and in the anterior stroma (d). Same areas of the cornea after 3 months of specific therapy: no signs of cysts either in epithelium (**e**) or in stroma (**f**)

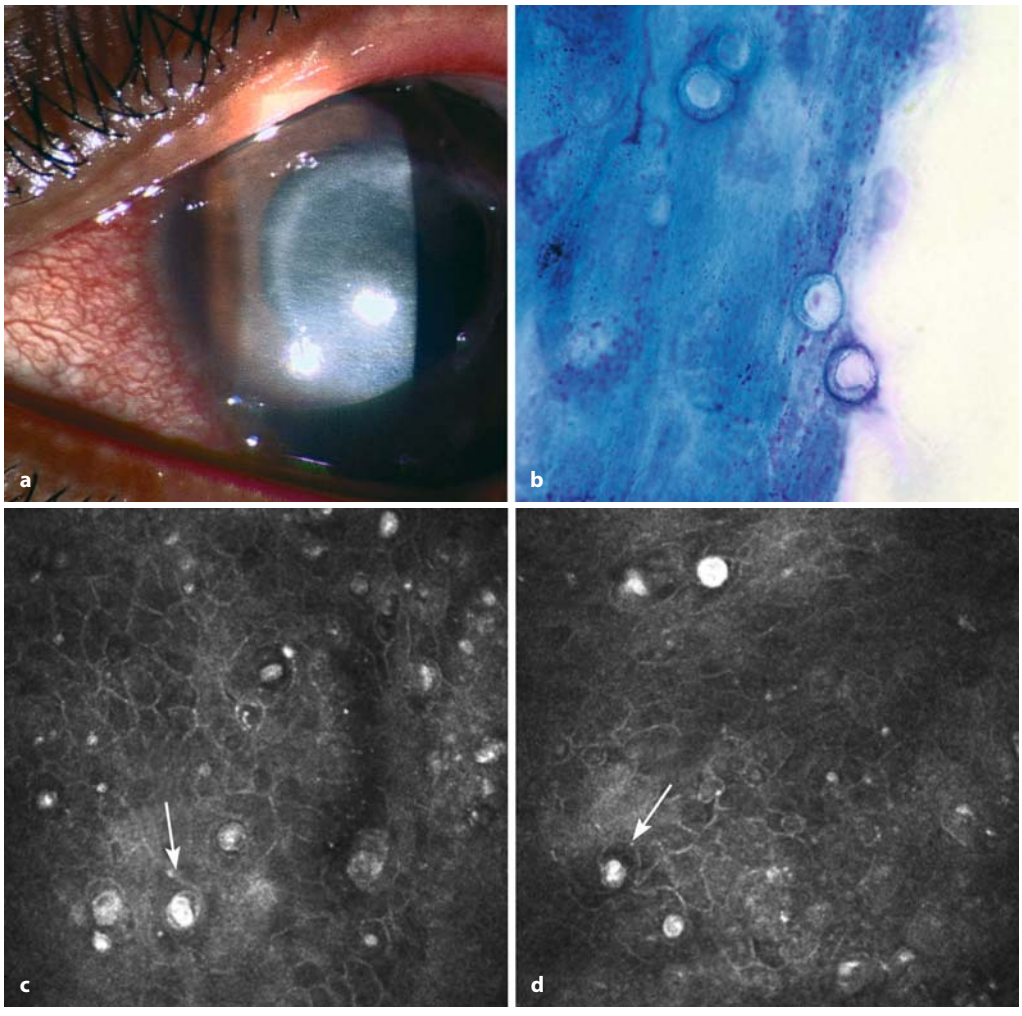

Fig. 5.71 *Acanthamoeba* keratitis. **a** Slit-lamp photograph of the right eye of a 22-year-old woman with *Acanthamoeba* keratitis. **b** *Acanthamoeba* cysts on cytological analysis. **c, d** *Acanthamoeba* cysts observed by confocal in vivo microscopy

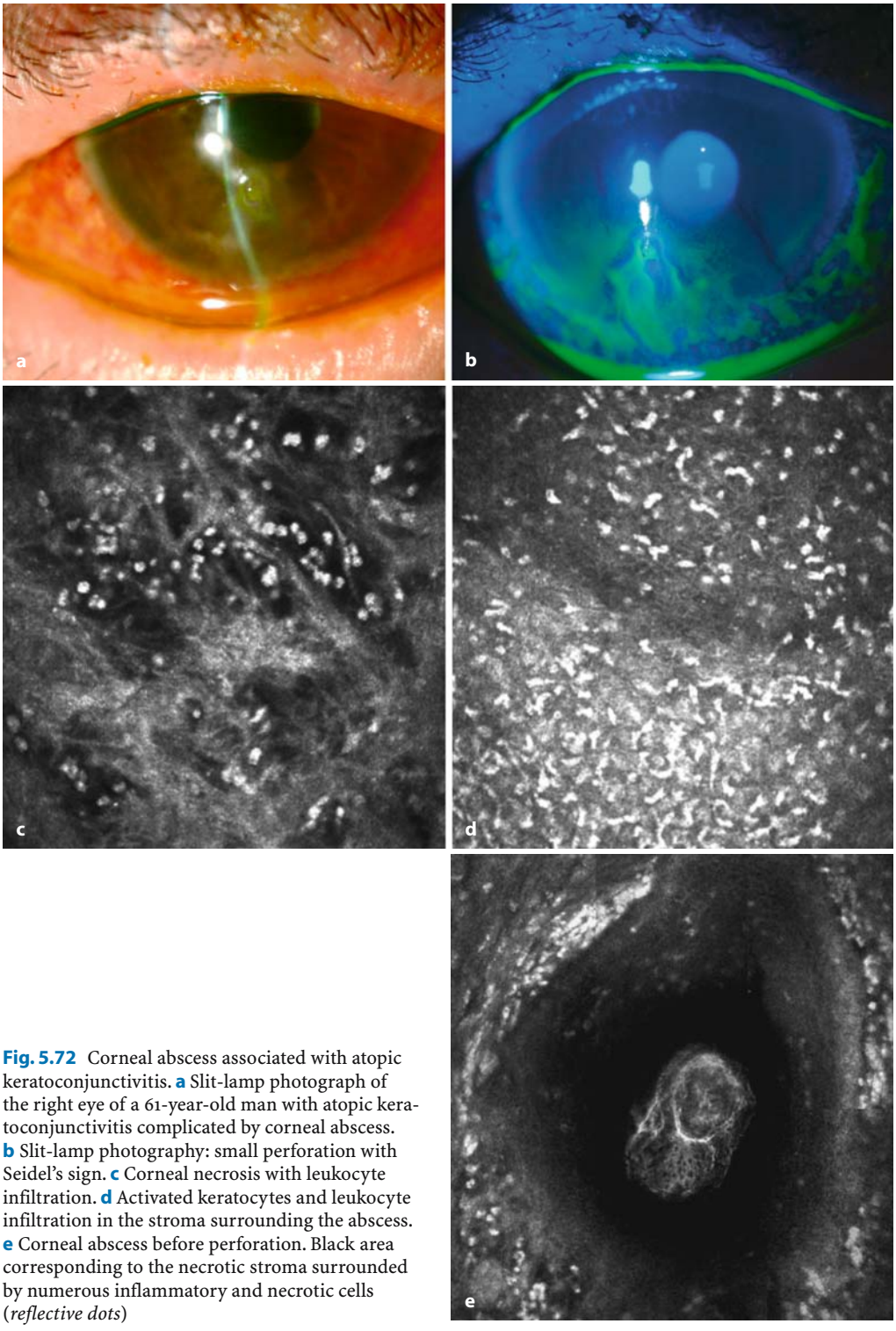

Fig. 5.72 Corneal abscess associated with atopic keratoconjunctivitis. **a** Slit-lamp photograph of the right eye of a 61-year-old man with atopic keratoconjunctivitis complicated by corneal abscess. **b** Slit-lamp photography: small perforation with Seidel's sign. **c** Corneal necrosis with leukocyte infiltration. **d** Activated keratocytes and leukocyte infiltration in the stroma surrounding the abscess. **e** Corneal abscess before perforation. Black area corresponding to the necrotic stroma surrounded by numerous inflammatory and necrotic cells (*reflective dots*)

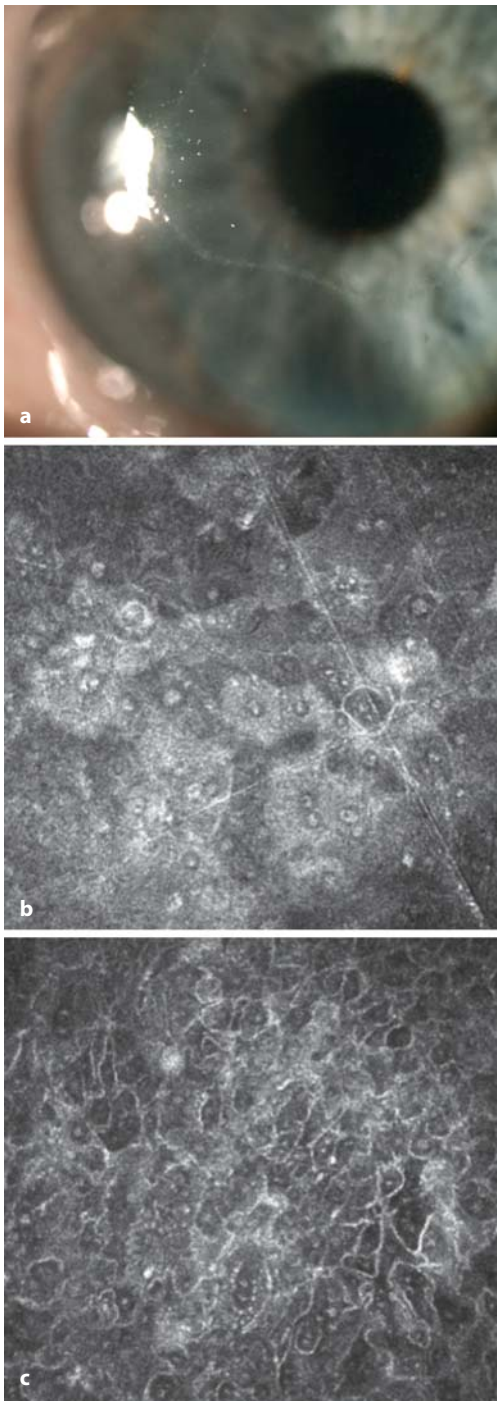

Fig. 5.73 Viral keratitis. **a** Slit-lamp photograph of the right eye of a 44-year-old man with viral keratitis, with immune infiltrates surrounding the keratitis. **b, c** Epithelial cell abnormalities, reflective nuclei, and binucleated cells

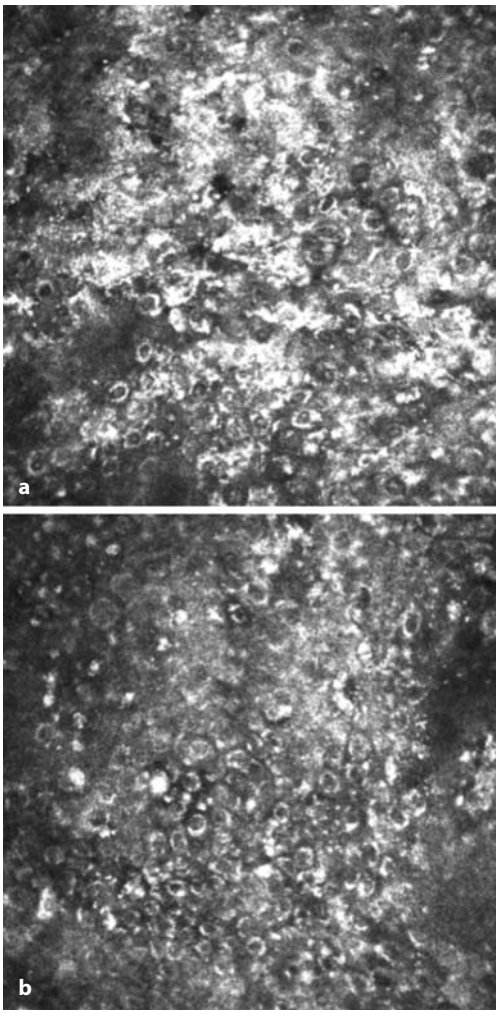

Fig. 5.74 Corneal wound healing: corneal ulcer. Multiple cellular abnormalities at the ulcer edges: hyperreflective cells, reflective nuclei, and polymorphism

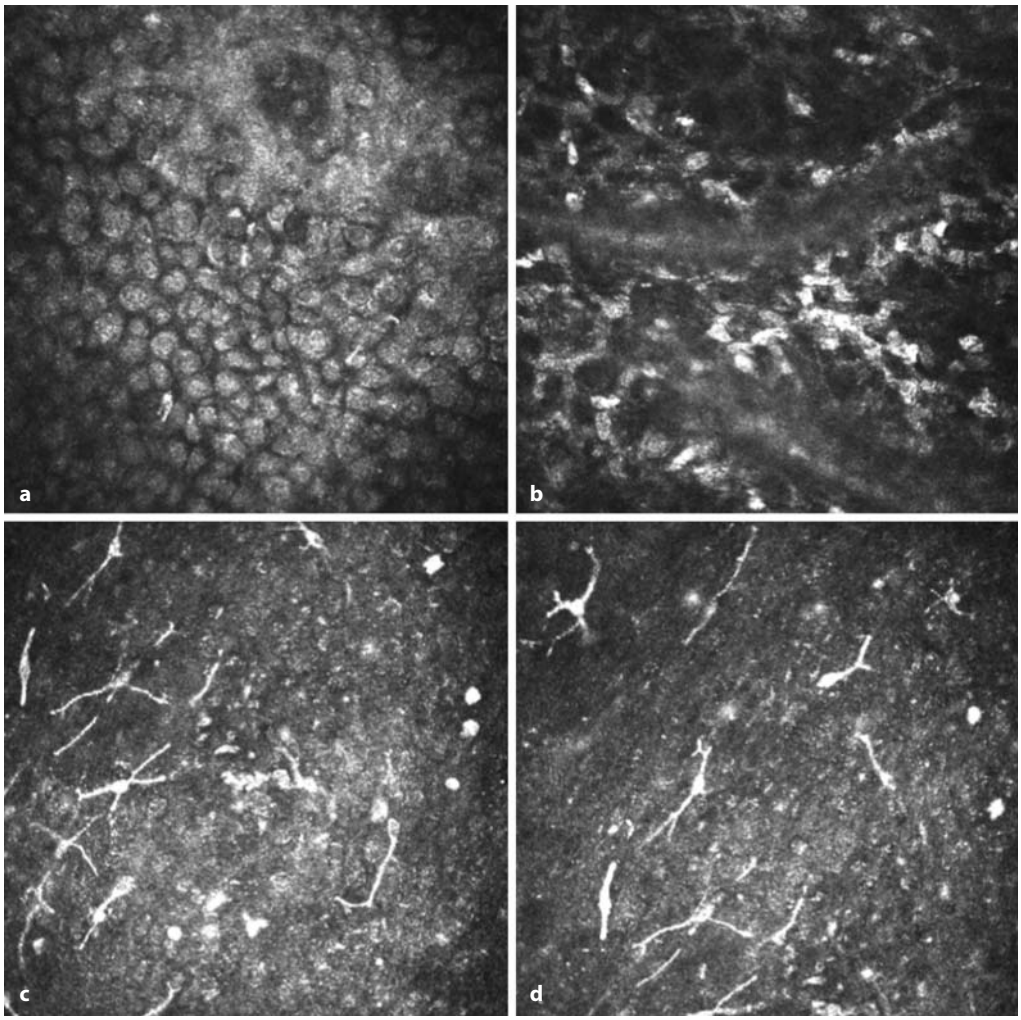

Fig. 5.75 Corneal wound healing: recently healed ulcer. **a** Activated corneal epithelium with reflective cells. **b** Numerous activated keratocytes in the anterior stroma below Bowman's layer. **c, d** Multiple inflammatory cells: dendritic cells

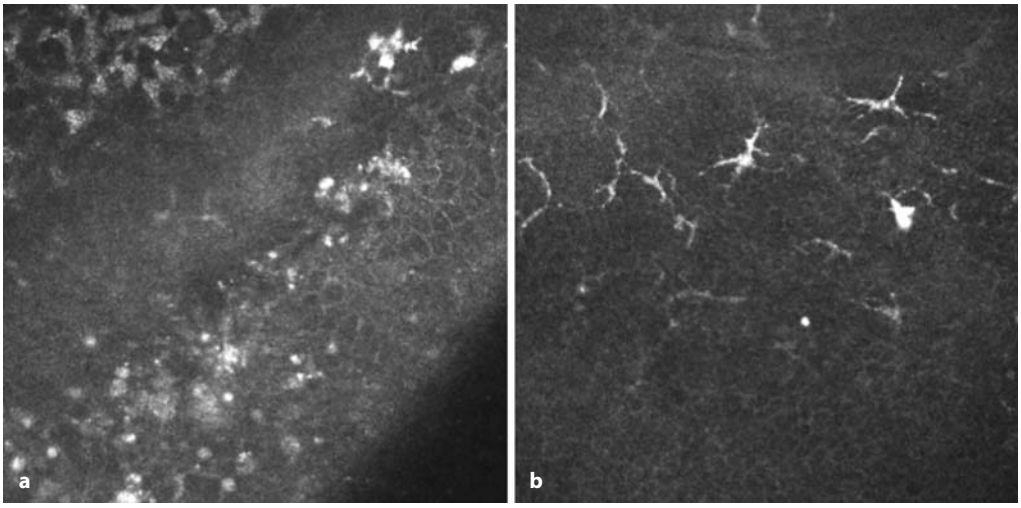

Fig. 5.76 Penetrating keratoplasty. **a** Oblique section showing the corneal graft: irregular and hyperreflective epithelium and activated stroma. **b** Dendritic cells at the edge of the corneal graft

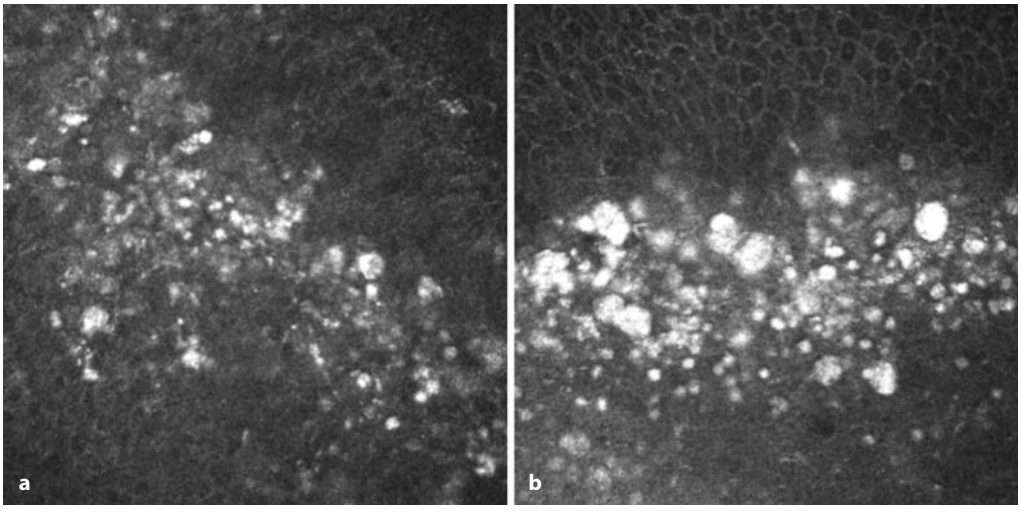

Fig. 5.77 Penetrating keratoplasty. Immune ring at the edge of a corneal graft in a case of epithelial rejection, with precipitates (*reflective dots*) in the corneal epithelium

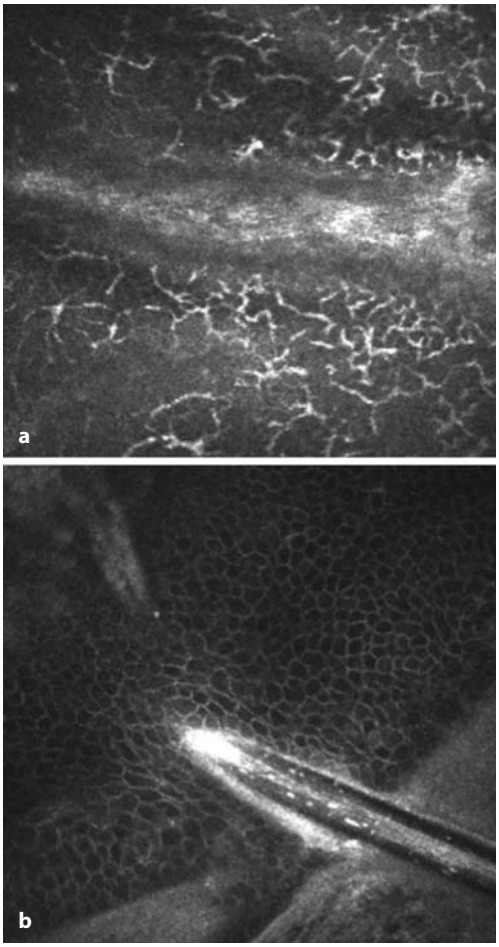

Fig. 5.78 Penetrating keratoplasty. **a** Periphery of the corneal graft: inflammatory cells on both sides. **b** Corneal suture penetrating the basal corneal epithelium

Fig. 5.79 Refractive surgery: slit-lamp photograph of a radial keratotomy performed 15 years previously

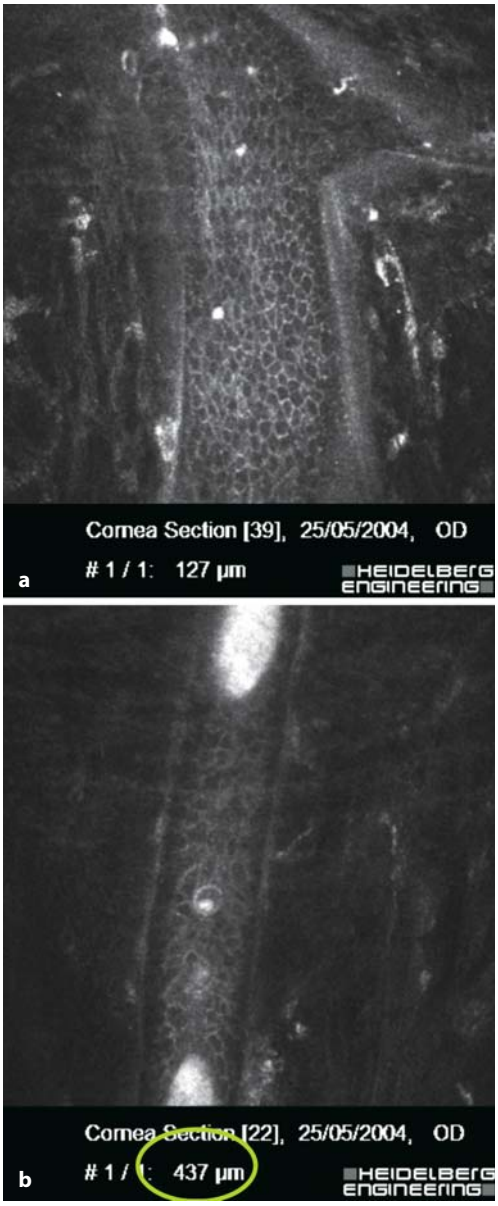

Fig. 5.80 Same patient as in Fig. 5.79: confocal microscopy images of a furrow. Note the presence of corneal epithelial cells located very deeply in the bed of the incision

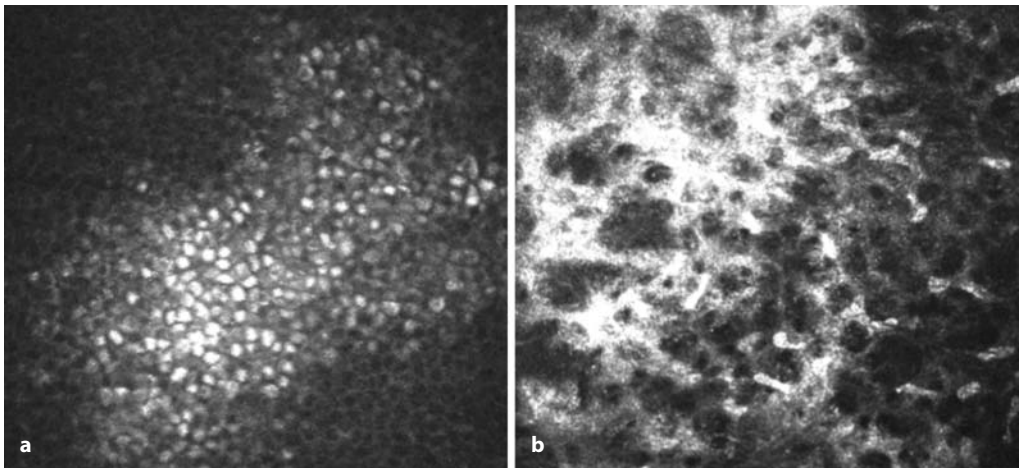

Fig. 5.81 Refractive surgery: photorefractive keratectomy. **a** Corneal haze 3 years after photorefractive keratectomy. Activated corneal epithelial cells are abnormally hyperreflective. **b** At a deeper level, fibrosis of the epithelial basement membrane, activated keratocytes, and hyperreflective deposits

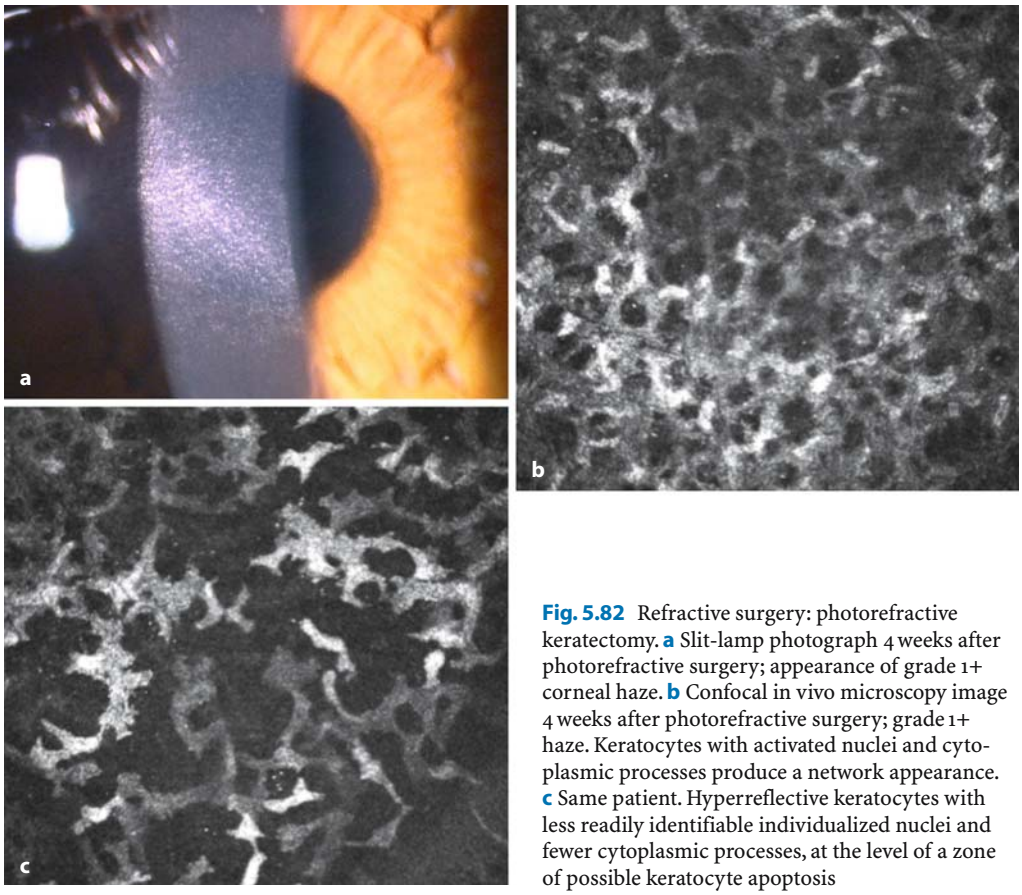

Fig. 5.82 Refractive surgery: photorefractive keratectomy. **a** Slit-lamp photograph 4 weeks after photorefractive surgery; appearance of grade 1+ corneal haze. **b** Confocal in vivo microscopy image 4 weeks after photorefractive surgery; grade 1+ haze. Keratocytes with activated nuclei and cytoplasmic processes produce a network appearance. **c** Same patient. Hyperreflective keratocytes with less readily identifiable individualized nuclei and fewer cytoplasmic processes, at the level of a zone of possible keratocyte apoptosis

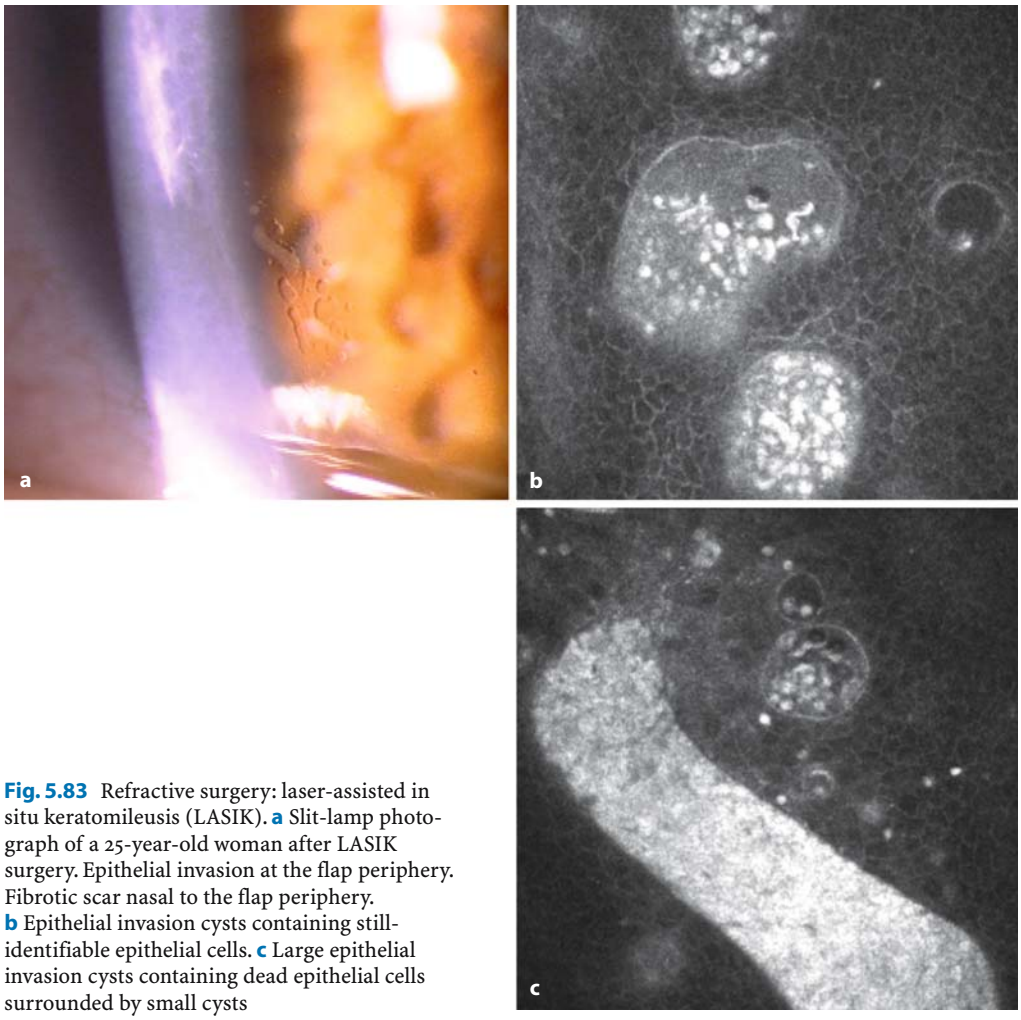

Fig. 5.83 Refractive surgery: laser-assisted in situ keratomileusis (LASIK). **a** Slit-lamp photograph of a 25-year-old woman after LASIK surgery. Epithelial invasion at the flap periphery. Fibrotic scar nasal to the flap periphery. **b** Epithelial invasion cysts containing still-identifiable epithelial cells. **c** Large epithelial invasion cysts containing dead epithelial cells surrounded by small cysts

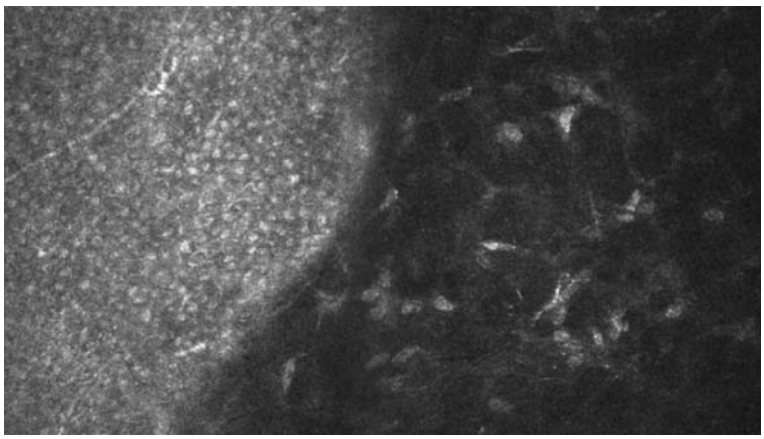

Fig. 5.84 Refractive surgery: laser-assisted in situ keratomileusis (LASIK). Confocal microscopy image of epithelial invasion at the interface with the stroma

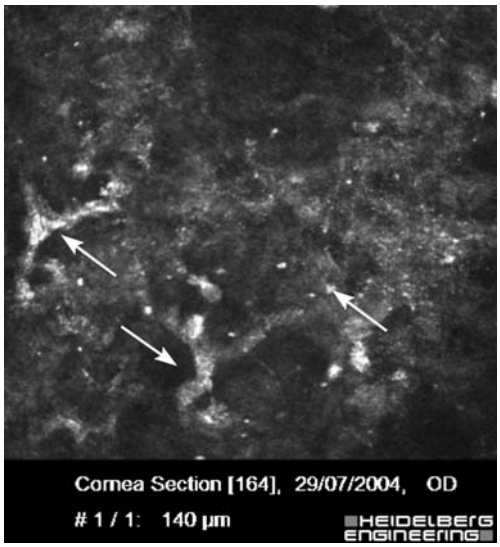

Fig. 5.85 Refractive surgery: laser-assisted in situ keratomileusis (LASIK). Confocal microscopy image of keratocyte activation 1 week after LASIK

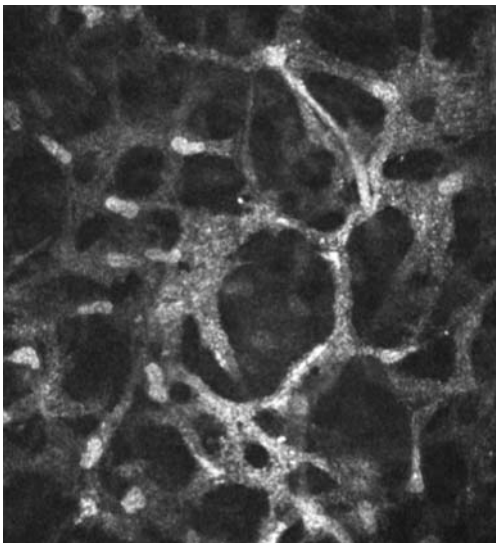

Fig. 5.86 Refractive surgery: laser-assisted in situ keratomileusis (LASIK). Confocal microscopy image of keratocyte activation 1 month after LASIK

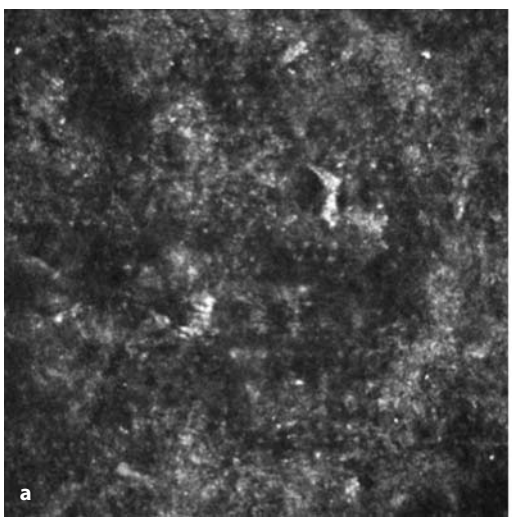

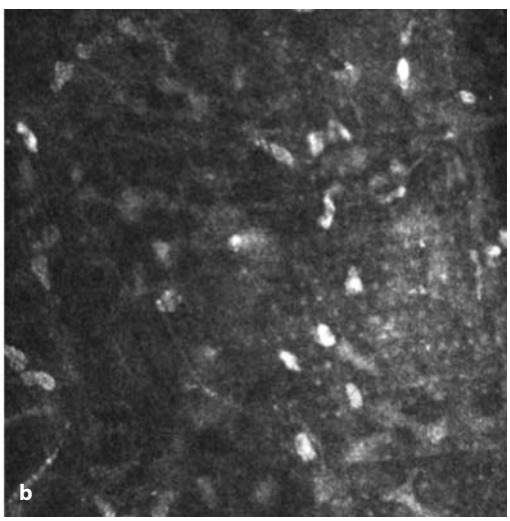

Fig. 5.87 Refractive surgery: laser-assisted in situ keratomileusis. **a, b** Early after flap creation with femtosecond laser (IntraLase) showing the existence of regularly disposed spots, probably corresponding to the microcysts created by laser impact. These spots disappear in the weeks following the procedure

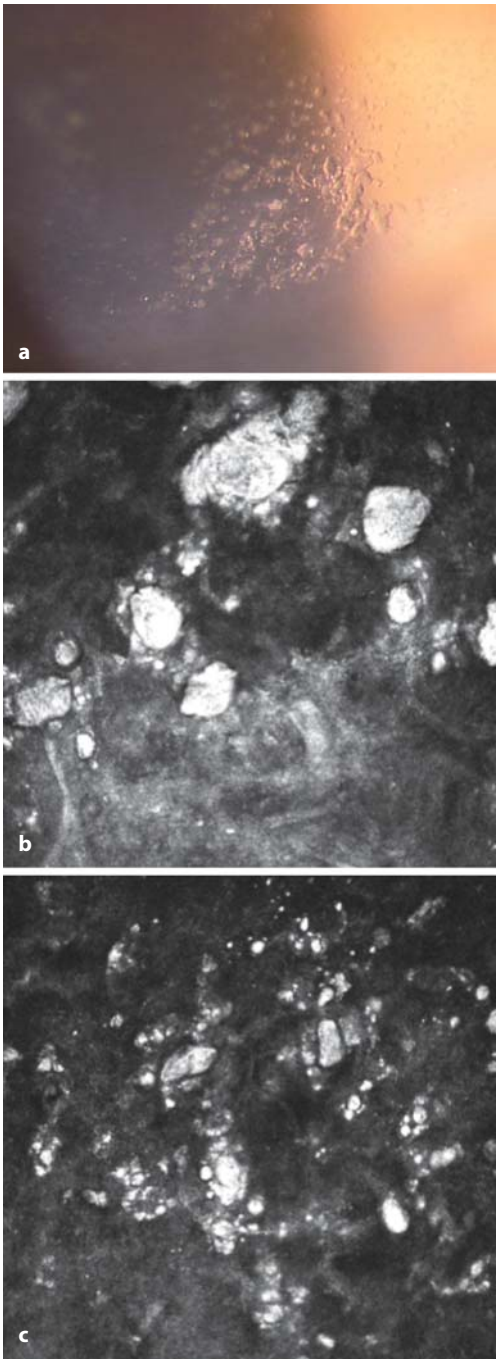

Fig. 5.88 Refractive surgery: laser-assisted in situ keratomileusis (LASIK). **a** Slit-lamp photograph of brightly reflective deposits at the LASIK interface. **b, c** Confocal in vivo microscopy image of these reflective deposits at the LASIK interface

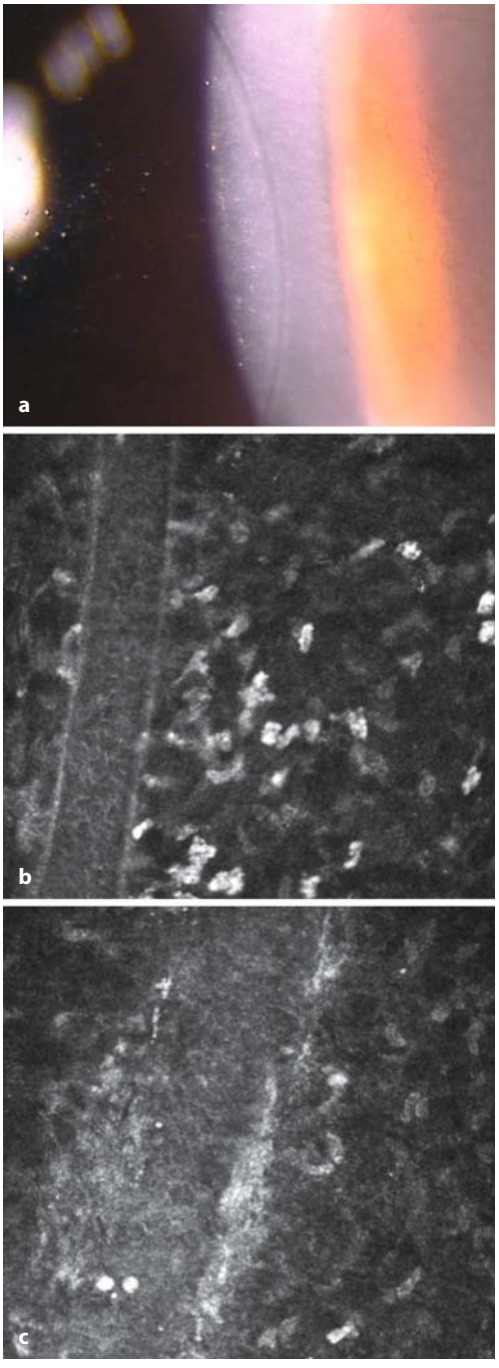

Fig. 5.89 Refractive surgery: laser-assisted in situ keratomileusis (LASIK). **a** Slit-lamp photograph of the flap margin after the IntraLase procedure. **b** Corresponding confocal in vivo microscopy image. **c** Confocal in vivo microscopy image showing the flap margin created by the mechanical microkeratome. Note the less clearly recognizable incision compared with IntraLase

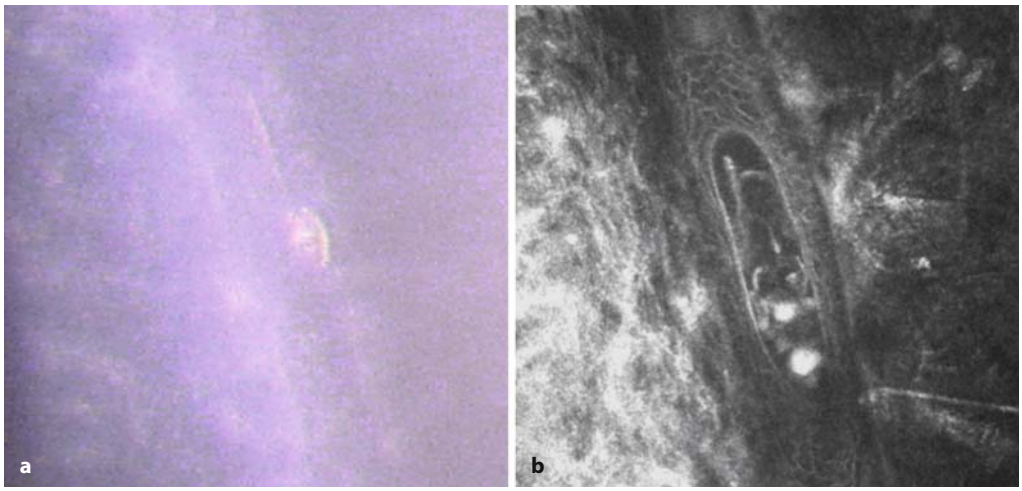

Fig. 5.90 Refractive surgery: laser-assisted in situ keratomileusis. **a** Slit-lamp photograph of an epithelial cyst induced by an inclusion at the flap periphery. **b** Corresponding confocal in vivo microscopy image

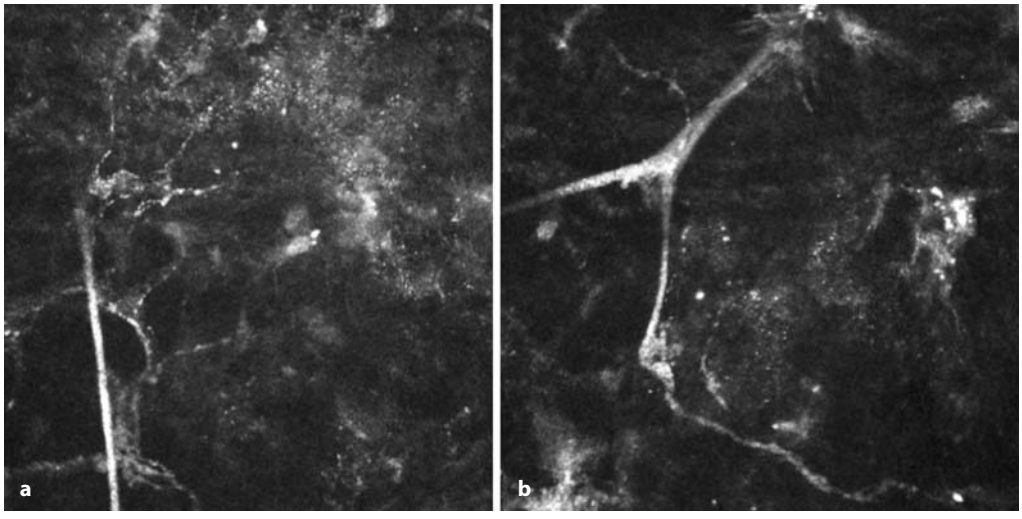

Fig. 5.91 Refractive surgery: laser-assisted in situ keratomileusis at 6 months. Corneal nerves are again visible ahead of the interface

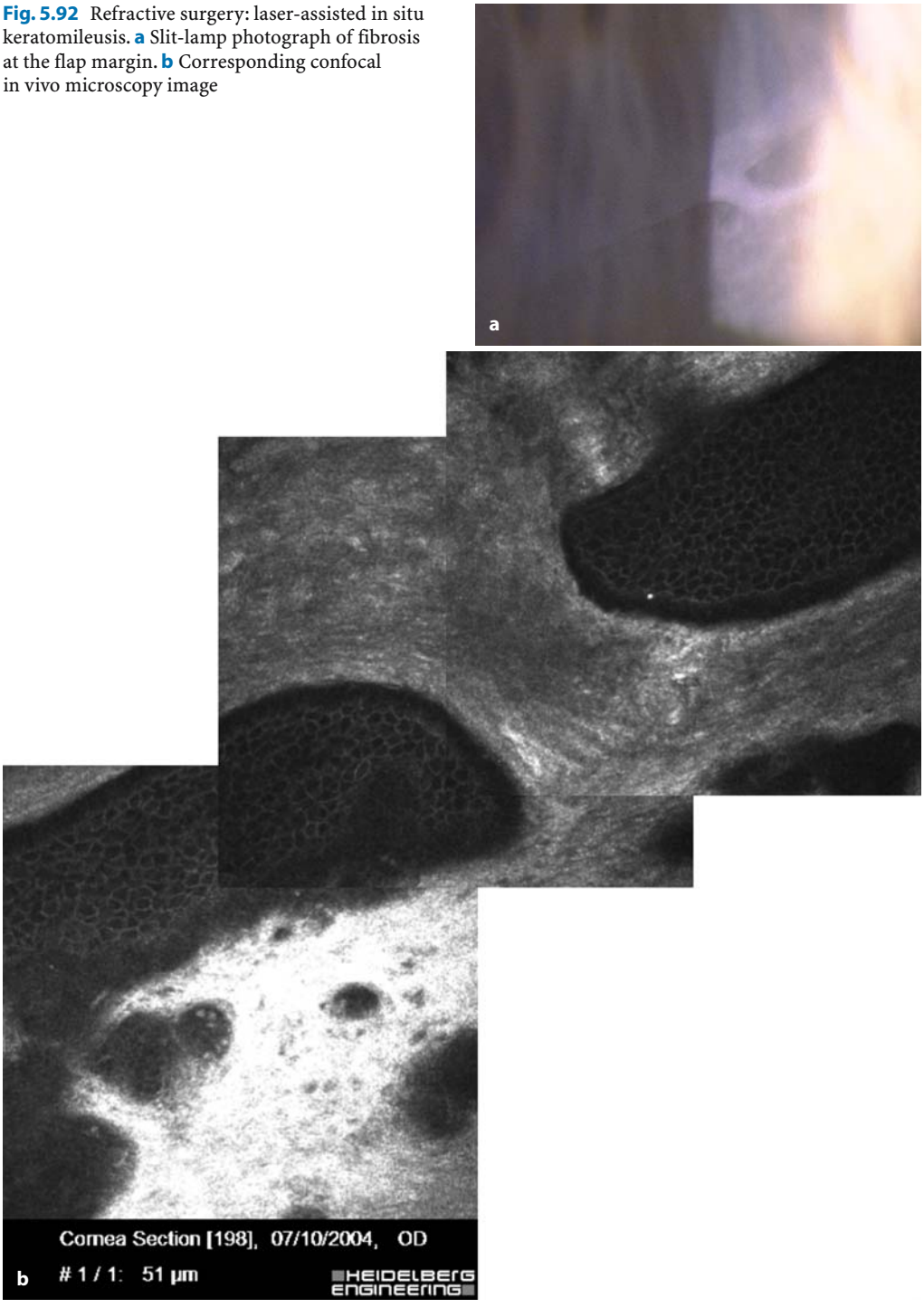

Fig. 5.92 Refractive surgery: laser-assisted in situ keratomileusis. **a** Slit-lamp photograph of fibrosis at the flap margin. **b** Corresponding confocal in vivo microscopy image

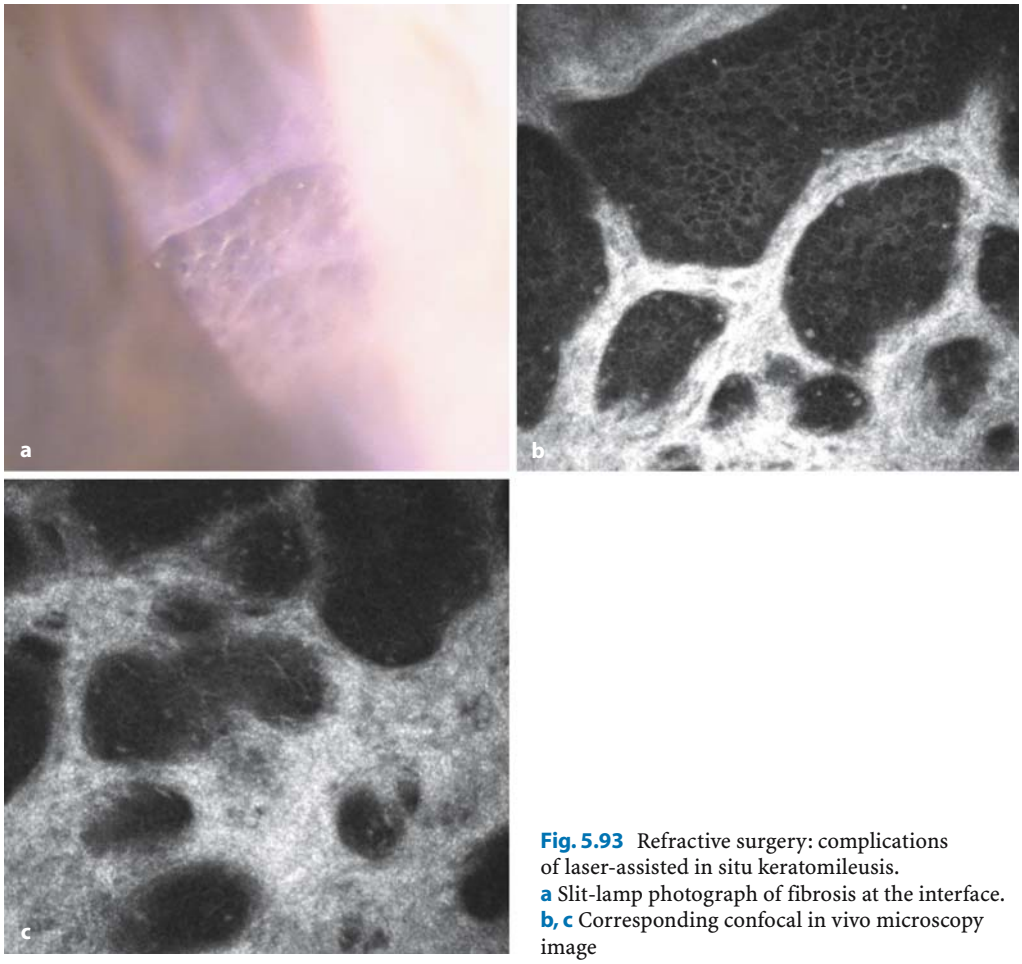

Fig. 5.93 Refractive surgery: complications of laser-assisted in situ keratomileusis.
a Slit-lamp photograph of fibrosis at the interface.
b, c Corresponding confocal in vivo microscopy image

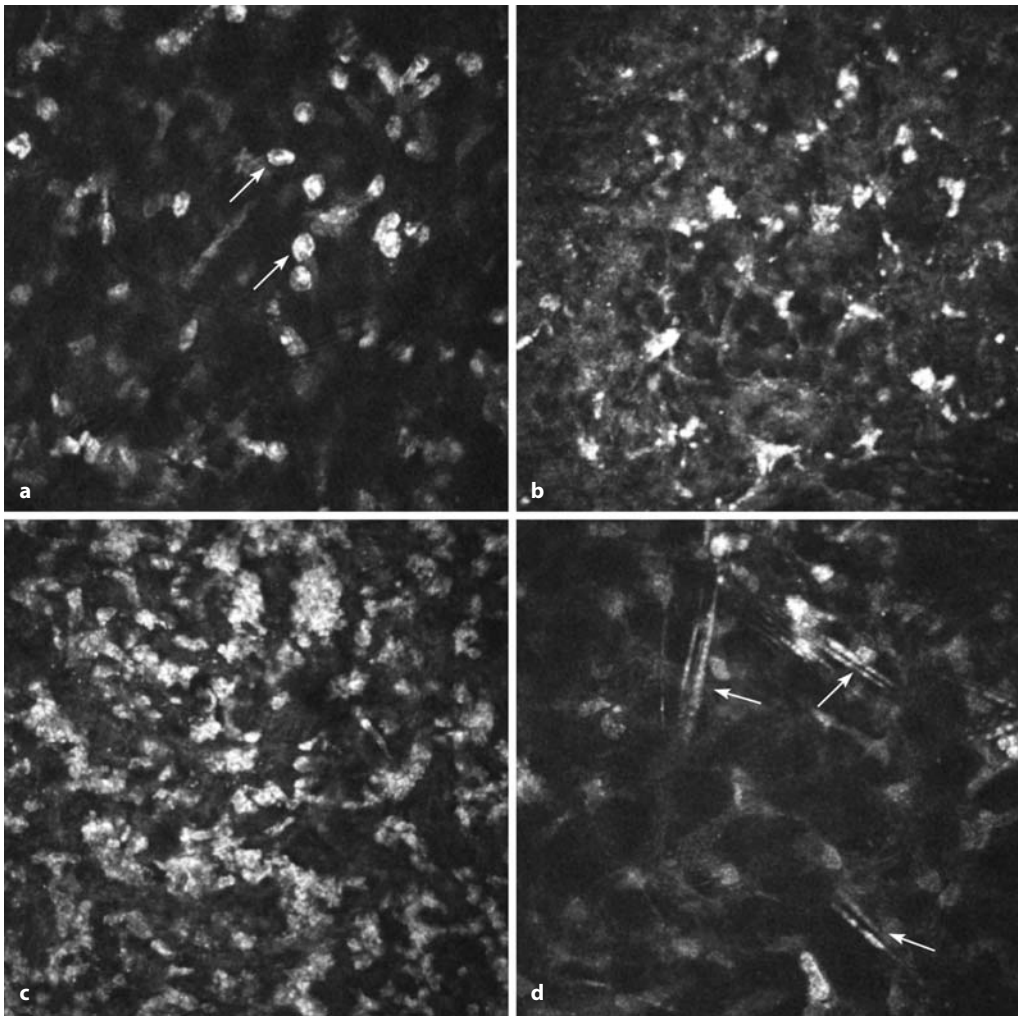

Fig. 5.94 Refractive surgery: complications of laser-assisted in situ keratomileusis. **a** Sands of Sahara syndrome on day 5. Reflective inflammatory cells. **b** Residual inflammatory cells at the interface on day 7. **c** Multiple reflective cells, possibly corresponding to neutrophils. **d** Numerous switchlike structures possibly corresponding to degradation products of neutrophils

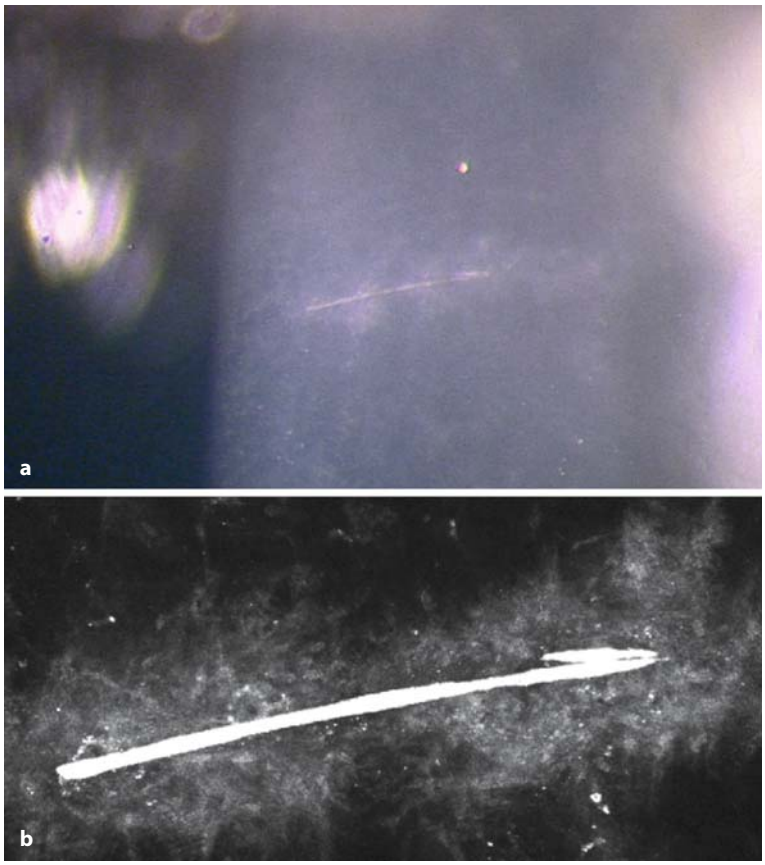

Fig. 5.95 Refractive surgery: complications of laser-assisted in situ keratomileusis). **a** Slit-lamp photograph of a fiber from a microsponge at the interface. **b** Corresponding confocal in-vivo microscopy image

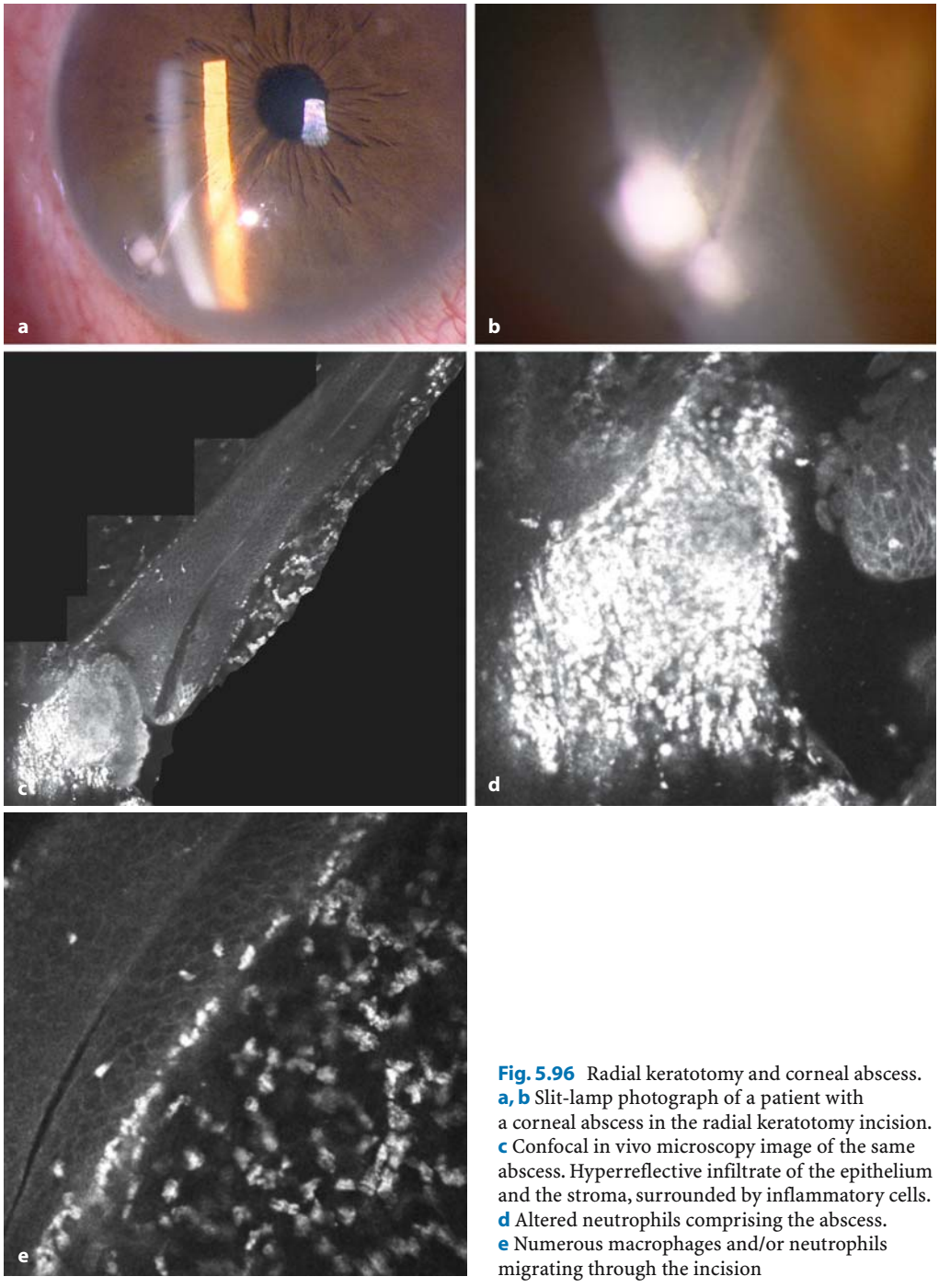

Fig. 5.96 Radial keratotomy and corneal abscess. **a, b** Slit-lamp photograph of a patient with a corneal abscess in the radial keratotomy incision. **c** Confocal in vivo microscopy image of the same abscess. Hyperreflective infiltrate of the epithelium and the stroma, surrounded by inflammatory cells. **d** Altered neutrophils comprising the abscess. **e** Numerous macrophages and/or neutrophils migrating through the incision

5.6 Descemet's Membrane

5.6.1 Normal Anatomy

Like Bowman's membrane, Descemet's membrane has an amorphous appearance and is therefore not visualized in healthy subjects.

5.6.2 Pathological Findings

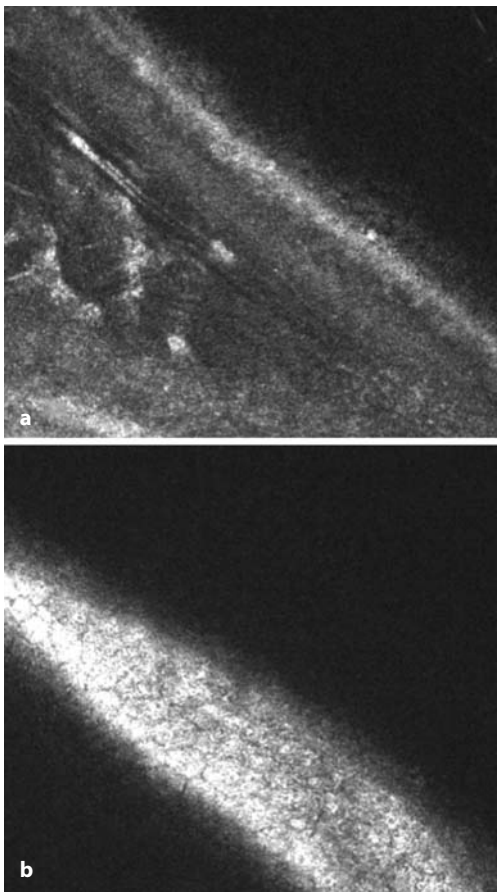

Fig. 5.97 Fold in Descemet's membrane. **a** Due to the oblique section, the changing structure is visible between the posterior stroma and the endothelium. **b** The borders of the endothelial cells are fading

5.7 Endothelial Cells and Trabecular Structures

5.7.1 Normal Anatomy

The endothelium consists of a regular pattern of hexagonal reflective cells. The cell nuclei cannot usually be visualized. The cell borders reflect less light than the cytoplasm, with the result that a network of dark cell borders appears between areas of bright cytoplasm. Endothelial cell density can be determined by counting (Figs. 5.98–5.102).

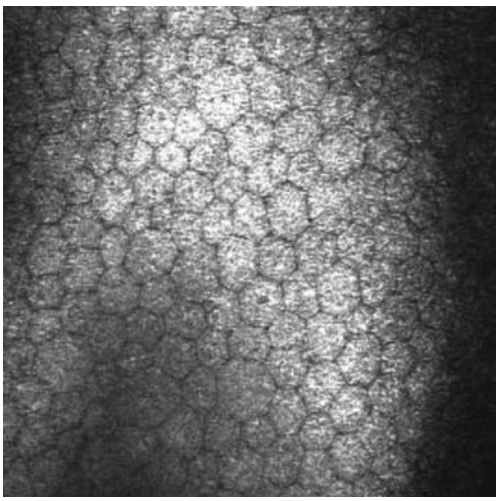

Fig. 5.98 Endothelium. A monolayer of regularly arranged hexagonal cells completely covering the posterior surface of the cornea. Unlike the basal cells, these cells have a brightly reflecting cytoplasm and dark cell borders. The cell nucleus is not visible

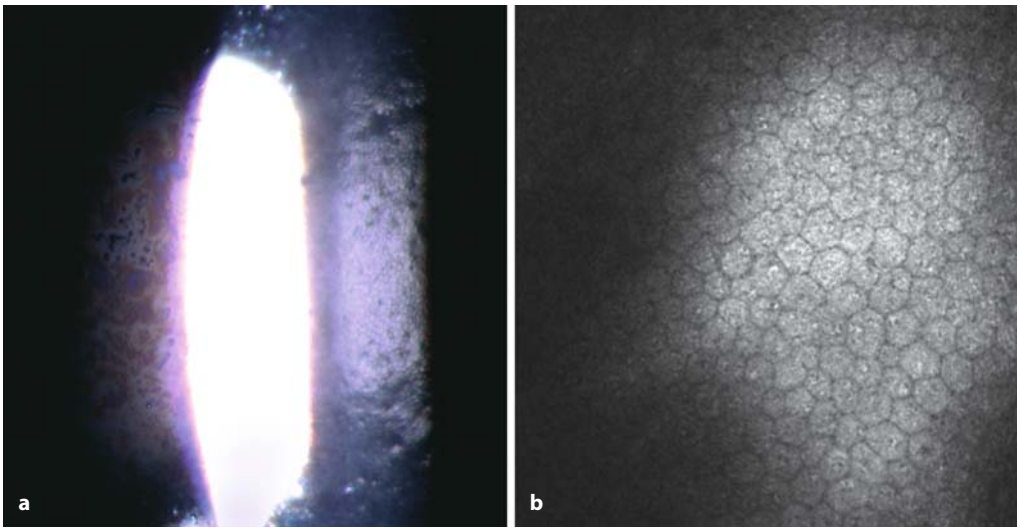

Fig. 5.99 Endothelium. **a** Slit-lamp photograph of normal endothelial cells. **b** Confocal in vivo microscopy image of normal endothelial cells

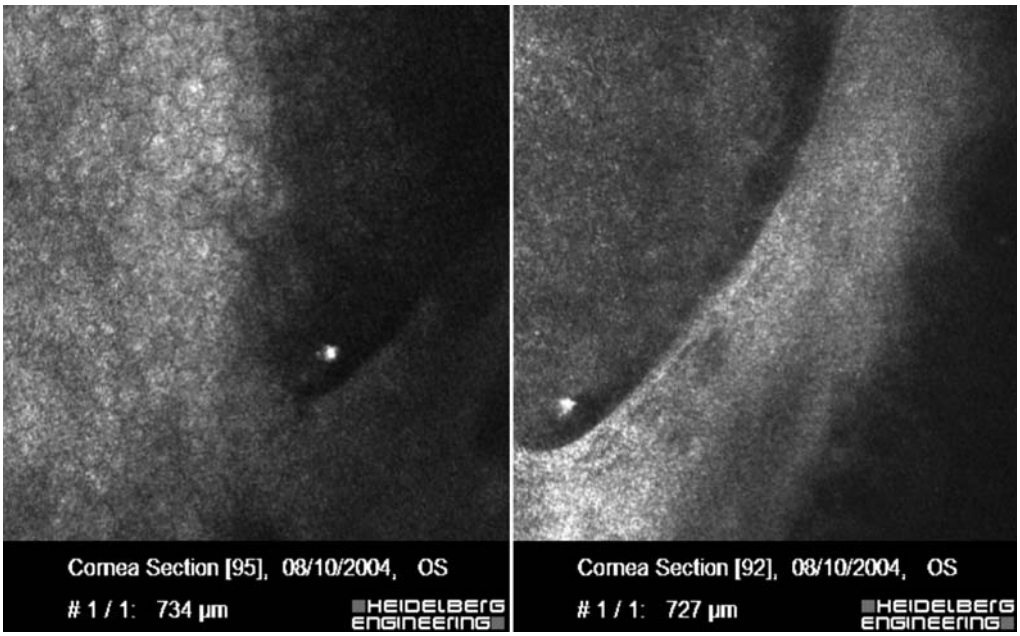

Fig. 5.100 Trabeculum. Schwalbe's ring at the periphery of the endothelium

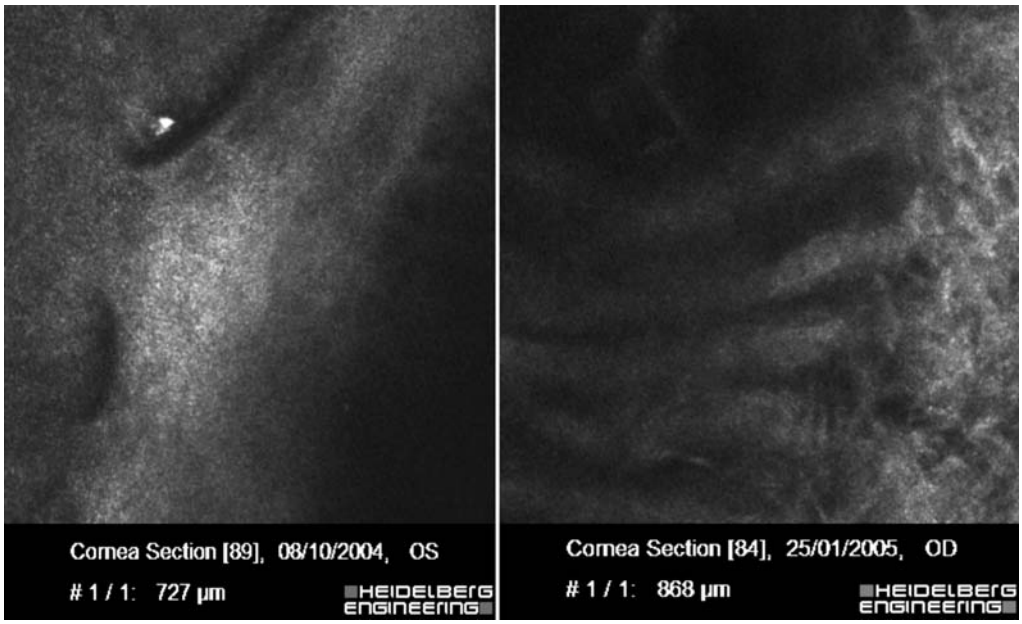

Fig. 5.101 Trabeculum. Schwalbe's ring and trabecular meshwork

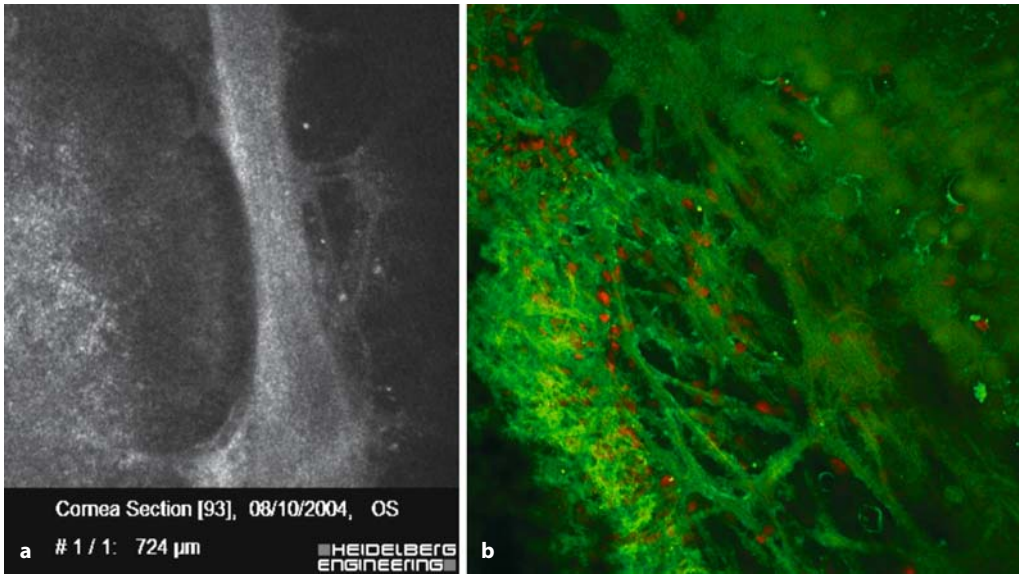

Fig. 5.102 Trabeculum. **a** Confocal in vivo microscopy image of Schwalbe's ring and trabecular meshwork. **b** Ex vivo histologic image of the same area

5.7.2 Pathological Findings

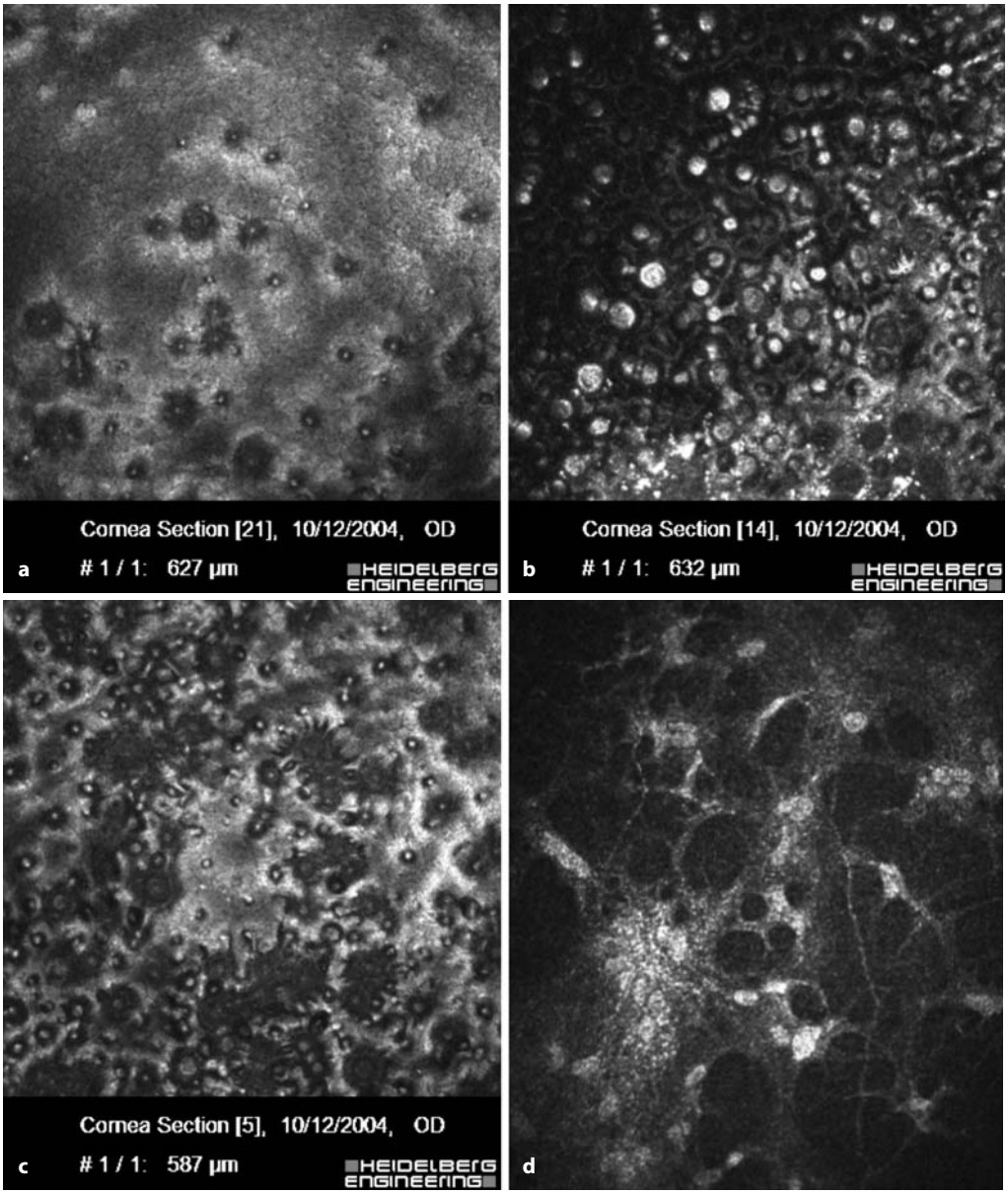

Fig. 5.103 a–f Endothelial dystrophy: cornea guttata. **a–c** Round hyporeflective structures (guttae) with occasional central reflective material at the level of the endothelium. **d–f** Stroma: fibrosis and activated keratocytes

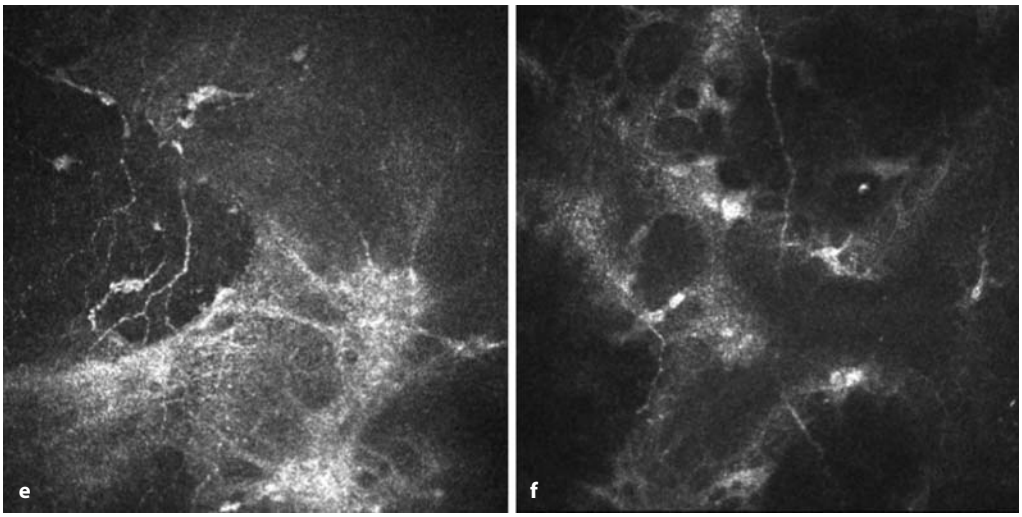

Fig. 5.103 (*continued*) Endothelial dystrophy: cornea guttata. **a–c** Round hyporeflective structures (guttae) with occasional central reflective material at the level of the endothelium. **d–f** Stroma: fibrosis and activated keratocytes

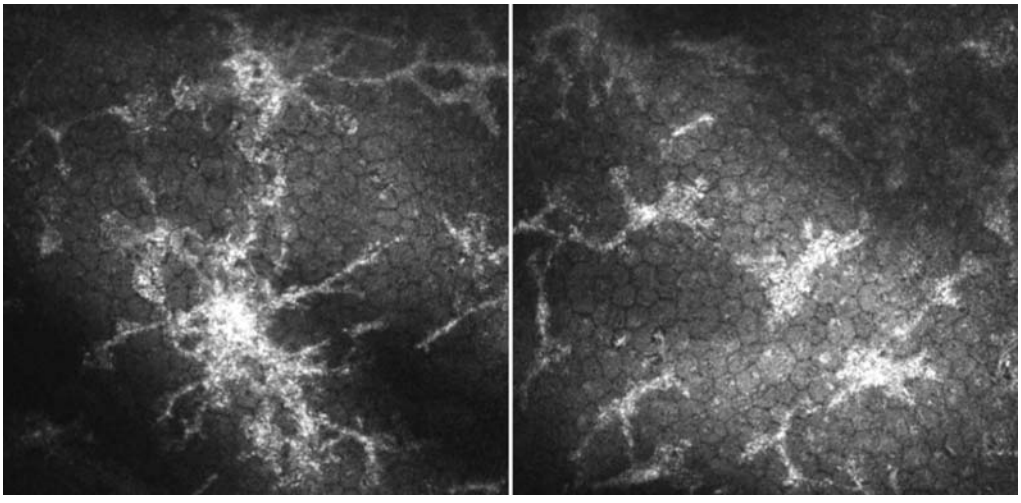

Fig. 5.104 Keratic precipitates

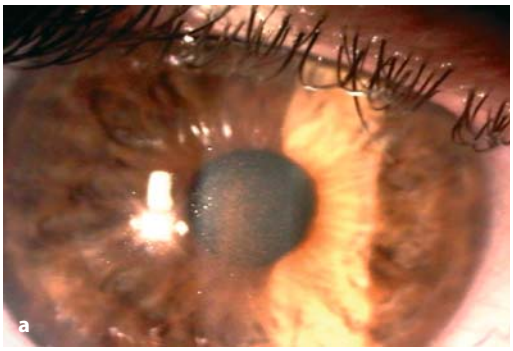

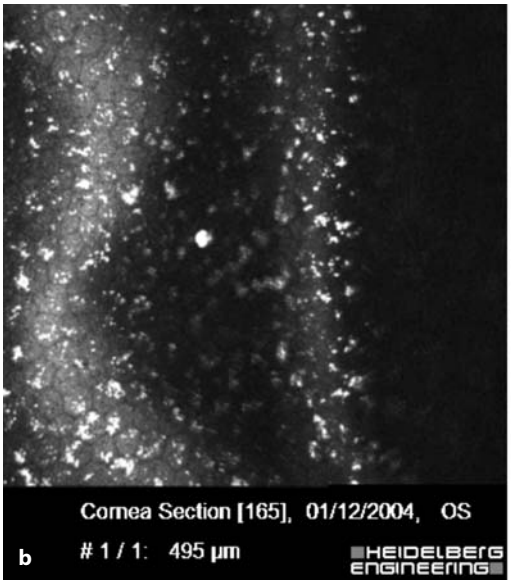

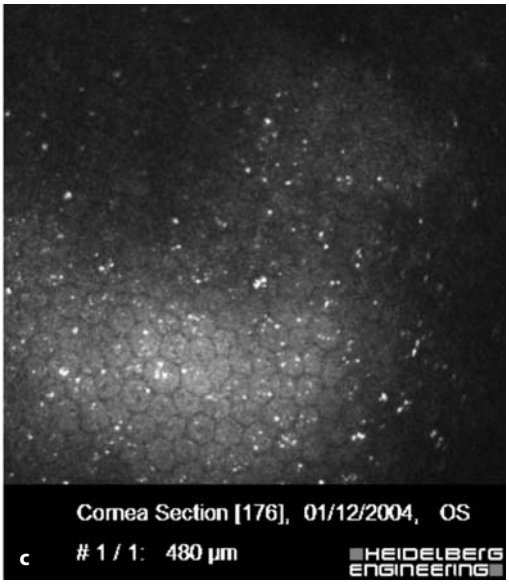

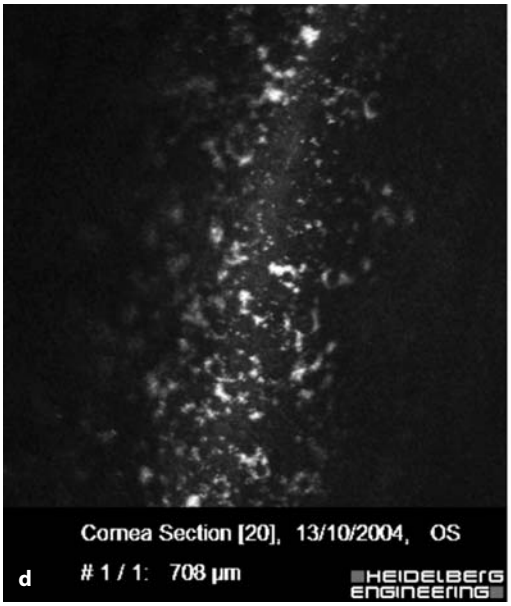

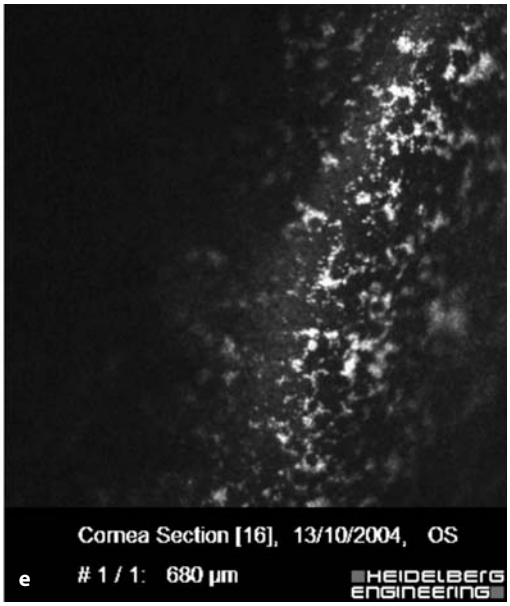

Fig. 5.105 Pigment dispersion. **a** Slit-lamp photograph of a 50-year-old man showing a Krukenberg's spindle. **b–e** Pigment dispersion: pigment deposits on the endothelium

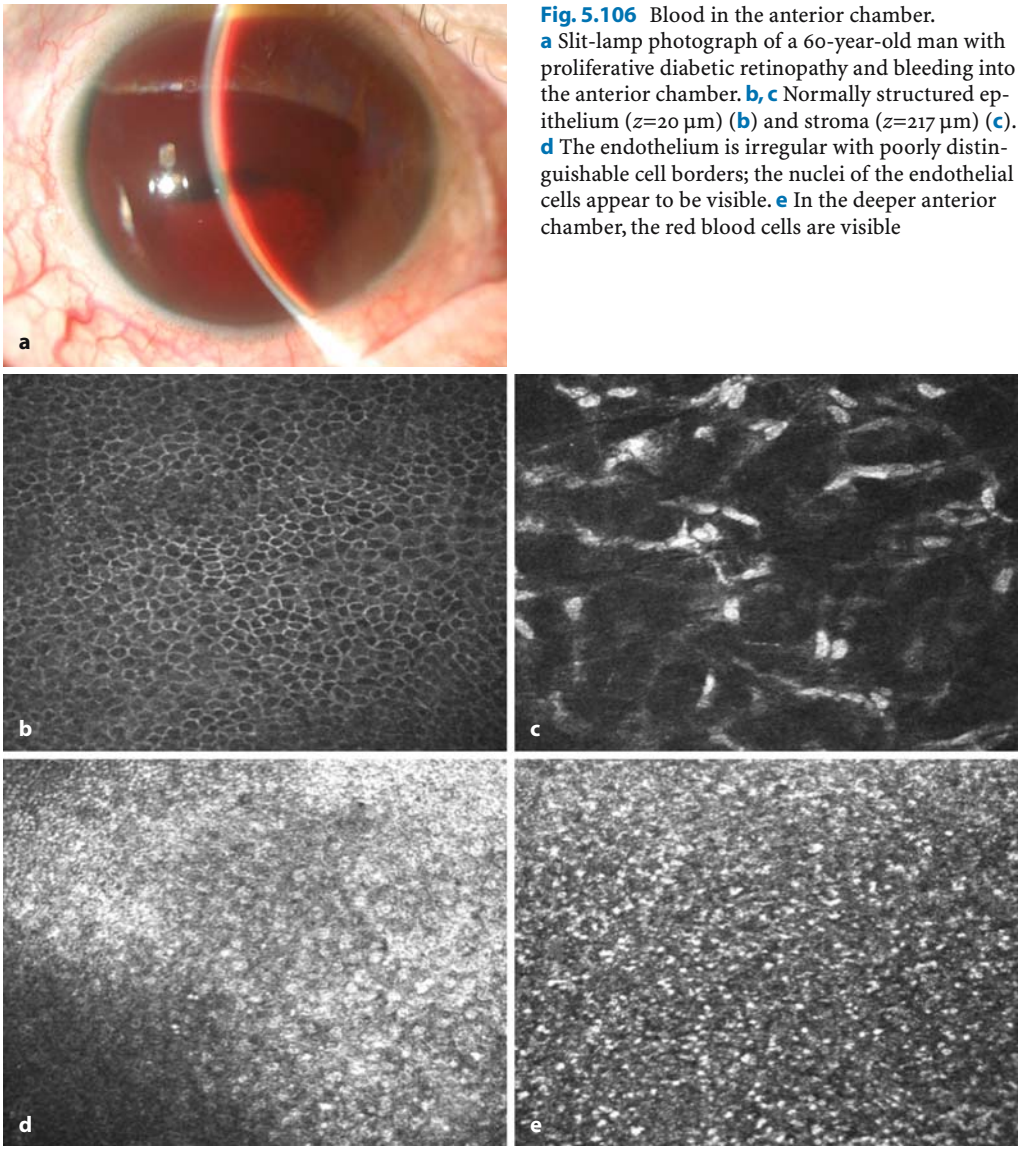

Fig. 5.106 Blood in the anterior chamber. **a** Slit-lamp photograph of a 60-year-old man with proliferative diabetic retinopathy and bleeding into the anterior chamber. **b, c** Normally structured epithelium (z=20 µm) (**b**) and stroma (z=217 µm) (**c**). **d** The endothelium is irregular with poorly distinguishable cell borders; the nuclei of the endothelial cells appear to be visible. **e** In the deeper anterior chamber, the red blood cells are visible

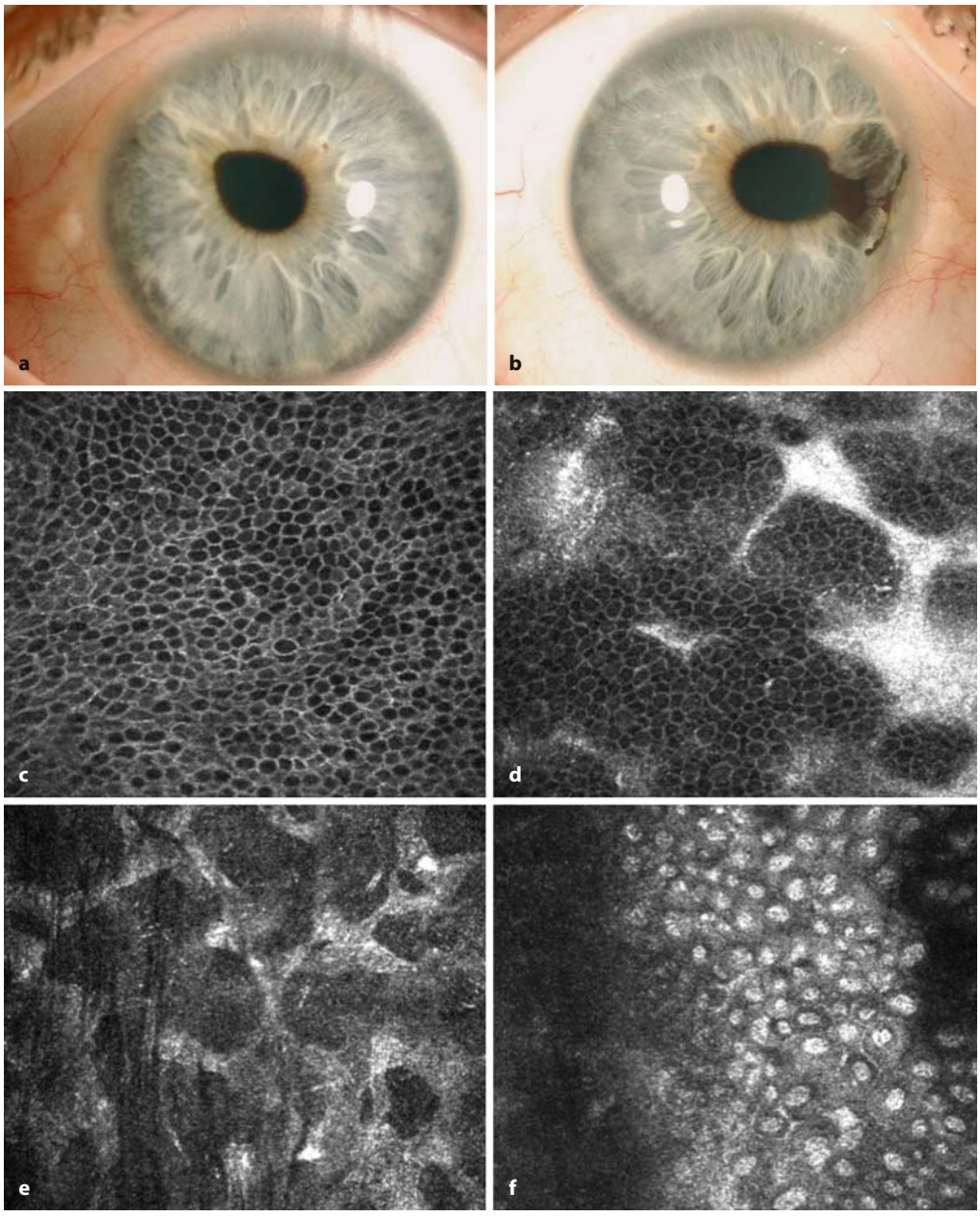

Fig. 5.107 Iridocorneal syndrome. **a, b** Slit-lamp photographs of right (**a**) and left (**b**) eye of a 35-year-old woman with iridocorneal syndrome. **c** Normal intermediate cells (z=28 µm). **d** Highly reflective fibers are visible between normally structured cells at the level of basal cell layer (z=49 µm). **e** In the stroma the cytoplasm is visible, possibly due to keratocyte activation (z=149 µm). **f** The endothelium displays a very abnormal structure, with rounded rather than hexagonal cells, with clearly visible, highly reflective nuclei (z=621 µm)

5.8 Intraocular Structures (Lens, Iris)

5.8.1 Normal Anatomy

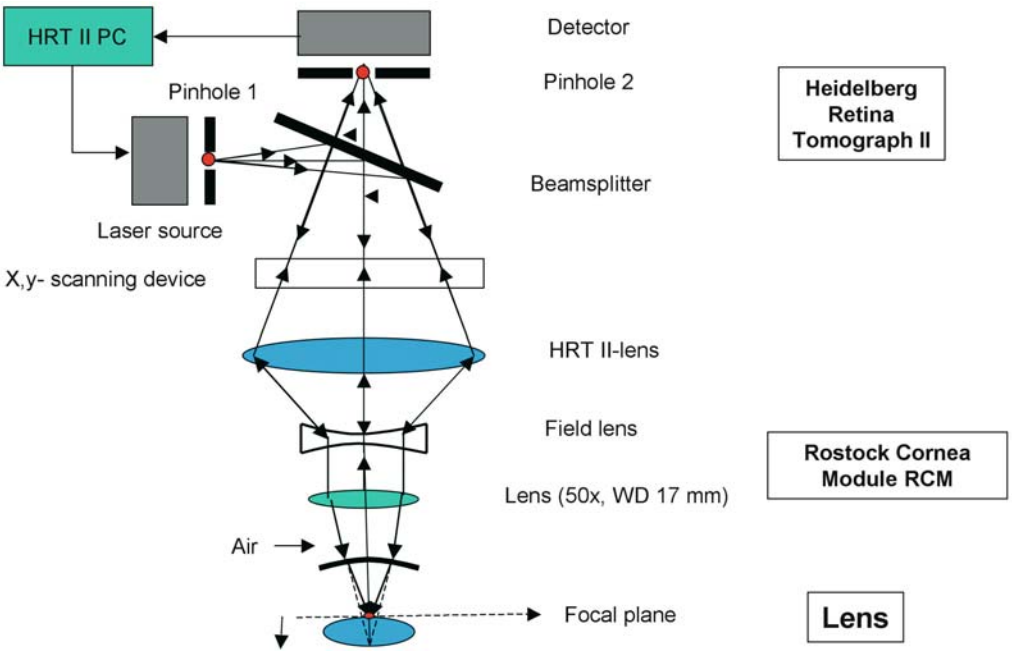

Fig. 5.108 Noncontact confocal laser scanning in vivo microscopy of the lens. Optical principle

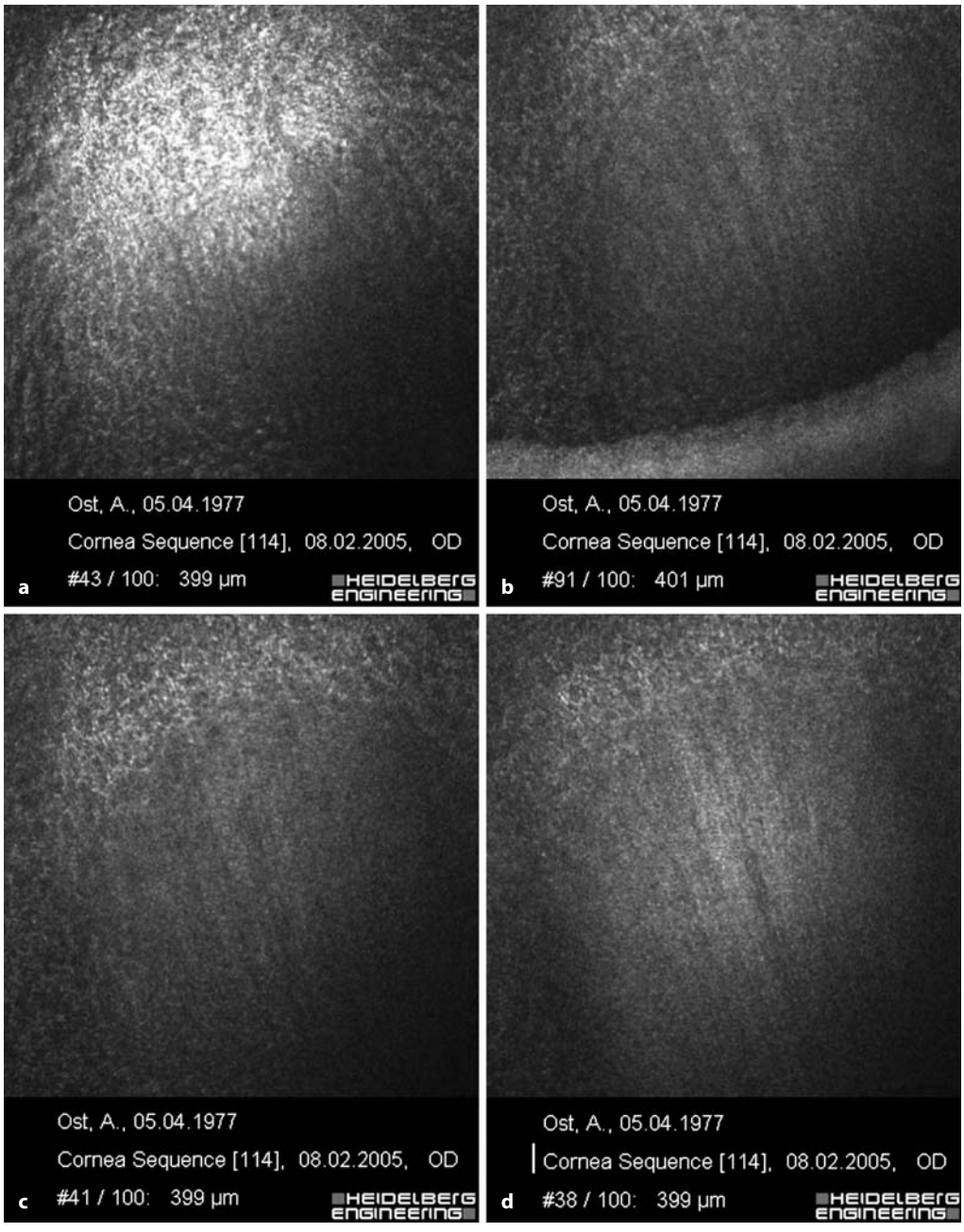

Fig. 5.109 Noncontact confocal microscopy (Nikon ×50; tube: 20 mm). **a** Lens epithelium. **b–d** Fibers

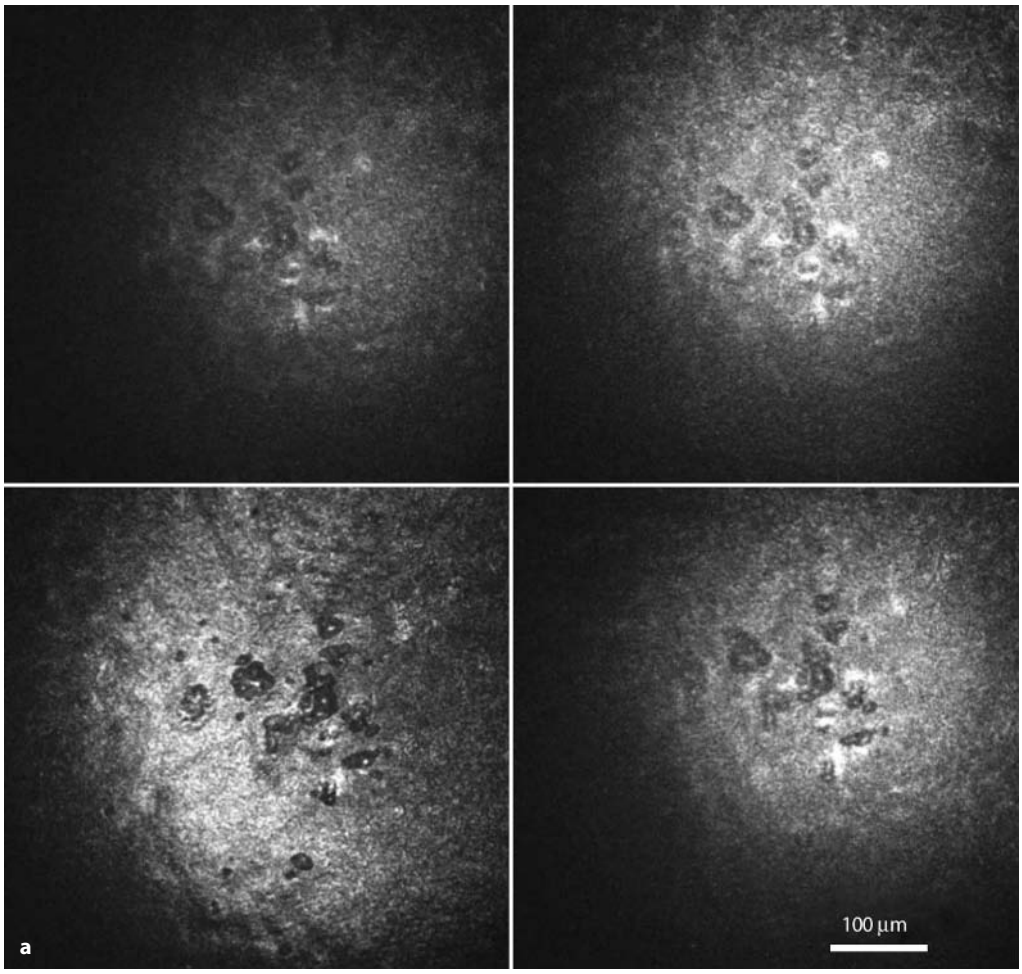

Fig. 5.110 a–c *Z*-scan (in vivo) through the human lens. **a** Lens epithelium

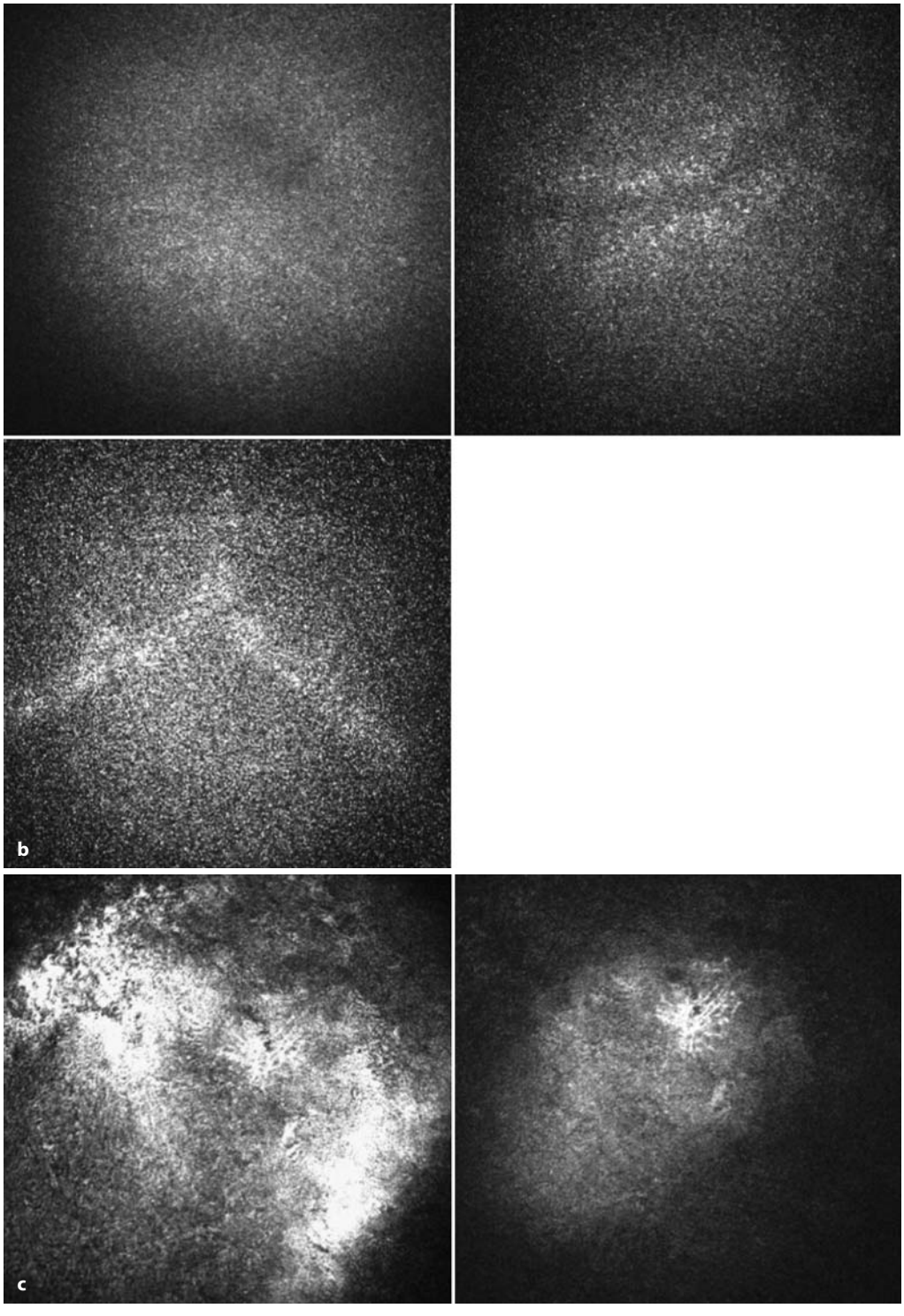

Fig. 5.110 (*continued*) **b** Lens nucleus with fibers. **c** Reverse side of the lens

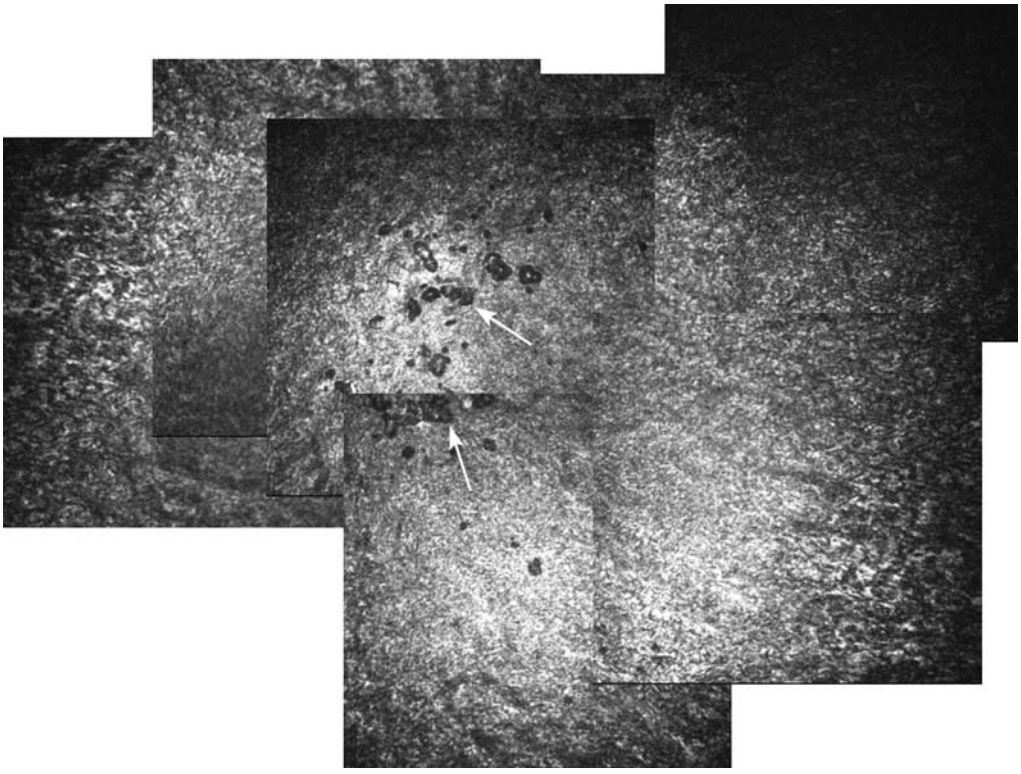

Fig. 5.111 Front side of the lens epithelium with small defects (*arrows*)

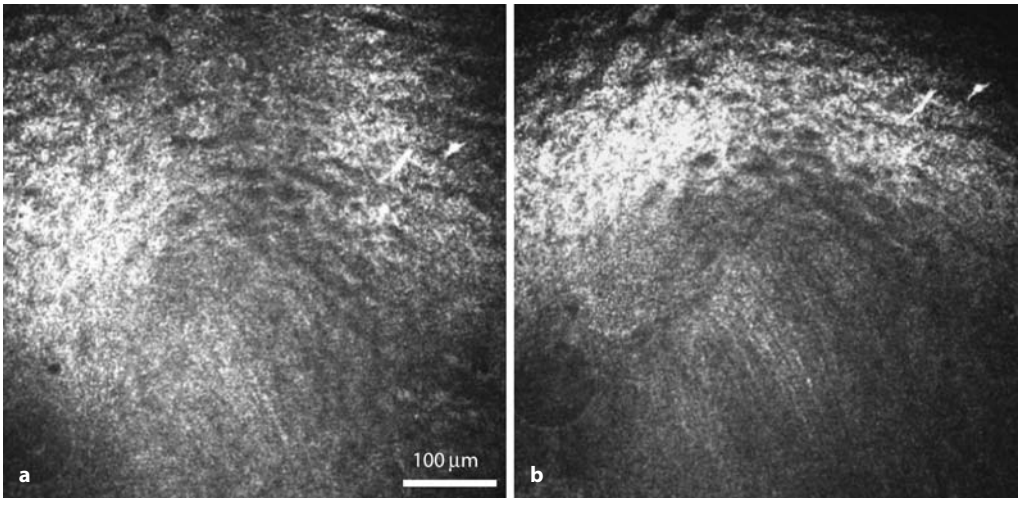

Fig. 5.112 **a–f** Microstructures of the lens. **a** Lens epithelium. **b–e** Lens fibers

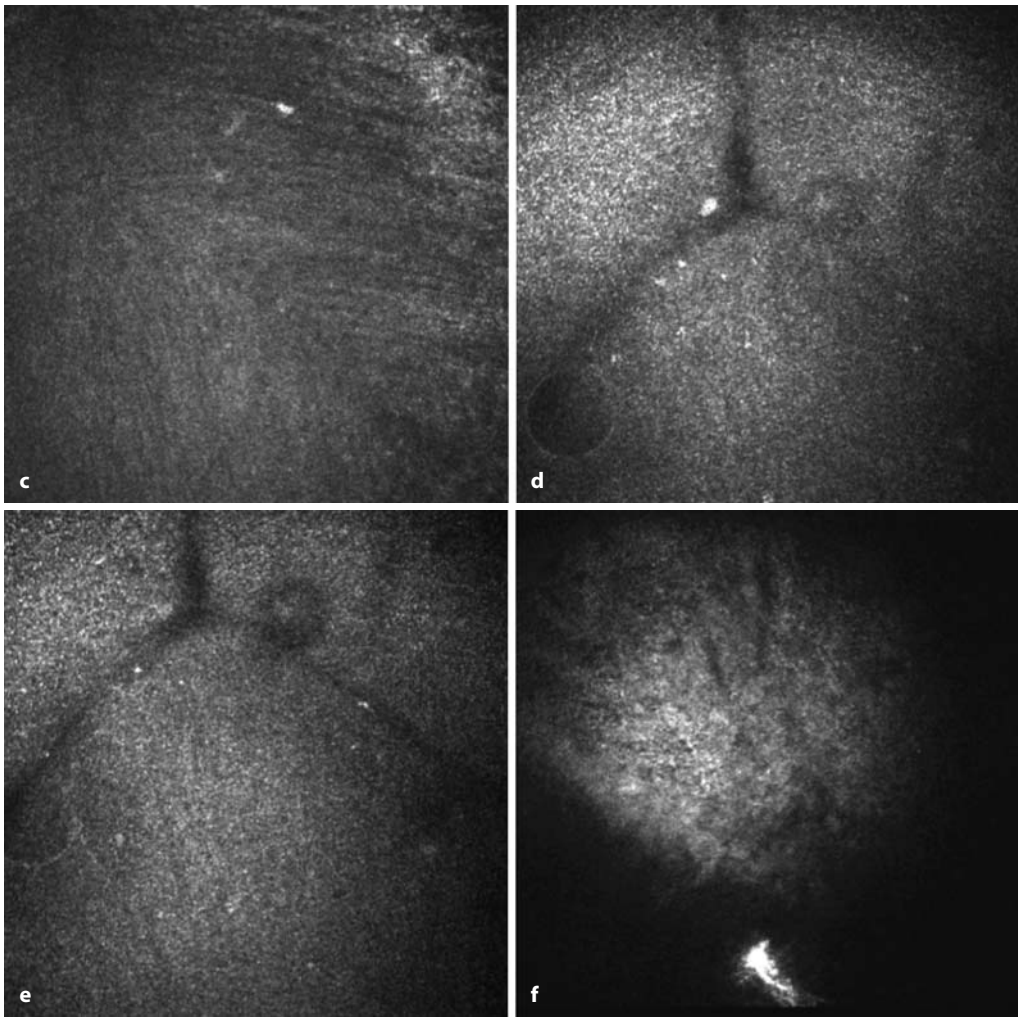

Fig. 5.112 (*continued*) **b–e** Lens fibers. **f** Cell structures on the posterior capsular bag

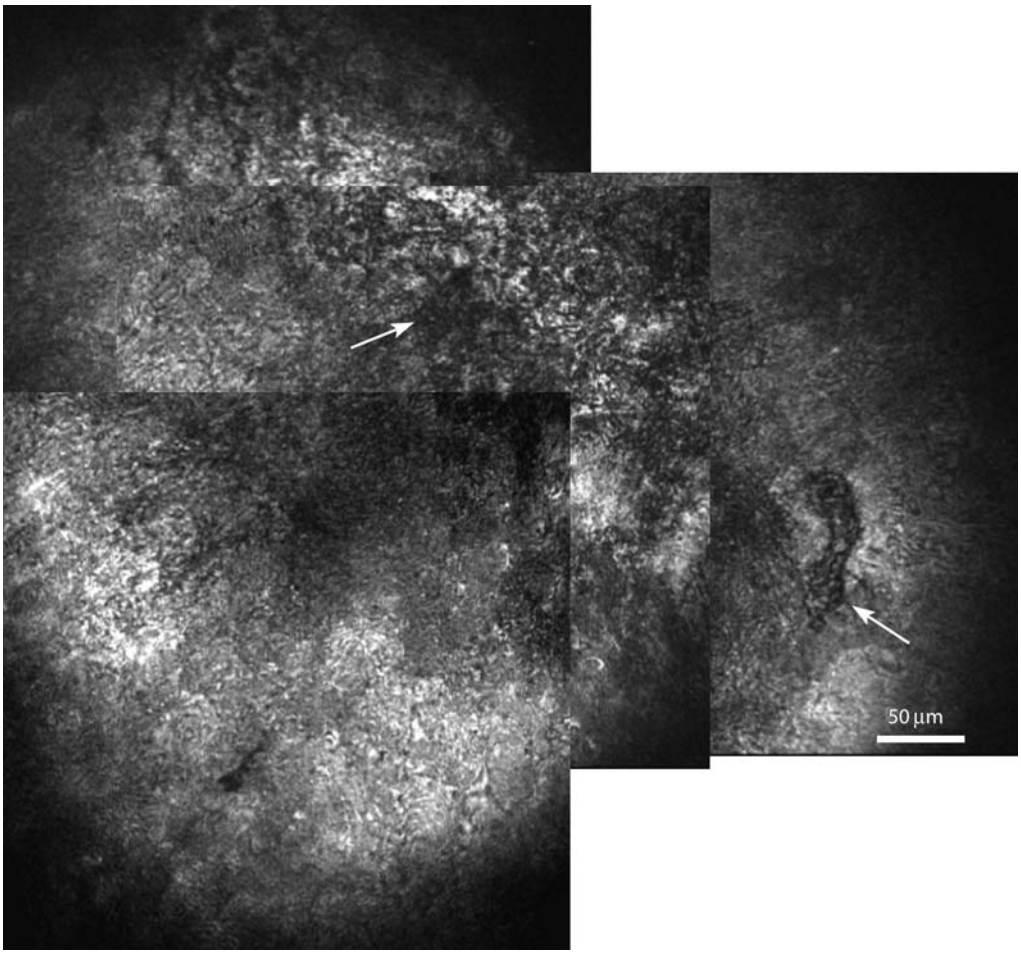

Fig. 5.113 Reverse side of the human lens (in vivo). Cell structures with defects (*arrows*)

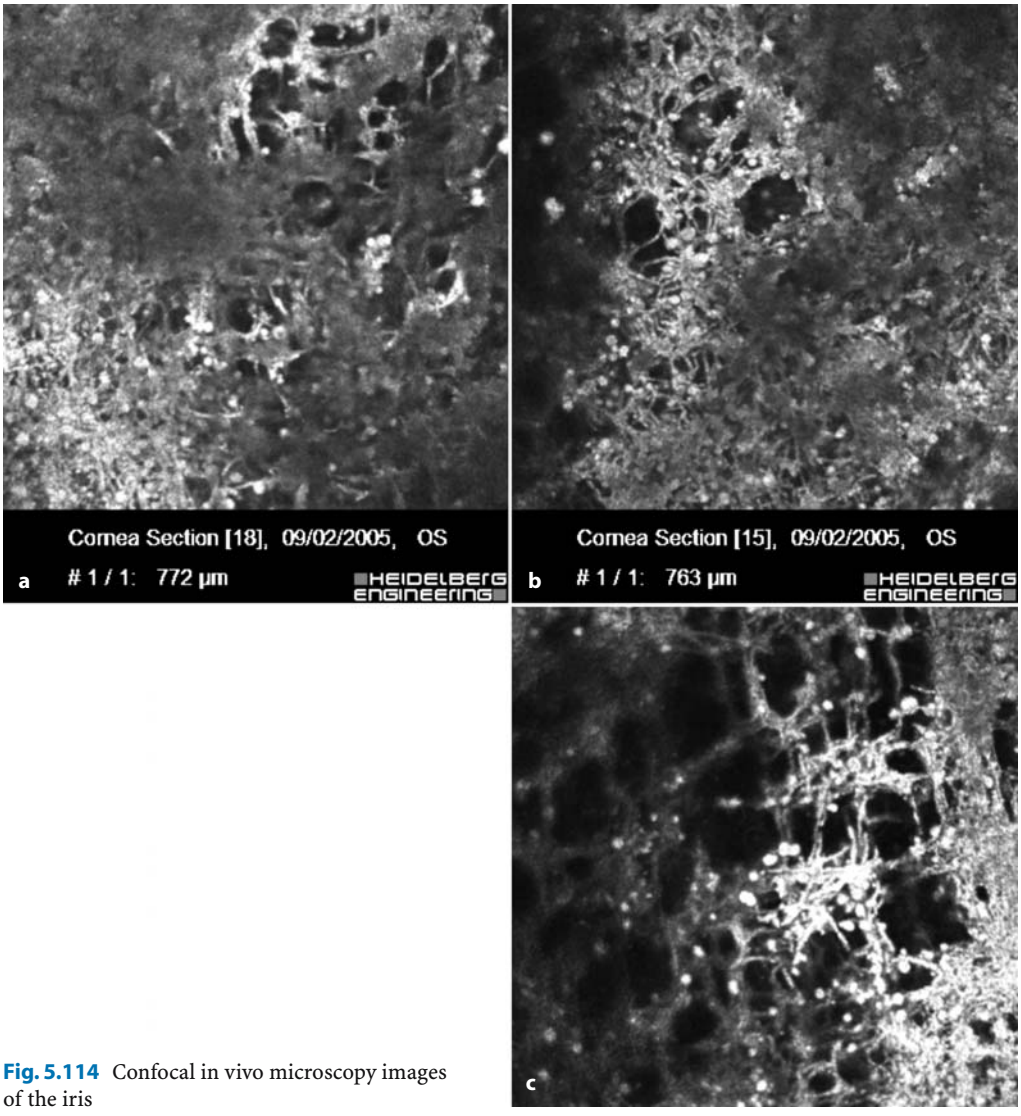

Fig. 5.114 Confocal in vivo microscopy images of the iris

5.8.2 Pathological Findings

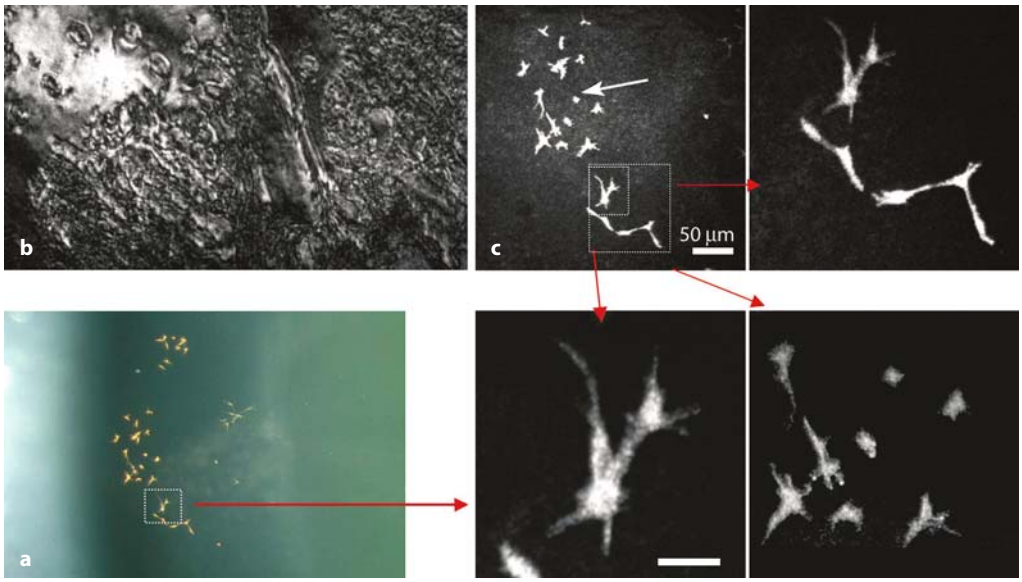

Fig. 5.115 Congenital ectopic iris. **a** Slit-lamp photograph. **b** Reverse side of the lens. **c** Pigment epithelial cells (*arrows*)

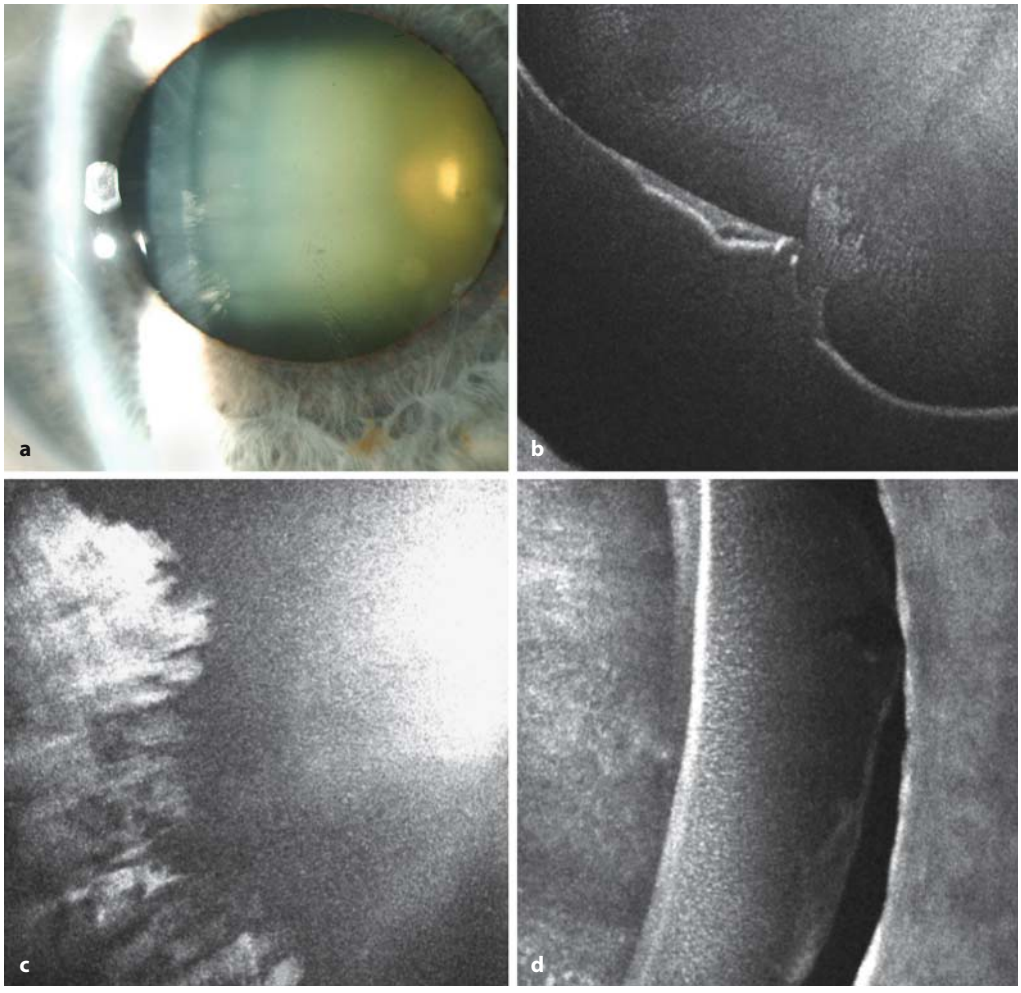

Fig. 5.116 Pseudoexfoliation glaucoma and cataract. **a** Slit-lamp photograph of an 80-year-old woman with pseudoexfoliation glaucoma and cataract, visual acuity 12/20 (right eye) and 16/20 (left eye); confocal images, noncontact examination. **b** Pseudoexfoliation line at the anterior lens surface. **c** Cataract formation of the peripheral lens. **d** Pseudoexfoliation line visible at the right side of the iris

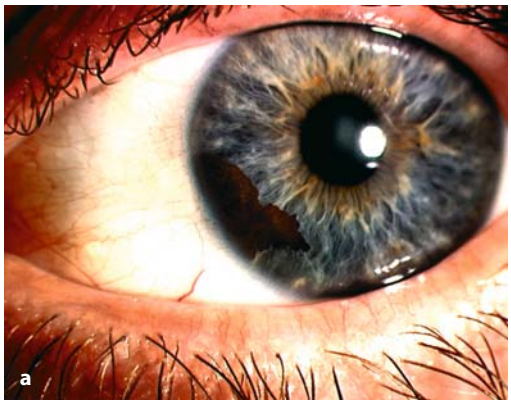

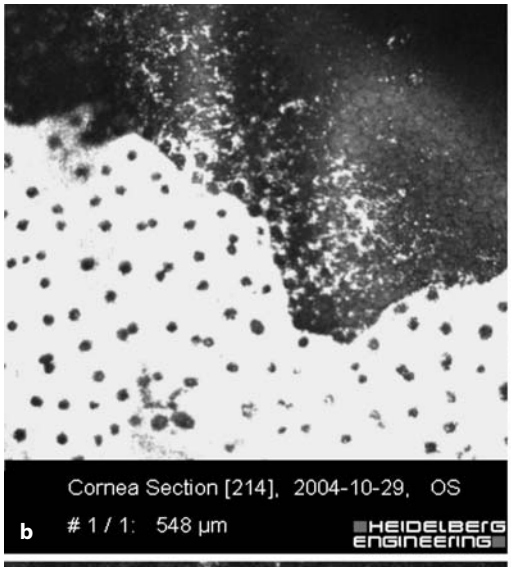

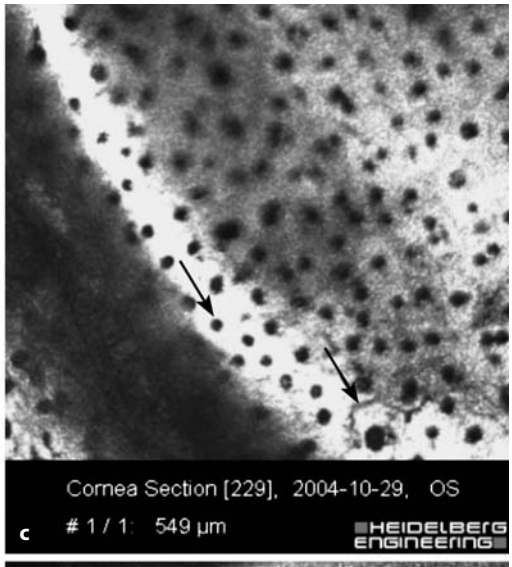

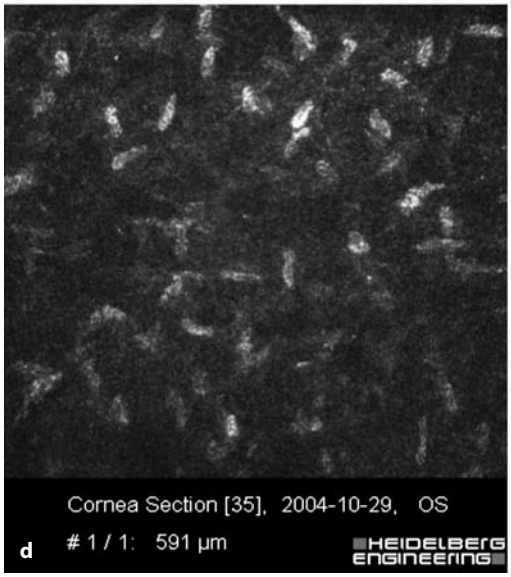

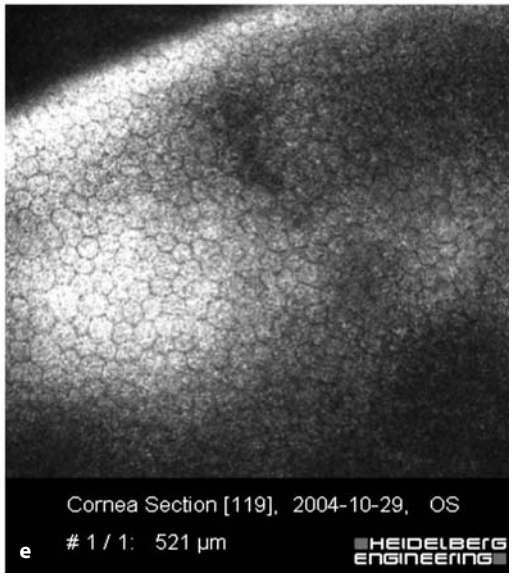

Fig. 5.117 Pigmented nevus of the iris. **a** A 43-year-old woman complained of a dark brown spot on the eye. Slit-lamp examination of the left eye revealed a pigmented flat tumor situated at the posterior surface of the cornea nasally. **b** Confocal laser scanning microscopy shows hyperreflective tissue lying behind the endothelium with pigment dispersed on the adjacent endothelial surface. **c** The hyporeflective cytosomal structures resembling cell nuclei are visible, and cell walls can be distinguished. **d, e** There are no signs of infiltration of corneal layers, the corneal stroma above the alterations is unchanged, and the surrounding endothelium is not distorted

5.9 Limbal Region

5.9.1 Normal Anatomy

Because it forms a junctional zone with the conjunctiva, the limbal region is especially important. Inflammatory cells migrate across it into the cornea in immunological disease; it is the source of new inbudding corneal vessels; and, not least, it also plays an important role in corneal regeneration as the site of origin of corneal stem cells.

The limbal region is where the corneal epithelium forms a junction with the conjunctival epithelium, which comprises approximately 10–12 cell layers. This region also contains a radial arrangement of trabecular conjunctival processes (the limbal palisades of Vogt) that are considered to be the site of origin of corneal stem cells [16, 74]. Overall, the organization of the conjunctival epithelium is less uniform because different epithelial cell types (goblet cells, for example) occur here and the arrangement of the individual cell layers is also not so strictly parallel with the surface [17].

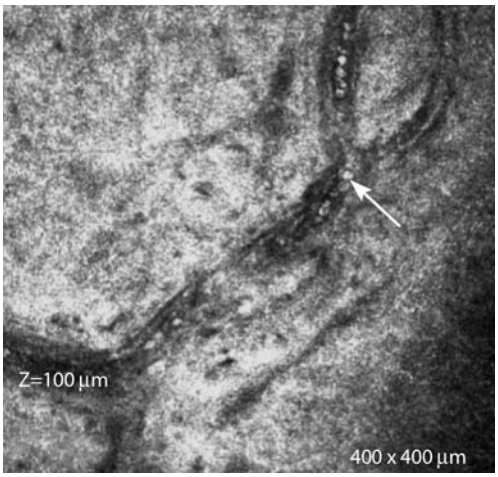

Fig. 5.119 Branched conjunctival vessel close to the limbus with erythrocytes visible (*arrow*), near limbus at 9 o'clock

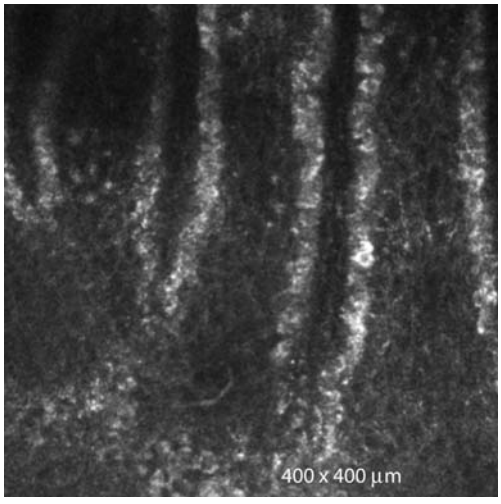

Fig. 5.118 Limbal palisades of Vogt (near limbus at 6 o'clock). Trabecular extensions of the conjunctiva are growing from outside (in this case, from below) in a radial pattern toward the cornea

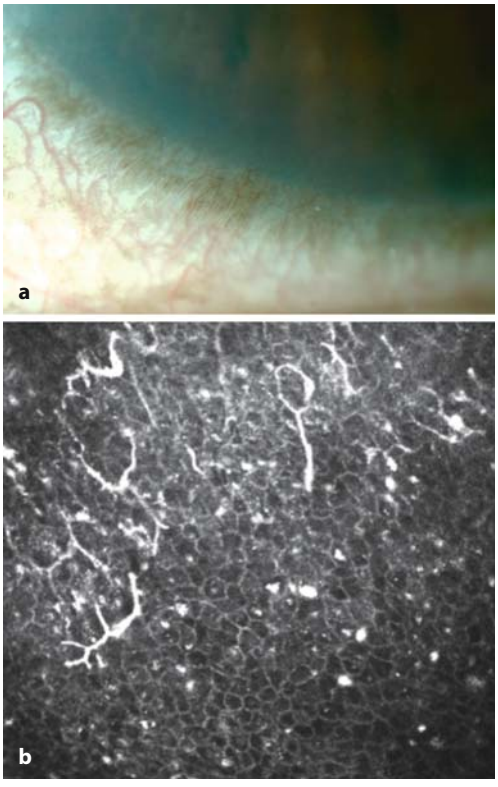

Fig. 5.120 Limbus. **a** Slit-lamp photograph of a pigmented limbus. **b** Peripheral corneal cells: numerous dendritic cells and hyperreflective structures corresponding to pigment deposits

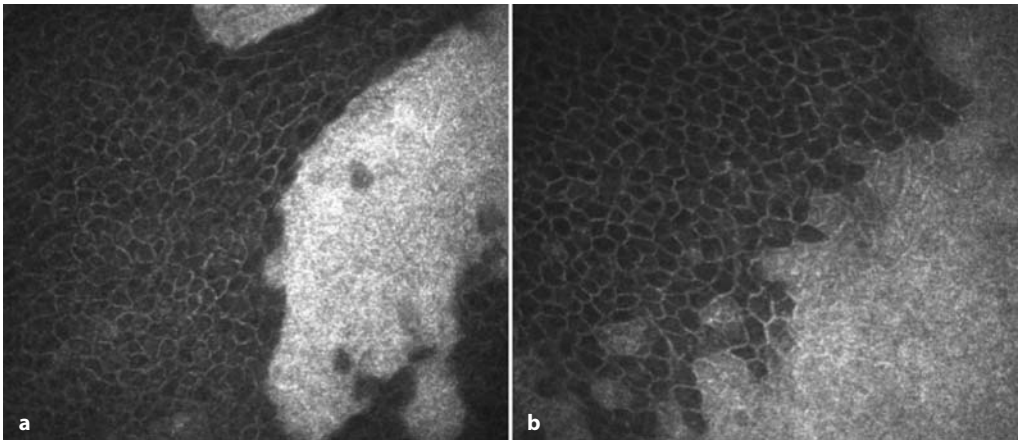

Fig. 5.121 Limbus. Normal junction between corneal cells (*black cells*) and conjunctival cells (*reflective cells*)

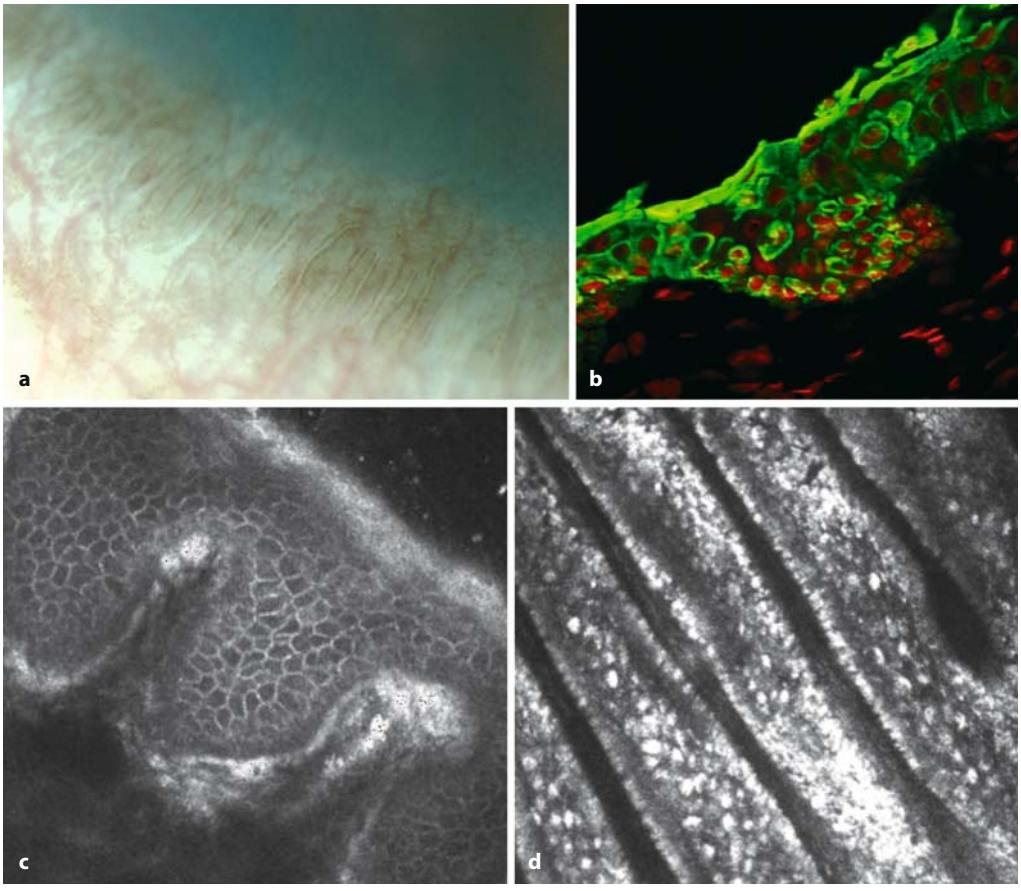

Fig. 5.122 Normal limbus. **a** Slit-lamp photography of normal limbus and palisades of Vogt. **b** Immunohistology of normal limbus: immunostaining with cytokeratin K19 (*green*) and propidium iodide (*red*). **c** Confocal in vivo microscopy image, oblique section: palisades of Vogt. **d** Confocal in vivo microscopy image: palisades of Vogt

On confocal microscopy, the epithelial cells of the conjunctiva, unlike those of the cornea, are more reflective, smaller, and less well demarcated. Their nucleus is relatively large and bright. The junctional zone is characterized by inhomogeneous reflectivity and marked variation in cell shape and size. The limbal palisades of Vogt can often be visualized as parallel trabecular extensions of the conjunctival epithelium (Fig. 5.118). In the immediate junctional zone, the conjunctival epithelium commonly exhibits tonguelike extensions that are mostly well demarcated, especially in the deeper layers, and at the end of which are located isolated cells or cell groups with very bright cell borders and a bright cytoplasm. These may be secretory cells. Subepithelially, in the region of the conjunctiva close to the limbus, are the blood vessels of the limbal vascular plexus, in the lumen of which flowing blood cells can be seen (Figs. 5.119–5.123).

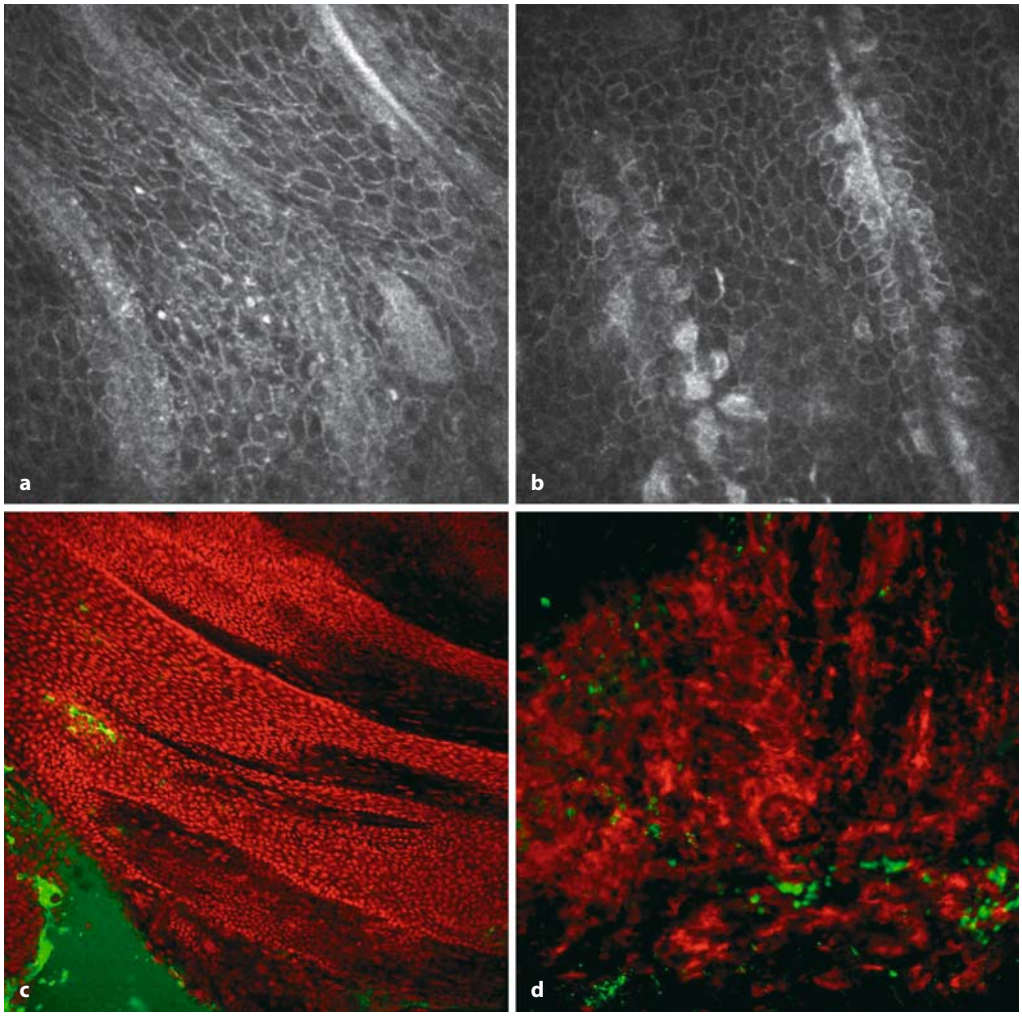

Fig. 5.123 Normal limbus and palisades of Vogt. **a, b** Palisades of Vogt at two different depths. Epithelial stem cells are thought to be located between the palisades of Vogt. **c, d** Immunohistological images of the palisades of Vogt: epithelial cells (*red*), stem cells stained with ABCG2 (*green*)

5.9.2 Pathological Findings

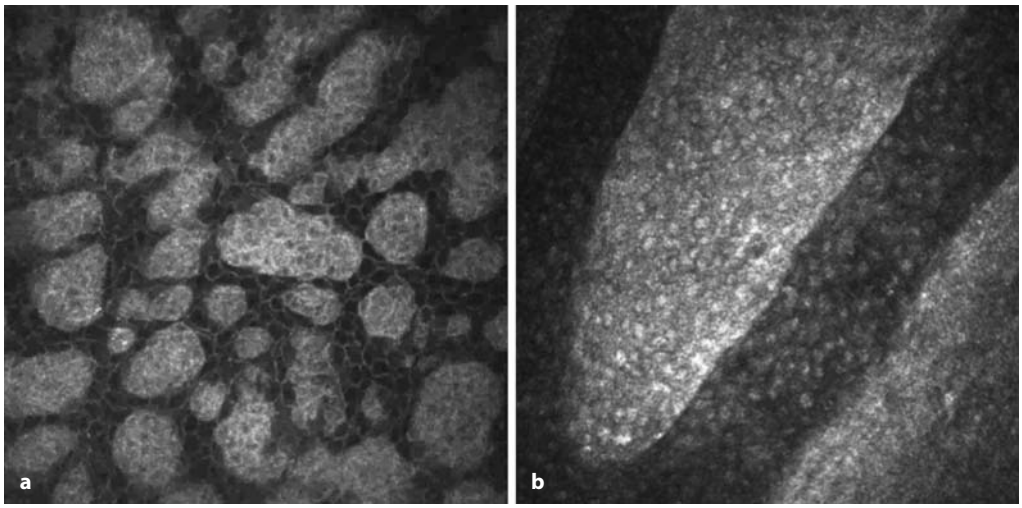

Fig. 5.124 Pathological limbus in inflammatory diseases: abnormal junction between corneal cells (*black cells*) and conjunctival cells (*reflective cells*)

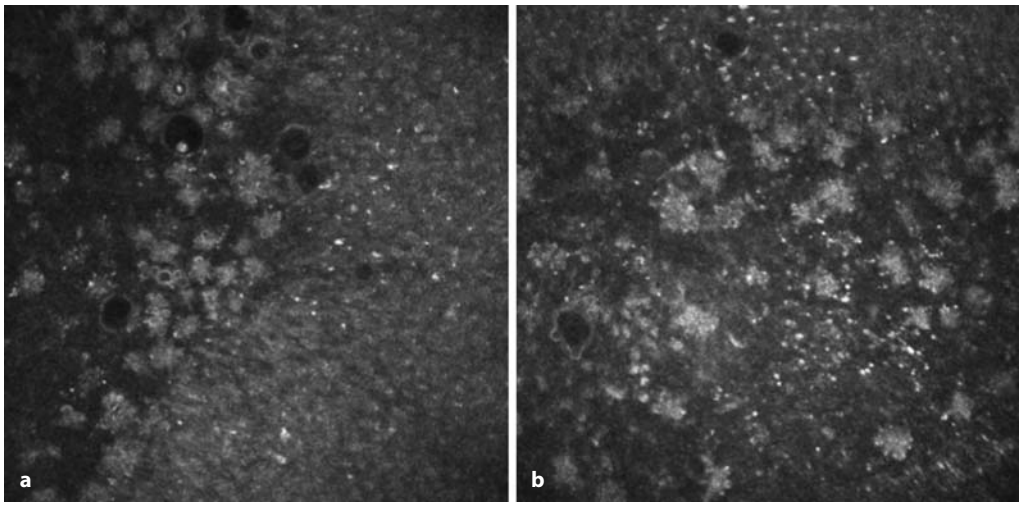

Fig. 5.125 Pathological limbus in a case of vernal keratoconjunctivitis. Islets of inflammatory cells and conjunctival cells within the corneal epithelium

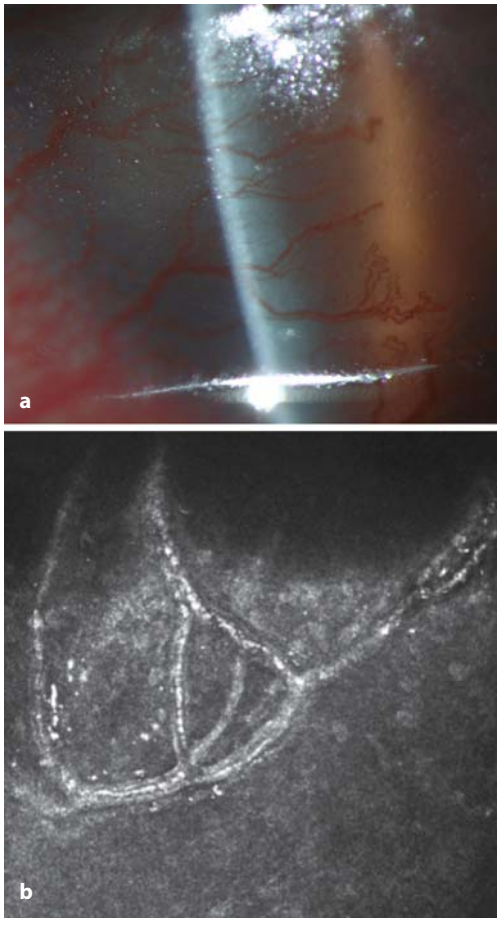

Fig. 5.126 Corneal neovascularization. **a** Slit-lamp photograph of corneal neovascularization. **b** Confocal in vivo microscopy image of corneal neovascularization: neovascular loops

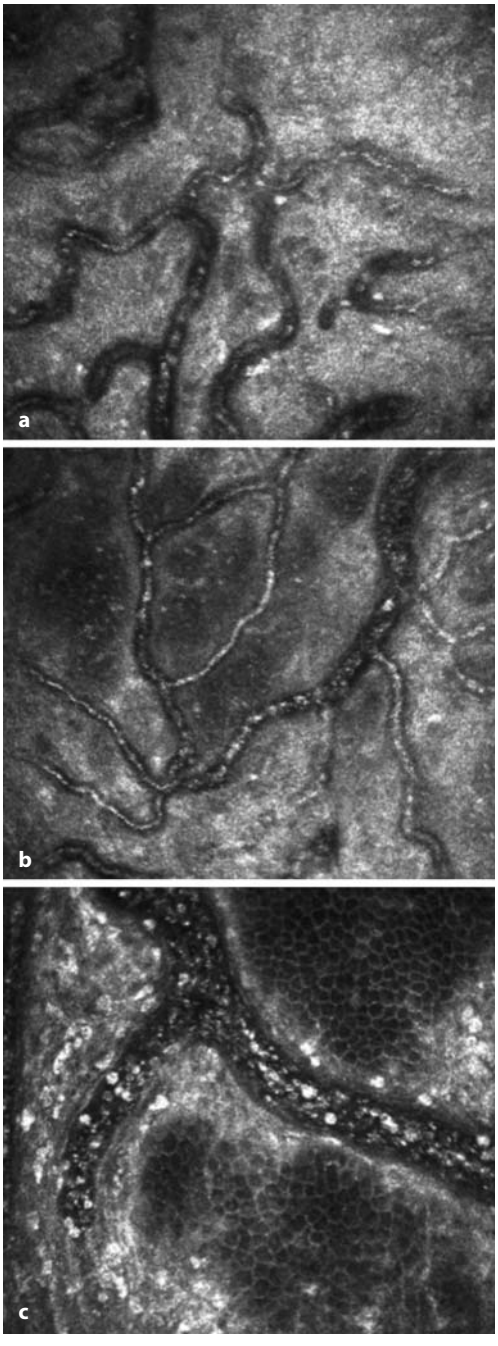

Fig. 5.127 Corneal neovascularization. **a, b** Corneal blood vessels. **c** Corneal neovascularization. Hyperreflective inflammatory cells surround the blood vessels and intravascular round reflective cells

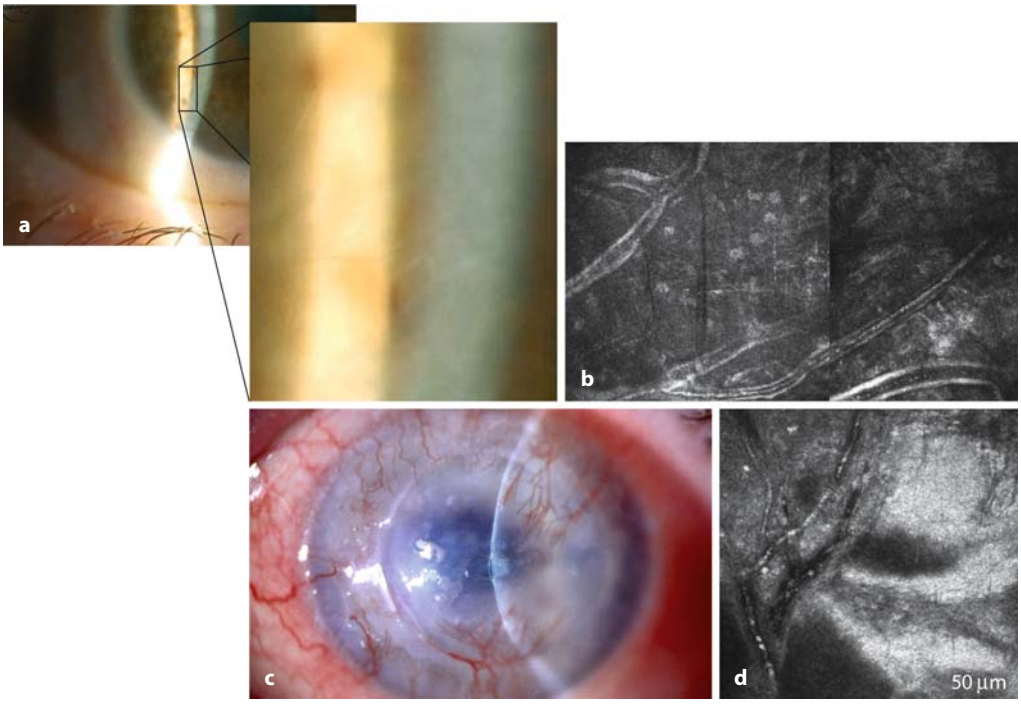

Fig. 5.128 Vascularization of the cornea. **a** Slit-lamp photograph of 53-year-old woman with ghost vessels. **b** Confocal microscopic images show empty vessels at the periphery of cornea at the level of the posterior stroma. **c** Slit-lamp photograph of 73-year-old woman with corneal vascularization of donor and recipient cornea after penetrating keratoplasty. **d** Confocal images show blood capillaries with bright cell bodies (erythrocytes) in the corneal epithelium

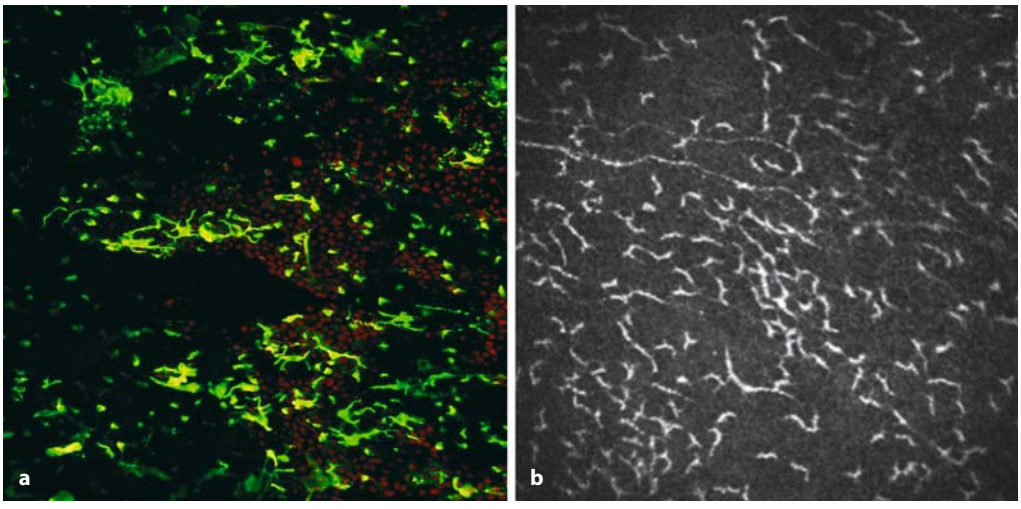

Fig. 5.129 Inflammation, dendritic cells. **a** Immunohistology: dendritic cells (*green*) in the peripheral cornea (*red*). **b** Confocal in vivo microscopy: hyperreflective dendritic cells

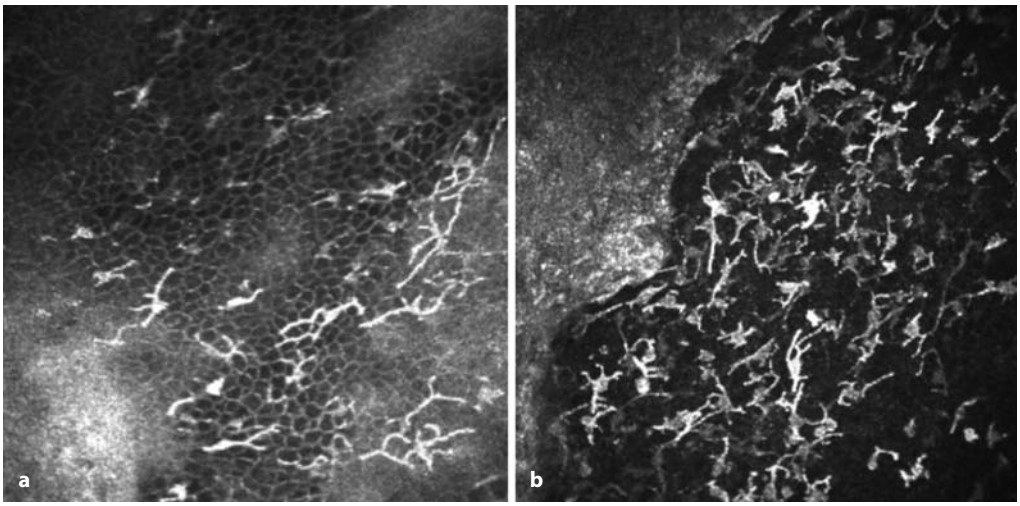

Fig. 5.130 Inflammation, dendritic cells. Numerous hyperreflective dendritic cells in the peripheral cornea of patients with ocular surface inflammatory diseases

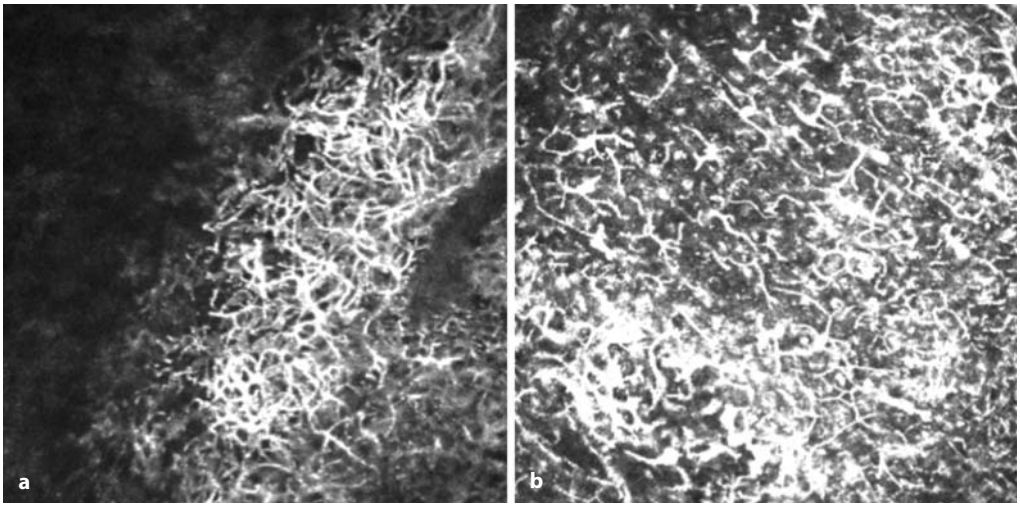

Fig. 5.131 Inflammation, dendritic cells. Major corneal infiltration of dendritic cells in a severe case of vernal keratoconjunctivitis

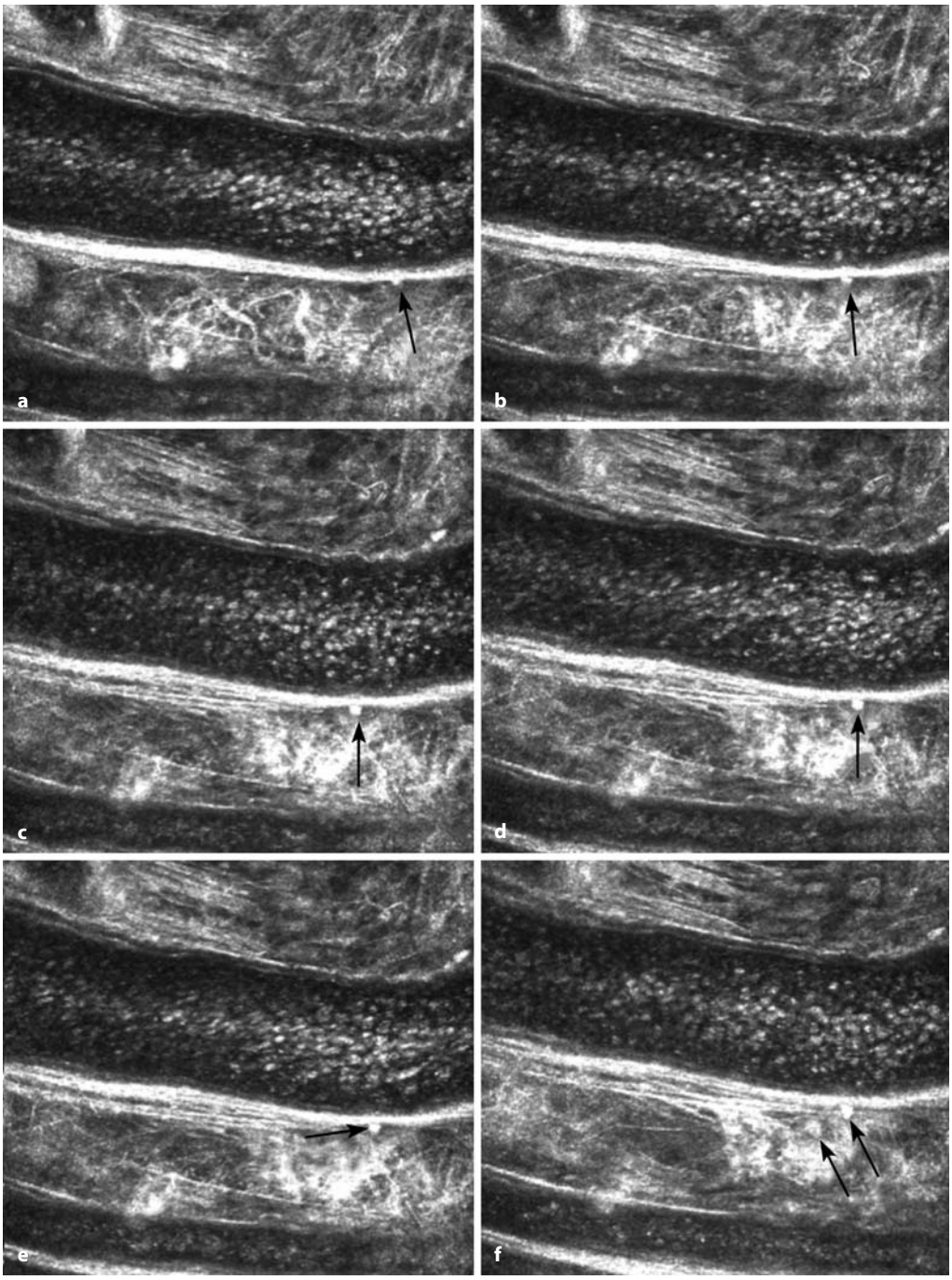

Fig. 5.132 Inflammation, rolling diapedesis. **a–e** Confocal in vivo microscopy sequence showing diapedesis. An inflammatory cell (*arrows*) crosses the vascular endothelium and then acquires the mature phenotype of a dendritic cell (**e, f**)

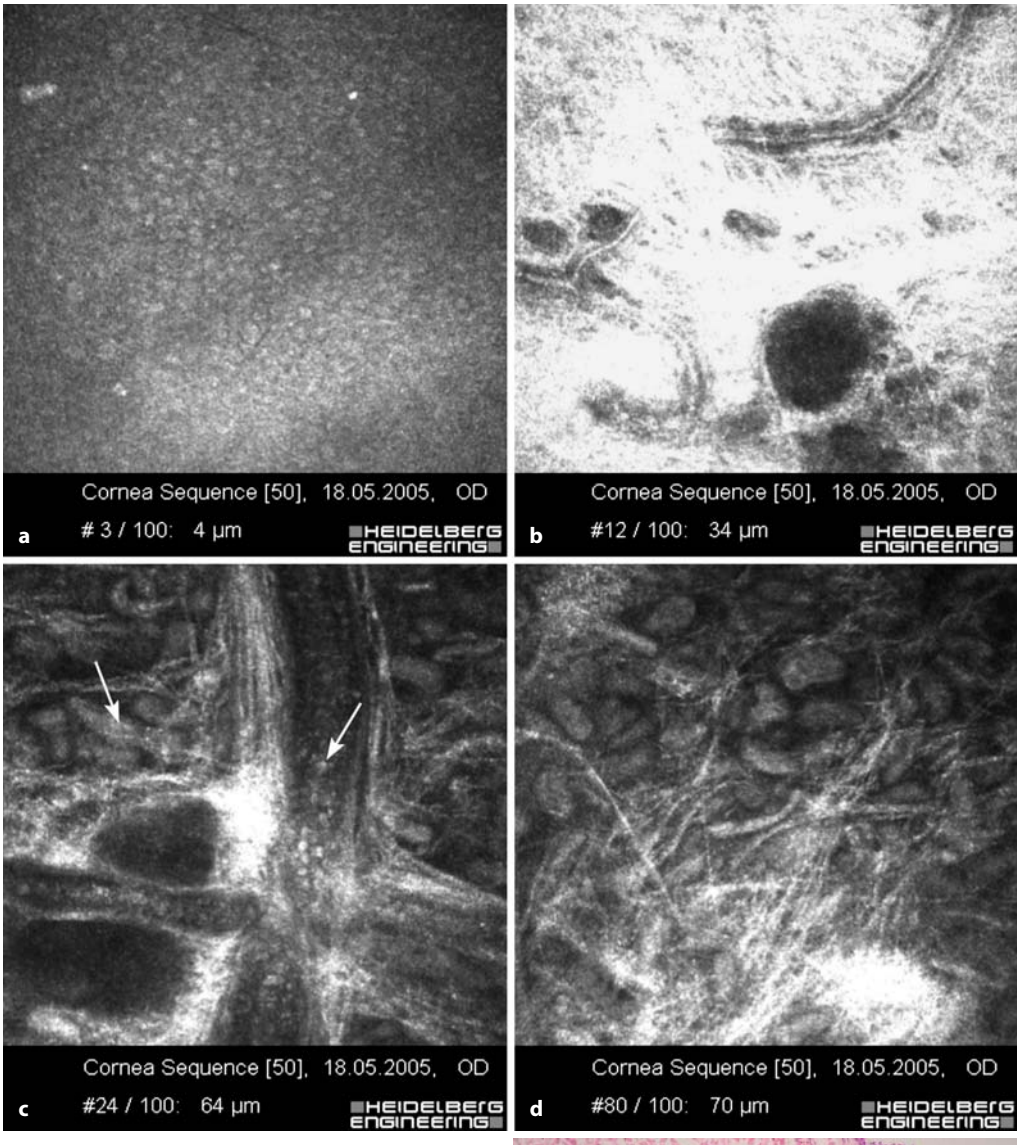

Fig. 5.133 Amyloidosis. **a–e** Under normally structured conjunctiva (**a**) and in the subconjunctival space (**b**) between blood vessels (*right arrow*), a lobular tissue pattern (*left arrow*) is visible (**c, d**), which shows a high degree of consistency with histology after invasive biopsy

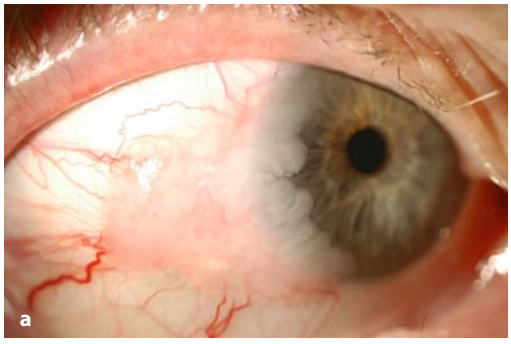

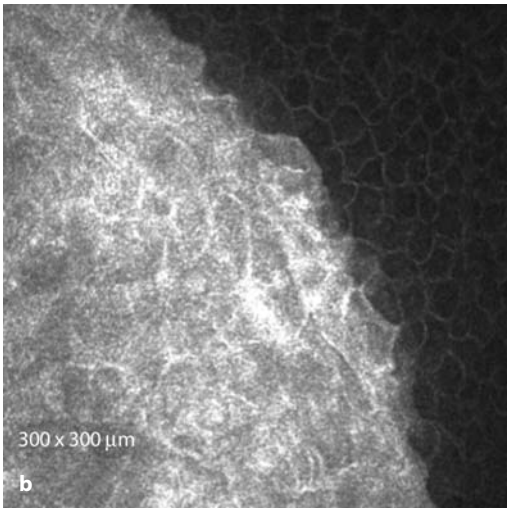

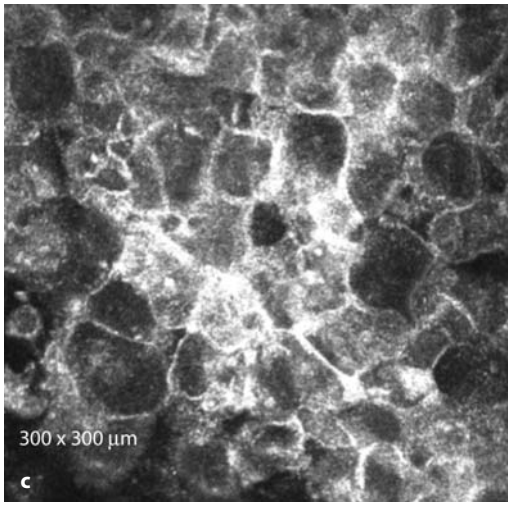

Fig. 5.134 a–e Conjunctival neoplasia. **a** Slit-lamp examination. White conjunctival neoplasia with neovascularization is shown growing temporal to the transparent cornea. This tissue is located in the plane of the epithelium and superficial stroma. **b** Highly reflective metaplastic conjunctival tissue at the border with corneal epithelium (wing cell layer). **c** Surface of the neoplastic corneal tissue. Polymorphic cells with variable cytoplasmic reflections are present.

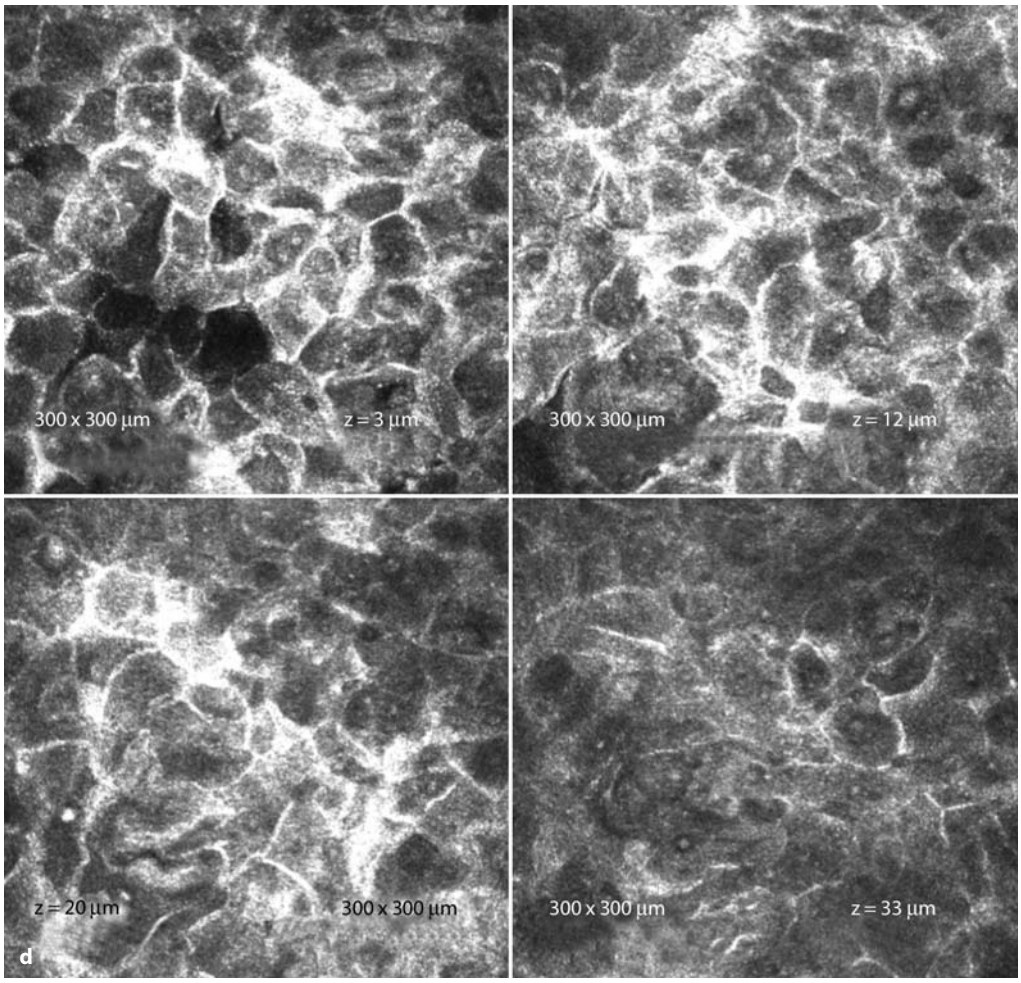

Fig. 5.134 (*continued*) **d, e** Image series with increasing focal depth from the loose structured epithelial surface to deeper low-contrast neoplastic tissue

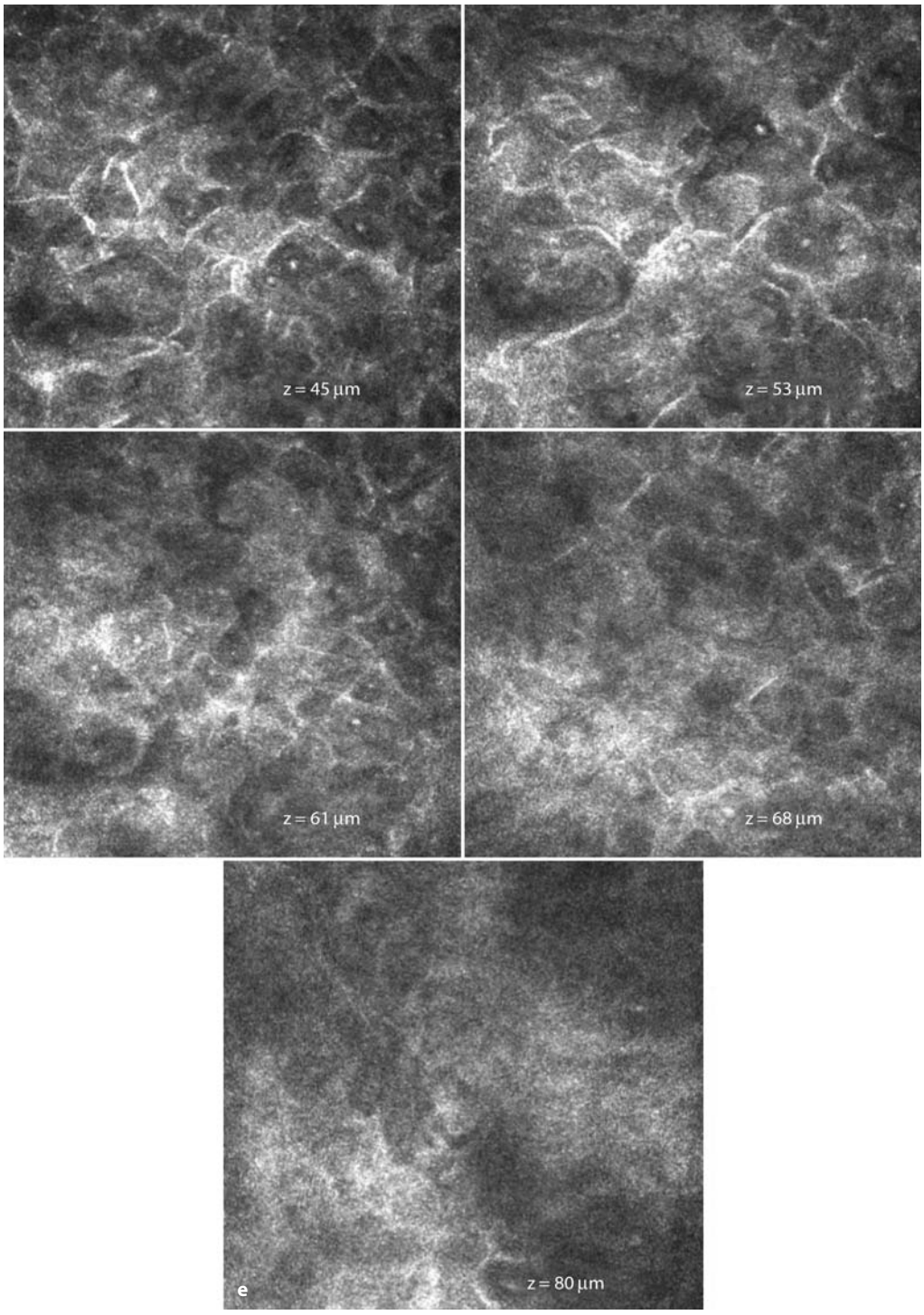

Fig. 5.134 (*continued*) **d, e** Image series with increasing focal depth from the loose structured epithelial surface to deeper low-contrast neoplastic tissue

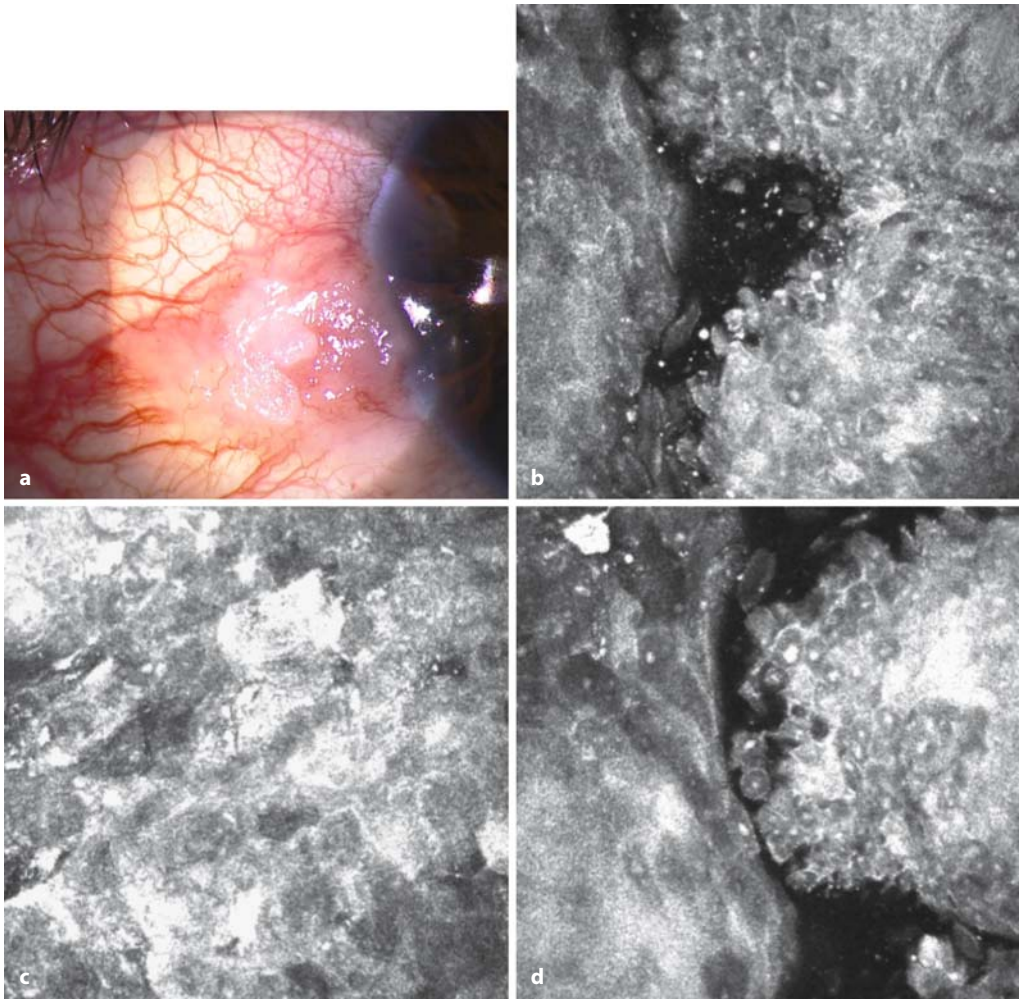

Fig. 5.135 Conjunctival and limbal tumors. **a** Slit-lamp photograph of a 55-year-old woman with a limbal tumor. **b–d** Numerous cellular abnormalities: nuclear abnormalities, polymorphism

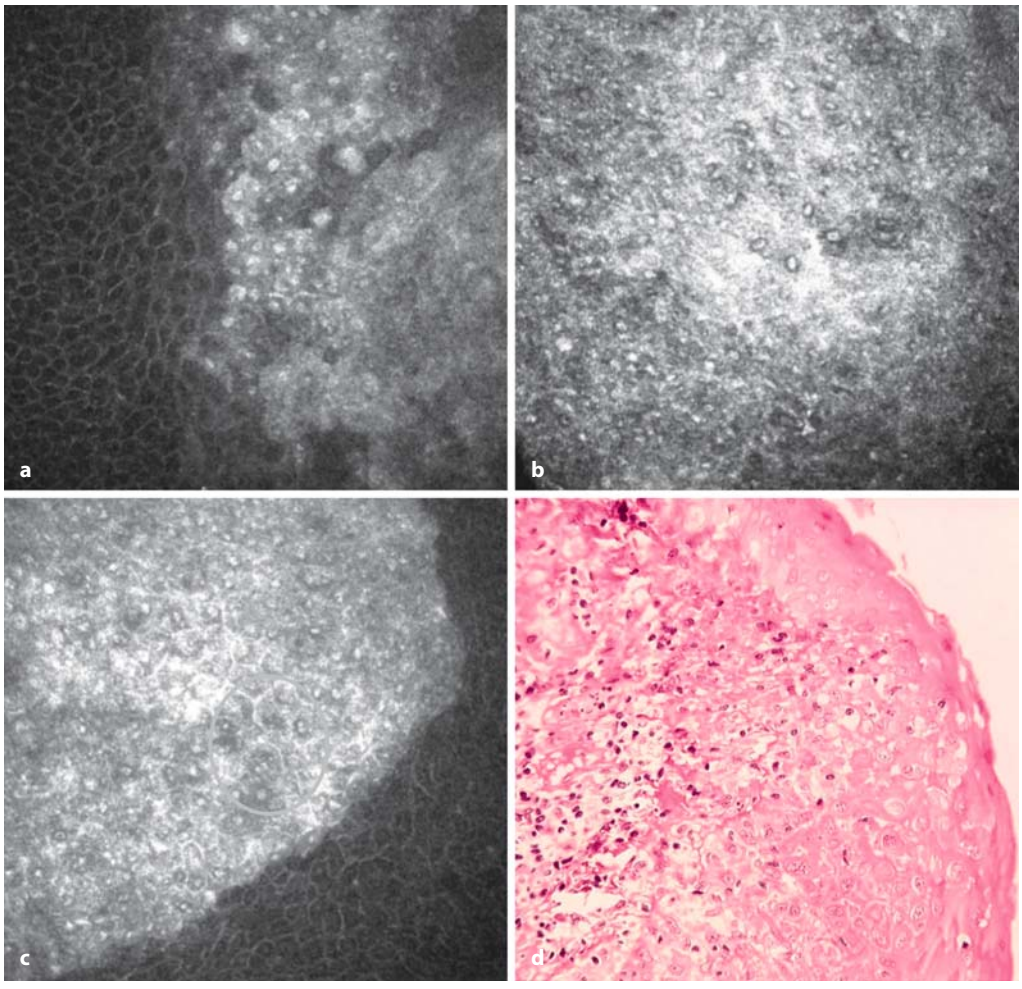

Fig. 5.136 Conjunctival and limbal tumors, epithelioma. **a–c** Numerous cellular abnormalities. **d** Histology

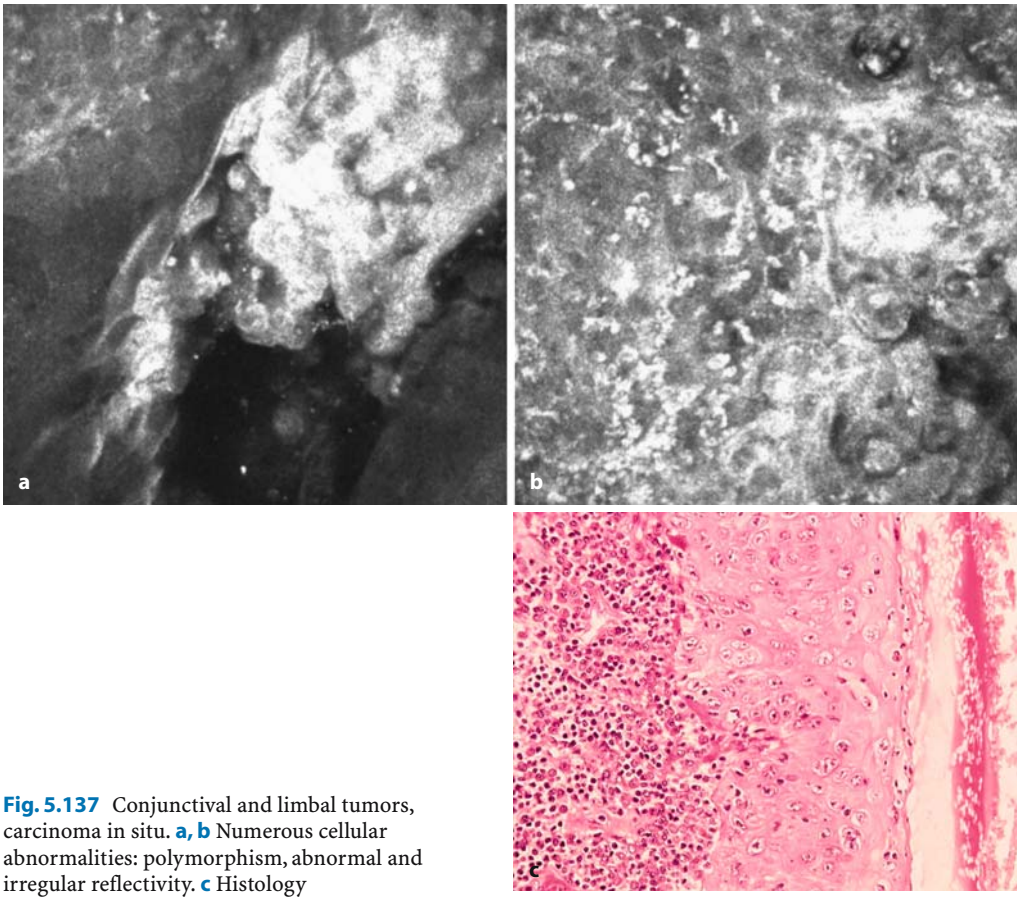

Fig. 5.137 Conjunctival and limbal tumors, carcinoma in situ. **a, b** Numerous cellular abnormalities: polymorphism, abnormal and irregular reflectivity. **c** Histology

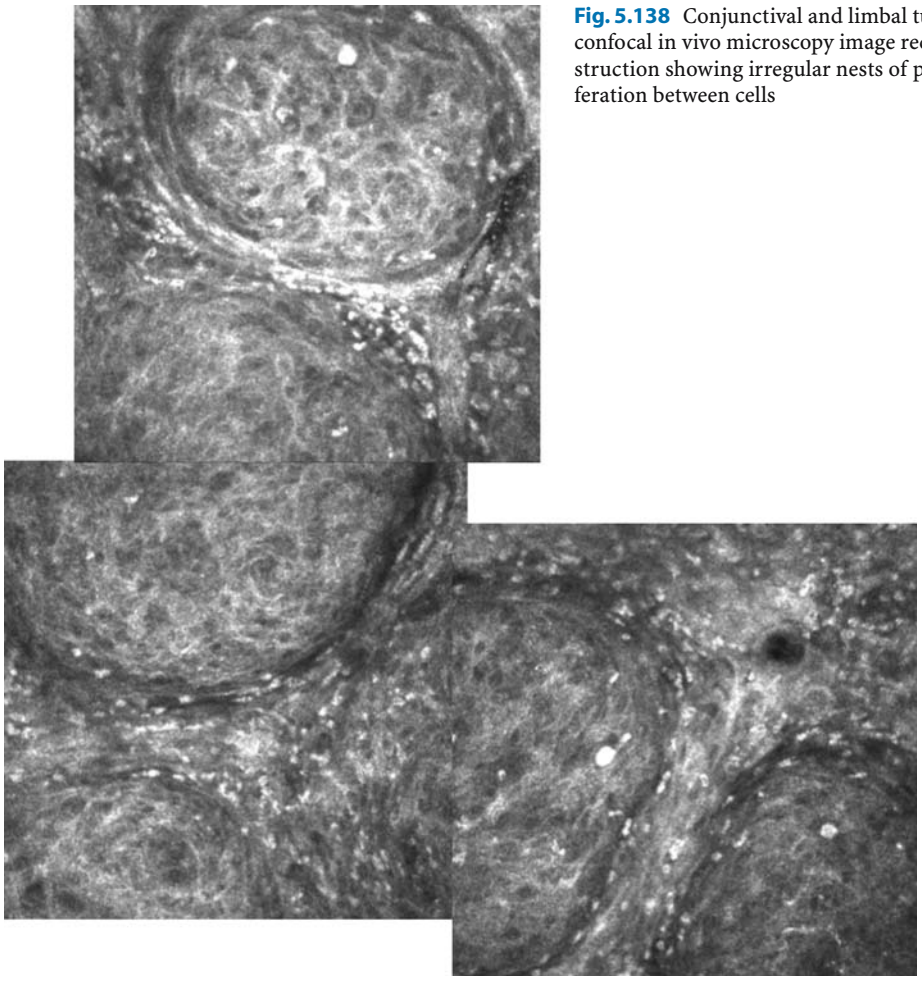

Fig. 5.138 Conjunctival and limbal tumors: confocal in vivo microscopy image reconstruction showing irregular nests of proliferation between cells

5.10 Conjunctiva

The different areas of the conjunctival epithelium display varying morphology.

The tarsal conjunctiva consists of two or three layers of cylindrical epithelium and contains individual goblet cells and lymph vessels. Deep to the epithelium is located the loosely meshed, highly vascular fiber lattice of the lamina propria with its papillary structure; this contains free cells (lymphocytes, plasma cells) and occasional lymph follicles, which are present in vastly increased numbers in inflammatory conditions, as well as smaller glandular packages. The lamina propria is continuous with the deeper-lying subconjunctival lamina, which is denser and is tightly fused with the tarsal plate.

The bulbar conjunctiva, in contrast, is characterized by several layers of squamous epithelium with numerous goblet cells. Deep to the epithelium is a very loosely meshed, highly mobile connective tissue with a pronounced capillary network.

5.10.1 Normal Anatomy

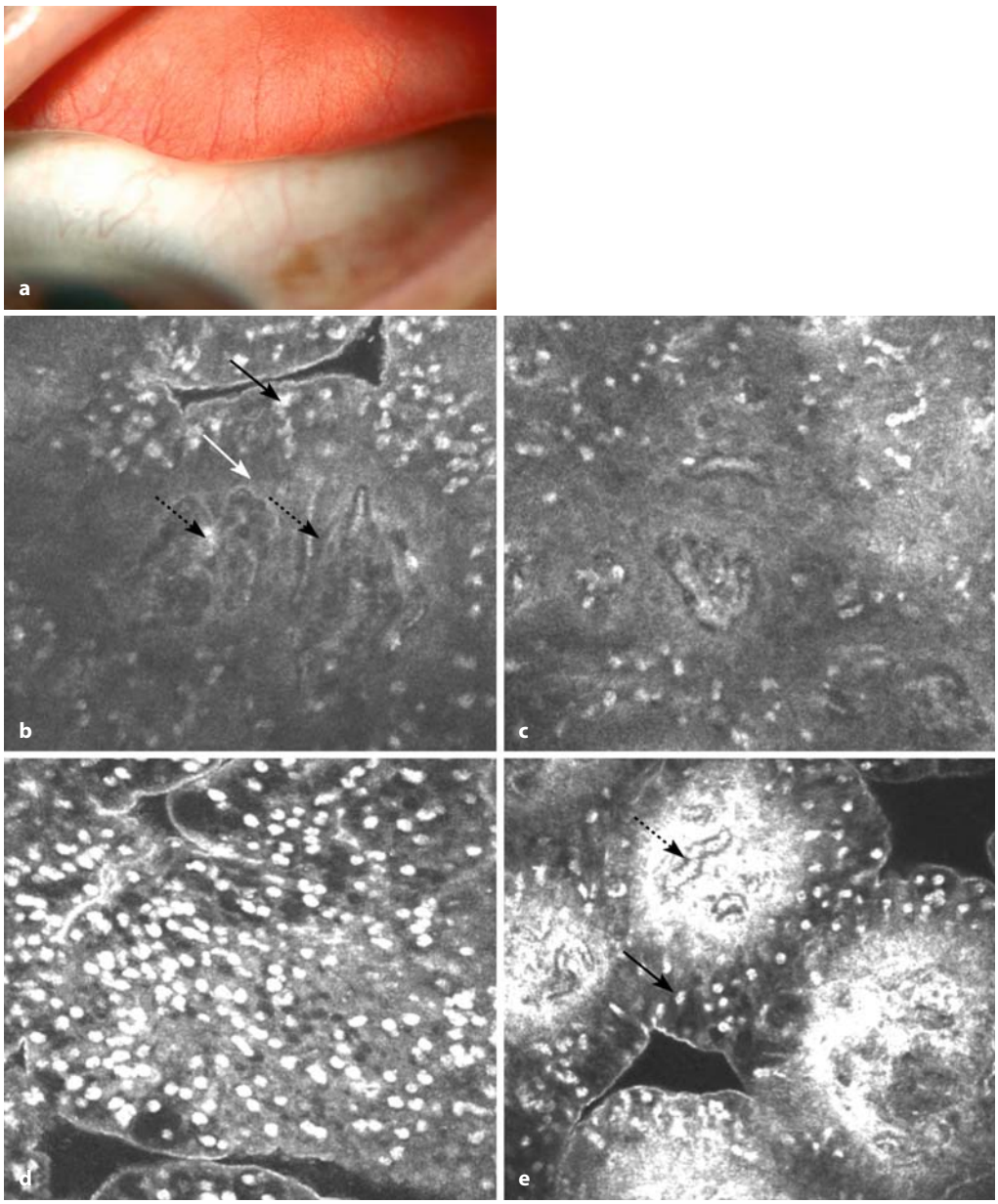

Fig. 5.139 Tarsal conjunctiva. **a** Slit-lamp photograph of the healthy tarsal conjunctiva of the upper lid. **b** Conjunctival epithelium with some highly reflective cells, possibly goblet cells (*black arrow*); under the basal membrane (*white arrow*) the lamina propria of the underlying connective tissue is seen with numerous small blood vessels and some highly reflective round cells, possibly lymphocytes (*dashed-line arrows*). **c** Subconjunctival connective tissue with blood vessels and highly reflective cells (lymphocytes, plasma cells). **d** Lymphatic follicle of the conjunctiva in a healthy person. **e** Epithelium (*black arrow*), lamina propria with blood vessels (*dashed-line arrow*)

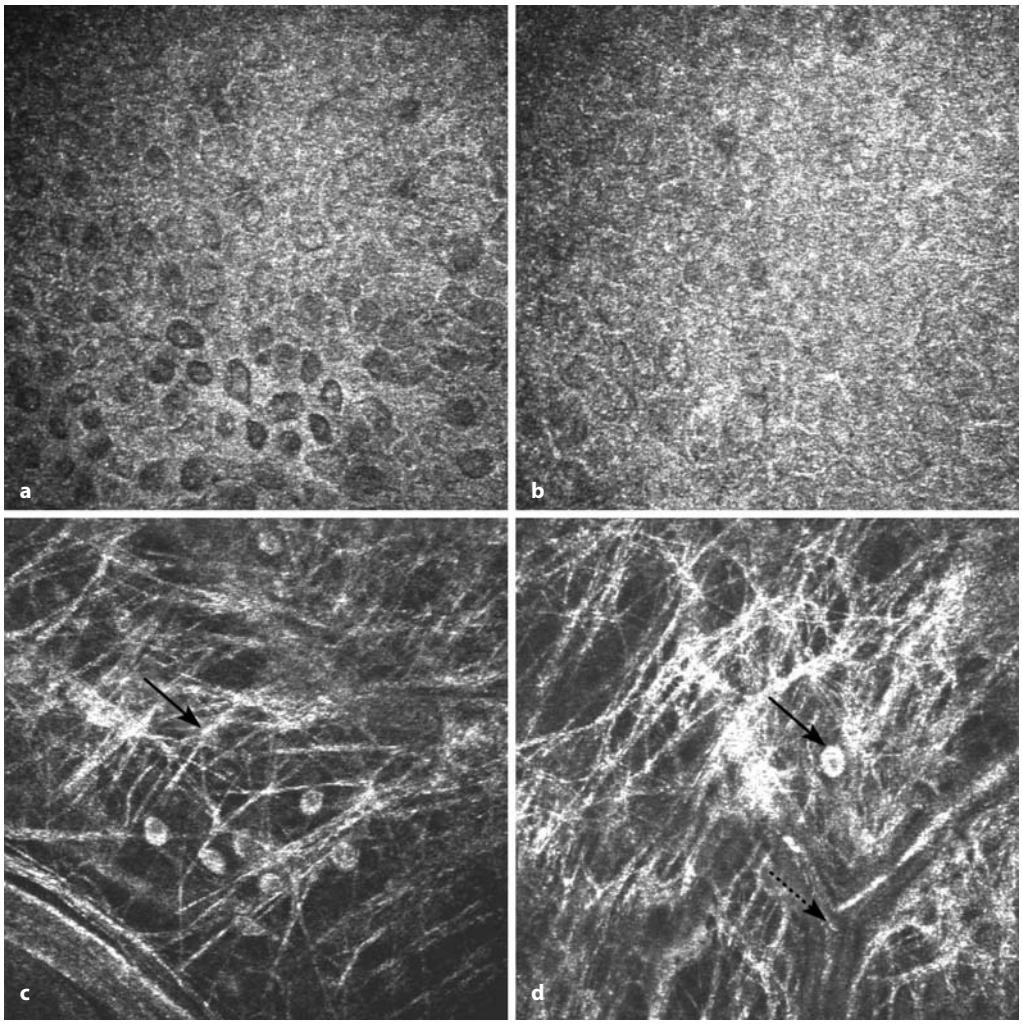

Fig. 5.140 Bulbar conjunctiva. **a** Superficial conjunctival epithelium (z=3 µm). Tthe epithelial structure is not as well organized as in the cornea; the cell borders are brighter than the cytoplasm, and in some cells a bright nucleus is visible. **b** Deeper conjunctival epithelium (z=10 µm). **c–e** Lamina propria with highly reflective latticelike connective tissue and some highly reflective cells (*black arrows*) and blood vessels (*dashed-line arrows*). **f, g** Oblique sections: epithelium (*black arrow*), underlying connective tissue (*dashed-line arrow*), blood vessels (*white arrow*)

5.10.2 Pathological Findings

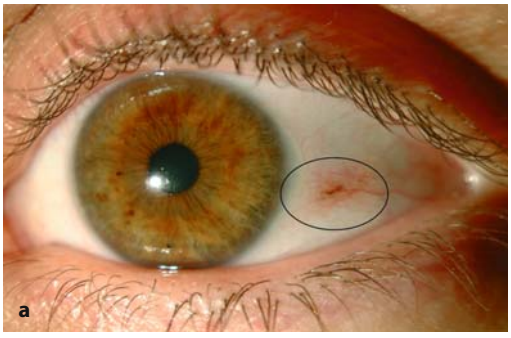

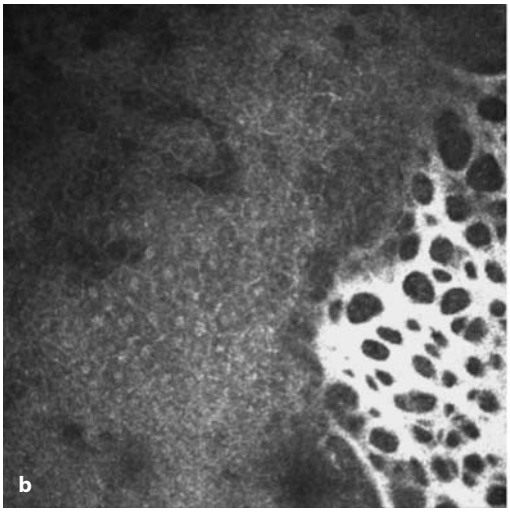

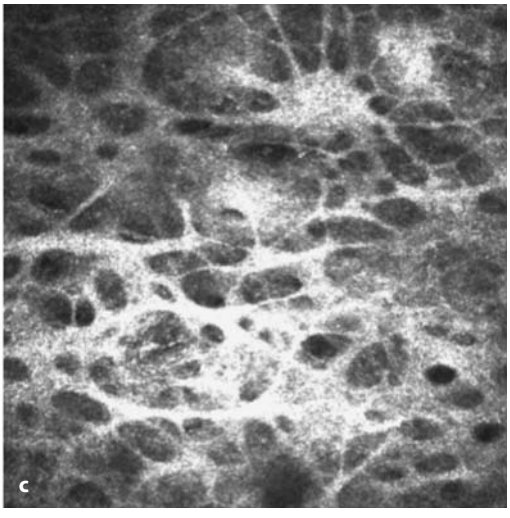

Fig. 5.141 Pinguecula. **a** Slit-lamp photograph of a pinguecula. **b, c** Confocal in vivo microscopy images showing hyperreflective tissue between conjunctival cells

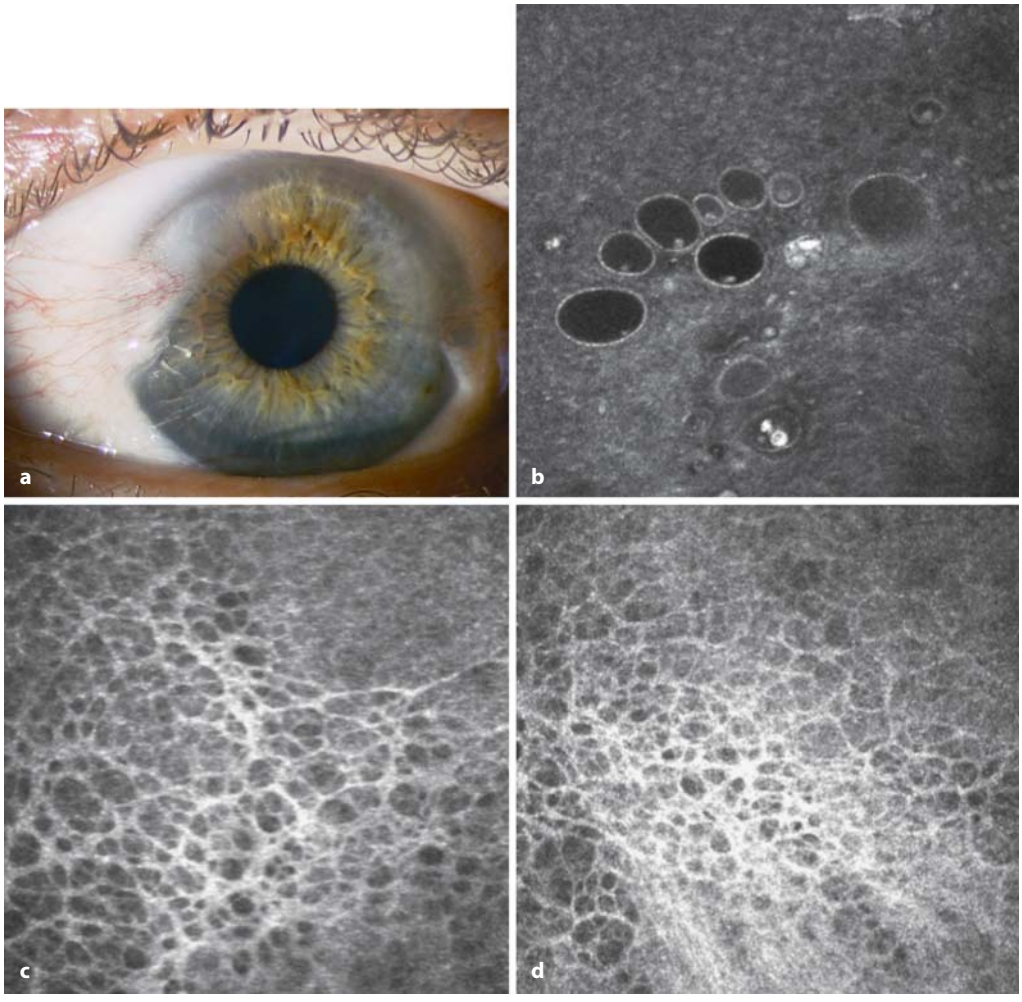

Fig. 5.142 Pterygium. **a** Slit-lamp photograph of a 33-year-old man with pterygium. **b** Superficial confocal in vivo microscopy image of pterygium: microcysts between conjunctival epithelial cells. **c, d** Reflective stroma of pterygium

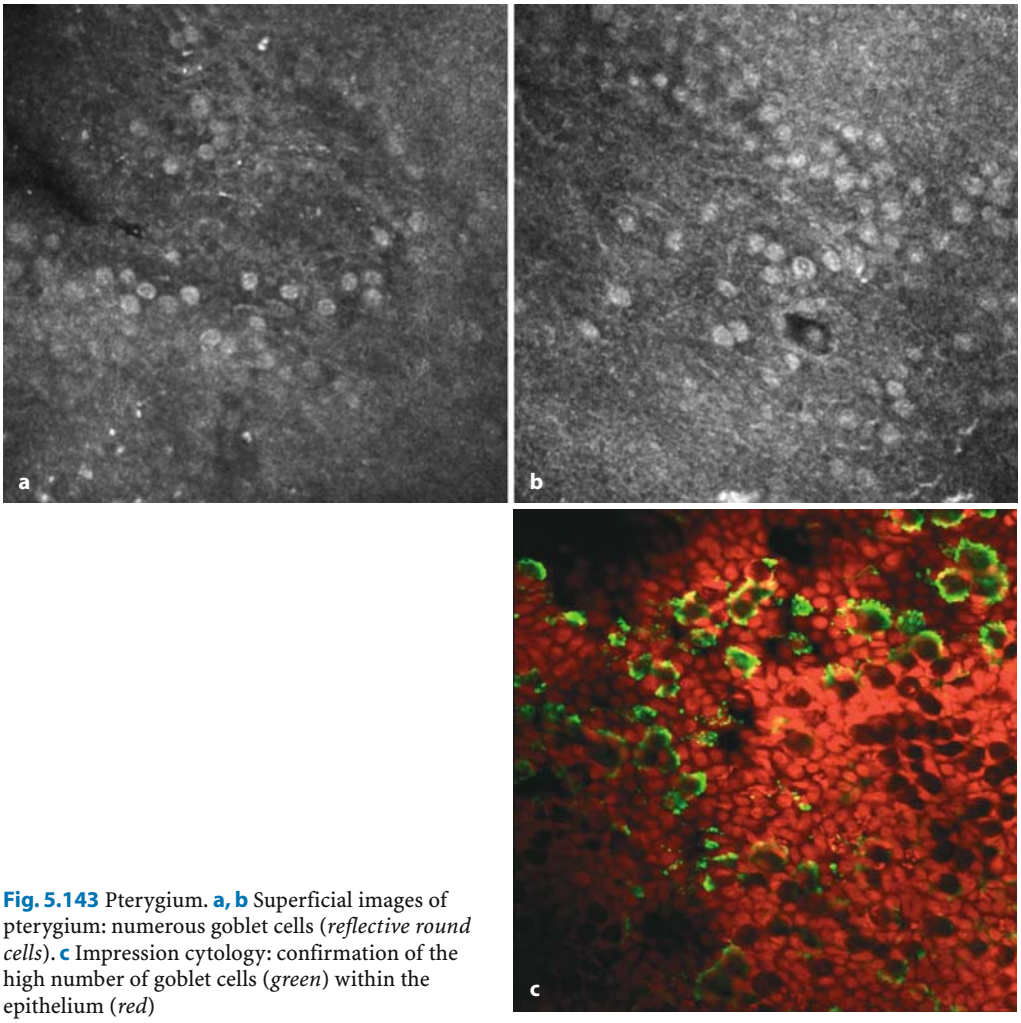

Fig. 5.143 Pterygium. **a, b** Superficial images of pterygium: numerous goblet cells (*reflective round cells*). **c** Impression cytology: confirmation of the high number of goblet cells (*green*) within the epithelium (*red*)

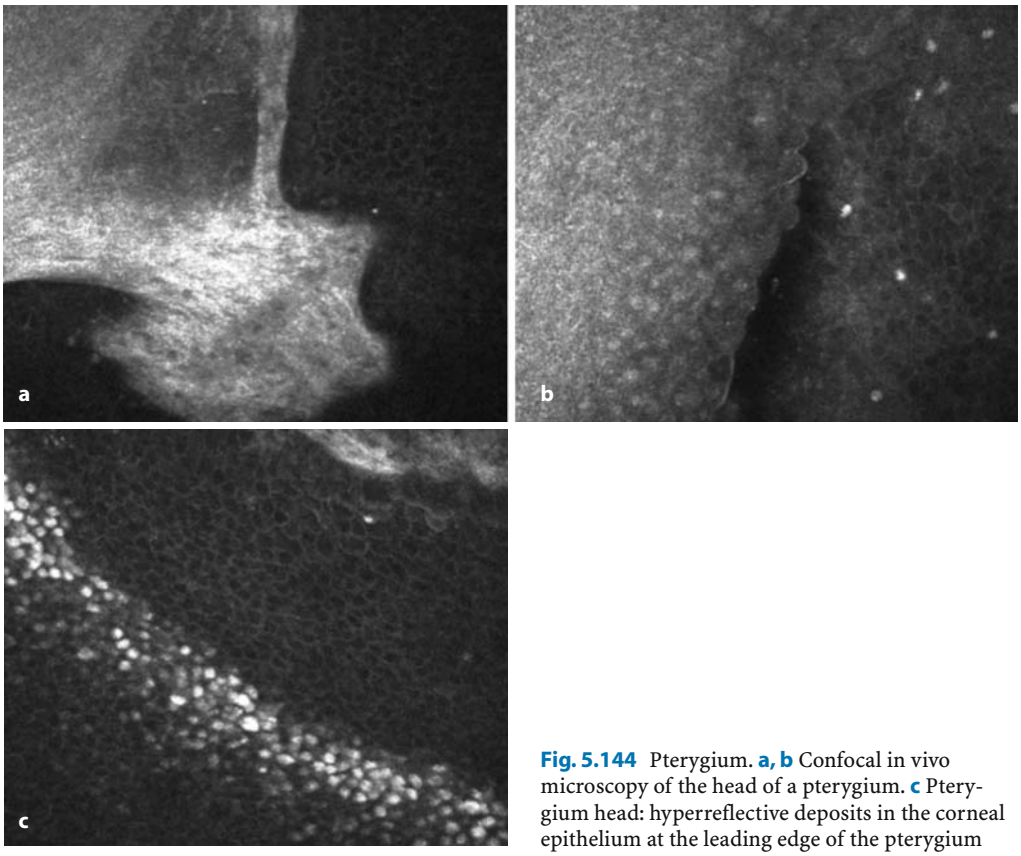

Fig. 5.144 Pterygium. **a, b** Confocal in vivo microscopy of the head of a pterygium. **c** Pterygium head: hyperreflective deposits in the corneal epithelium at the leading edge of the pterygium

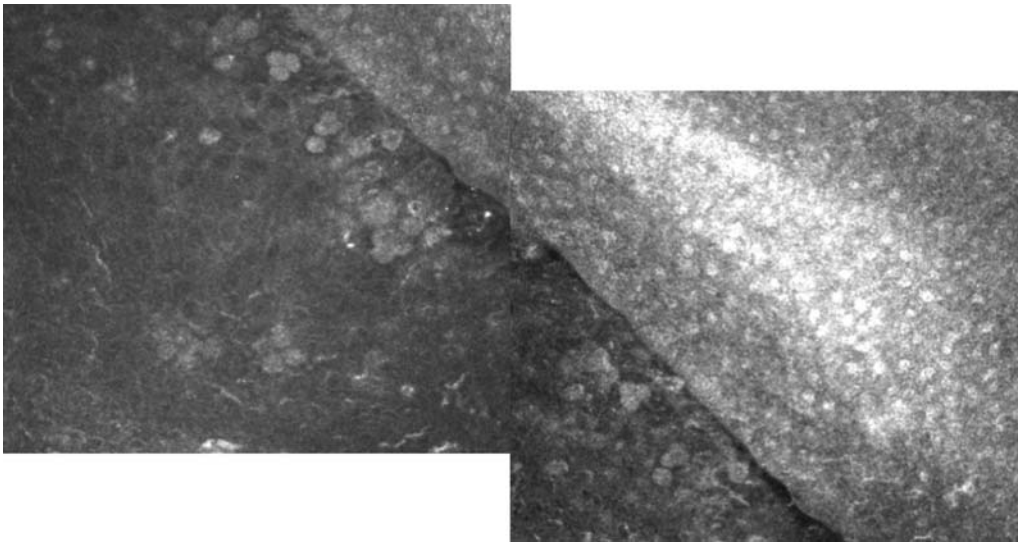

Fig. 5.145 Pterygium. Head of pterygium, infiltration of conjunctival cells (*reflective cells*) within the corneal epithelium at the edge of the pterygium

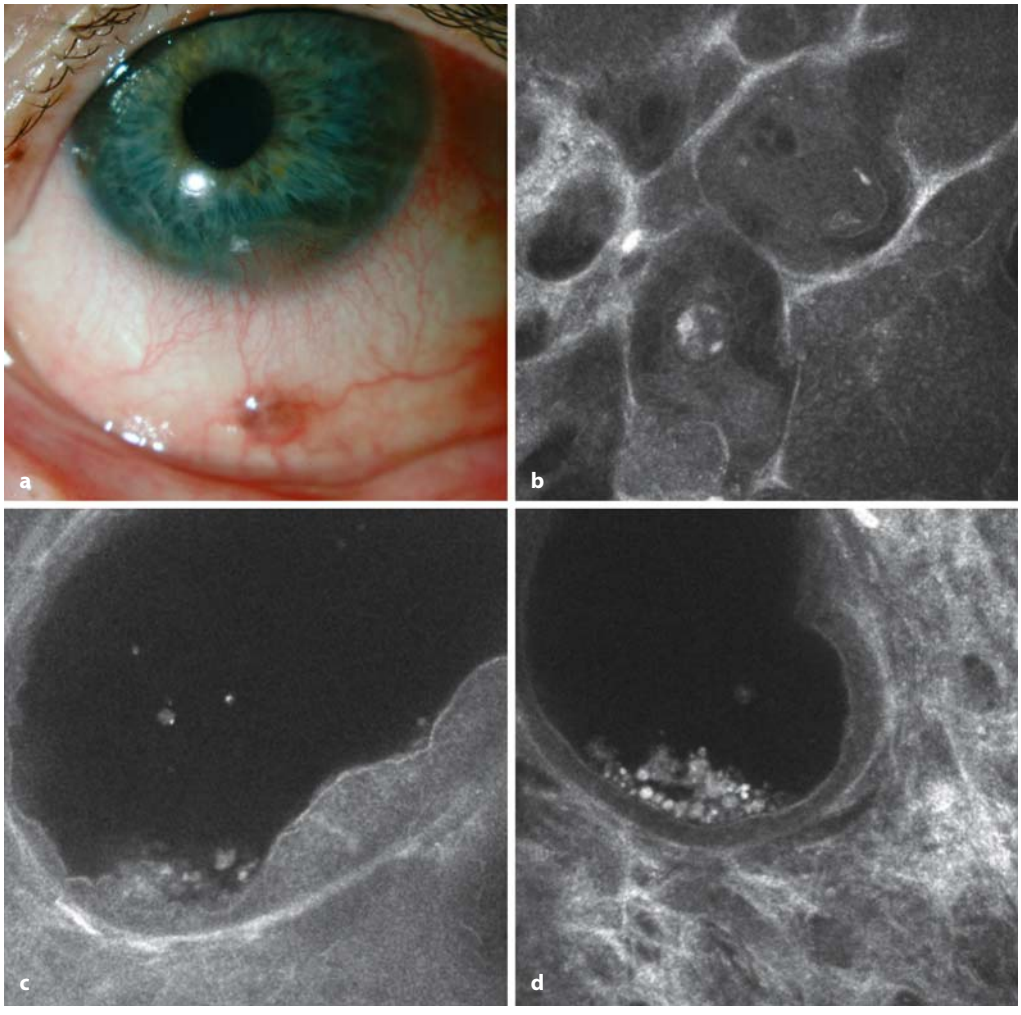

Fig. 5.146 Nevus and conjunctival melanosis. **a** Slit-lamp photograph of a 50-year-old man with an inferior conjunctival nevus. **b–d** Confocal in vivo microscopy images showing cysts within the nevus

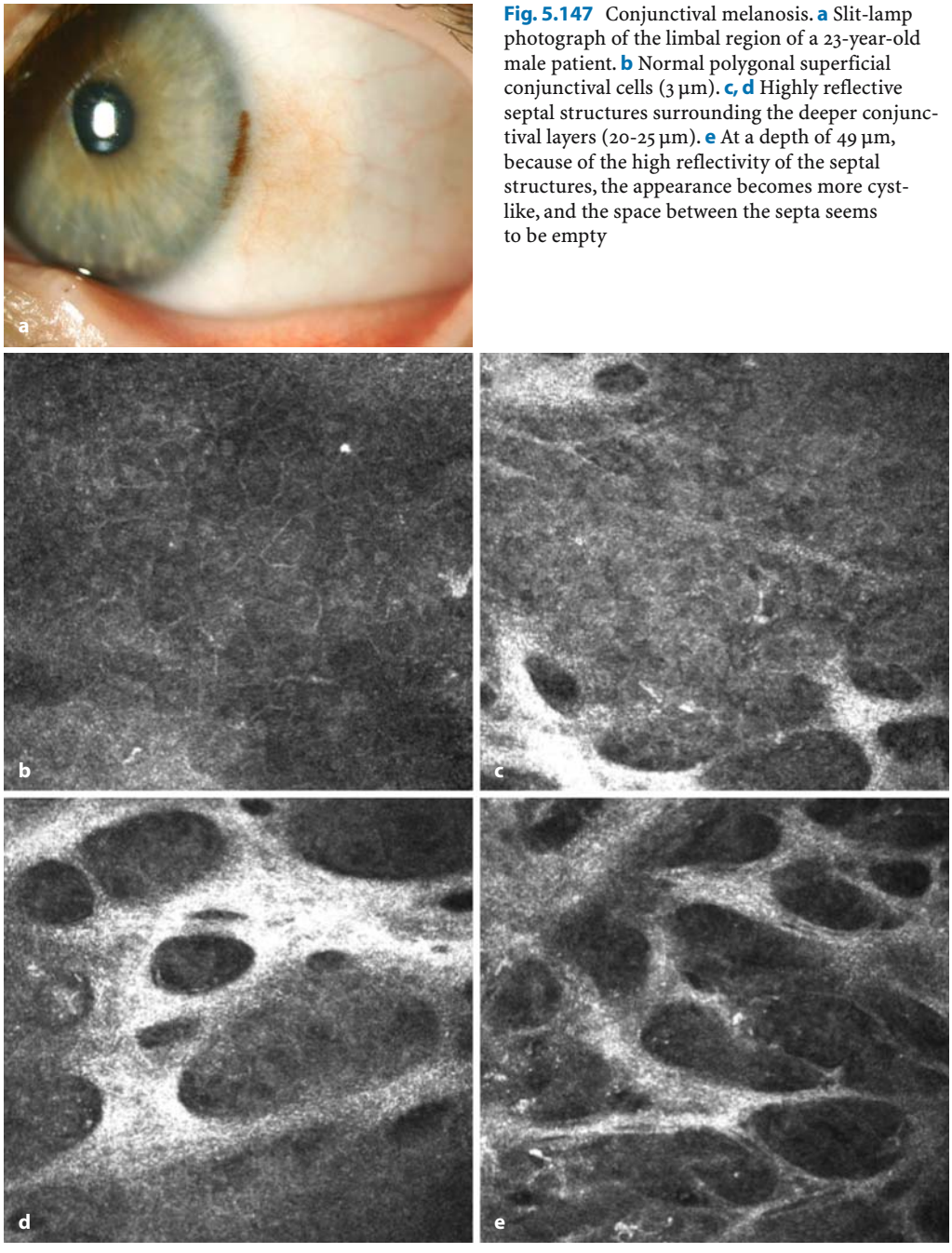

Fig. 5.147 Conjunctival melanosis. **a** Slit-lamp photograph of the limbal region of a 23-year-old male patient. **b** Normal polygonal superficial conjunctival cells (3 µm). **c, d** Highly reflective septal structures surrounding the deeper conjunctival layers (20-25 µm). **e** At a depth of 49 µm, because of the high reflectivity of the septal structures, the appearance becomes more cyst-like, and the space between the septa seems to be empty

5.11 Eyelid

5.11.1 Normal Anatomy

The human eyelid consists of four layers [67]. The innermost layer is the conjunctiva (refer to Sect. 5.10), which is separated from the eyeball by the tear film. The conjunctival tissue comprises a thin layer of nonkeratinized epithelium scattered with goblet cells and a stromal portion containing many blood vessels as well as immunocompetent cells.

Applied closely to the conjunctiva is the tarsal plate of the eyelid. This is a layer of dense fibrous connective tissue that stabilizes and confers shape on the human eyelid [56]. The tarsal plate is one of the main insertion points for the levator palpebrae muscle [2].

A third, muscular layer consists of the orbicularis oculi muscle and parts of the levator palpebrae muscle. The orbicularis oculi muscle is notionally divided into three zones: orbital, preseptal, and pretarsal.

The outermost layer of the eyelid is the epidermis. Compared with the surrounding epidermal structures, the eyelid epidermis is extremely thin, comprising only three to four cell layers. The eyelid margin is covered with cutaneous epithelium [96]. A mucocutaneous junction with the conjunctiva, known as Marx's line or the gray line, is located at the inner edge of the margin [15]. At its anterior edge the eyelashes emerge, and the inner edge contains the excretory ducts of the meibomian glands. A small elevation known as the lacrimal point is located about one-sixth of the distance along the eyelid margin from the medial canthus. The eyelashes are thick, short, curved hairs, characteristically arranged in two or three rows [21].

The human eyelid contains different types of glands, the largest being the meibomian glands. Arranged in 20–25 noncommunicating tubes in each eyelid, these are found in the tarsal plates. Each gland tube has its own orifice through which lipid is secreted. Images of the meibomian glands obtained by confocal in vivo microscopy have been presented in the literature [36, 55]. However, confocal visualization appears to be problematic because of the deep location of these glands in the tarsal plate.

Smaller glands found in the eyelid are the accessory glands of Wolfring, located at the upper border of the tarsal plate, and the accessory glands of Krause, located near the fornix. The glands of Zeis, which are attached directly to the follicles of the eyelashes, produce a sebaceous secretion. The glands of Moll, essentially a type of specialized sweat gland, are situated close to the eyelid margin. Sweat glands are found scattered throughout the dermal layer of the eyelid [67].

The function of the eyelid is to protect the eye from trauma and excessive light. With each blink of the eyelids, the tear film is spread over the eyeball to protect it from drying (see Sect. 5.1).

The superficial structures of the eyelids can be examined by confocal microscopy, and pathologic changes, such as tumors or inflammation, display changes in microscopic morphology, as illustrated in the following section. Confocal microscopy facilitates objective assessment of the clinical situation in blepharitis, not merely in terms of diagnosis and disease severity but also for the purposes of classification and as an aid in deciding whether additional anti-inflammatory therapy is necessary.

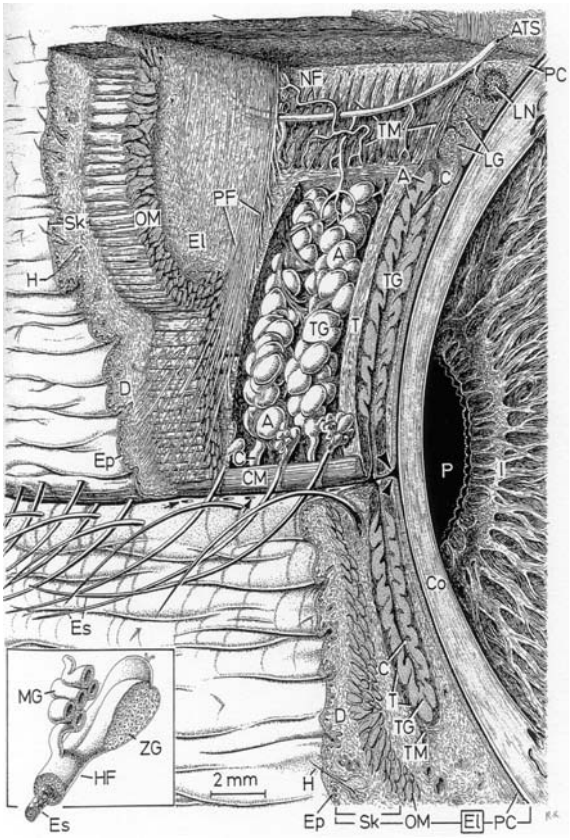

Fig. 5.148 Schematic illustration of the eyelid structures (adapted from Krstić RV. *Human Microscopic Anatomy: An Atlas for Students of Medicine and Biology*. Berlin, Heidelberg, New York: Springer-Verlag, 1991 [39])

Fig. 5.149 Slit-lamp photograph of the normal eyelid

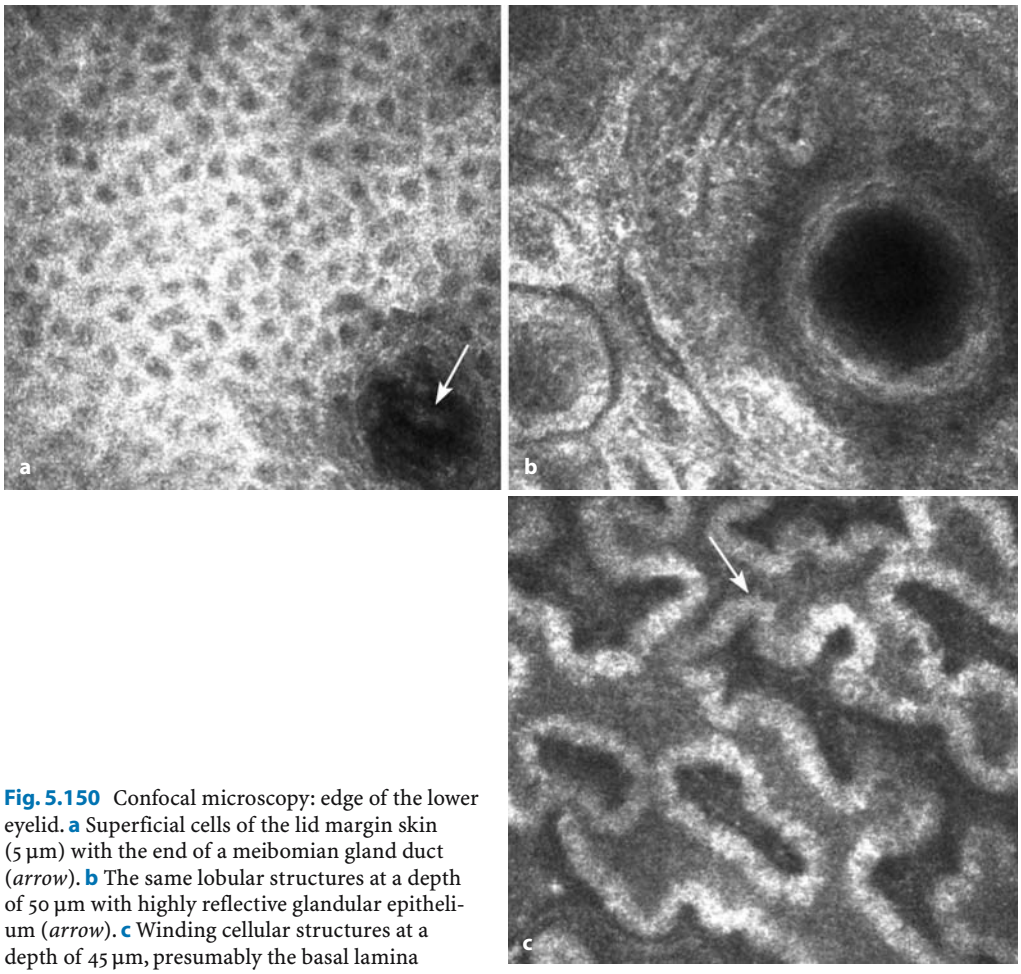

Fig. 5.150 Confocal microscopy: edge of the lower eyelid. **a** Superficial cells of the lid margin skin (5 µm) with the end of a meibomian gland duct (*arrow*). **b** The same lobular structures at a depth of 50 µm with highly reflective glandular epithelium (*arrow*). **c** Winding cellular structures at a depth of 45 µm, presumably the basal lamina

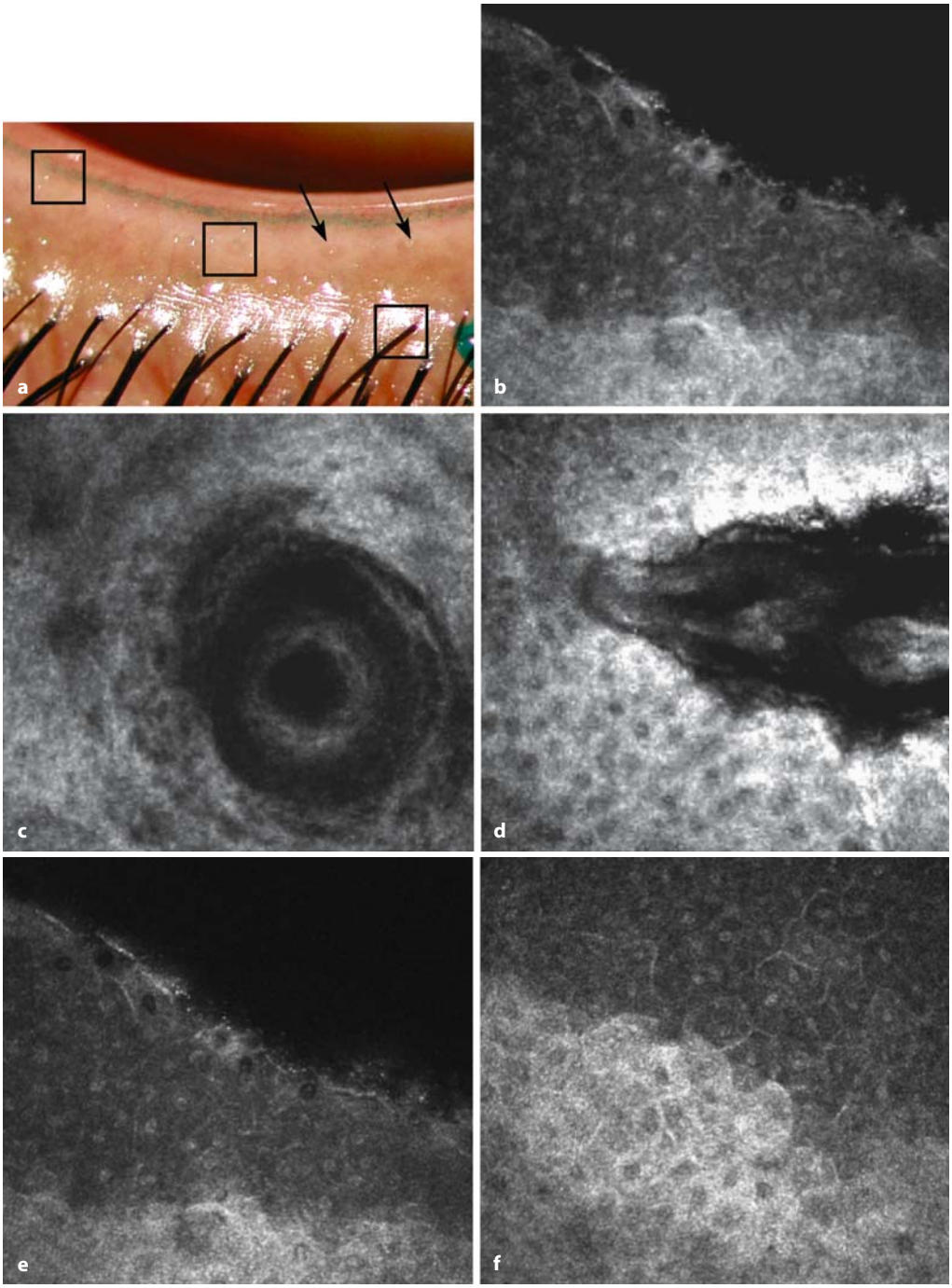

Fig. 5.151 **a** Slit-lamp photograph of the lower eyelid. Marx's line is stained with lissamine green. *Arrows* indicate the location of the orifices of the meibomian glands. **b** Confocal image of the inner edge of the eyelid and the mucocutaneous junction. **c** Excretory duct of a meibomian gland. **d** Hair follicle of an eyelash. **e, f** Confocal image of Marx's line, the junction between the cutaneous eyelid epithelium (*lighter cells*) and the tarsal conjunctiva (*darker cells*)

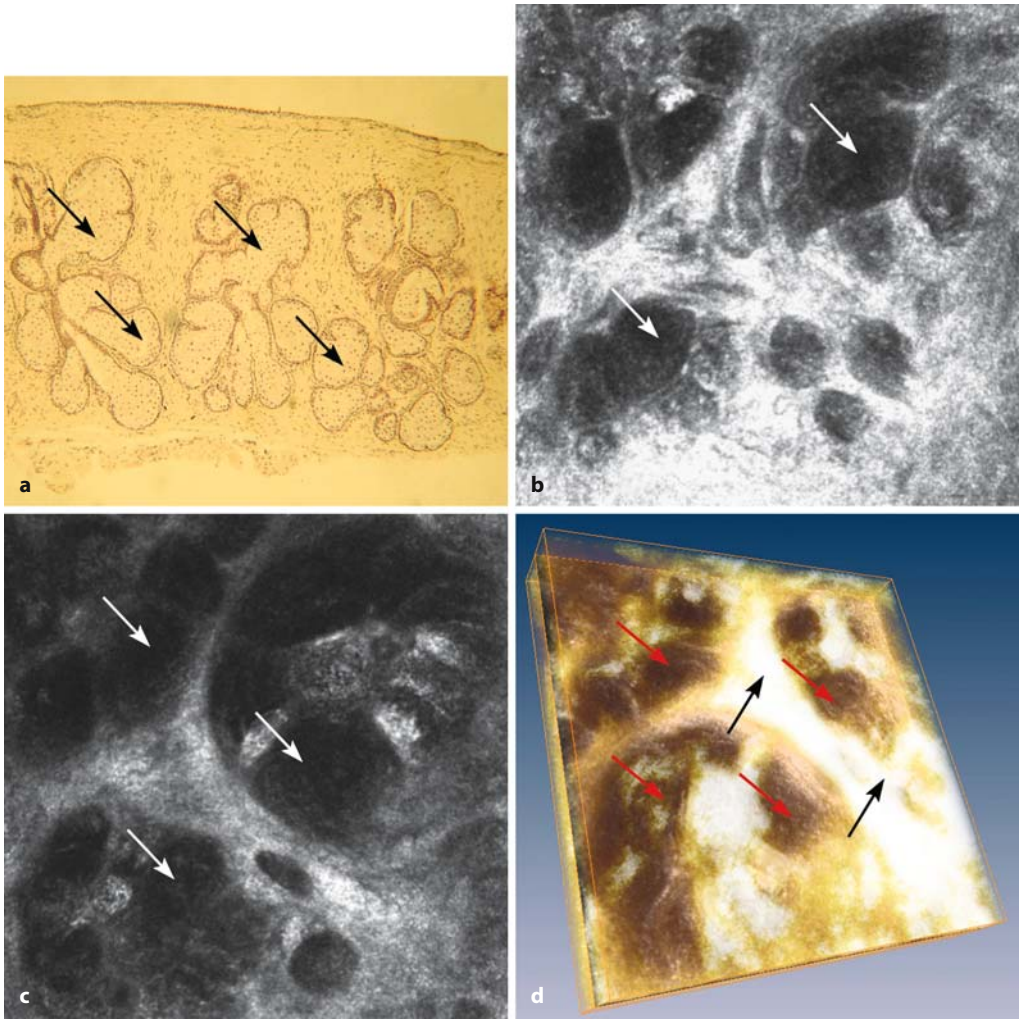

Fig. 5.152 Meibomian glands. **a** Histological sagittal section of the human eyelid. Meibomian glands are marked with *arrows*. **b, c** Confocal images obtained from a sagittal eyelid section ex vivo immediately after excision. Depth difference between the pictures is 20 µm. The meibomian glands are marked with *arrows*. **d** Three-dimensional reconstruction of the image series, showing the meibomian glands (*red arrow*) within the fibrous tissue of the tarsal plate (*black arrows*)

5.11.2 Pathological Findings

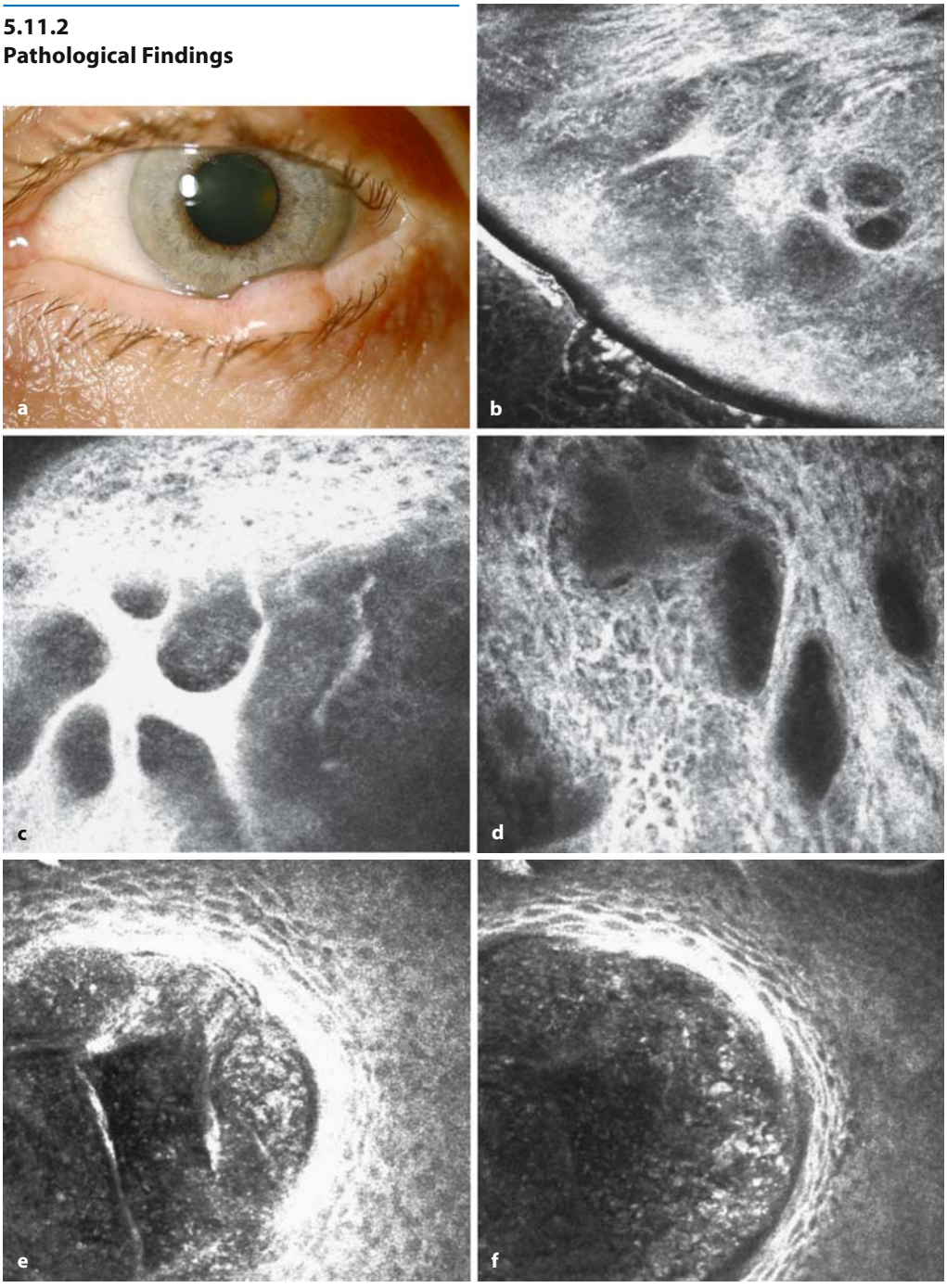

Fig. 5.153 Papilloma. **a** Slit-lamp photograph of the lower lid of a 64-year-old woman. **b** Confocal microscopy (45 µm) of the edge of the lesion (oblique section): the tear film is visible in the lower left corner. **c** Confocal microscopy (51 µm): highly reflective septa due to the lobular structure of the lesion. **d** In the deeper layers the lesion appears show cystic organization. **e, f** Center of the lesion, superficial (7–12 µm): cystic structure surrounded by epithelium. This may be an enlarged meibomian or other gland

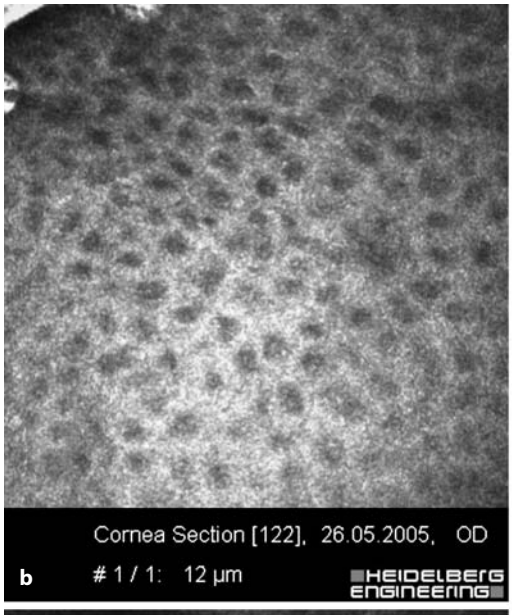

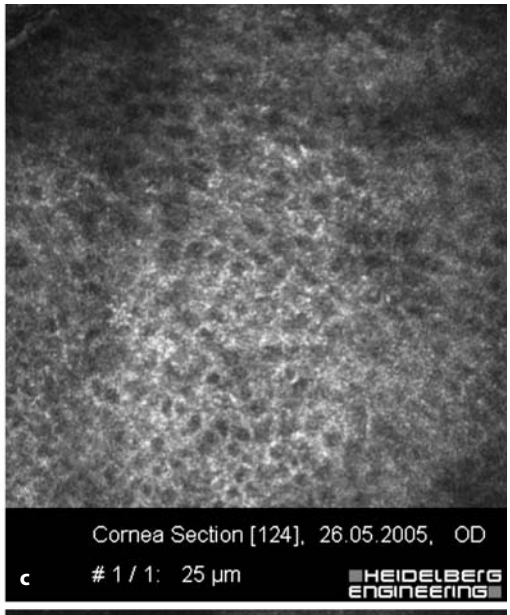

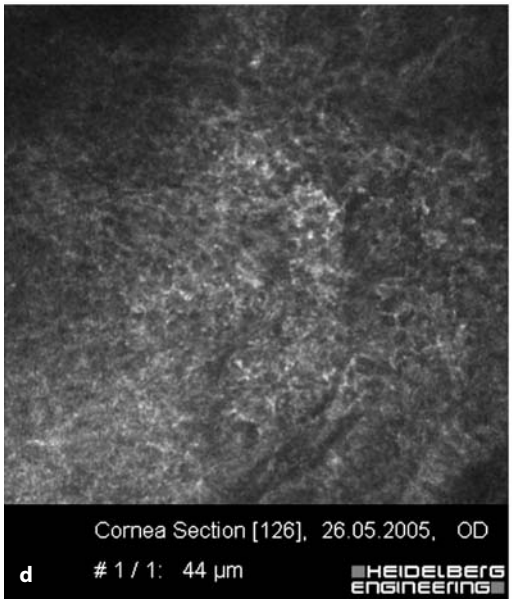

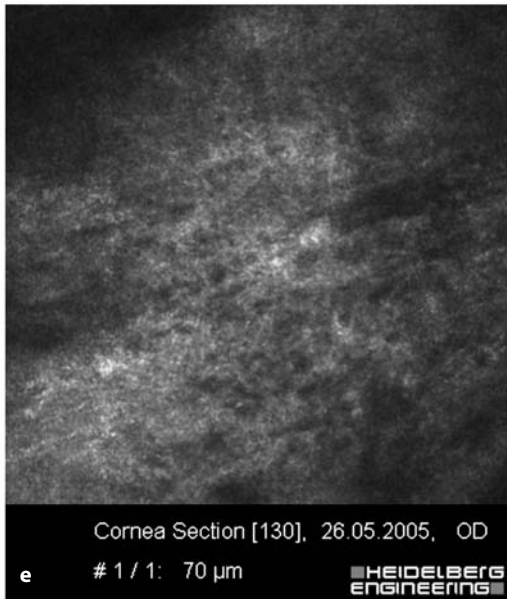

Fig. 5.154 Basal cell carcinoma. **a** Slit-lamp photograph of the lower lid of the right eye of a 69-year-old man. **b–e** Confocal microscopy: irregular epithelium with varying cell size and shape, especially in the deeper layers

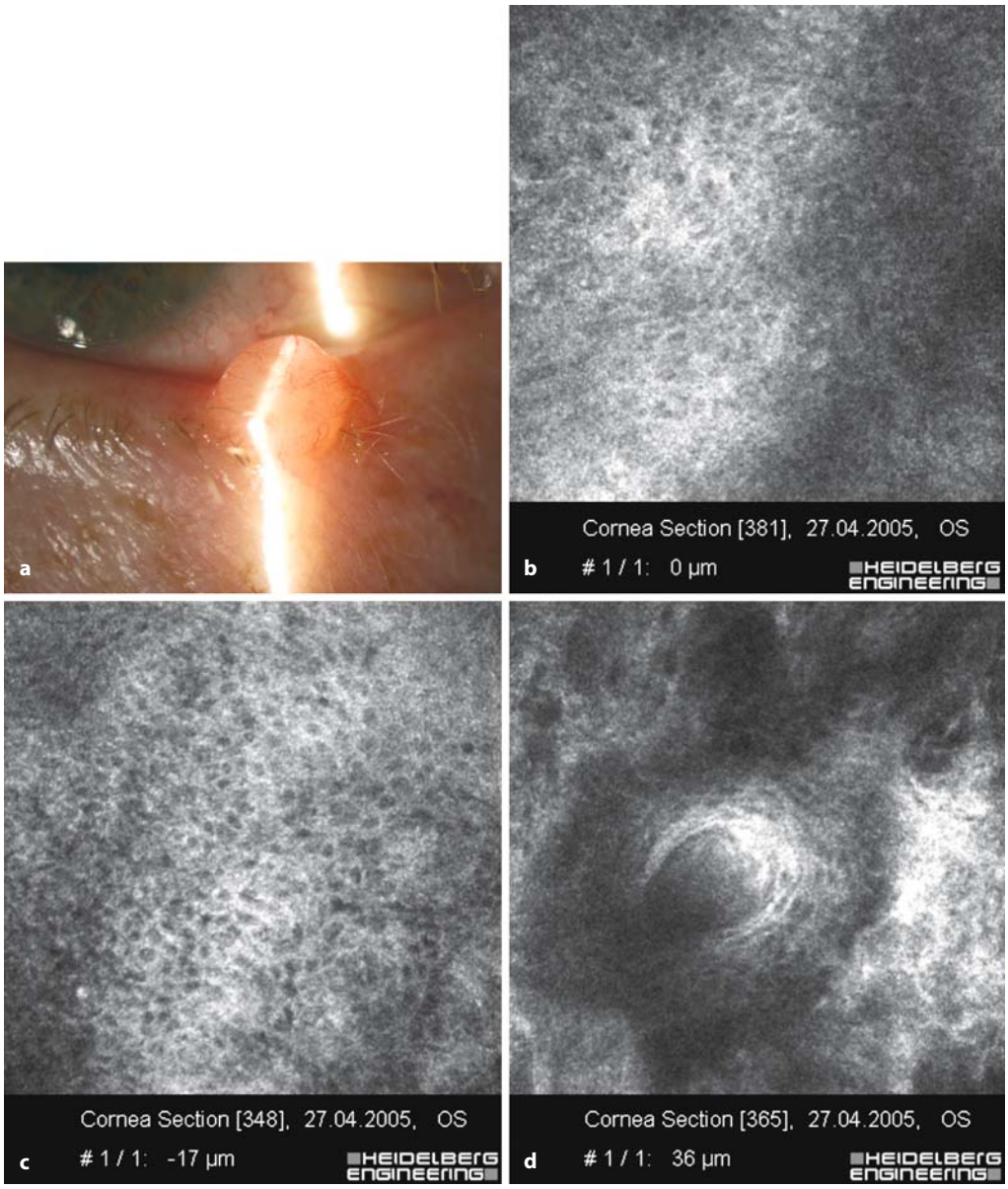

Fig. 5.155 a–f Basal cell carcinoma. **a** Nodular basal cell carcinoma of the lower lid of the right eye in a 76-year-old male patient. **b, c** Confocal microscopy: irregular epithelium with varying cell size and shape. **d–f** Completely irregular and polymorphic histology in the deeper layers with glandlike and cystlike structures

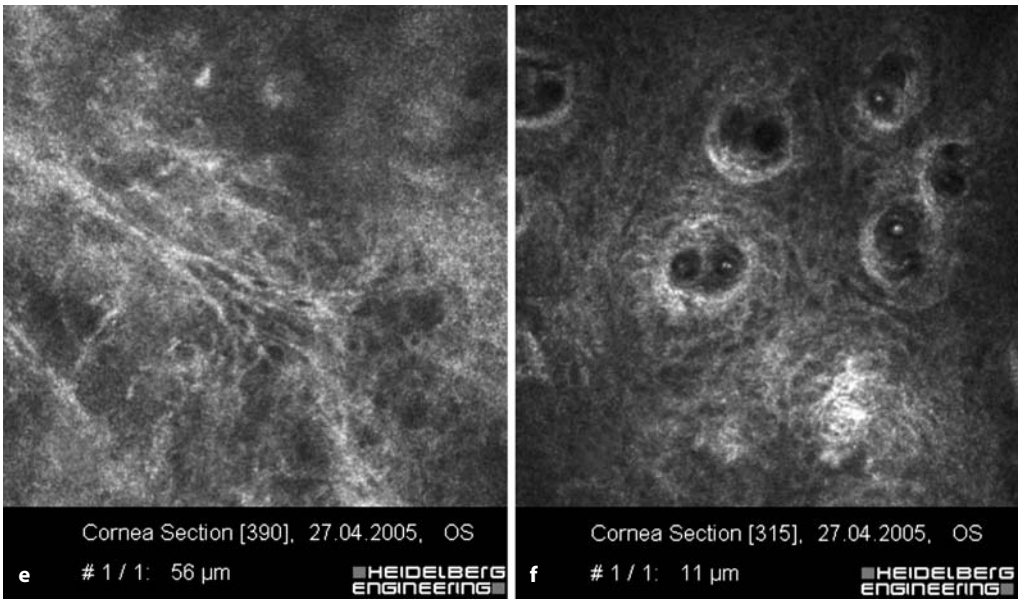

Fig. 5.155 (*continued*) **d–f** Completely irregular and polymorphic histology in the deeper layers with gland-like and cystlike structures

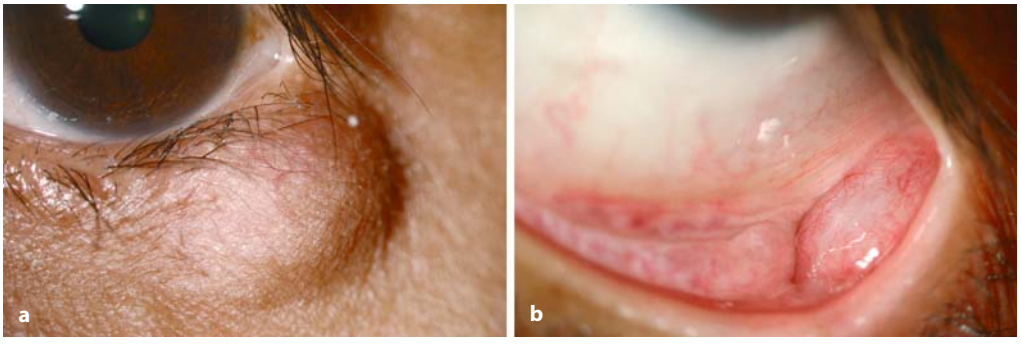

Fig. 5.156 **a–e** Chalazion. **a, b** Slit-lamp photographs of a 45-year-old woman with a chalazion

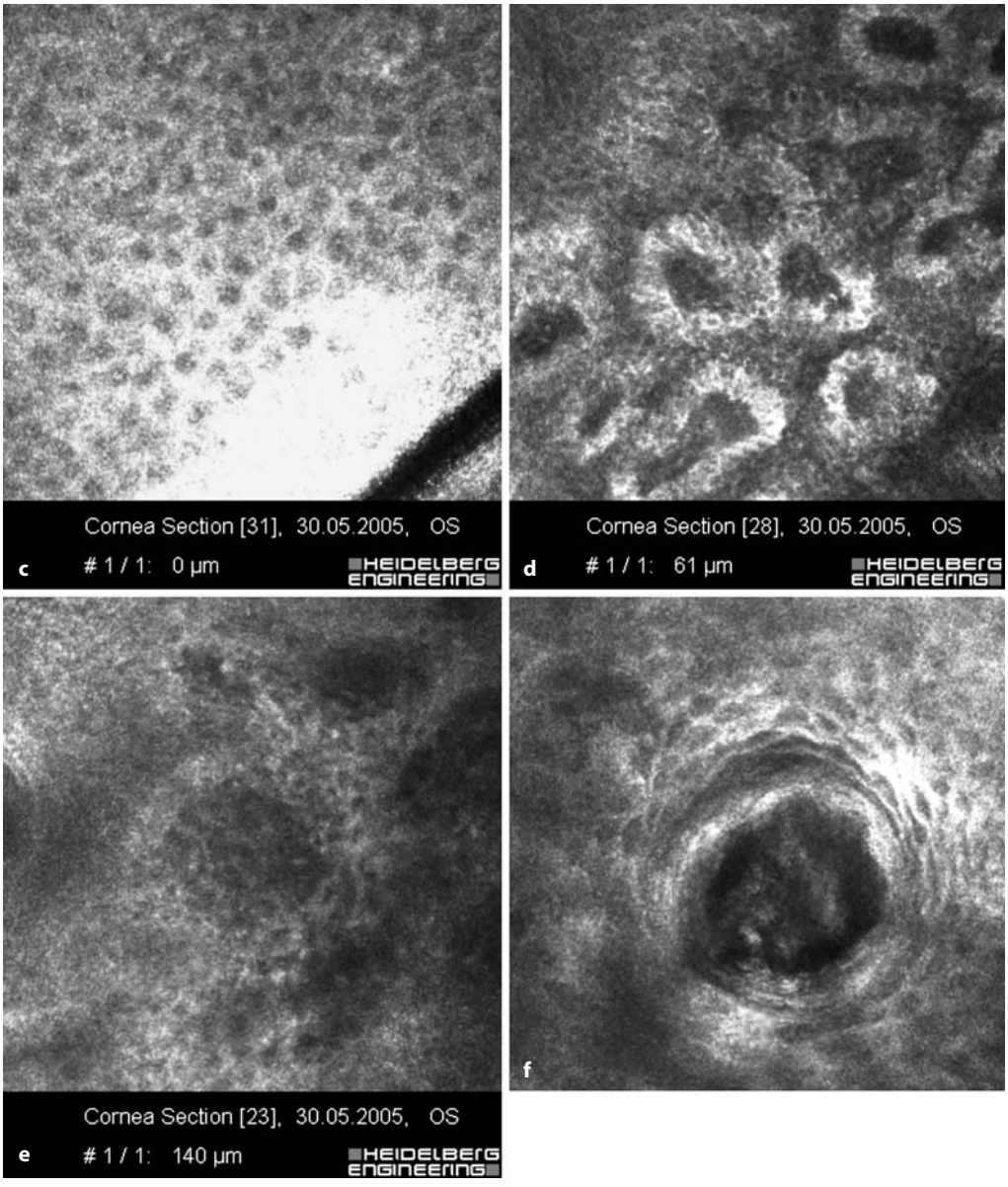

Fig. 5.156 (*continued*) **c–e** Confocal microscopy through the conjunctiva: conjunctival epithelium (**c**), deeper lobular structures, presumably horizontal cone sections of the epithelial layers (**d, e**). **f** Obstructed excretory duct of a meibomian gland